https://doi.org/10.15388/vu.thesis.417
https://orcid.org/0000-0003-0697-3404

VILNIAUS UNIVERSITETAS
FIZINIŲ IR TECHNOLOGIJOS MOKSLŲ CENTRAS

Agnė Zdaniauskienė

Biomolekulių charakterizavimas nanodalelių, padengtų apsauginiu sluoksniu, sustiprinta Ramano spektroskopija

DAKTARO DISERTACIJA

Gamtos mokslai,
Chemija (N 003)

VILNIUS 2022

Disertacija rengta 2018–2022 metais Fizinių ir technologijos mokslų centre. Mokslinius tyrimus rėmė Lietuvos mokslo taryba.

Mokslinis vadovas – **prof. habil. dr. Gediminas Niaura** (Fizinių ir technologijos mokslų centras, gamtos mokslai, chemija, N 003).

Gynimo taryba:

Pirmininkas – prof. dr. Ričardas Makuška (Vilniaus universitetas, gamtos mokslai, chemija, N 003).

Nariai:

prof. dr. Justinas Čeponkus (Vilniaus universitetas, gamtos mokslai, fizika, N 002),

prof. dr. Tautgirdas Ruzgas (Malmės universitetas, gamtos mokslai, mokslo kryptis, chemija, N 003),

prof. dr. Aušra Valiūnienė (Vilniaus universitetas, gamtos mokslai, chemija, N 003),

dr. Linas Vilčiauskas (Fizinių ir technologijos mokslų centras, gamtos mokslai, chemija, N 003).

Disertacija ginama viešame Gynimo tarybos posėdyje 2022 m. gruodžio mėn. 16 d. 10 val. Fizinių ir technologijos centro D401 auditorijoje. Adresas: Saulėtekio al. 3, Vilnius, Lietuva), tel. +370 52649211; el. paštas: office@ftmc.lt.

Disertaciją galima peržiūrėti Vilniaus universiteto ir Fizinių ir technologijos mokslų centro bibliotekose ir VU interneto svetainėje adresu: *https://www.vu.lt/naujienos/ivykiu-kalendorius*

https://doi.org/10.15388/vu.thesis.417
https://orcid.org/0000-0003-0697-3404

VILNIUS UNIVERSITY
CENTER FOR PHYSICAL SCIENCES AND TECHNOLOGY

Agnė Zdaniauskienė

Characterization of biomolecules by shell-isolated nanoparticle-enhanced Raman spectroscopy

DOCTORAL DISSERTATION

Natural sciences,
Chemistry (N 003)

VILNIUS 2022

The dissertation was prepared between 2018 and 2022 at the Center for Physical Sciences and Technology. The research was supported by the Research Council of Lithuania.

Scientific supervisor – prof. habil. dr. Gediminas Niaura (Center for Physical Sciences and Technology, Natural sciences, Chemistry, N 003).

This doctoral dissertation will be defended in a public meeting of the Dissertation Defence Panel:

Chairman – Prof. Dr. Ričardas Makuška (Vilnius University, Natural sciences, Chemistry, N 003).

Members:

Prof. Dr. Justinas Čeponkus (Vilnius University, Natural sciences, Physics, N 002),

Prof. Dr. Tautgirdas Ruzgas (Malmo University, Natural sciences, Chemistry, N 003),

Prof. Dr. Aušra Valiūnienė (Vilnius University, Natural sciences, Chemistry, N 003),

Dr. Linas Vilčiauskas (Center for Physical Sciences and Technology, Natural sciences, Chemistry, N 003).

The dissertation shall be defended at a public meeting of the Dissertation Defence Panel at 10 h on 16th December 2022 in meeting room D401 of the Center for Physical Sciences and Technology. Address: Saulėtekio av. 3, Vilnius, Lithuania, tel. +370 52649211; e-mail: office@ftmc.lt.

The text of this dissertation can be accessed at the libraries of Vilnius University and Center for Physical Sciences and Technology, as well as on the website of Vilnius University: *https://www.vu.lt/naujienos/ivykiu-kalendorius*

TURINYS

1. ĮVADAS

Biomolekulės, įskaitant makromolekules (baltymus, nukleino rūgštis, angliavandenius, lipidus) ir mažas molekules (pirminius metabolitus, natūralius produktus), yra gyvuose organizmuose esančios medžiagos, kurios atlieka esminį vaidmenį cheminiuose, biocheminiuose ir biologiniuose procesuose[1]. Gebėjimas kontroliuoti sąveikas tarp biomolekulių, stebėti procesus, vykstančius fazių riboje, yra itin aktualus bioinžinerijos, farmacijos, aplinkos tyrimų ir kitoms mokslo sritims[2]. Norint suprasti fazių riboje vykstančius procesus, reikalingos molekulinio lygmens žinios. Vis dėlto tirti biomolekulinius vyksmus fazių riboje molekuliniame lygmenyje yra sunku dėl itin mažos tiriamųjų medžiagų paviršinės koncentracijos. Tokiems tyrimams reikia specialių tyrimo metodų, kurie pasižymėtų keliomis esminėmis savybėmis: (i) specifiškumas paviršiui (turi netrukdyti šalutinis signalas nuo tirpalo arba molekulių, esančių medžiagos tūryje), (ii) būtų pakankamai jautrūs, bet nedestruktyvūs, kad būtų galima detektuoti itin mažus medžiagų kiekius ir (iii) galėtų suteikti molekulinio lygmens informaciją apie biomolekulių savitvarką, sudėtį, struktūrą, funkciją ir orientaciją. Vienas tokių tyrimų metodų – paviršiaus sustiprinta Ramano spektroskopija (ang. *Surface-Enhanced Raman Spectroscopy,* SERS). SERS populiarumą biomolekulių tyrimuose taip pat lėmė ir silpna vandens Ramano sklaida, todėl biomolekules galima tirti jų natūralioje aplinkoje[3]. Tačiau SERS turi keletą fundamentinių trūkumų, apribojančių metodo taikymą fazių riboje esančių biomolekulių tyrimuose. Pagrindinis SERS trūkumas – Ramano signalo stiprinimui naudojami Au, Ag, arba Cu šiurkštūs paviršiai, nanostruktūros ar nanodalelės. Metalai gali tiesiogiai sąveikauti su tiriamomis biomolekulėmis taip modifikuodami visą tiriamą sistemą. Taip pat atliekant tyrimus elektrocheminėje fazių riboje gali susidaryti kontaktinis potencialų skirtumas tarp naudojamos nanodalelės ir tiriamo metalo paviršiaus su adsorbatu. Taigi daugiau nei prieš dešimt metų buvo pasiūlyta kaip alternatyvą šiurkštiems paviršiams panaudoti Au ir Ag nanodaleles, apsaugotas plonu SiO_2 sluoksniu (Au@SiO_2, Ag@SiO_2)[4]. Tokiu atveju nanodalelės branduolys sustiprina Ramano sklaidos signalus, o išorinis dielektrinis apvalkalas tuo pat metu neleidžia metalui tiesiogiai sąveikauti su tiriamomis ar aplinkos molekulėmis ir apsaugo nanodaleles nuo degradacijos ar oksidacijos. Toks patobulintas paviršiaus sustiprintos Ramano spektroskopijos metodas, pavadintas nanodalelių, padengtų apsauginiu sluoksniu, sustiprinta Ramano spektroskopija (ang. *Shell-Isolated Nanoparticle-Enhanced Raman Spectroscopy*, SHINERS) atvėrė naujas galimybes adsorbcijos, katalizės,

krūvio pernašos ir kitų procesų tyrimuose ant lygių, monokristalinių paviršių, taip pat ant dvidimensinių medžiagų. SHINERS tapo itin perspektyviu bet kokių paviršių tyrimo metodu. Šioje disertacijoje tirti skirtingi objektai, kuriuos vienija molekuliniame lygmenyje charakterizuojamos biomolekulės, esančios fazių riboje. Darbe pademonstruotos SHINERS metodo galimybės ir iššūkiai tiriant nevienodas molekulines sistemas, atskleisti skirtingų biomolekulių struktūros bei funkcijos ypatumai.

Pagrindinis **disertacijos tikslas** – pritaikyti SHINERS metodą fazių riboje esančių biomolekulių (nuo savitvarkių monosluoksnių iki gyvų mikroorganizmų) molekulinės struktūros ir funkcionalumo tyrimuose. Šiam tikslui pasiekti buvo suformuluoti 4 **uždaviniai**:

1. Susintetinti ir charakterizuoti skirtingos prigimties dielektriniais apvalkalais dengtas plazmonines nanodaleles, rasti optimaliausias sąlygas didesnių nei 50 nm dydžio plazmoninės šerdies ir 2 – 3 nm inertinio apvalkalo storio nanodalelių sintezei.

2. Charakterizuoti savitvarkį monosluoksnį, suformuotą iš tiolių su funkcine imidazolo žiedo ir amido grupėmis grandinėje, elektrocheminiu SHINERS (ang. *Electrochemical Shell-Isolated Nanoparticle-Enhanced Raman Spectroscopy*, EC-SHINERS) metodu.

3. Parodyti SHINERS metodo pritaikymo galimybes siekiant gauti molekulinio lygmens informaciją apie adsorbatus grafeno paviršiuje ir grafeno struktūrinius defektus.

4. Ištirti itin sudėtingą molekulinę sistemą – gyvas mielių ląsteles SHINERS metodu.

Mokslinio darbo aktualumas ir naujumas

Iškeltiems uždaviniams pasiekti buvo pritaikyti skirtingi tyrimų ir analizės metodai. Visus tyrimų ir analizės metodus galima suskirstyti į 3 grupes pagal taikymo sritis: nanodalelių su išoriniu apvalkalu sintezė ir charakterizavimas, monosluoksnių ir kitų modelinių molekulinių sistemų formavimas bei biomolekulinių sistemų tyrimas ir analizė.

Taigi, pirmiausia, aukso ir sidabro šerdies nanodalelės buvo sintetinamos keliais skirtingais būdais modifikuojant J. F. Li ir kt. bei F. Liu ir kt. sintezės metodus[5,6], išbandyti skirtingos prigimties nanodaleles izoliuojantys apvalkalai ir jų stabilumas skirtinguose organiniuose tirpikliuose. Pirmą kartą rastos optimalios sintezės sąlygos 90 ± 10 nm šerdies

dydžio Ag nanodalelėms su 2,5 – 3 nm storio SiO_2 apvalkalu naudojant sidabro nitratą ir tik vieną redukuojantį bei stabilizuojantį agentą – natrio citratą, o apvalkalo formavimui – (3-aminopropil)trietoksilaną (APTES) ir skystą stiklą. Remiantis Au@SiO_2 nanodalelių stabilumo rezultatais skirtinguose tirpikliuose parodyta, kad iki šiol plačiausiai mokslininkų naudojamas silanas apvalkalo formavimo etape – (3-aminopropil)trimetoksilanas (APTMS) nėra itin tinkamas siekiant ilgesnio nanodalelių stabilumo. Formuojant apvalkalą susidaro APTMS šalutinis reakcijos produktas – metanolis, kuris laikui bėgant ardo išorinį apvalkalą. Naudojant APTES šalutinis reakcijos produktas – etanolis, kurio įtaka apvalkalo vientisumui nepastebima. Susintetintų nanodalelių dydis, forma, apvalkalo storis ir defektingumas charakterizuoti didelės skyros pralaidumo elektroninės mikroskopijos, UV-Vis spektroskopijos, ciklinės voltamperometrijos ir Ramano spektroskopijos metodais.

SHINERS eksperimentai pradėti nuo savitvarkių monosluoksnių ant lygių Au paviršių tyrimų. Doktorantūros studijų darbui susintetintas naujas junginys – N-(2-(1H-imidazol-4-il)etil)-6-merkaptoheksanamidas (IMHA), turintis keturias funkcines dalis: (i) paviršiui aktyvi tiolinė grupė (SH); (ii) angliavandenilinė grandinė ($-(CH_2)_5-$); (iii) amido grupė ($-CO-NH-$); (iv) imidazolo žiedas. Imidazolo žiedas (Im) yra aminorūgšties histidino funkcinė grupė, galinti dalyvauti daugybėje molekulinių sąveikų. Viena svarbiausių sąveikos rūšių, kur dalyvauja Im žiedas – pereinamųjų metalų jonų surišimas aktyviuose baltymų centruose, todėl imidazolas atlieka itin svarbų vaidmenį fermentų sandaroje ir veikloje[7]. Amido grupė, įterpta į alkilinę grandinę, sudaro vandenilinių ryšių tinklą tarp gretimų molekulinių grandinių, o tai ženkliai padidina monosluoksnio stabilumą[8]. Skirtingą laiką adsorbavus IMHA ant Au paviršių atspindžio-sugerties infraraudonosios spektroskopijos (ang. *Reflection-Absorption Infrared Spectroscopy*, RAIRS) metodu nustatyta, kad po beveik trijų valandų (162 min) tvarkingo monosluoksnio susidarymas įpusėja, o po 6 valandų monosluoksnis tampa tvarkingas ir tinkamas tolimesniems tyrimams. IMHA adsorbcija ant paviršiaus sukėlė IMHA molekulės tautomerinį pasikeitimą iš tautomero I (N1–H, N3) į tautomerą II (N1, N3–H). EC-SHINERS duomenys įrodė, kad tautomero II forma yra vyraujanti visame potencialo lange ir tik nedidelė molekulių dalis tampa tautomero I formos elektrodo potencialui pasiekus –0,8 V (atž. Ag/AgCl). Ramano temperatūriniai ir tankio funkcijos teorijos (ang. *Density Functional Theory*, DFT) modeliavimo duomenys padėjo nustatyti imidazolo žiedo judėjimo laisvumui ir vandenilinio ryšio stipriui jautrią virpesinę juostą ties 1492 cm^{-1}. Šios juostos analizė atskleidė nuo potencialo priklausomą Im

žiedo elgseną: prie –0,8 V (atž. Ag/AgCl) elektrodo poliarizacijos Im žiedas yra daug labiau suvaržytas ir sudaręs stipresnius vandenilinius ryšius nei esant –0,4 V (atž. Ag/AgCl). Taip pat pirmą kartą nustatyta imidazolo žiedo IMHA monosluoksnyje pK_a vertė, kuri yra 3,14 ± 0,34.

Tiriant adsorbuotą riboflaviną ant grafeno pirmą kartą palyginti grafeno sustiprintos Ramano spektroskopijos (ang. *Graphene-Enhanced Raman Spectroscopy,* GERS) ir SHINERS metodų ypatumai. GERS atveju stiprinami virpesiai tik tų atomų riboflavino žiede, kurie dalyvauja π elektronų sąveikoje. Tuo tarpu SHINERS spektroskopija suteikia išsamią informaciją ne tik apie Rf žiedo virpesius, bet ir apie kai kuriuos ribitilo grandinės virpesius. Taip pat nustatyta, kad kai kurių virpesinių juostų intensyvumas SHINERS spektruose buvo net 26 kartus didesnis lyginant su GERS spektrais. Be to, parodyta, jog SHINERS spektre aiškiai matomos vario oksido, ant kurio padėklo suformuotas grafeno monosluoksnis, anglies tinklo ir grafeno defektų virpesinės juostos. Vis dėlto vienas įdomiausių rezultatų SHINERS spektre – intensyvi, plati juosta apie 1321 cm^{-1}. Juostos kilmę ir prigimtį padėjo išsiaiškinti kvantinės chemijos modeliavimo duomenys, kuomet nustatyta, jog 1321 cm^{-1} juostos atsiradimas gali būti siejamas su riboflavino adsorbcijos sukeltu grafeno sluoksnio išlinkiu ir pakrypimu. Šis pastebėjimas išryškina SHINERS metodo galimybes nustatant lokalias sistemos perturbacijas.

Galiausiai Au@SiO_2 nanodalelės pritaikytos *Metschnikowia pulcherrima* mielių ląstelių tyrimuose, kuomet pirmą kartą užregistruoti *Metschnikowia pulcherrima* SHINERS spektrai. Gauti rezultatai padėjo identifikuoti mielių ląstelių sienelę ir joje esančius funkcinius elementus – baltymus, lipidus ir aminorūgštis. Parodyta, kad naudojant apvalkalu dengtas nanodaleles mielių ląstelių spektrai atsikartoja, virpesinių juostų dažniai nekinta, išorinis apvalkalas neleidžia sąveikauti metalinėms nanodalelėms su ląstelėmis, todėl spektruose neatsiranda papildomų virpesinių juostų. Aminorūgščių, C–N, amidiniai virpesiai atspindi gyvos ląstelės bioaktyvumą, vykstančią baltymų sekreciją, antrinės struktūros kitimą, tai parodo, kad SHINERS metodas tinkamas *in situ* sekti ląstelės biocheminių procesų eigą.

Ginamieji teiginiai

1. SHINERS spektroskopijai optimaliausias – SiO_2 nanodalelių apvalkalas. Patobulinta apvalkalais dengtų nanodalelių sintezės metodika, pakeičiant kaitinimo būdą iš konvekcinio į mikrobangų, leidžia suformuoti didesnes nanodaleles su mažiau defektingu išoriniu dielektriko apvalkalu.

2. Imidazolo žiedo monosluoksnyje pK_a vertė yra daug mažesnė nei laisvo histidino tirpale. Taip pat elektocheminėje fazių riboje, kintant potencialui nuo −0,4 V iki –0,8 V (atž. Ag/AgCl), imidazolo žiedo vandenilinio ryšio sąveika stiprėja.

3. Riboflavino molekulė sąveikauja su grafeno monosluoksniu per π elektroninę sistemą. Riboflavino adsorbcija iššaukia lokalinį grafeno plokštumos išsilenkimą. SHINERS metodas leidžia detaliau ištirti adsorbuotą riboflaviną ant grafeno, lyginant su GERS metodu.

4. SHINERS metodas leidžia gauti patikimus ir atsikartojančius spektrus nuo mielių ląstelių paviršiaus, iš kurių gali būti nustatyti mielių ląstelių sieneles sudarantys funkciniai elementai.

Šioje disertacijoje pateikiamos 6 mokslinės publikacijos, kurios išsprendžia kai kuriuos iššūkius ir suteikia naujų perspektyvų tiriant bei analizuojant biomolekules ar biologines sistemas. Pirmos 3 publikacijos apima pirmąjį disertacijos darbo uždavinį, 4 publikacija – antrąjį, 5 – trečiąjį ir 6 – ketvirtąjį. Visos publikacijų kopijos pateikiamos disertacijos pabaigoje.

1.1. Publikacijų sąrašas

1. T. Charkova, **A. Zdaniauskienė**. Synthesis and comparison of gold nanoparticles coated with silicon, manganese, and titanium dioxides. *Chemija **31** (2020) 197–202.* https://doi.org/10.6001/chemija.v31i4.4316.

Autorės indėlis: atliktas Ramano spektroskopijos tyrimas, dalis nanodalelių sintezės, spektroskopinių duomenų analizė ir grafinis apipavidalinimas, dalis rankraščio rašymo.

2. T. Charkova, **A. Zdaniauskienė**, I. Ignatjev. Silica shell-isolated gold nanospheres: synthesis, investigation of stability in organic solvents, and application in shell-isolated nanoparticle-enhanced Raman spectroscopy. *Chemical Data Collections **29** (2020) 100497.* https://doi.org/10.1016/j.cdc.2020.100497.

Autorės indėlis: atlikti Ramano ir UV-Vis spektroskopiniai tyrimai, duomenų analizė ir grafinis apipavidalinimas, aprašyti spektriniais metodais gauti rezultatai.

3. E. Daublytė, **A. Zdaniauskienė**, M. Talaikis, A. Drabavičius, T. Charkova. A facile microwave-assisted synthesis of $Ag@SiO_2$ nanoparticles for Raman spectroscopy. *New Journal of Chemistry **45** (2021) 10952.* https://doi.org/10.1039/d1nj01439k.

Autorės indėlis: atlikta spektrinių duomenų analizė ir kuravimas, grafinis apipavidalinimas, aprašyti spektriniais metodais gauti rezultatai.

4. **A. Zdaniauskienė**, M. Talaikis, T. Charkova, R. Sadzevičienė, L. Labanauskas, G. Niaura. Electrochemical shell-isolated nanoparticle-enhanced Raman spectroscopy of imidazole ring functionalized monolayer on smooth gold electrode. *Molecules **27** (2022) 6531.* https://doi.org/10.3390/molecules27196531.

Autorės indėlis: atliktas bandinių paruošimas, SHINERS, EC-SHINERS, RAIRS eksperimentiniai tyrimai, spektroskopinių duomenų analizė ir grafinis apipavidalinimas, rankraščio rašymas.

5. **A. Zdaniauskienė**, I. Ignatjev, T. Charkova, M. Talaikis, A. Lukša, A. Šetkus, G. Niaura. Shell-isolated nanoparticle-enhanced Raman spectroscopy for probing riboflavin on graphene. *Materials **15** (2022) 1636.*

https://doi.org/10.3390/ma15051636.

Autorės indėlis: atliktas bandinių paruošimas ir eksperimentinis SHINERS tyrimas, spektrinių duomenų analizė ir kuravimas, grafinis apipavidalinimas, rankraščio rašymas.

6. **A. Zdaniauskienė**, T. Charkova, I. Ignatjev, V. Melvydas, R. Garjonytė, I. Matulaitienė, M. Talaikis, G. Niaura. Shell-isolated nanoparticle-enhanced Raman spectroscopy for characterization of living yeast cells. *Spectrochimica Acta Part A: Molecular and Biomolecular Spectroscopy* ***240*** *(2020) 118560.*
https://doi.org/10.1016/j.saa.2020.118560.

Autorės indėlis: atliktas bandinių paruošimas, SHINERS eksperimentinis tyrimas, grafinis apipavidalinimas, rengiant rankraštį aprašyti gauti rezultatai.

Kitos publikacijos:

7. E. Daublytė, **A. Zdaniauskienė**, T. Charkova. Microwave synthesis of silver core-silica decorated nanoparticles. *Chemija* ***33*** *(2022) 1-6.*
https://doi.org/10.6001/chemija.v33i1.4657.

8. **A. Zdaniauskienė**, T. Charkova, I. Matulaitienė, O. Eicher-Lorka, A. Matijoška, M. Skapas, A. Selskis, G. Niaura. Electrochemical shell-isolated nanoparticle-enhanced Raman spectroscopy: Bonding, structure, and ion-pairing of the positive charge bearing pyridinium ring terminated monolayer at smooth gold electrode. *Journal of Physical Chemistry C* ***122*** *(2018) 1234–1242.*
https://doi.org/10.1021/acs.jpcc.7b09970.

1.2. Pranešimai mokslinėse konferencijose

1. G. Niaura, T. Charkova, M. Dagys, O. Eicher-Lorka, I. Ignatjev, I. Matulaitiene, M. Talaikis, **A. Zdaniauskienė**. Surface Enhanced Raman Spectroscopy of Biomolecules at Electrochemical Interface. *23rd Topical Meeting of the International Society of Electrochemistry: Electrochemistry for Investigation of Biological Objects: from Functional Nanomaterials to Micro/Nano-Electrodes, Vilnius, Lithuania, May 8-11, 2018.*

2. **A. Zdaniauskienė**, T. Charkova, I. Ignatjev, V. Melvydas, R. Garjonytė, I. Matulaitienė, G. Niaura. Shell-Isolated Nanoparticle-Enhanced Raman Spectroscopic Analysis of Living Yeast Cells. *Advanced Properties and Processes in Optoelectronic Materials and Systems - APROPOS-16, Vilnius, Lithuania, October 10-12, 2018.*

3. **A. Zdaniauskienė**, T. Charkova, I. Ignatjev, V. Melvydas, R. Garjonytė, I. Matulaitienė, G. Niaura. Mielių Ląstelių Sienelės Sudėties Analizė SHINERS Metodu. *9-toji doktorantų ir jaunųjų mokslininkų konferencija "FizTech 2019", Vilnius, Lietuva, Spalio 23-24 d., 2019.*

4. **A. Zdaniauskienė**, T. Charkova, I. Ignatjev, G. Astromskas, R. Pauliukaitė, G. Niaura. Shell-Isolated Nanoparticle-Enhanced Raman Spectroscopy of Riboflavin Monolayer Adsorbed at Graphene. *Open readings 2019: 62th international conference for students of physics and natural sciences, Vilnius, Lithuania, March 19-22, 2019.*

5. **A. Zdaniauskienė**, T. Charkova, I. Ignatjev, G. Niaura. Synthesis of Au Nanoparticles with SiO_2, MnO_2, and TiO_2 Shells for Surface Enhanced Raman Spectroscopy. *Lithuanian Chemists Conference Chemistry And Chemical Technology, Vilnius, Lithuania, May 16, 2019.*

6. **A. Zdaniauskienė**, T. Charkova, I. Ignatjev, V. Melvydas, R. Garjonytė, I. Matulaitienė, G. Niaura. Metschnikowia Rūšies Mielių Ląstelių Tyrimas Paviršiaus Sustiprintos Ramano Spektroskopijos Metodu Panaudojant Aukso Nanodaleles su Išoriniu SiO_2 Sluoksniu. *43-oji Lietuvos nacionalinė fizikos konferencija, Kaunas, Lietuva, spalio 3-5 d., 2019.*

7. **A. Zdaniauskienė**, T. Charkova, R. Sadzevičienė, G. Niaura. In-Situ SHINERS Analysis of SAM from Thiols with Imidazole Ring and Intrachain Amide Groups. *Advanced Properties and Processes in*

Optoelectronic Materials and Systems - APROPOS-17, Vilnius, Lithuania, September 30 – October 1, 2020.

8. **A. Zdaniauskienė**, T. Charkova, M. Talaikis, R. Sadzevičienė, L. Labanauskas, G. Niaura. Savitvarkių Monosluoksnių su Imidazolo Žiedo Funkcine ir Amido Grupėmis Grandinėje Tyrimas SHINERS Metodu. *10-toji doktorantų ir jaunųjų mokslininkų konferencija "FizTech 2020", Vilnius, Lietuva, Spalio 22-23 d., 2020.*

9. **A. Zdaniauskienė**, T. Charkova, M. Talaikis, R. Sadzevičienė, L. Labanauskas, G. Niaura. Savitvarkių Monosluoksnių, Suformuotų iš Tiolių iu Imidazolo Žiedo Funkcine ir Amido Grupėmis Grandinėje, Tyrimas Nanodalelių, Padengtų Išoriniu Sluoksniu, Sustiprintos Ramano Spektroskopijos Metodu. *13-toji jaunųjų mokslininkų konferencija "Bioateitis: gamtos ir gyvybės mokslų perspektyvos" , Vilnius, Lietuva, Gruodžio 4d., 2020.*

10. **A. Zdaniauskienė**, M. Talaikis, T. Charkova, R. Sadzevičienė, L. Labanauskas, G. Niaura. Adsorbuotų biomolekulių elektrocheminėje fazių riboje charakterizavimas SHINERS metodu. *11-toji doktorantų ir jaunųjų mokslininkų konferencija "FizTech 2021", Vilnius, Lietuva, Spalio 20-21 d., 2021.*

11. **A.Zdaniauskienė**, T. Charkova, R.Sadzevičienė, G. Niaura. In-situ SHINERS analysis of imidazole ring terminated monolayer at electrochemical interface. *Open readings 2021: 64th international conference for students of physics and natural sciences, Vilnius, Lithuania, March 16-19, 2021.*

12. D. Dunajevas**, A. Zdaniauskienė**, M. Talaikis, R. Sadzevičienė, G. Niaura. Study of SAM with imidazole functional group by surface and shell-isolated nanoparticle enhanced Raman Spectroscopy. *Open readings 2021: 64th international conference for students of physics and natural sciences, Vilnius, Lithuania, March 16-19, 2021.*

13. E. Daublytė, **A. Zdaniauskienė**, T. Charkova. Microwave-assisted synthesis of silver nanoparticles with polyols. *Open readings 2021: 64th international conference for students of physics and natural sciences, Vilnius, Lithuania, March 16-19, 2021.*

1.3. Trumpos žinios apie autorę

Agnė Zdaniauskienė
1993-02-26, Ukmergė, Lietuva

Išsilavinimas:

Ukmergės Jono Basanavičiaus gimnazija | 2008 – 2012
Brandos atestatas su pagyrimu

Vilniaus universitetas, Fizikos fakultetas | 2012 – 2016
Fizikos bakalauro laipsnis

Vilniaus universitetas | 2014 – 2016
Pedagogo kvalifikacija

Vilniaus universitetas, Fizikos fakultetas | 2016 – 2018
Biofizikos magistro laipsnis, *Magna Cum Laude*

Fizinių ir Technologijos Mokslų Centras | 2018 – 2022
Doktorantūros studijos

Darbo patirtis:

Jaunesnioji mokslo darbuotoja | 2020 – dabar
Lietuvos mokslo tarybos finansuojamas aukšto lygio MTEP projektas „Magnetoplazmoninės nanodalelės biologinių paviršių SERS analizei (SMARTSERS)" (01.2.2-LMT-K-718-03-0078).

Jaunesnioji mokslo darbuotoja | 2019 – dabar
Fizinių ir technologijos mokslų centras, Organinės chemijos skyrius, spektroelektrochemijos laboratorija.

Inžinierė | 2017 – 2019
Lietuvos mokslo tarybos finansuojamas projektas pagal nacionalinę mokslo programą „Link ateities technologijų" „Anglies elektronikos grandynas su integruotais lauko tranzistoriumi ir grafeno superkondensatoriumi detektorių moduliams (G-SUPERCAP)" (LAT-11/2016).

Inžinierė | 2017 – 2019
Fizinių ir technologijos mokslų centras, Organinės chemijos skyrius, spektroelektrochemijos laboratorija.

Jaunesnioji metrologė | 2016 – 2017
UAB "Altechna", metrologijos laboratorija.

2. TYRIMŲ METODAI

2.1 Ramano spektroskopija

Ramano spektroskopija – virpesinės spektroskopijos rūšis, leidžianti gauti molekulinio lygmens informaciją apie šviesos sąveiką su medžiaga ir tos medžiagos molekulių virpesinę energiją. Remiantis molekulių virpesiais galima nustatyti medžiagos sandarą, struktūrą, sąveikas tarp molekulinių grupių ar atskirti funkcines grupes, nustatyti molekulių konformacinius pokyčius. Ramano spektroskopija išsiskiria ir tuo, kad metodas yra neardantis, galimi tyrimai *in situ* vandeninėje terpėje.

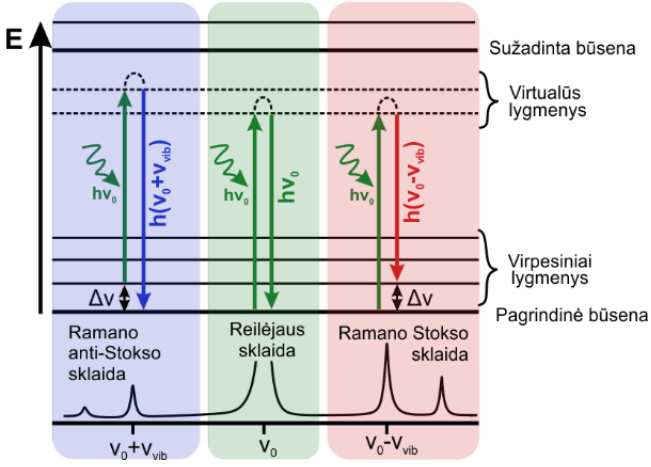

1 pav. Reilėjaus ir Ramano sklaidos spektrų kilmės schema (adaptuota pagal [2]).

Šviesa, susidūrusi su medžiaga, vienaip ar kitaip sąveikauja, bet dažniausiai yra sugeriama, atspindima arba išsklaidoma. Vykstant sklaidai dauguma susidūrimų – tamprieji, todėl išsklaidytųjų fotonų energija nekinta (Reilėjaus sklaida). Ramano sklaida yra žinoma kaip neelastinė šviesos sklaida, kurios metu pakinta į medžiagą kritusios monochromatinės šviesos dažnis[9]. Ramano sklaidos atveju sklindanti šviesos banga suteikia molekulei tam tikrą perteklinę energiją, dėl to molekulė yra sužadinama į virtualųjį lygmenį. Bangai prasklidus molekulė per ~10^{-14} s relaksuoja išspinduliuodama fotoną (1 pav.). Priklausomai nuo to, į kurį virpesinį energijos lygmenį relaksuos molekulė (aukštesnį ar žemesnį lyginant su pradiniu), išspinduliuoto kvanto energija pagal tvermės dėsnį gali sumažėti ($h(\nu_0-\nu_{vib})$) arba padidėti ($h(\nu_0+\nu_{vib})$). Išsklaidytos šviesos spektre matoma ilgabangė Ramano juosta ($h(\nu_0-\nu_{vib})$, dar vadinama Stokso juosta, trumpabangė ($h(\nu_0+\nu_{vib})$ – anti-Stokso

juosta. Ramano anti-Stokso juosta kambario temperatūroje visada yra mažiau intensyvi nei Ramano Stokso juosta, nes visi energiniai šuoliai, lemiantys anti-Stokso juostos intensyvumą, vyksta iš sužadintų virpesinių lygmenų, kurių užpilda mažesnė esant termodinaminei pusiausvyrai[10].

Pagrindiniai sklaidos dėsningumai gali būti aprašyti remiantis klasikine mechanika[10]. Šuolių tarp energijos lygmenų tikimybė Ramano šviesos sklaidos spektre susijusi su molekulės poliarizuojamumu, todėl ir Ramano sklaidos spektras gaunamas tik tada, kai dėl šuolių pasikeičia molekulės poliarizuojamumas. Taigi molekulė, patekusi į viendažnės elektromagnetinės bangos kintantį elektrinį lauką, poliarizuojasi. Indukuotas dipolinis momentas yra proporcingas elektrinio lauko stipriui:

$$\mu = \alpha E, \tag{1}$$

čia α – molekulės poliarizuojamumas. Sukurto elektrinio lauko stipris tam
tikrame erdvės taške yra periodinė laiko funkcija:

$$E = E_0 \cos(2\pi\upsilon_0 t), \tag{2}$$

vadinasi ir indukuotas dipolinis momentas yra periodinė laiko funkcija. Dipolis, virpantis dažniu ν_0, spinduliuos tokio paties dažnio elektromagnetines bangas, bet svarbu nepamiršti, kad molekulės branduoliai visada virpa tam tikru dažniu ν_{vib} aplink pusiausvyros padėtį, todėl atstumo tarp branduolių priklausomybė nuo laiko yra periodinė funkcija:

$$x = x_0 \cos[(2\pi\upsilon_{vib} t) + \varphi_0], \tag{3}$$

čia x – nuokrypis nuo pusiausvyros padėties, x_0 – virpesių amplitudė, φ_0 – pradinė fazė.

Kintant atstumui tarp branduolių, molekulės poliarizuojamumas irgi kinta. Kai virpesių amplitudė maža, poliarizuojamumo modulis skleidžiamas Teiloro eilute pusiausvyros taško aplinkoje:

$$\alpha = \alpha_0 + \left(\frac{d\alpha}{dx}\right)_e x + \frac{1}{2}\left(\frac{d^2\alpha}{dx^2}\right)_e x^2 + \cdots. \tag{4}$$

Tuomet naudojantis (1) ir (3) išraiškomis, gauname indukuoto dipolinio momento modulį:

$$\mu = \left[\alpha_0 + \left(\frac{d\alpha}{dx}\right)_e x_0 \cos(2\pi\upsilon_{vib} t + \varphi)\right] E_0 \cos(2\pi\upsilon_0 t). \tag{5}$$

Atlikus matematinius veiksmus gaunama išraiška, iš kurios nesunku pastebėti, kad molekulėje indukuotas dipolinis momentas kinta dažniais ν_0, $\nu_0+\nu_{vib}$, $\nu_0-\nu_{vib}$.

$$\mu = \alpha_0 E_0 cos(2\pi \upsilon_0 t) + \left(\frac{d\alpha}{dx}\right)_e x_0 E_0 \cdot cos[2\pi(\nu_0 + \nu_{vib})t + \varphi_0] + \\ + \left(\frac{d\alpha}{dx}\right)_e x_0 E_0 \cdot cos[2\pi(\nu_0 - \nu_{vib})t + \varphi_0]. \quad (6)$$

Pirmas išraiškos narys aprašo Reilėjaus sklaidą, antrasis Ramano anti-Stokso sklaidą, trečiasis – Ramano Stokso sklaidą[10].

Deja, Ramano spektroskopija ilgą laiką laikyta nejautriu molekulių tyrimo metodu dėl itin mažo Ramano sklaidos efektyvumo, nes tik 1 iš ~10^8 fotonų virsta Ramano fotonu. Požiūris pasikeitė praėjus 50 metų nuo Ramano sklaidos reiškinio atradimo, kuomet 1974 metais M. Fleishmannas tirdamas adsorbuotą piridiną ant nelygaus sidabro elektrodo užregistravo netikėtą, net 10^5 karto padidėjusį, Ramano signalo intensyvumą[11]. Toks eksperimentinis atradimas, dabar gerai žinomas kaip paviršiaus sustiprinta Ramano sklaida (SERS), ženkliai paspartino Ramano spektroskopijos vystymąsi.

2.2 Paviršiaus sustiprinta Ramano spektroskopija

Po M. Fleishmanno SERS atradimo praėjus 3 metams buvo išsiaiškinta, kas lėmė tokį reikšmingą Ramano signalo padidėjimą. Dvi mokslininkų grupės, nepriklausomai viena nuo kitos, paneigė pirminę M. Fleishmanno teoriją, aiškinusią, kad signalas galimai išaugo dėl didesnio nelygaus elektrodo ploto ir pasiūlė savo intensyvaus Ramano signalo priežasties teorijas, kurios yra pripažįstamos iki šiol: cheminis (M. G. Albrecht ir J. A. Creighton)[12] ir elektromagnetinis (D. L. Jeanmaire ir R. P. Van Duyne)[13] stiprinimo mechanizmai.

Cheminis stiprinimas

Cheminis stiprinimas, kitaip krūvio pernešos mechanizmas, galimas tik tada, kai molekulė sudaro cheminį ryšį su metalo paviršiumi, dėl to padidėja molekulės poliarizuojamumas. Dėl metalo ir molekulės komplekso susidarymo atsiranda nauji krūvio pernešimo keliai – elektronai, esantys metalo Fermi lygmenyje šoka į žemiausią neužpildytą molekulės energetinį lygmenį – LUMO. Elektronas, patekęs į LUMO orbitalę, sužadina cheminio ryšio virpesius, o grįždamas į pagrindinę būseną išspinduliuoja fotoną, kuris įnešą indėlį į vieną iš Stokso juostų[14]. Cheminio stiprinimo indėlis SERS spektre yra nedidelis – vidutiniškai 10 – 100 kartų, nes įprastai pasireiškus SERS efektui Ramano signalas sustiprinamas 10^4 – 10^6 kartų. Vadinasi, pagrindinė Ramano signalo stiprinimo dedamoji – elektromagnetinis stiprinimas.

Elektromagnetinis stiprinimas

Elektromagnetinis stiprinimas atsiranda tik tada, kai tiriamoji molekulė adsorbuojasi ant nelygaus metalo paviršiaus arba yra kelių nanometrų atstumu nuo jo. Nelygumai metalo paviršiuje leidžia susidaryti lokalizuotiems, metalo kristalo paviršiuje esantiems, elektronų svyravimams, kitaip plazmonų rezonansui. Toliau elektromagnetinio lauko sužadinimas ir stiprinimas vyksta keliais etapais (2 pav.).

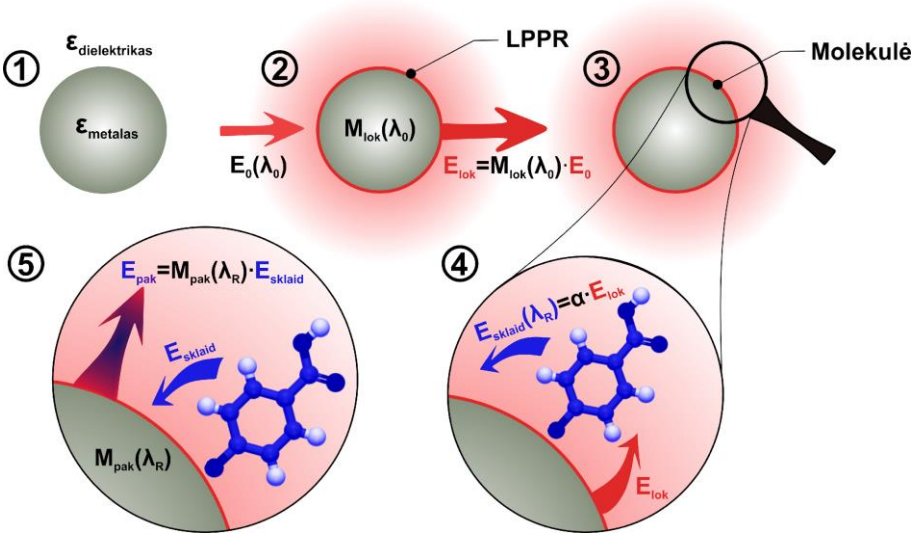

2 pav. Elektromagnetinio stiprinimo mechanizmo schema (adaptuota pagal[15]).

Pirma, elektromagnetinė spinduliuotė E_0 (prie žadinančio bangos ilgio λ_0), sąveikaudama su paviršiaus elektronais, sukelia lokalizuotą paviršiaus plazmonų rezonansą (LPPR) (2 pav. 2). Plazmonų osciliacija, vykstanti statmenai paviršiui, sustiprina elektromagnetinį lauką aplink tiriamąją molekulę, sustiprindama jos Ramano signalus. Šio etapo metu lokalus metalo dalelės sustiprintas laukas gali būti apibrėžtas kaip pradinės elektromagnetinės spinduliuotės E_0 ir lokalaus stiprinimo faktoriaus sandauga:

$$E_{lok} = M_{lok}(\lambda_0)E_0. \quad (7)$$

Sustiprintas laukas paveikia molekulės elektroninį debesėlį, priversdamas visomis kryptimis išspinduliuoti Ramano sklaidą, kurios bangos ilgis λ_R. Molekulės išspinduliuotas elektromagnetinis laukas atitinka:

$$E_{sklaid}(\lambda_R) = \alpha E_{lok} = \alpha M_{lok}(\lambda_0)E_0, \quad (8)$$

kur α – molekulės poliarizuojamumas (2 pav. 4).

Sukelta molekulės Ramano sklaida (E_{sklaid}) taip pat poliarizuoja metalo daleles ir sukelia papildomą stiprinimą, kuris apibūdinamas kaip pakartotinis spinduliavimas (2 pav. 5):

$$E_{pak} = M_{pak}(\lambda_R)E_{sklaid} = \alpha M_{pak}(\lambda_R)E_{lok} = \\ = \alpha M_{pak}(\lambda_R)M_{lok}(\lambda_0)E_0. \quad (9)$$

Taigi bendras paviršiaus sustiprintos Ramano sklaidos intensyvumas bus proporcingas:

$$I_{SERS} = M_{lok}^2(\lambda_0)M_{pak}^2(\lambda_R)I_0 = GI_0, \quad (10)$$

čia I_0 – molekulės Ramano sklaidos signalo intensyvumas be stiprinimo, G – bendras elektromagnetinio stiprinimo faktorius.

Žadinančios spinduliuotės ir Ramano sklaidos bangų ilgiai skiriasi tik per kelias dešimtis nanometrų, todėl įprasta sakyti, kad SERS stiprinimo faktorius lygus:

$$G \approx M^4_{lok}. \quad (11)$$

Akivaizdu, kad pagrindinį vaidmenį elektromagnetinio stiprinimo procese vaidina lokalizuotų paviršiaus plazmonų rezonansas, kuriam vykti būtina sąlyga – dažnio sutapimas su žadinančios šviesos dažniu. LPPR dažnis priklauso nuo nanostruktūrų dydžio bei formos[16], bet svarbiausia – nuo elektronų koncentracijos, kuri atspindi metalo prigimtį.

Elektromagnetinės spinduliuotės sąveiką su metalu nusako dielektrinė funkcija, kuri charakterizuoja elektronų sąveiką tarpusavyje, elektronų sąveiką su branduoliais ir elektronų atsaką į šviesą. Dielektrinė funkcija remiantis Drudės modeliu aprašoma:

$$\varepsilon(\omega) = \varepsilon_\infty \left(1 - \frac{\omega_p^2}{\omega^2 + i\gamma_0\omega}\right), \quad (12)$$

čia ε_∞ – katijonų atsakas, ω – elektrinio lauko dažnis, γ_0 – slopinimo faktorius, aprašantis elektronų susidūrimus su katijonais ir defektais, ω_p – laisvųjų elektronų savaiminis plazmos virpesių dažnis:

$$\omega_p = \sqrt{\frac{ne^2}{m\varepsilon_0\varepsilon_\infty}}, \quad (13)$$

kur n – laisvųjų elektronų koncentracija, e – elektrono krūvis, m – efektinė elektrono masė, ε_0 – vakuumo dielektrinė skvarba.

Metalų dielektrinę funkciją išskyrus į realią ir menamąją dalis gaunamos dvi išraiškos:

$$Re\big(\varepsilon(\omega)\big) = \varepsilon_\infty \left(1 - \frac{\omega_p^2}{\omega^2 + \gamma_0^2}\right); \tag{14}$$

$$Im\big(\varepsilon(\omega)\big) = \frac{\varepsilon_\infty \omega_p^2 \gamma_0}{\omega(2 + \gamma_0^2)}. \tag{15}$$

Realioji dielektrinės funkcijos dalis aprašo šviesos sklaidą, menamoji – sugertį. Esant sąlygoms, kai elektrinio lauko dažnis mažesnis už laisvųjų elektronų plazmos virpesių dažnį, metalai šviesą atspindi, priešingu atveju šviesa – sugeriama.

LPPR sužadinamas metalinėse nanostruktūrose, todėl nagrinėjant sferinę metalo nanodalelę, kurios matmenys (r) gerokai mažesni už lazerinės spinduliuotės bangos ilgį (λ_L), ($\lambda_L >> r$), gauname, kad metalo dalelėje sukelto elektromagnetinio lauko priklausomybė nuo žadinančios lazerio spinduliuotės aprašoma:

$$E_d = E_L \left(\frac{\varepsilon(\omega) - \varepsilon_0}{\varepsilon(\omega) + 2\varepsilon_0}\right), \tag{16}$$

E_d – elektromagnetinis laukas dalelės paviršiuje, E_L – lazerinės spinduliuotės elektromagnetinis laukas, $\varepsilon(\omega)$ – nuo žadinančios spinduliuotės dažnio priklausoma metalo dielektrinė konstanta, ε_0 – terpės, supančios metalo dalelę, dielektrinė konstanta.

Plazmoninis rezonansas pasiekiamas, kai vardiklis priartėja prie 0, reiškia $\varepsilon(\omega) = -2\varepsilon_0$, o optinė sugertis – maža. Iš čia seka plazmonų rezonanso sąlygos:

$$Re[\varepsilon(\omega)] \approx -2\varepsilon_0; \tag{17}$$

$$Im[\varepsilon(\omega)] - mažas. \tag{18}$$

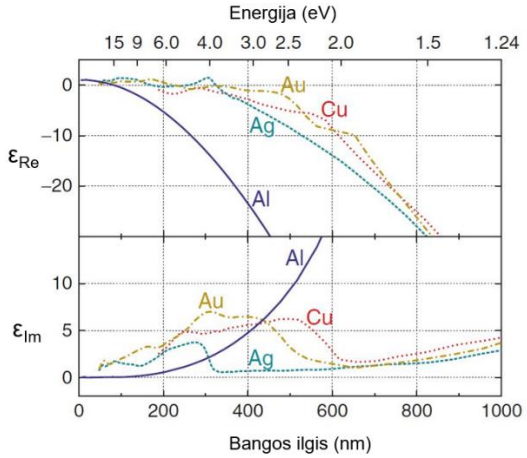

3 pav. Metalų dielektrinių funkcijų priklausomybė nuo spinduliuotės bangos ilgio[17].

Daugumos metalų ω_p yra UV spektrinėje srityje, kas leidžia tikėtis LPPR regimojoje spektro srityje, tačiau tik aukso, sidabro ir vario dielektrinės funkcijos menamosios dalies vertės pakankamai mažos regimojoje spektro srityje (3 pav.). Taigi Au, Ag ir Cu yra pagrindiniai SERS aktyvūs metalai, pasižymintys dideliu LPPR intensyvumu regimajame spektro ruože.

LPPR dažnį bei intensyvumą galima moduliuoti keičiant nanostruktūrų dydį, formą, metalų kompoziciją ar supančią aplinką[16,18–20]. Didėjant nanostruktūrų dydžiui paviršiaus plazmonų rezonanso maksimumas slenkasi į ilgesnių bangų pusę[21–23]. Palyginus sferinės formos struktūras su anizotropinėmis pastebima, kad pastarosios išsiskiria net keliomis LPPR juostomis[24]. Nanolazdelės pasižymi dvejomis atskiromis plazmonų sugerties smailėmis, atitinkančiomis vertikalią ir horizontalią dedamąsias[25]. LPPR smailės padėtis taip pat gali būti skirtinga priklausomai nuo metalų kompozicijos, pavyzdžiui nuo aukso ir sidabro santykio bendrame darinyje[26]. Žinoma, periodiškumas tarp nanostruktūrų ir jų kampuotumas ypač lemia „karštųjų“ taškų susidarymą, kur lokalaus elektrinio lauko stipris gali padidėti iki 10^9–10^{11} kartų[27,28].

SERS aktyvūs paviršiai

Paviršiai, stiprinantys Ramano sklaidą, skirstomi į tris pagrindines grupes[29].

(1) Nanostruktūriniai metaliniai paviršiai – ypač tvarkingos metalinės struktūros, suformuotos ant lygių metalo padėklų, silicio ar kito paviršiaus

nanolitografijos būdu. Naudojant skirtingas litografijos technikas (lazerinė abliacija, elektronų pluošto litografija ar kt.) galima gauti chemiškai stabilias, periodiškai išdėstytas metalines nanostruktūras, kurios generuoja homogenišką SERS signalą visame paviršiaus plote. Vis dėlto įprastai tokie paviršiai panaudojami tik vieną kartą, todėl tyrimų ant tokių paviršių kaina gana didelė.

(2) Elektochemiškai pašiurkštinti elektrodai. Elektrocheminės oksidacijos – redukcijos metodu Au, Ag ar Cu elektrodo paviršiuje suformuojami nanodariniai. Keičiant oksidacijos – redukcijos procedūras ir sąlygas galima gauti skirtingos formos, dydžio ir tvarkos struktūras elektrodo paviršiuje. Nors elektrocheminis elektrodų šiurkštinimas yra paprastas, greitas ir pigus, susiduriama su paviršiaus stabilumo problemomis laikui bėgant bei nedideliu spektriniu atsikartojamumu naudojant Ramano mikroskopą, kuomet lazerio spindulys fokusuojamas vos į kelių mikrometrų dėmę[30,31].

(3) Koloidiniai tirpalai dažniausiai gaunami vykdant cheminę metalų druskų redukciją iki neutralių metalo atomų vandeninėje terpėje esant stabilizuojantiems junginiams. Be druskų redukcijos yra nemažai kitų būdų gauti koloidinėms nanodalelėms (sonochemija, fotochemija, auginimas terpėje esant mažų metalo užuomazgų). Įprastos Au, Ag ar Cu nanodalelės nėra pakankamai stabilios, turi specifinį spektrą, kuris gali persikloti su tiriamo objekto Ramano spektru. Be to vienas svarbiausių plazmoninių dalelių trūkumų, ypač tiriant biomolekules – tiesioginė sąveika su analite (redox, katalizės procesai ir kt.), o tai dažnai sutrikdo visą sistemą ar dramatiškai iškreipia rezultatus[32]. Nepaisant greitos ir nesudėtingos nanodalelių sintezės bei daug didesnio signalo stiprinimo nei pašiurkštintų elektrodų atveju[31], minėti trūkumai mokslininkus paskatino ieškoti dar efektyvesnių Ramano sklaidos stiprinimo alternatyvų.

2.3 Nanodalelių, padengtų apsauginiu sluoksniu, sustiprinta Ramano spektroskopija

Siekiant praplėsti SERS metodo galimybes ir išspręsti metodines problemas, 2010 metais Z. Q. Tian su bendraautoriais pasiūlė panaudoti Au ir Ag nanodaleles, apsaugotas plonu SiO_2 sluoksniu[4]. Naujasis metodas, pavadintas SHINERS (ang. *Shell-Isolated Nanoparticle-Enhanced Raman Spectroscopy*), išsiskiria tuo, kad plazmoninis nanodalelės branduolys stiprina Ramano sklaidą, o itin plonas, vos kelių nanometrų storio silicio dioksido sluoksnis ženkliai padidina dalelių stabilumą, neleidžia branduolio metalui tiesiogiai sąveikauti su tiriamuoju paviršiumi. Taigi dielektriko sluoksnis

padeda išvengti cheminės sąveikos su aplinka ir neleidžia vykti krūvio pernašai. Tyrimo metu atstumas tarp plazmoninio branduolio ir tiriamojo paviršiaus gali būti lengvai kontroliuojamas keičiant SiO_2 sluoksnio storį.

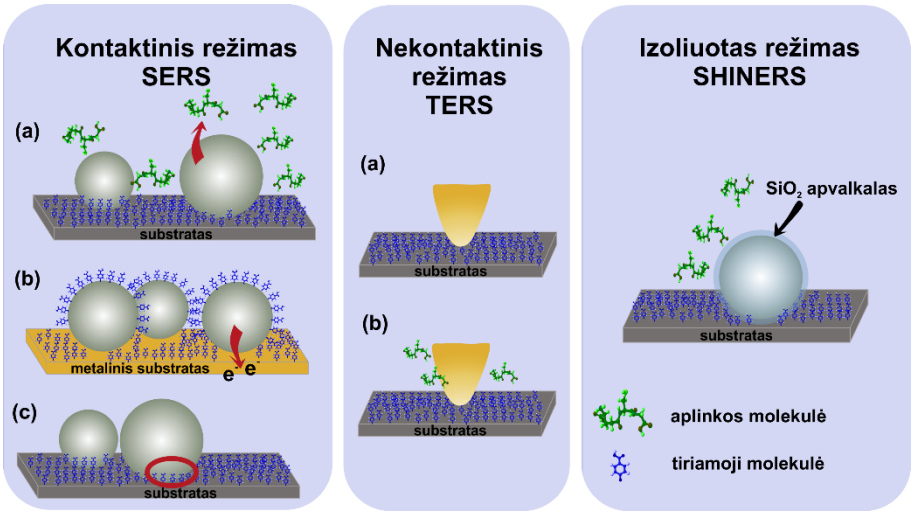

4 pav. Ramano sklaidos stiprinimo metodų palyginimas.

SHINERS metodo privalumai tampa akivaizdūs palyginus gimininga Ramano signalo stiprinimo technikas (4 pav.). Kontaktinio režimo atveju plazmoninės nanodalelės, nors ir stiprina ant monokristalinių ar lygių paviršių adsorbuotų medžiagų Ramano sklaidą, tačiau tuo pat metu gali tiesiogiai sąveikauti su aplinka, pvz. elektrocheminės ar biologinės sistemos skysčių komponentais, su aplinkos dujomis (a). Dėl to galima nanodalelių aglomeracija ar papildomų juostų atsiradimas Ramano spektre[33]. Naudojant metalinį substratą su adsorbatais gali vykti nepageidaujama krūvio pernaša ar susidaryti kontaktinis potencialų skirtumas tarp nanodalelės ir substrato dėl skirtingų Fermi lygmenų (b). Tokie procesai gali stipriai paveikti tiriamos sistemos elektroninę struktūrą, o tai ypač svarbu, pavyzdžiui, katalitinėse reakcijose su pereinamaisiais metalais (platina ar paladis), kai katalizatoriaus elektroninė struktūra gali paveikti katalizinį veikimą[34,35]. Taip pat neišvengiama tiesioginė metalinės nanodalelės sąveika su tiriamomis molekulėmis ar atskiromis jų funkcinėmis grupėmis perturbuoja sistemą ir gali iššaukti pokyčius registruojamuose spektruose (c), t.y. virpesinių juostų poslinkį[36].

Adata sustiprinta Ramano spektroskopija (ang. *Tip–Enhanced Raman Spectroscopy*, TERS) apjungia atominės jėgos mikroskopą ir Ramano

spektrometrą, kur adata veikia tarsi mažas stiprintuvas – zondas tuo pačiu metu. Nors ši technika ir pasižymi ypač aukšta erdvine skiriamąja geba, tačiau gaunamas Ramano signalas vis vien ganėtinai silpnas, nes tik viena adata veikia kaip stiprintuvas (a). Žinoma, svarbu paminėti, kad naudojama metalinė adata gali lengvai sąveikauti su tiriamojo objekto aplinkoje esančiais komponentais, dėl to galima medžiagų adsorbcija ant adatos (b). Adsorbuotos medžiagos neretai įneša papildomų virpesinių juostų registruojamame spektre, tai apsunkina duomenų analizę ir iškreipia rezultatus[37]. Tačiau svarbu pažymėti, kad TERS metodas leidžia tirti bet kokio metalo monokristalinius, lygius ar biomolekulinius paviršius t.y. pašalina vieną iš pagindinių SERS trūkumų.

Apibendrinant galima teigti, kad SHINERS apjungia kontaktinį ir nekontaktinį režimus, nes nanodalelių branduoliai tampa tūkstančiais mažų stiprintuvų, kurie generuoja aukštą Ramano signalo stiprinimą, o plonas, inertiškas apvalkalas padeda išvengti visų kontaktinio režimo problemų. SHINERS metodas tinkamas tirti molekulinius vyksmus nuo bet kokių paviršių. Galima analizuoti vykstančias katalizines reakcijas ant platinos, geležies, paladžio, nikelio, nemažiau svarbu, jog paviršiai gali būti lygūs ir monokristaliniai. Taip pat naudojant daleles su inertiniu apvalkalu tampa galimi elektrocheminių sistemų tyrimai *in-situ* esant kontroliuojamam elektrodo potencialui vandeninėje terpėje ar net biologinėje sistemoje. Taigi SHINERS atveria naujas galimybes tiriant itin sudėtingas, bet jau seniai mokslininkus dominančias sistemas ir gauti molekulinio lygmens informaciją apie tų sistemų mažiausių struktūrinių elementų pokyčius ar sąveikas[38].

SHINERS metodas universalus ir daug žadantis tiriant kompleksiškas molekulines sistemas, tačiau svarbu pabrėžti, kad šio metodo taikymas kelia ir tam tikrus iššūkius. Pagrindiniai metodo trūkumai ir problemos susijusios su naudojamomis nanodalelėmis. Pavyzdžiui, SHINERS spektrų stiprinimas priklauso nuo kelių faktorių, bet vieni svarbiausių – nanodalelių atstumas nuo tiriamojo objekto ir dalelių dydis.

Sintetinant nanodaleles su išoriniu inertišku apvalkalu svarbu užtikrinti apvalkalo tolygumą ir vientisumą, nes apvalkalas tinkamai atlieka savo funkciją tik tada, kai jo struktūroje išvengiama defektų – skylių. Skylėtas apvalkalas neužtikrina ilgalaikio dalelių stabilumo, nedidelės molekulės, esančios aplinkoje, gali prasiskverbti iki metalinio branduolio ir ten adsorbuotis. Apvalkalo storį, o tikėtina ir skylių kiekį, galima kontroliuoti keičiant apvalkalo formavimo laiką[39], tačiau norint gauti pakankamą Ramano signalo stiprinimą būtina užtikrinti, kad apvalkalas nebūtų pernelyg storas.

Storėjant apvalkalui didėja atstumas tarp tiriamojo objekto ir metalo nanodalelės, tai lemia elektromagnetinio lauko stiprio sumažėjimą analitės buvimo vietoje. Ryškus elektromagnetinio lauko kitimas gali būti paaiškinamas palaipsniui[40]. Pirma, lazerinės spinduliuotės indukuotas dipolinis momentas sferinėje metalo nanodalelėje aprašomas:

$$P(\omega) = \frac{\varepsilon(\omega) - \varepsilon_0}{\varepsilon(\omega) + 2\varepsilon_0} r^3 E_L, \tag{19}$$

r – nanodalelės spindulys.

Toliau žinoma, kad elektrinio lauko stipris nanodalelėje tolygus ir silpnėja tolstant nuo jos. Atstumu d nuo nanodalelės indukuoto dipolio elektrinio lauko stipris E_{dip} išreiškiamas:

$$E_{dip} = r^3 \frac{\varepsilon(\omega) - \varepsilon_0}{\varepsilon(\omega) + 2\varepsilon_0} E_L \frac{1}{(r+d)^3}. \tag{20}$$

Bendras molekulę veikiantis elektrinio lauko stipris E_b yra lazerinės spinduliuotės ir indukuoto dipolio elektrinio lauko stiprių suma:

$$E_b = E_L + E_{dip}. \tag{21}$$

2.2 skyriuje aptartą elektromagnetinio stiprinimo faktorių galima užrašyti ir kiek kitaip:

$$G = \left|\frac{E_b(\omega_{SERS})}{E_L}\right|^2 \left|\frac{E_b(\omega_L)}{E_L}\right|^2, \tag{22}$$

ω_{SERS} – paviršiaus sukelto elektromagnetinio lauko dažnis, ω_L – lazerinės spinduliuotės dažnis.

Pasinaudoję 20 ir 21 išraiškomis perrašome 22 lygtį:

$$G = \left|\frac{\varepsilon(\omega_L) - \varepsilon_0}{\varepsilon(\omega_L) + 2\varepsilon_0}\right|^2 \left|\frac{\varepsilon(\omega_{SERS}) - \varepsilon_0}{\varepsilon(\omega_{SERS}) + 2\varepsilon_0}\right|^2 \left(\frac{r}{r+d}\right)^{12}. \tag{23}$$

Akivaizdu, kad tiesioginis molekulės kontaktas su metalo paviršiumi nėra būtina sąlyga SERS spektrams gauti, tačiau tolstant molekulei nuo nanodalelės paviršiaus, pvz., storėjant išoriniam nanodalelės apvalkalui, stiprinimas žymiai mažėja. Tą pačią tendenciją iliustruoja ir eksperimentiniai duomenys (5 pav.).

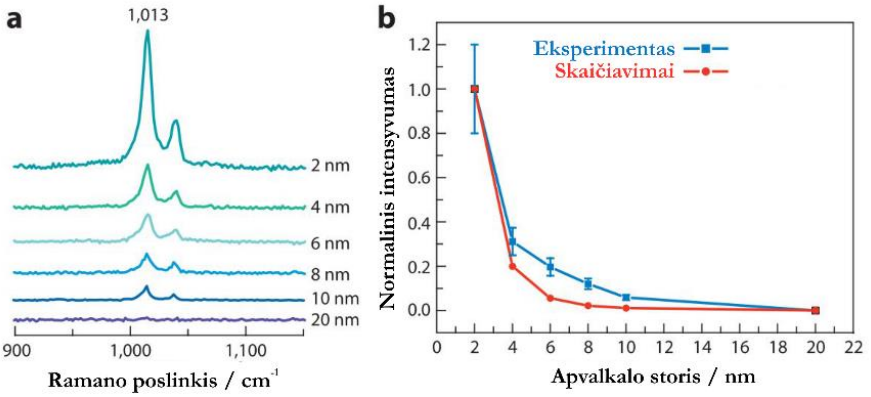

5 pav. SHINERS spektrų intensyvumo priklausomybė nuo apvalkalo storio. (a) Adsorbuoto piridino ant lygaus Au paviršiaus SHINERS spektrai naudojant 55 nm Au šerdies dydžio nanodaleles su skirtingu SiO_2 apvalkalo storiu; (b) piridino normalinio 1013 cm^{-1} juostos intensyvumo priklausomybė nuo nanodalelės SiO_2 apvalkalo storio[31].

Taip pat eksperimentinių skaičiavimų duomenys parodė, kad sferinių Au@SiO_2-2 nm ir Au@ SiO_2-4 nm nanodalelių sudaryti dimerai maksimaliai gali pasiekti 140 ir 85 kartus išaugusį elektrinio lauko stiprį. Atitinkamai skaičiuojama, kad Ramano sklaidos stiprinimo faktoriai kiekvienu atveju atskirai būtų – $4 \cdot 10^8$ ir $5 \cdot 10^7$. Įdomu tai, kad palikus tik vieną Au@ SiO_2-4 nm nanodalelę Ramano sklaidos faktorius sumažėja nuo $5 \cdot 10^7$ iki $9 \cdot 10^6$. Tai reiškia, jog Ramano sklaidos stiprinimo faktorius išlieka pakankamai didelis net ir vienos nanodalelės su išoriniu apvalkalu atveju, todėl atliekant eksperimentus nėra būtina padengti paviršiaus tankiu nanodalelių sluoksniu[31]. Vis dėlto akivaizdu, kad maksimalus elektromagnetinis stiprinimas prarandamas naudojant apvalkalais izoliuotas nanodaleles, todėl norint sumažinti apvalkalo įtaką stiprinimo faktoriui reikia varijuoti su plazmoninės dalelės šerdies dydžiu ir forma. Eksperimentiškai įrodyta, kad didėjant nanodalelių dydžiui sustiprintos Ramano sklaidos intensyvumas taip pat didėja[19,41–43]. G. Kumari ir kt. pademonstravo, kad didinant sidabro nanodalelės dydį iki 90 nm atstumas nuo tiriamos analitės, kuomet dar stebimas SERS efektas, yra 5 nm[43] (6 pav.). Tačiau reikia pažymėti, jog maksimalus atstumas iki analitės, dar registruojant SERS signalus, toliau didinant plazmoninės šerdies dydį nebedidės, bet priešingai, nuo ~ 100 nm dydžio nanodalelių pradės mažėti, nes didesnės nei 100 nm nanodalelės nėra efektyviausios SERS stiprinimui.

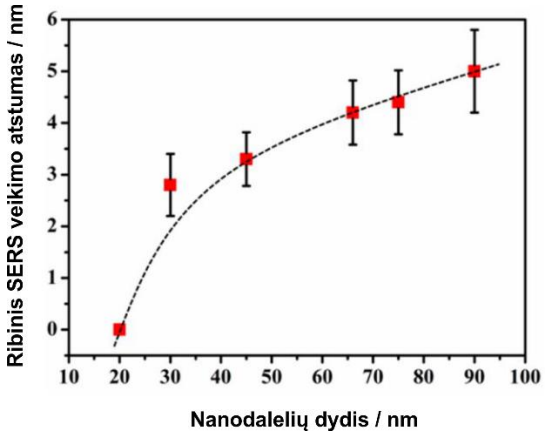

6 pav. Atstumo nuo tiriamos analitės, kuomet dar stebimas SERS efektas, priklausomybė nuo Ag nanodalelių dydžio[43].

Žinoma, žymiai didesnius stiprinimus elektromagnetinė teorija numato deformuotiems sferoidams, kuomet stiprinimo faktorius gali pasiekti ir 10^{10} eilę[44,45], todėl eksperimentinėmis sąlygomis, kai analitė negali/neturi adsorbuotis ant plazmoninės nanodalelės ar tyrimo objektas nepasižymi intensyviomis virpesinėmis juostomis Ramano spektre, vertėtų naudoti kampuotos formos nanodaleles.

3. TYRIMŲ KRYPTYS

3.1 Nanodalelės: galimybės ir iššūkiai

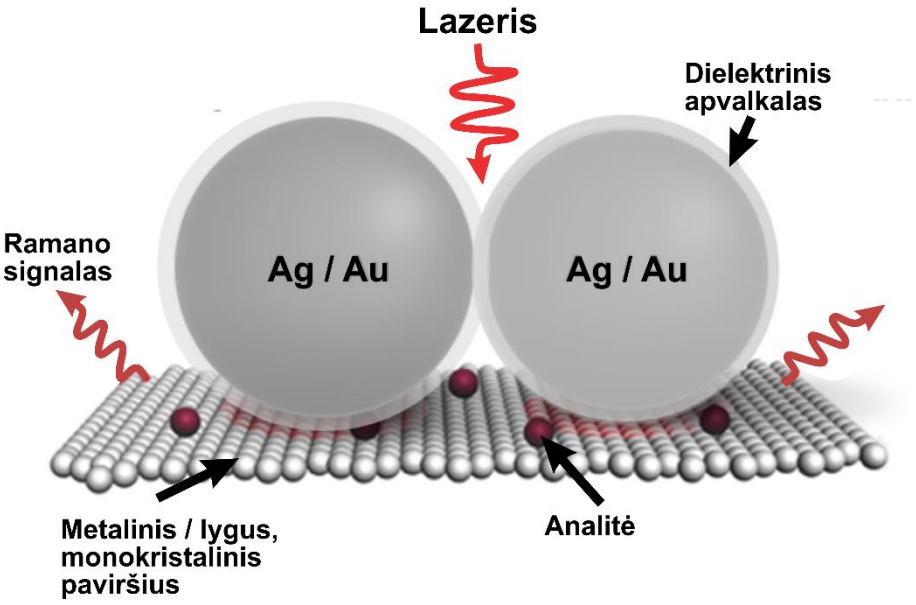

Biomolekulių charakterizavimas SHINERS metodu neįmanomas prieš tai nesusintetinus ir nuodugniai neištyrus naudojamų nanodalelių. Nanodalelių pritaikymas Ramano spektroskopijoje suteikia daug galimybių tiriant sudėtingas, kompleksines molekulines sistemas, tačiau svarbu pabrėžti, kad tuo pačiu metu didžiausios kylančios SHINERS metodo problemos taip pat susijusios su nanodalelėmis, jų sinteze ir grynumu.

Pagrindiniai rezultatai ir išvados

Nanodaleles dengiant skirtingos prigimties apvalkalais galima išgauti nevienodomis savybėmis pasižyminčias daleles. Atsižvelgiant į tiriamos sistemos terpės pH reikia tinkamai pasirinkti, kokiu apvalkalu padengti nanodaleles. Silicio dioksido apvalkalas gali ištirpti šarminėje terpėje, tačiau mangano dioksidas yra itin stabilus šarminiuose tirpaluose, bet pasižymi menku stabilumu rūgštyse[46].Tuo tarpu titano dioksido apvalkalas yra ypač stabilus aukštose temperatūrose ir išsiskiria aukštu lazerinės spinduliuotės pažeidimo slenksčiu[47]. Vis dėlto, ne vien teisingas išorinio nanodalelės apvalkalo pasirinkimas lemia eksperimentinių duomenų patikimumą. Svarbu atkreipti dėmesį į tai, kad išorinį apvalkalą sudarančios molekulės gali turėti tam tikrą indėlį virpesiniame spektre ir taip iškreipti tiriamojo objekto spektrą. Norint įsitikinti, kuriose spektrinėse vietose galima tikėtis skirtingos prigimties apvalkalo virpesinių juostų, buvo atliktas palyginamas nanodalelių eksperimentas su SiO_2, MnO_2 ir TiO_2 apvalkalais. SHINERS spektrų registravimui pasirinktas modelinis tiofenolio savitvarkis monosluoksnis, suformuotas ant lygaus Au paviršiaus. Nustatyta, kad Au@MnO_2 nanodalelės turi specifinį spektrą, kuris persikloja su tiofenolio virpesinėmis modomis 400–700 cm^{-1} srityje. Analogiški rezultatai gauti ir su Au@TiO_2 nanodalelėmis, kurių virpesiai su tiriamojo objekto virpesiais persiklojo 1200–1600 cm^{-1} spektro srityje. Au@SiO_2 nanodalelės taip pat pasižymi specifiniu virpesiniu spektru, bet virpesinių juostų intensyvumas itin mažas lyginant su SHINERS tiofenolio spektru ir rezultatus paveikia minimaliai. Taigi išorinių nanodalelių apvalkalų įvairovė leidžia pasirinkti tinkamiausią konkrečiam eksperimentui ir taip suteikia galimybę atlikti išsamius kompleksinių sistemų tyrimus.

Kita nanodalelių su išoriniu apvalkalu panaudojimo SHINERS eksperimentuose problema – elektrostatinis krūvis. Išorinį nanodalelės paviršinį krūvį nulemia apvalkalo cheminė struktūra (7 pav.) ir ją supanti aplinka (elektrolito tirpalo sudėtis bei savybės). Dalinai neigiamas apvalkalo krūvis ne visada leidžia tirti molekulines sistemas su neigiamą krūvį turinčiomis funkcinėmis grupėmis. Dėl elektrostatinės sąveikos nanodalelės

negali pakankamai priartėti prie tiriamo paviršiaus ir sustiprinti Ramano sklaidos. Siekiant pakeisti nanodalelės krūvį, išorinis apvalkalas modifikuojamas. Modifikavimas gali būti atliktas prijungiant molekules su dalinai teigiamą krūvį turinčiomis grupėmis, pvz. $–NH_2$. Apvalkalas modifikuojamas ir dėl kitų priežasčių: metalų jonų surišimui ir detekcijai tirpale, didelių molekulinių struktūrų pritraukimui, reakcijų katalizavimui ar kt.[38]. Išorinio apvalkalo modifikavimas neretai atliekamas organiniuose tirpikliuose, todėl studijų metu ištirtas SiO_2 apvalkalo stabilumas 17-oje skirtingų tirpiklių. Gauti praktiniai rezultatai padeda iš anksto pasirinkti tinkamas SiO_2 apvalkalo modifikavimo sąlygas ir taip optimizuoti tolimesnius nanodalelių sintezės etapus.

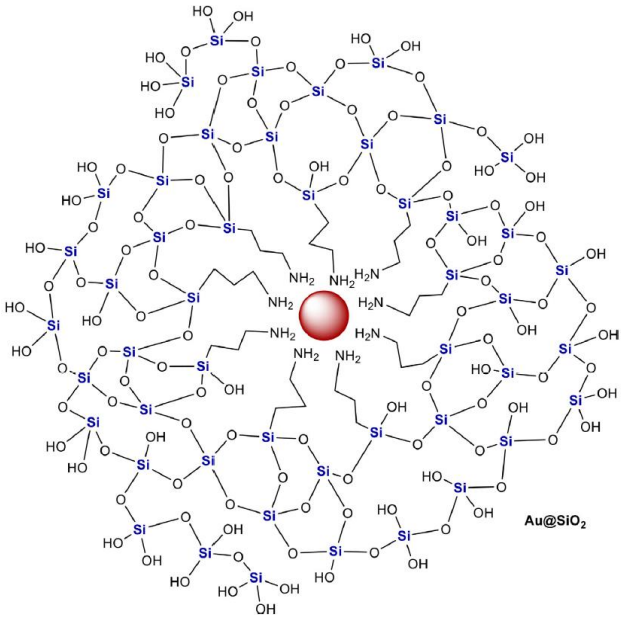

7 pav. Au nanodalelės su išoriniu SiO_2 apvalkalu schema.

Platesnį SHINERS metodo pritaikomumą riboja ir pati nanodalelių sintezė. Nors nanodaleles susintetinti nėra sudėtinga (sintezė vykdoma dviem etapais: branduolio ir apvalkalo formavimas), bet užtrunka apie 2 val., o tai ne visada yra patogu. Taip pat atliekant standartinę sintezę gaunamos apie 50 nm dydžio nanodalelės su 2 – 4 nm storio silicio dioksido apvalkalu[5], jos įprastai Ramano signalą stiprina $\sim 10^7$ kartų[31]. Deja, tiriant sudėtingas molekulines sistemas nepakanka tokio stiprinimo, todėl siekiant gauti didesnį Ramano sklaidos intensyvumą reikia ieškoti alternatyvių ir efektyvesnių nanodalelių sintezės būdų. Vienas tokių sintezės būdų metalinėms nanodalelėms sintetinti pasiūlytas 2000 metais, kai W. Tu ir H. Liu panaudojo mikrobangas

homogeniniams, polimerais stabilizuotiems, Pt, Ir, Rh, Pd, Au ir Ru koloidiniams klasteriams sintetinti[48]. Vėliau mikrobangų kaitinimo būdas buvo modifikuotas skirtingiems metalų koloidams su skirtingais stabilizuojančiais agentais išgauti[49]. Mikrobangų sintezė išsiskiria tuo, kad veikiant mikrobangoms sumažėja reakcijos aktyvacijos energijos barjeras, tai ir lemia gerokai sutrumpėjusį sintezės laiką: nuo valandų kaitinant konvekciniu būdu iki minučių ar sekundžių šildant mikrobangomis. Be to, trumpesnis reakcijos laikas sumažina nepageidaujamų šalutinių produktų atsiradimo tikimybę, todėl gaunama didesnė produkto išeiga. Žinoma, atliekant nanodalelių sintezę uždarame mikrobangų (MW) reaktoriuje užtikrinamos daug geresnės švarumo sąlygos, nes reakcijos mišinys nesąveikauja su aplinka. Taip pat vienalytis MW laukas aplink reakcijos mišinį, griežtai kontroliuojamos reakcijos sąlygos (kaitinimo greitis, trukmė, maišymas ir kt.) užtikrina aukštą reakcijų atkuriamumą, tai leidžia lengvai optimizuoti reakcijos sąlygas norint gauti skirtingus produktus[50].

Doktorantūros studijų metu mikrobangų sintezė buvo modifikuota taip, kad sintetinamos nanodalelės su išoriniu SiO_2 apvalkalu būtų kaip įmanoma didesnės per maksimaliai trumpą laiką nenaudojant daug skirtingų stabilizuojančių agentų. Buvo siekiama gauti kuo švaresnes nanodaleles, kad SHINERS spektre neatsirastų pašalinių juostų nuo pačių nanodalelių. Mikrobangų poveikyje susintetintos nanodalelės stabilizuotos natrio citratu, kurio perteklius po sintezės lengvai pašalinamas plaunant vandeniu. Taip pat mikrobangų sintezės metu susiformuoja plonas, bet kokybiškesnis išorinis apvalkalas lyginant su įprastos sintezės konvekciniu būdu gautomis nanodalelėmis. Apvalkalo kokybės įvertinimas gali būti atliekamas keliais skirtingais metodais – didelės skyros pralaidumo elektroninės mikroskopijos (ang. *High Resolution Transmission Electron Microscopy*, HR-TEM)[39], Ramano spektroskopijos[5] ir ciklinės voltamperometrijos (CV)[51]. Peršvietimo elektronų mikroskopijos nuotraukos gali suteikti informacijos apie apvalkalo storį, tolygumą, bet apie apvalkalo defektus – skyles iš nuotraukų spręsti sunku. Dėl to dažniausiai skylių kokybinis įvertinimas atliekamas Ramano spektroskopijos ir ciklinės voltamperometrijos metodais. 8 pav. pateikti eksperimentiniai skylių įvertinimo duomenys gauti: **A** – Ramano spektroskopijos, **B** – ciklinės voltamperometrijos metodais.

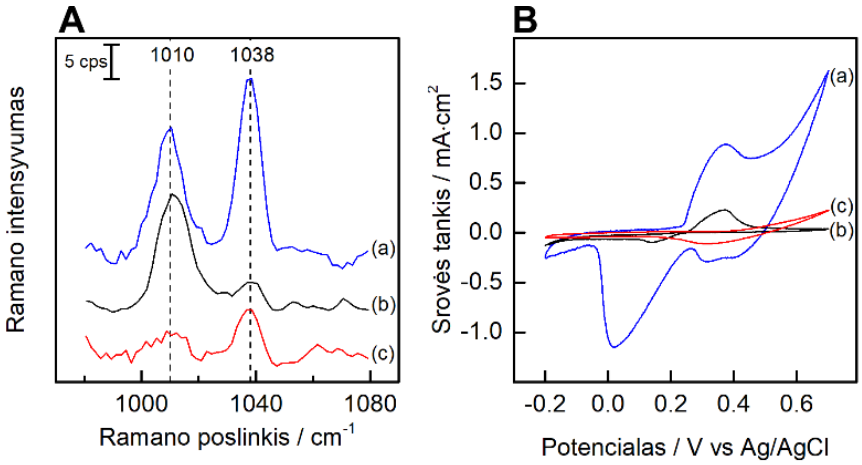

8 pav. (A) 80 nm dydžio Ag nanodalelių (a – mėlyna kreivė), Ag@SiO_2 (3 nm SiO_2) nanodalelių, sintetintų kaitinant konvekciniu būdu (b – juoda kreivė) ir Ag@SiO_2 nanodalelių, sintetintų kaitinant MW poveikyje (c – raudona kreivė) SHINERS spektrai ant Si su 10^{-3} M piridinu. **(B)** 80 nm dydžio Ag nanodalelių (a – mėlyna kreivė), Ag@SiO_2 (3 nm SiO_2) nanodalelių, sintetintų kaitinant konvekciniu būdu (b – juoda kreivė) ir Ag@SiO_2 nanodalelių, sintetintų kaitinant MW poveikyje (c – raudona kreivė) ciklinės voltamperogramos ant stiklo anglies elektrodo 0,5 M H_2SO_4 tirpale. Atvaizduotos 3 ciklo voltamperogramos, skleidimo greitis 50 mV/s.

Skylių įvertinimas nanodalelių apvalkale atliktas naudojant 80 nm dydžio Ag nanodaleles be išorinio apvalkalo, sintetintas MW poveikyje (8 pav. A(a)), Ag@SiO_2 (apvalkalo storis 3 nm) nanodaleles, sintetintas kaitinant konvekciniu (8 pav. A(b)) būdu ir MW poveikyje (8 pav. A(c)). Ramano eksperimentas vykdytas ant Si paviršiaus užlašinus ir nudžiovinus po 10 µL kiekvienų iš dalelių, tuomet ant sausų dalelių užlašinta po 20 µL 10^{-3} M piridino tirpalo ir uždėtas kvarcinis stikliukas. Taip paruošus visus tris bandinius registruoti Ramano spektrai. Neabejotinai intensyvios, aiškios virpesinės piridino juostos ties 1010 ir 1038 cm^{-1} registruotos Ag nanodalelių be apvalkalo atveju, nes piridinas gali tiesiogiai sąveikauti su metalo paviršiumi. Ag@SiO_2 dalelių, sintetintų konvekciniu būdu, atveju juostų intensyvumas mažesnis, bet vis vien matomas, o Ag@SiO_2 nanodalelių, sintetintų MW poveikyje, piridino juostų intensyvumas Ramano spektre itin nedidelis. Tokie eksperimentiniai rezultatai įrodo, jog nepriklausomai, kokia sintezės strategija taikyta išorinio SiO_2 apvalkalo dengimui ant Ag nanodalelių, išorinis apvalkalas susidaro ir izoliuoja metalo branduolį nuo sąveikos su piridino molekulėmis. Vis dėlto apvalkalą formuojant MW poveikyje jo kokybė geresnė ir defektų išoriniame dielektriniame sluoksnyje yra mažiau. Siekiant gauti papildomų įrodymų apie apvalkalo kokybę

priklausomai nuo SiO_2 dengimo būdo, užregistruotos Ag nanodalelių be išorinio apvalkalo (8 pav. B(a)) ir Ag@SiO_2 (apvalkalo storis 3 nm) nanodalelių, sintetintų kaitinant konvekciniu (8 pav. B(b)) būdu ir MW poveikyje (8 pav. B(c)), ciklinės voltamperogramos. Mėlyna kreivė aiškiai rodo tipišką Ag nanodalelių elektrocheminį atsaką, kur redukcinė smailė ties 0,02 V (atž. Ag/AgCl), tuo tarpu nanodalelių su SiO_2 apvalkalu voltamperogramos mažiau išraiškingos, tai indikuoja, kad apvalkalas riboja metalo oksidacijos – redukcijos procesus.

Taigi itin plonais nemetaliniais apvalkalais izoliuotos nanodalelės sintetinamos siekiant apsaugoti plazmoninę šerdį ir išvengti tiesioginio kontakto su analitinėmis molekulėmis ar aplinka. Pakeitus eksperimento metodiką iš tiesioginio kontakto (SERS) arba nekontaktinio (TERS) į apvalkalais izoliuotą režimą – SHINERS, buvo eliminuoti daugybę metų varžę medžiagų ir morfologijos apribojimai. SHINERS tapo tinkamu būdu aptikti, charakterizuoti ir identifikuoti molekules ant įvairių medžiagų ir substratų, ypač ant monokristalinių paviršių. Be to, įvairios galimos išorinio apvalkalo medžiagos gali atlikti skirtingas funkcijas. Pavyzdžiui, SiO_2 ir grafenas pasižymi geru biologiniu suderinamumu, TiO_2 yra populiariausia fotokatalitinė medžiaga, o Al_2O_3 gali būti naudojamas kaip atraminis sluoksnis kitiems nanokatalizatoriams. Taigi atliekant įvairius fundamentinius ir taikomuosius apvalkalais izoliuotų nanodalelių tyrimus, galima kurti naujas, funkcionalizuotas šerdies ir apvalkalo nanodaleles, skirtas SHINERS ar kitoms paviršiaus sustiprintoms spektroskopijoms[38].

3.2 Savitvarkių monosluoksnių, suformuotų iš tiolių su funkcine imidazolo žiedo ir amido grupėmis grandinėje, tyrimas

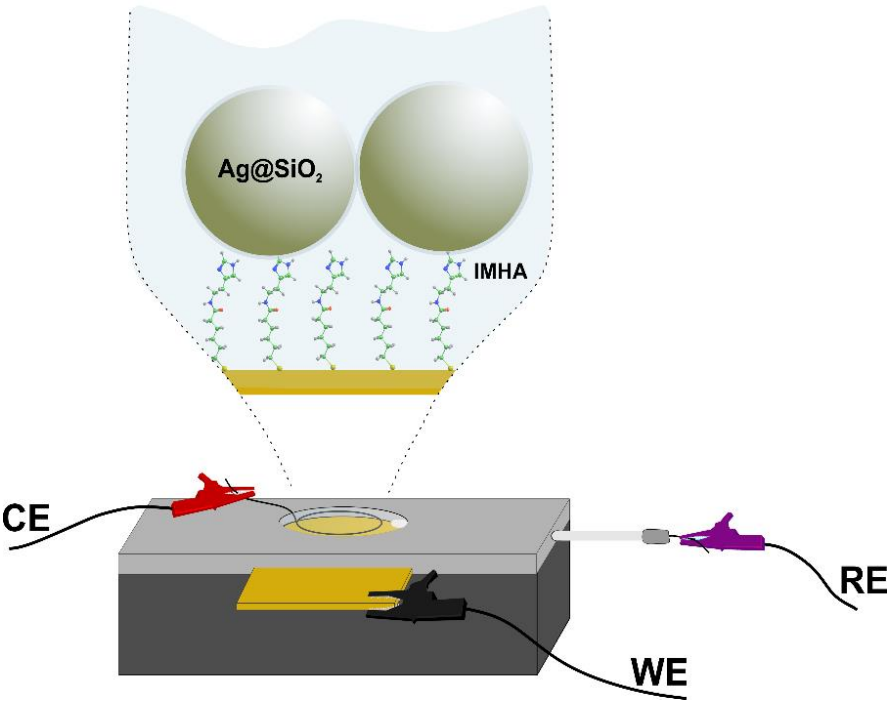

Histidinas (His) vaidina ypač svarbų vaidmenį fermentų sandaroje ir veikloje, nes suriša pereinamųjų metalų jonus aktyviuose metaloproteinų centruose[7,52]. Bendrai histidino universalumas susijęs su daugybe skirtingų sąveikų, kuriose gali dalyvauti jo šoninės grandinės grupė – imidazolo žiedas (Im) (9 pav.): (i) katijonas-π sąveika, (ii) π-π ar (iii) vandenilis-π sąveika (iv), taip pat koordinacinio ryšio susidarymas su metalo katijonais per azoto nesuporuotą elektronų porą ar (v) vandenilinio ryšio susidarymas[7]. Dėl daugybės galimų skirtingų imidazolo žiedo sąveikų Im yra ypač tinkamas paviršių tyrimuose ir pritaikyme panaudojant savitvarkius monosluoksnius (SAM)[53–58]. Im žiedu funkcionalizuoti SAM gali būti naudojami biojutikliuose, fermentų aktyvumo moduliavimui, biologiškai svarbių molekulių gryninimui, korozijos prevencijai ir kt.[55–58].

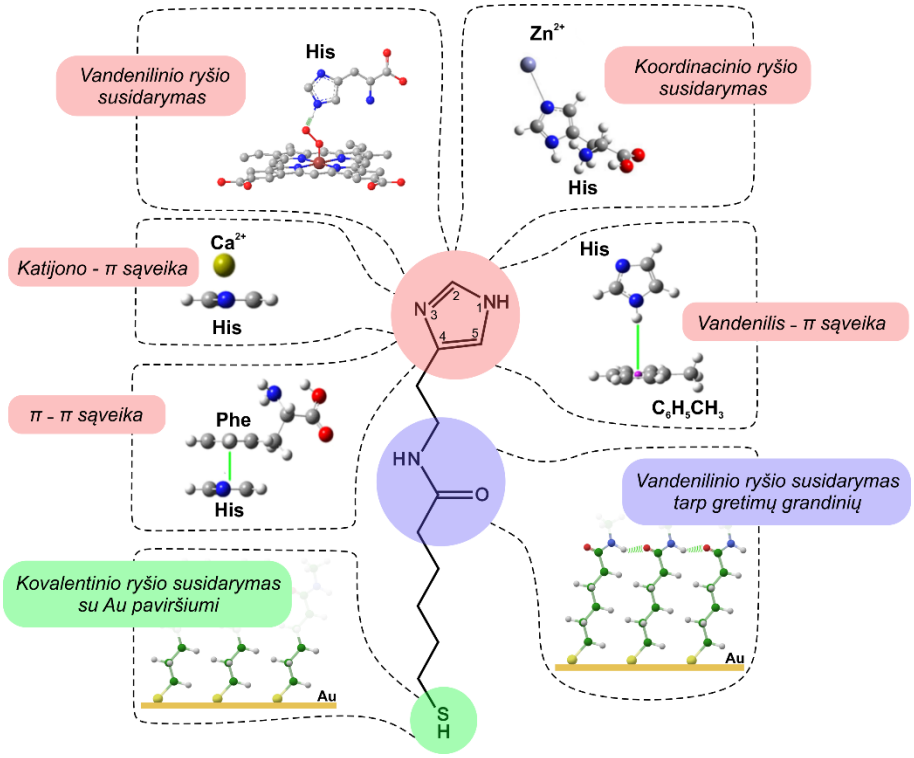

9 pav. IMHA molekulinė struktūra. Kartu pavaizduotos imidazolo žiedo sąveikos rūšys, įterptos amido grupės grandinėje ir tiolinės dalies funkcijos. Imidazolo žiede nurodyta atomų numeracija.

Histidino tirpale pK_a vertė yra 5,9 (ir daugiau nei 14), todėl fiziologinėmis sąlygomis vienas iš azoto atomų, N1 arba N3, yra protonuojamas ir susidaro dvi galimos tautomerinės formos (tautomeras I (T–I) arba tautomeras II (T–II), atitinkamai). Temperatūra ir pH gali pakeisti

tautomerinę pusiausvyrą[59], tačiau esant neutraliam pH ir kambario temperatūrai, T–I yra energetiškai palankesnis. Paviršiuje adsorbuotų molekulių tautomerinė pusiausvyra gali skirtis nuo tirpalo pusiausvyros dėl tarpmolekulinės sąveikos tarp gretimų Im žiedų ir paviršiaus krūvio efekto. Aiškus vyraujančios tautomerinės formos perėjimas iš T–I į T–II buvo pastebėtas, kai Im funkcionalizuoti lipoinės rūgšties dariniai adsorbavosi ant sidabro elektrodo[60]. Virpesinė spektroskopija, ypač Ramano sklaida, yra itin efektyvi Im tyrimuose dėl metodo gebėjimo atskirti dvi neutralias tautomerines formas ar protonuotą žiedo formą, taip pat dėl galimybės ištirti sąveiką su pereinamųjų metalų katijonais[59–68]. Pavyzdžiui, trijų gerai žinomų Ramano juostų porų 1568/1585, 1282/1260 ir 983/1004 cm^{-1} analizė leidžia atskirti T–I ir T–II formas[69]. Kai protonuojamas vienas Im azotas, kitas gali būti dvivalenčių metalų katijonų (N1–M arba N3–M) surišimo vieta. Taip pat žinoma, kad sukoordinavus metalo joną, ženkliai sumažėja Im žiedo C4=C5 ryšio ilgis, dėl to virpesinis dažnis ν(C4=C5) padidėja 5–20 cm^{-1} lyginant su pradiniu: nuo 1568 iki 1573 (T–I atveju) ir nuo 1583 iki 1588 cm^{-1} (T–II atveju)[66]. Svarbu tai, kad imidazolo katijonas, kurio vandeniliai pakeičiami deuteriais (ImD_2^+), pasižymi intensyvia, aiškia spektrine juosta ties 1405 cm^{-1}, o tai yra itin naudinga tiriant imidazolo deuterinimą įprastų Ramano eksperimentų metu[70,71]. Vienas tokių atvejų, kai panaudotas 1405 cm^{-1} spektrinis žymuo, buvo UV-rezonansinės Ramano spektroskopijos tyrimas histidino Im žiedo deuterinimo būsenos įvertinimui baltymuose[72,73].

Paviršiaus sustiprinta Ramano spektroskopija suteikia detalią molekulinio lygmens informaciją apie paviršiuje adsorbuotų molekulių ryšius, orientaciją ir struktūrą[29], tačiau SERS reikalauja naudoti šiurkščius metaliniu paviršius, dėl kurių atsiranda nemažai problemų objektyviam tyrimui atlikti. Nelygus metalo paviršius gali pakeisti molekulės adsorbciją ar perturbuoti visą sistemą, todėl norint tirti molekulines sistemas nedarant įtakos konkrečiam tyrimo objektui būtina taikyti alternatyvią, bet tokią pat informatyvią tyrimo metodiką. Prieš daugiau nei dešimtmetį pasiūlyta naudoti nanodalelių, padengtų apsauginiu sluoksniu, sustiprintą Ramano spektroskopiją, kuri panaikina pagrindinius SERS trūkumus, nes plazmoninę nanodalelės šerdį izoliuojantis SiO_2, TiO_2 ar kito dielektriko apvalkalas neleidžia tiriamoms molekulėms sąveikauti su metalo šerdimi, padidina nanodalelių stabilumą ir veikia kaip dielektrinis barjeras tarp analitės ir branduolio, užkertant kelią krūvio pernašai ir dvigubo sluoksnio perturbacijai. SHINERS metodika jau parodė didelį potencialą analizuojant *in situ* molekulių adsorbciją, struktūrą ar molekulių sąveikas paviršiuje ir elektrocheminėje fazių riboje[38,39,74–78].

Šiam doktorantūros studijų darbui susintetintas naujas junginys – N-(2-(1H-imidazol-4-il)etil)-6-merkaptoheksanamidas (IMHA) (9 pav.) turi keturias funkcines dalis: (i) paviršiui aktyvi tiolinė grupė (SH); (ii) angliavandenilinė grandinė (−$(CH_2)_5$−); (iii) amido grupė (−CO−NH−); (iv) imidazolo žiedas. Amido grupė, įterpta į alkilinę grandinę, sudaro vandenilinių ryšių tinklą tarp gretimų molekulinių grandinių, tai ženkliai padidina monosluoksnio stabilumą. Kiek anksčiau įrodyta, kad tokia sąveika stipriai padidina desorbcijos temperatūrą, taigi ir monosluoksnio cheminį stabilumą[8]. Taigi darbe pateikiama naujo IMHA junginio sintezė ir monosluoksnių, adsorbuotų ant atomiškai lygių Au paviršių, charakterizavimas elektrocheminėje fazių riboje SHINERS ir *ex-situ* RAIRS metodais. Nuodugniai įvertintas elektrodo potencialo poveikis monosluoksnio struktūrai ir imidazolo žiedo tautomerizacijai bei vandenilinio ryšio sąveikos stipriui elektrocheminėje fazių riboje.

Pagrindiniai rezultatai ir išvados

Pirmiausia atliktas IMHA virpesinių juostų Ramano spektre priskyrimas. Šiam tikslui susintetintas panašus į IMHA tiolinis junginys be galinės funkcinės grupės – Im žiedo (fragmento junginys (IMHA frag.)) (10 pav.). Palyginti IMHA, IMHA frag. ir histidino miltelių bei fragmento, ištirpinto H_2O IR D_2O tirpaluose, Ramano spektrai. Spektrų palyginimas leido tiksliai identifikuoti Ramano juostas, susijusias su Im žiedo virpesiais, taip pat fragmento molekulės miltelių ir tirpalų lyginamosios analizės metu identifikuota amido ir tiolinė grupės. Toliau norėdami įvertinti Ramano virpesines juostas, susijusias su molekulinėmis ir tarpmolekulinėmis sąveikomis bei jautriais alkilinės grandinės tvarkai, atlikome temperatūrinius Ramano tyrimus su IMHA miltelių junginiu. Iš temperatūrinių matavimų galima daryti kelias išvadas. Pirma, vidutinio intensyvumo juostos 1566, 1321 ir 983 cm^{-1} prie 22 °C aiškiai parodo tautomero I Im žiedo formą, o pačios juostos atitinkamai priskirtos ν(C4=C5) valentiniam, ν(Im) kvėpavimo + δ(C5H), ir β(CH) deformaciniams virpesiams[69]. Temperatūrai pasiekus 130–135 °C pasirodo petys prie 1582 ir 1345 cm^{-1}, tai aiškiai įrodo tautomero II atsiradimą. Toliau iš integralinių juostų intensyvumo santykio $A_{1582}/(A_{1582} + A_{1564})$ nustatytas santykinis procentinis tautomerinių formų pasiskirstymas prie skirtingų temperatūrų: prie 22 °C – 0 % tautomero II, kai tuo tarpu prie 130 °C atsiranda 16 %, o prie 135 °C – 32 % tautomero II forma, likusi procentinė dalis tenka tautomerui I. Svarbu pažymėti, kad intensyvios juostos 1321 cm^{-1} dažnis pasislenka iki 1305 cm^{-1}, kai temperatūra pasiekia 135 °C, be to, juosta stipriai išplinta. Tokie spektriniai pokyčiai atspindi vandenilinės

sąveikos stiprumo sumažėjimą N3 vietoje, nes ν(N3–C2) virpesiai priklauso tautomero I formai[69]. Iš miltelių IMHA frag. junginio Ramano temperatūrinių spektrų galima atpažinti tik nedidelio intensyvumo amido I (Am-I) juostą ties 1636 cm^{-1}. Šis spektrinis žymuo yra susijęs su C=O valentiniais virpesiais (83 %), sujungtais su priešingoje fazėje vykstančiais ν(C−N) ir δ(C−C−N) virpesiais, ir gali būti panaudotas kaip diagnostikos priemonė nustatant antrinę peptidų struktūrą[3]. Taip pat akivaizdus 14 cm^{-1} dažnio poslinkis, pereinant iš medžiagos kietos fazės į skystą, aiškiai rodo vandenilinio ryšio susilpnėjimą amido C=O grupėje.

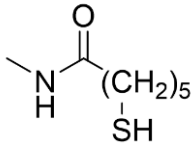

10 pav. IMHA fragmento molekulės struktūra.

Siekiant įvertinti, kaip nuo adsorbcijos laiko kinta formuojamų monosluoksnių orientacija ir susipakavimas, užregistruoti IMHA monosluoksnio, adsorbuoto skirtingą laiko tarpą (10 s – 24 val.) ant lygaus aukso paviršiaus, RAIRS spektrai. Spektrinės juostos ties 1645, 1556 ir 1264 cm^{-1} priskiriamos amidinėms juostoms, atitinkamai Am–I, Am–II ir Am–III, o netoli esančios 1460 ir 1380 cm^{-1} juostos – metileno grupės žirklniams ir vėduokliniams deformaciniams virpesiams δ(CH_2). RAIRS paviršiaus atrankos taisyklė leidžia tiksliai nustatyti molekulinių grupių orientaciją, nes konkretaus spektrinio žymens intensyvumas tiesiogiai priklauso nuo molekulinės grupės pereinamojo dipolio momento projekcijos į paviršiaus normalę[79]. Nors Am–I ir Am–II yra orientuoti statmenai vienas kitam amidinio ryšio plokštumoje, jie taip pat turi statmeną ir lygiagrečią pereinamojo dipolinio momento orientaciją angliavandenilinės grandinės atžvilgiu[79]. Taigi tikimasi, kad tvarkingai supakuoto IMHA monosluoksnio spektre dominuos Am–II juosta. Iš tiesų, palaipsniui ilgėjant inkubacijos laikui IMHA tirpale, Am–II intensyvumas ties 1556 cm^{-1} didėja, o Am–I intensyvumas ties 1645 cm^{-1} mažėja. Integralinis intensyvumo santykis Am–II/Am–I yra kokybinis molekulės persiorientavimo matas, todėl atlikus gilesnę analizę nustatyta, kad adsorbcijos procesas įpusėja per 162 min. IMHA frag. monosluoksnio, inkubuoto 24 val., RAIRS spektre Amido II spektrinė juosta yra pasislinkusi per 12 cm^{-1} į trumpesnių bangų pusę palyginus su IMHA SAM, inkubuoto vienodą laiką. Toks spektrinis skirtumas rodo, kad IMHA frag. atveju susidaro stipresnis vandenilinis ryšys N–H grupėje. Taip

pat nustatyta, kad molekulių adsorbcija ant paviršiaus iš tirpalo fazės iššaukė Am–II juostos poslinkį abiejų (IMHA ir IMHA frag.) monosluoksnių atveju: –20 cm^{-1} IMHA molekulei ir 13 cm^{-1} IMHA frag. molekulei. Toks skirtingas dažnio poslinkis yra susijęs su molekulių susipakavimo efektyvumu medžiagos tūryje ir monosluoksnyje. Im žiedas IMHA molekulėje sukuria sterines kliūtis kaimyniniams amidams formuoti optimalų vandenilinių ryšių tinklą.

Užregistravus ant lygaus aukso paviršiaus adsorbuoto IMHA monosluoksnio Ramano ir SHINERS spektrus bei juos palyginus išryškėjo Ag@SiO_2 nanodalelių funkcionalumas: atsirado aiškios, charakteringos virpesinės juostos, kurios suteikia išsamią informaciją apie molekulės struktūrą. Pavyzdžiui, intensyvi juosta SHINERS spektre ties 702 cm^{-1} atitinka $\nu(C{-}S)_T$ IMHA valentinius virpesius, kurie tampa pastebimi molekulei įgavus vertikalią orientaciją paviršiaus atžvilgiu ties C−S ryšiu. Tuo pat metu stebima ir $\nu(C{-}S)_G$ juosta apie 622 cm^{-1}, tačiau juostos intensyvumas gana nedidelis, todėl tokie spektriniai duomenys tik patvirtina RAIRS eksperimento rezultatus, jog dominuojanti pilnai susiformavusio monosluoksnio konfigūracija yra *trans*. Taip pat iš užregistruoto spektro akivaizdu, kad tautomerinė pusiausvyra ant aukso adsorbuoto IMHA monosluoksnio skiriasi nuo tirpalo fazės. Virpesinė juosta ν(C4=C5) + ν(C4–C6) + β(C5H), esanti 1582 cm^{-1}, yra artima T–II būdingai modai 1588–1583 cm^{-1} [66]. Kitos dvi juostos ties 1261 H_2O ir 1257 cm^{-1} D_2O tirpaluose atitinkamai patvirtina IMHA paviršiaus T–II formą[66].

Siekiant objektyviai interpretuoti gana kompleksišką vidurinio diapazono spektrinę sritį, kur yra imidazolo žiedo, amido ir metileno grupių virpesiai, atliktas tirpiklio pakeitimas iš H_2O į D_2O. Tokiu būdu nustatyta Am–I juostų vieta: 1643 ir 1676 cm^{-1}, šių juostų dažnis sumažėja 7–8 cm^{-1} pakeitus tirpiklį. Taip pat pastebėta, kad virpesinės juostos, esančios 1300–1610 cm^{-1} srityje, irgi yra jautrios tirpiklio pakeitimui. Pavyzdžiui, T–II priklausanti C=C valentinio virpesio juosta Im žiede ν(C4=C5) aiškiai pasislenka iš 1590 į 1571 cm^{-1} [80]. Kita intensyvi juosta ties 1333 cm^{-1} išryškėja D_2O tirpale, o tai leidžia daryti išvadą, kad tai protonuoto histidino T–II žymuo (N3D)[81].

Toliau, norint įvertinti monosluoksnio funkcionalumą elektrocheminėje fazių riboje, užregistruoti IMHA monosluoksnio SHINERS spektrai prie skirtingų sistemos elektrinio potencialo verčių. Nustatyta, kad Au–S ryšį atspindinčios virpesinės juostos dažnis padidėja nuo 257 cm^{-1} iki 279 cm^{-1} keičiant potencialo vertę nuo –0,8 V iki 0,2 V (atž. Ag/AgCl). Toks pokytis rodo Au–S ryšio stiprio padidėjimą dėl elektrodo poliarizacijos

pasikeitimo ir Štarko efekto[39,82]. Kalbant apie S–C ryšį, *trans/goš* konformerų santykis lygus 1 esant –0,8 V (atž. Ag/AgCl), tačiau teigiamėjant elektrodo poliarizacijai *trans* konformacija tampa vyraujančia ir *trans/goš* santykis pasikeičia į 3 prie 0,2 V (atž. Ag/AgCl). Vadinasi, potencialo pokytis iš neigiamo į teigiamą sukelia C–S ryšio stiprio sumažėjimą, priešingai nei Au–S ryšiui[83]. Be to, visame keičiamo potencialo lange imidazolo tautomerizacijos žymenys ties 1262 ir 1597 cm^{-1} išlieka būdingi N3–H protonuotai formai (T–II)[69]. Visgi potencialui tapus –0,8 V (atž. Ag/AgCl) atsiranda petys ties 1573 cm^{-1}, kas yra siejama su T–I forma. Taigi EC-SHINERS duomenys įrodo, kad T–II tautomerinė forma yra vyraujanti visame potencialo lange, ir tik nedidelė molekulių dalis tampa T–I formos esant neigiamiausiam potencialui. Toliau nustatyta, kad keičiant potencialo vertę link teigiamos Am–I juostos dažnis padidėja per 11,2 cm^{-1}. Siekiant tiksliau išsiaiškinti, kas sukelia tokį dažnio poslinkį, buvo išanalizuotas Am–I juostų 1631 ir 1680 cm^{-1} intensyvumų santykis. 1631 cm^{-1} juosta atspindi stiprią vandenilinę sąveiką, o 1680 cm^{-1} – susilpnėjusį vandenilinį ryšį. Intensyvumų santykis I_{1631}/I_{1680} tolygiai mažėja nuo 3,4 iki 2,3, potencialui keičiantis iš neigiamo į teigiamą. Galiausiai tampa aišku, jog tiek Am–I juostos dažnio poslinkis, tiek juostų intensyvumų santykis rodo teigiamo potencialo įtaką vandenilinio ryšio stiprio sumažėjimui tarp gretimų grandinių.

Ramano temperatūriniai ir DFT modeliavimo duomenys padėjo nustatyti imidazolo žiedo judėjimo laisvumui ir vandenilinio ryšio stipriui jautrią virpesinę juostą ties 1492 cm^{-1}. Šios juostos analizė atskleidė nuo potencialo priklausomą Im žiedo elgseną: prie –0,8 V (atž. Ag/AgCl) elektrodo poliarizacijos Im žiedas yra daug labiau apribotas ir sudaręs stipresnius vandenilinius ryšius nei esant –0,4 V (atž. Ag/AgCl). Toliau potencialui teigiamėjant (nuo –0,4 V iki 0,2 V(atž. Ag/AgCl)) sąveika ties Im nežymiai padidėja.

Kita aktuali IMHA junginio tyrimų kryptis, nepublikuota mokslinėje spaudoje, imidazolo žiedo IMHA monosluoksnyje rūgšties disociacijos konstantos (pK_a) nustatymas. Vienos iš pagrindinių fizikocheminių paviršiaus parametrų – pK_a vertės išsiaiškinimas leidžia suprasti monosluoksnio funkciją, kaip monosluoksnis reaguoja į besikeičiančią tirpalo aplinką, taip suteikiant galimybę valdyti norimas paviršiaus savybes kuriant ar tobulinant biojutiklius, kitus biotechnologinius prietaisus. Svarbu pabrėžti, jog to paties junginio monosluoksnio (pK_a vertė fazių riboje) ir tirpalo pK_a vertės gali gerokai skirtis dėl kelių priežasčių. Pirma, skirtumai tarp paviršiuje adsorbuotos ir tūryje esančios medžiagos pK_a gali būti gaunami dėl skirtingų

eksperimentinių sąlygų, kurios medžiagos tūryje ir lokaliai ant tam tikro paviršiaus gali būti visiškai kitokios[84]. Taip pat yra tyrimų, kuriuose galima aiškiai matyti, jog rūgštys ir bazės adsorbuotos paviršiuje pasižymi mažesnėmis rūgštinėmis ir bazinėmis savybėmis, tai gali iššaukti pK_a vertės pokyčius fazių riboje[85]. Kita priežastis, lemianti paviršiaus jonizacijos pokyčius – krūvio susikaupimas ir dvigubo elektrinio sluoksnio susidarymas. Gerai žinoma, jog lokali jonų koncentracija dvigubame sluoksnyje skiriasi nuo tūrinio tirpalo, todėl krūvį turinčių paviršių reaktyvumas iš esmės skiriasi nuo tūrinio tirpalo dėl dvigubo sluoksnio susidarymo. Be to, protonavimo procesui įtakos turi ir sumažėjusi dielektrinė konstanta fazių riboje, pasikeitęs įmobilizuotų molekulių laisvės laipsnių skaičius ar vandenilinių ryšių susidarymas tarp gretimų rūgštinių/bazinių grupių[85]. Verta paminėti ir tai, jog skirtingais metodais nustatant net to paties monosluoksnio pK_a vertę gali būti gaunamos irgi šiek tiek skirtingos reikšmės[84]. Taip yra todėl, kad metodų, leidžiančių tiksliai nustatyti tirpalų pK_a vertes yra nemažai[86], tačiau tiriant medžiagų paviršines savybes elektrocheminėse fazių ribose vis dar kyla daugybė iššūkių[87]. Šiuo metu yra keletas tyrimų metodų, leidžiančių *in-situ* nustatyti monosluoksnių pK_a vertes, bet vienas tinkamiausių – SHINERS.

Taigi prieš pateikiant eksperimentinius duomenis apie imidazolo žiedo monosluoksnyje pK_a vertę svarbu nurodyti konkrečias eksperimentines sąlygas. Eksperimentas atliktas naudojant dviejų tipų monosluoksnius: vieną sudarė tik IMHA molekulės, adsorbuotos parą laiko ant lygaus Au paviršiaus, kitą – IMHA molekulės kartu su IMHA frag. junginiu (30 % IMHA ir 70 % IMHA frag.). Eksperimentas atliktas palaikant pastovų elektrodo potencialą (–0,1 V (atž. Ag/AgCl)), kuris artimas atviros grandinės potencialui. Terpės pD vertės keistos nuo 7,5 iki 2,1 naudojant deuteruotus 0,05 M buferinius tirpalus (fosfatinis buferis (pD 7,5), citratinis buferis (pD 6,2 – 3,1) ir chloridinis buferis (pD 2,7 – 2,1)). Kiekvienu atveju registruoti SHINERS spektrai stebint virpesinės juostos – 1405 cm^{-1} (Im ν(N1C2N3), kuri yra pagrindinis deuteriu pakeisto imidazolo žiedo katijono spektrinis žymuo[71], intensyvumo pokyčius (11 pav. A). Apdorojant duomenis visi spektrai sunormuoti į rūgštingumui nejautrią juostą ties 1297 cm^{-1} ($t(CH_2)$). Spektrus aproksimavus Lorenso ir Gauso kreivėmis nustatyti juostos 1405 cm^{-1} intensyvumo pokyčiai prie skirtingų terpės pD verčių (11 pav. B). Taškai aproksimuoti sigmoidinėmis kreivėmis, o jų vidurio taškas ir atitinka imidazolo žiedo monosluoksnyje pK_a vertes.

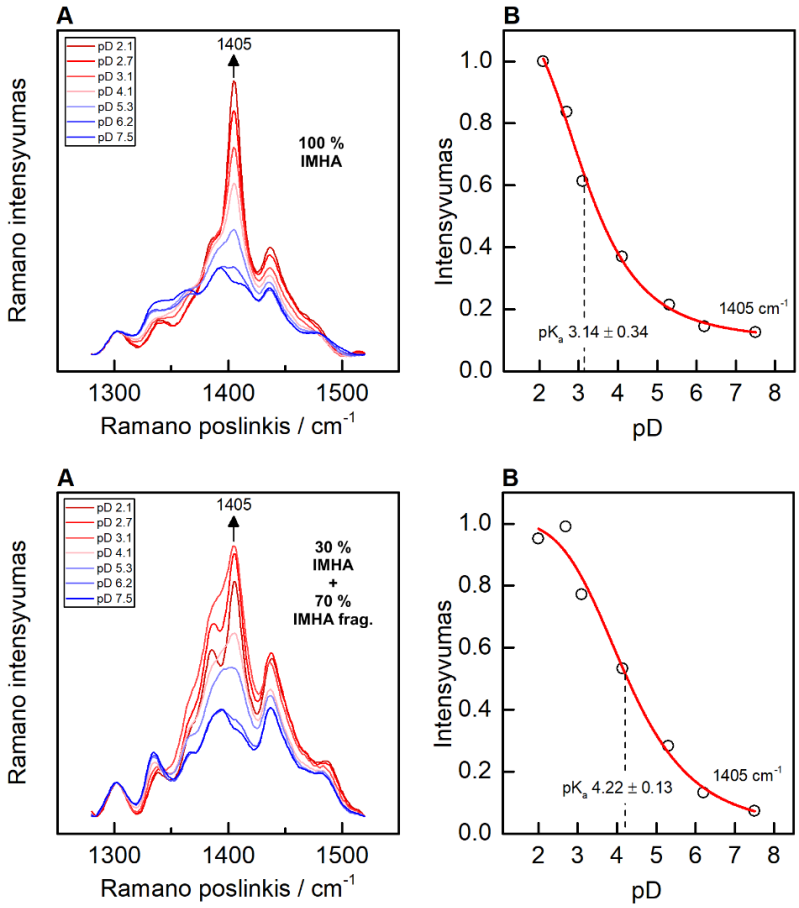

11 pav. (A) IMHA monosluoksnio (aukščiau) ir IMHA + IMHA frag. monosluoksnio (žemiau) SHINERS spektrai prie skirtingų terpės pD verčių, palaikant pastovų –0,1 V (atž. Ag/AgCl) potencialą. **(B)** Juostos 1405 cm^{-1} intensyvumo kitimas nuo terpės rūgštingumo: pavaizduoti taškai atitinka trijų eksperimentų vidurkius, aproksimuotos sigmoidinės formos kreivės, pK_a vertės nurodytos su standartiniu nuokrypiu.

Lyginant nustatytas vertes (3,14±0,34 100% IMHA monosluoksniui ir 4,22±0,13 30% IMHA+70% IMHA frag. monosluoksniui) nustatyta, jog jos nuo laisvo histidino tirpale vertės, kuri arti neutralaus pH (5,9), skiriasi per 2,76 ir 1,68 atitinkamai. Lyginant pKa vertes skirtingos kompozicijos monosluoksniuose, galime daryti išvadą, jog monosluoksnyje su praskiedėju Im žiedas lengviau prisijungia protoną, tai lemia retesnis žiedų išsidėstymas. Gauti rezultatai svarbūs tolimesniems tyrimams vystant bioelektronikos prietaisus, kuomet siekiama geriau suprasti imidazolo žiedo sąveikas bei funkcionalumą elektrocheminėje fazių riboje.

3.3 Riboflavino, adsorbuoto ant grafeno, tyrimas

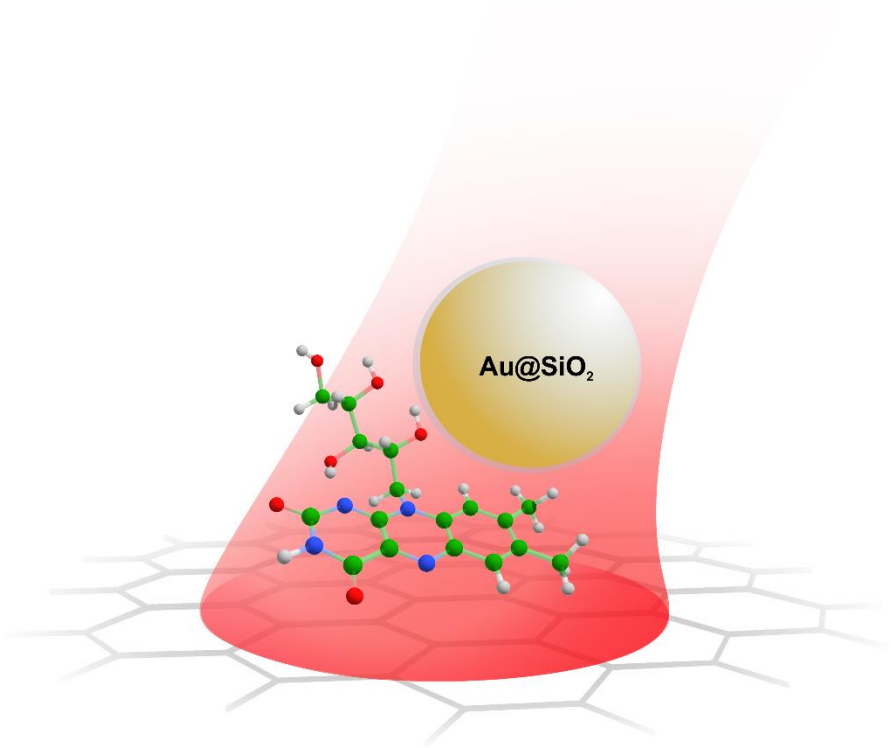

Ištyrus modelinę biomolekulinę sistemą ant laidaus Au paviršiaus, pereita prie sudėtingesnės sistemos: riboflavino adsorbuoto ant grafeno paviršiaus tyrimo SHINERS metodu.

Grafeno elektroninės savybės ir funkcija priklauso nuo paviršiaus struktūros, defektų prigimties[88,89], legiravimo tipo bei priemaišų[90–93], molekulių ir jonų adsorbcijos ant paviršiaus[94,95]. Žinoma, kad adsorbuotos molekulės gali pakeisti grafeno sluoksnio krūvininkų judrį[95], todėl nekontroliuojamos adsorbcijos atveju sunku sukurti elektronines sistemas su norimomis ir nekintančiomis savybėmis. Plėtojant grafeno pagrindu kuriamas technologijas būtina kontroliuoti adsorbcijos procesus ir suprasti, kaip defektai ir priemaišos keičia šių sistemų fizikines bei chemines savybes molekuliniu lygmeniu. Kiek anksčiau buvo nustatyta, kad aromatinės molekulės, adsorbuotos ant vieno sluoksnio grafeno, pakeičia Fermi lygmenį[96]. Be to, siekiant padidinti įkraunamų ličio jonų baterijų talpumą, įterpiami grafeno nanosluoksniai, prieš tai modifikavus paties grafeno struktūrą[97]. Taigi grafeno pagrindu kuriamų sistemų paviršiaus ir fazių ribos tyrimai yra itin svarbūs fizikinėje chemijoje ir medžiagų moksle.

Ramano spektroskopija yra neardantis ir jautrus tyrimo metodas, galintis pateikti išsamią struktūrinę informaciją apie įvairias anglies nanostruktūras[98,99]. Be to, rezonansinė Ramano sklaida gali suteikti svarbios informacijos apie medžiagos elektroninę struktūrą[100]. Dėl plačios grafeno π-elektronų sistemos sužadinimas matomoje spektrinėje srityje leidžia registruoti rezonansiškai sustiprintus Ramano spektrus[98,100]. Vis dėlto nors rezonansinė Ramano spektroskopija ir suteikia informacijos apie grafeno karkaso struktūrą[98], bet tiesioginė informacija apie molekulinių grupių, kovalentiškai prijungtų prie anglies matricos ar adsorbuotų junginių, struktūrą negaunama. Kai kuriais atvejais adsorbuotos organinės molekulės gali būti tiriamos naudojant grafeno sustiprintą Ramano spektroskopiją (GERS)[101–107]. GERS atveju pagrindinis Ramano signalo stiprinimo mechanizmas yra cheminis, susijęs su krūvio pernašos sužadinimu[103,107], todėl stiprinimas labai priklauso nuo adsorbato energetinės būsenos ir molekulės struktūros[103]. Plokščios molekulės, turinčios D_{nh} simetriją, yra labiau tinkamos GERS, nes yra geriau suderinamos su grafeno struktūra[103]. Taigi GERS pasižymi išskirtiniu molekuliniu selektyvumu, nes visiškai priklauso nuo cheminio stiprinimo mechanizmo[102]. Norint stebėti funkcines grafeno oksido grupes, adsorbuotas priemaišas ar tikslingai adsorbuotus junginius ant grafeno, reikalinga alternatyvi spektroskopinė technika. Būtent čia puikia tinkama SHINERS spektroskopija. SHINERS jau taikyta molekulinio lygmens

informacijai apie įvairius paviršius gauti – nuo adsorbatų ant plokščių monokristalinių iki puslaidininkinių paviršių[5,31,113,38,39,76,108–112].

Riboflavinas (Rf) arba vitaminas B2 yra vandenyje tirpus vitaminas, atliekantis itin svarbų vaidmenį ląstelių biocheminiuose procesuose[114]. Mokslininkų susidomėjimas riboflavino elgsena ir molekulinių sąveikų tyrimais kyla dėl svarbaus Rf vaidmens užkertant kelią įvairioms ligoms, pavyzdžiui, migrenai, vėžiniams susirgimams, hipertenzijai ar lėtinėms ligoms, susijusioms su oksidaciniu stresu[115]. Rf dėl savo aromatinės prigimties (12 pav.) gali būti detektuojamas elektrochemiškai, todėl dažnai taikomas įvairiose elektrochemijos srityse. 2016 metais buvo ištirta riboflavino elektropolimerizacija įvairiose terpėse[116]. Riboflavino plėvelės buvo charakterizuojamos spektroskopiškai, mikroskopiškai ir elektrochemiškai, tuomet nustatyta, kad perspektyvūs jutikliai gali būti pagaminti iš hibridinių Rf-grafeno darinių. Tuo pačiu parodyta, kad virpesinė spektroskopija yra vienas tinkamiausių tyrimo metodų adsorbuoto Rf sąveikų ir struktūros analizėje. Visgi svarbu pabrėžti, kad ištirti adsorbuotą Rf ant labai orientuoto pirolitinio grafito Ramano spektroskopijos metodu itin sunku[116]. Taigi tiriant panašias molekulines sistemas vertėtų taikyti universalesnį – SHINERS metodą.

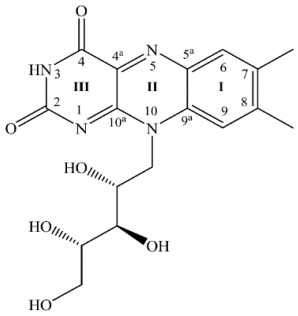

12 pav. Riboflavino molekulinė struktūra ir izoaloksazino žiedo atomų numeracija.

Pagrindinis šios tyrimų krypties tikslas buvo parodyti SHINERS metodo pritaikomumą siekiant gauti molekulinio lygio informaciją apie adsorbuotą Rf grafeno paviršiuje. Išsamios įžvalgos apie Rf ir grafeno sąveiką pateikiamos analizuojant SHINERS, GERS ir DFT metodais gautus rezultatus.

Pirmiausia su 532 nm lazerinės spinduliuotės žadinimu registruoti dviejų bandinių rezonansiniai Ramano spektrai: grafeno ant vario padėklo ir grafeno ant vario padėklo su adsorbuotu riboflavinu. Abejuose, kaip įprasta rezonansiniuose Ramano spektruose, nustatytos aiškios 2D ir G juostos, bet defektus charakterizuojančios D juostos apie 1350 cm^{-1} – nėra[98,117,118].

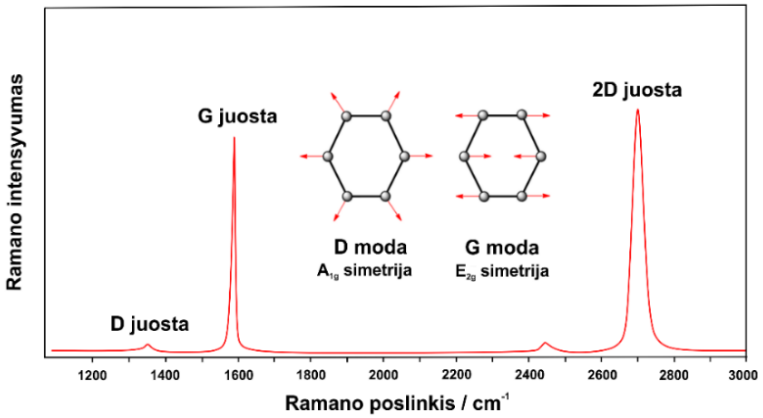

13 pav. Tipinis defektų turinčio grafeno Ramano spektras. Centre pavaizduoti D ir G modų virpesiai (adaptuota pagal[119]).

Pasinaudojus juostų intensyvumo santykiu I(2D)/I(G) įvertintas grafeno sluoksnių skaičius. Nustatyta, kad abiejų bandinių atveju santykis I(2D)/I(G) >1 (1,8 prieš riboflavino adsobciją ir 1,9 – po Rf adsorbcijos), o tai reiškia, jog tirti bandiniai sudaryti iš vieno grafeno sluoksnio[117]. Žemo dažnio srityje grafeno be Rf atveju užregistruotos kelios virpesinės juostos: 151, 220 ir 640 cm^{-1}, priskirtos Cu_2O nuo vario padėklo. Adsorbavus riboflaviną ant grafeno atsirado keli aiškūs spektriniai pokyčiai aukšto dažnio srityje. Pirma, abi charakteringos grafeno juostos pasislinko į trumpesnių bangų pusę ir atsirado papildomų virpesinių juostų srityje 1300–1650 cm^{-1}. G ir 2D juostų poslinkiai rodo riboflavino ir grafeno sąveiką. Naujos juostos ties 1351, 1411 ir 1536 cm^{-1} priklauso riboflavino žiedo charakteringiems virpesiams[116], šių juostų išryškėjimas rodo Ramano sklaidos sustiprėjimą dėl grafeno substrato, kitaip – pasireiškia GERS efektas. Žemo dažnio srityje neaptikta jokių papildomų juostų dėl riboflavino adsorbcijos ant grafeno. Taigi Ramano sklaidos žadinimas 532 nm lazerine spinduliuote suteikia galimybę aptikti adsorbuotą riboflaviną pasireiškus GERS Ramano sklaidos stiprinimo mechanizmui, tačiau užregistruotų adsorbato virpesinių juostų intensyvumas visgi yra mažas.

Norint gauti informatyvesnius ir intensyvesnius grafeno ir adsorbuoto Rf ant grafeno spektrus buvo panaudotas SHINERS metodas. Šiam tyrimui susintetintos 50 ± 5 nm dydžio Au@SiO_2 nanodalelės su 3 nm storio išoriniu dielektriko apvalkalu. Nustatyta, kad naudojant susintetintas Au@SiO_2 nanodaleles optimaliausias Ramano sklaidos žadinimo bangos ilgis 785 nm. Taigi pirmiausia užregistruoti grafeno ir grafeno su adsorbuotu riboflavinu Ramano spektrai, vėliau, ant analogiškų paviršių paskleidus Au@SiO_2 nanodalelių, užregistruoti SHINERS spektrai. Grafeno ir grafeno-riboflavino mėginių Ramano spektruose matoma tik viena plati juosta apie 609–619 cm^{-1}. Ši juosta įrodo, kad po grafeno sluoksniu yra ant Cu_2O oksido, tačiau jokios papildomos informacijos Ramano spektruose aptikti nėra galimybės. Ant grafeno paviršiaus užlašinus ir nudžiovinus Au@SiO_2 nanodaleles gautas SHINERS spektras su keliomis aiškiomis virpesinėmis juostomis. 1592 cm^{-1} juosta priskirta grafeno monosluoksnio G juostai, o juostos, esančios 1303–1336 cm^{-1} srityje, siejamos su grafeno D juosta, išryškėjusia dėl lokalių grafeno defektų. Kitos – žemo intensyvumo – juostos atsiranda dėl adsorbuotų priemaišų ant grafeno paviršiaus ir (arba) kovalentiškai prisijungusių funkcinių grupių grafeno plokštumoje, taip pat galimos ir priemaišos iš nanodalelių. Visiškai skirtingas SHINERS spektras užregistruotas prieš tai ant grafeno adsorbavus riboflaviną. Intensyviausia spektro juosta ties 1349 cm^{-1} priklauso riboflavino virpesiams, siejamiems su simetriniu valentiniu ν_s(C2–N3–C4) ir valentiniais I, II, III žiedų virpesiais. Taip pat spektre aiškiai matomos kitos riboflavino žiedo juostos ties 710, 740, 1158, 1407, 1457 ir 1525 cm^{-1}.

Šio tyrimo metu pirmą kartą palyginti GERS ir SHINERS metodų ypatumai tiriant adsorbuotą riboflaviną ant grafeno. Svarbu pabrėžti, kad GERS spektrai buvo žadinami 532 nm lazerio bangos ilgiu, o stiprinimo mechanizmas yra susijęs tik su krūvio pernašos sužadinimu, vadinasi, stiprinami virpesiai tik tų atomų Rf žiede, kurie dalyvauja π elektronų sąveikoje. Tuo tarpu SHINERS spektroskopija paremta plazmoninio stiprinimo mechanizmu ir suteikia išsamią informaciją ne tik apie Rf žiedo virpesius, bet ir apie kai kuriuos ribitilo grandinės virpesius. Taip pat nustatyta, kad juostos 1349 cm^{-1} santykinis intensyvumas, sunormuotas pagal lazerio galią, SHINERS spektruose buvo net 26 kartus didesnis, lyginant su GERS spektrais. SHINERS spektre identifikuotų ribitilo grandinės virpesinių juostų dažniai (1048, 981 ir 930 cm^{-1}) gerokai mažesni nei analogiškų, nors ir labai nedidelio intensyvumo, juostų dažniai riboflavino tirpalo Ramano spektre. Toks juostų poslinkis aiškiai rodo, kad riboflavino ribitilo grandinė sąveikauja su grafeno paviršiumi. Vis dėlto, vienas įdomiausių pastebėjimų

SHINERS spektre – intensyvi, plati juosta apie 1321 cm^{-1}. Ši juosta neregistruota nei riboflavino tirpalo ar miltelių Ramano spektre. Taip pat panaši juosta nepastebėta ir rezonansiniame grafeno Ramano spektre. Juostos kilmę ir prigimtį padėjo išsiaiškinti kvantinės chemijos modeliavimo duomenys, kuomet nustatyta, jog 1321 cm^{-1} juostos atsiradimas gali būti siejamas su riboflavino adsorbcijos sukeltu grafeno sluoksnio išlinkiu ir pakrypimu. Šis pastebėjimas išryškina SHINERS metodo galimybes nustatant lokalias sistemos perturbacijas.

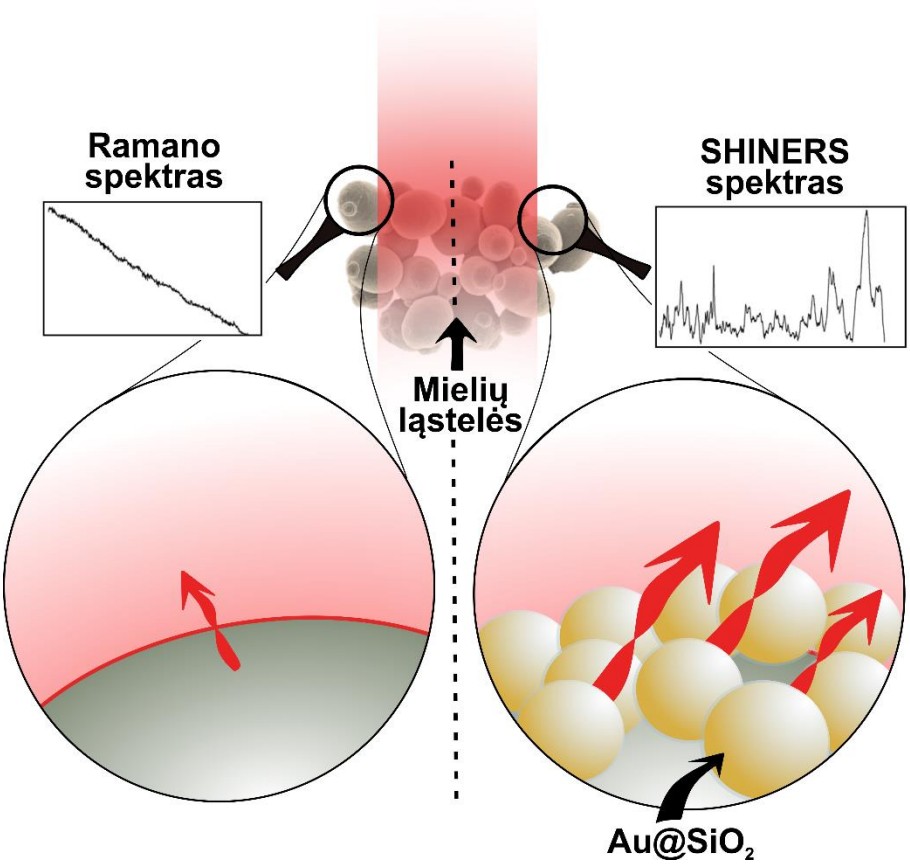
Ramano
spektras
SHINERS
spektras
Mielių
ląstelės
Au@SiO2

Įgyta SHINERS metodo taikymo patirtis tiriant skirtingas biomolekules leidžia pereiti prie itin kompleksiškų, nevienalyčių biologinių molekulinių sistemų tyrimų, tokių kaip gyvų mielių ląstelių.

Mielių ląstelės yra vienos iš labiausiai paplitusių ir intensyviausiai tyrinėjamų modelinių eukariotinių sistemų, sutinkamų taikomojoje biotechnologijoje ar medicinoje. Gyvosios ląstelės ir mikroorganizmai, įmobilizuoti ant skirtingų paviršių, dažnai taikomi kuriant biojutiklius ar kitus bioelektronikos prietaisus, aplinkos apsaugos srityje, maisto pramonėje[120–124]. *Saccharomyces cerevisiae* mielės šimtmečius buvo naudojamas maisto ir alkoholinių gėrimų fermentacijos procesuose[125]. Vis dėlto, kitos mielių rūšys – *Metschnikowia pulcherrima (Candida pulcherrima)* – pastaruoju metu tampa vis aktualesnės dėl savo unikalių savybių[126]. Tyrimo objektu pasirinktos *Metschnikowia* rūšies mielės augimo terpėje esant geležies (III) druskų išskiria netirpų raudoną pigmentą – pulcheriminą. Pulcheriminas yra geležies chelatas arba pulcherimino rūgšties druska (2,5-diizobutil-3,6-dihidroksipirazin-1,4-dioksidas), arba šio junginio tautomerinė forma[127–129]. Molekulinė pigmento struktūra pavaizduota 14 pav. Pulcherimino susidarymas prasideda nuo to, kad mielės į aplinką išskiria pulcherimino pirmtaką – pulcherimino rūgštį. Dėl pulcherimino rūgšties reakcijos su geležies (III) jonais aplink mielių kolonijas susidaro raudonos aureolės, kuriose yra išsodinto pulcherimino. Jeigu terpėje didėja geležies (III) jonų koncentracija, tuomet mažėja aureolių dydis, tačiau intensyvėja jų spalva, mielių ląstelių spalva iš baltos pasikeičia į raudoną. Susidarant netirpiam pulcheriminui, terpėje išeikvojama laisva geležis, todėl aplinka tampa netinkama kitiems mikroorganizmams, kurių augimui būtina geležis. Todėl *Metschnikowia pulcherrima* pasižymi veiksmingu antimikrobiniu aktyvumu prieš įvairius patogeninius mikroorganizmus[130,131]. Šios mielės aptinkamos ant prinokusių vynuogių ir vynuogių misos, todėl unikali *Metschnikowia* rūšies mielių savybė gali būti pritaikoma vyno gamybos pramonėje norint kontroliuoti nepageidaujamų mielių rūšių kiekį fermentacijos procese[132].

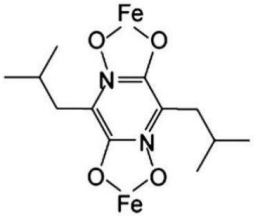

14 pav. Pigmento pulcherimino molekulinė struktūra.

Siekiant suprasti biocheminius procesus, vykstančius mielių ląstelėse, ir apie tai gauti molekulinio lygmens informaciją, reikalingas neardantis, bet itin jautrus tyrimo metodas. SERS leidžia tirti itin dideliu jautrumu vandeninėje terpėje biologinių junginių molekulines struktūras, adsorbuotas ant, ar esančias šalia plazmoninių paviršių[133–137]. Plazmoninių nanodalelių savybės ir anksčiau buvo pritaikytos biomolekulių ir gyvų ląstelių sudedamųjų dalių aptikimui ir struktūrinei analizei[40,137,138]. Žinoma, yra nemažai tyrimų, kuomet Ag ir Au nanodalelės buvo sėkmingai panaudotos mielių identifikavimui SERS metodu[139–148]. Šie tyrimai buvo atlikti remiantis panašia metodika, kuomet mielių ląstelių charakterizavimas atliekamas prieš tai jas inkubavus su Ag ar Au nanodalelių suspensija. Šių tyrimų metu nustatyta, kad yra nemažai veiksnių, tokių kaip nanodalelių adsorbcija ant atskirų ląstelės dalių ar pačių nanodalelių agregacija, kurie sąlygoja neatsikartojančius ląstelių SERS spektrus[139,140]. Verta paminėti ir tai, kad nors sidabras pasižymi didesniu SERS signalo stiprinimo faktoriumi nei kiti plazmoniniai metalai, Ag nanodalelės išskiria toksiškus sidabro jonus, kurie biologiškai nesuderinami su gyvomis ląstelėmis. Au nanodalelės yra stabilios ir netoksiškos, tačiau jas taikant ląstelių tyrimuose neįmanoma išvengti tiesioginės metalo sąveikos su ląstelėmis, tai gali pakeisti eksperimento metu stebimus biocheminius procesus. Puiki alternatyva, galinti išspręsti anksčiau minėtas problemas, – SHINERS metodo taikymas. SHINERS metodo galimybės tiriant *Saccharomyces cerevisiae* pirmą kartą parodytos 2010 metais. Tuomet nustatyta ląstelės sienelės struktūra, išskirtos aminorūgščių ir amido grupių virpesinės juostos, surasti manano-baltymų spektriniai žymenys[4].

Pagrindiniai rezultatai ir išvados

Doktorantūros studijų metu pasirinkta tirti *Metschnikowia pulcherrima* mielių ląstelės sienelės struktūrą SHINERS metodu. Ramano spektroskopija ypač tinkama ląstelių tyrimams ir dėl lengvo suderinamumo su mikroskopiniais metodais. Mikroskopo pagalba tyrimams galima pasirinkti atskirą ląstelę ar net jos dalį, lazerinę spinduliuotę fokusuoti į ląstelės sienelę ar tūrį. Taip gauti rezultatai standartizuojami, o jų analizė tampa lengvesnė. Taip pat Ramano spektroskopija leidžia registruoti spektrus itin plačioje virpesinio spektro srityje (nuo 100 iki 3600 cm^{-1}), todėl gaunama išsami informacija apie visų pagrindinių molekulinių grupių virpesius.

Taigi šiame darbe tirti du *Metschnikowia pulcherrima* mielių bandiniai – su didesne ir mažesne pulcherimino pigmento koncentracija terpėje. Eksperimentų metu pastebėta, kad registruojant mielių bandinių Ramano spektrus pasireiškia intensyvus fluorescencinis fonas, tačiau ant

mielių užlašinus Au@SiO_2 nanodalelių fluorescencinis fonas sumažėja 150 (mielėms su daugiau pigmento) ir 60 (mielėms su mažiau pigmento) kartų. Toks fluorescencijos gesinimo reiškinys, naudojant plazmonines dielektriko apvalkalu dengtas daleles, pastebėtas ir kitų autorių[149]. P.-P. Fang ir kt. nustatė, kad Au@SiO_2 nanodalelių atveju fluorescencija gesinama, kai apvalkalo storis mažesnis nei 5 nm; tuo tarpu didesnių nei 10 nm apvalkalo atveju fluorescencijos intensyvumas padidės (reiškinys žinomas kaip paviršiaus sustiprinta fluorescencija, SEF)[149]. Šiame darbe panaudotos nanodalelės su maždaug 5 nm SiO_2 apvalkalo storiu. Toks apvalkalas pakankamai plonas, kad būtų galima veiksmingai sumažinti fluorescencijos foną, užtektinai sustiprinti Ramano signalus. Aukso nanodalelės branduolio dydis pasirinktas 50 nm, nes anksčiau išsiaiškinta, kad toks plazmoninės šerdies dydis geriausiai tinka biologinių bandinių tyrimams[42].

Toliau nustatyta, kad naudojant Au@SiO_2 nanodaleles SHINERS spektrų atsikartojamumas iš skirtingų mėginio vietų yra daug geresnis nei SERS spektrų. SHINERS spektrų atveju smailių pozicijos nesikeičia ir neatsiranda papildomų virpesinių juostų. Priešinga tendencija pastebėta SERS spektruose: registruotos papildomos, neaiškios kilmės virpesinės juostos, tiek smailių santykiniai intensyvumai, tiek skirtingi dažniai įvairiose bandinių vietose. SHINERS ir SERS spektrų atkartojamumo skirtumai atsirado dėl tiesioginės mielių ląstelių sudedamųjų dalių sąveikos su Au nanodalelėmis. Biomolekulių sąveika su Au ar Ag nanodalelėmis priklauso nuo molekulių prigimties (poliškumo, lankstumo) ir kitų faktorių, tai dažnai ir iššaukia spektrų neatsikartojamumą[140].

Prieš aptariant atskirų funkcinių grupių virpesines juostas, svarbu paminėti, kad dauguma virpesinių juostų SHINERS spektruose visgi yra persidengusios ir kompleksinės, todėl virpesinių juostų priskyrimas gana sudėtingas. Visgi aiškiai išreikšta juosta ties 1200 cm^{-1} priskirta vyraujantiems triptofano ir fenilalanino funkcinių grupių virpesiams baltymuose. Kita charakteringa juosta apie 1000 cm^{-1} atspindi fenilalanino žiedo virpesius. Intensyvi juosta 1442–1444 cm^{-1} priskirta CH_2 grupės deformaciniams žirkliniams virpesiams baltymuose ir fosfolipiduose, o šalia esantis petys (1411 cm^{-1}) apibūdina karboksilato grupės simetrinius valentinius virpesius ν_s(COO). SHINERS spektruose aiškiai matoma juosta ties 1308 cm^{-1} identifikuota kaip CH_2 grupės deformaciniai virpesiai, siejami su baltymų antrine struktūra (α ir π spiralės), tai parodo SHINERS metodo jautrumą antrinei baltymų struktūrai. Kiek toliau apie 920–922 cm^{-1} esanti intensyvi juosta atitinka C−C ir C−O valentinius virpesius,

charakterizuojančius aminorūgščių liekanas. Plati virpesinė juosta, esanti 820–823 cm^{-1}, siejama bent su keliomis molekulinėmis grupėmis: metileno grupės švytuokliniai deformaciniai virpesiai, lipidų O−P−O grupės asimetriniai valentiniai virpesiai, tirozino žiedo ir polisacharidų ν(C−O−C)/ν(C−C) valentiniai virpesiai. Virpesiai tarp 823 ir 480 cm^{-1} priskiriami hidrofilinės galvutės grupės virpesiams fosfolipiduose.

Siekiant SHINERS spektre identifikuoti pigmento pulcherimino virpesines juostas buvo suformuotas mielių su daugiau pigmento ir mielių su mažiau pigmento skirtuminis SHINERS spektras. Skirtuminiame spektre išryškejo kelios virpesinės juostos, tačiau vienareikšmiškai išskirti pulcherimino virpesių nepavyko. Dėl to pasitelkti papildomi tyrimo metodai: kvantinės chemijos skaičiavimai, užregistruotas iš mielių išskirto pigmento Ramano spektras naudojant 830 nm žadinantį bangos ilgį ir išskirto pigmento ATR−FTIR (ang. *Attenuated Total Reflectance-Fourier Transform Infrared*) spektras. Remiantis gautais eksperimentiniais ir teoriniais duomeninis nustatytos kelios charakteringos pulcherimino virpesinės juostos SHINERS spektre. Viena jų, ties 622 cm^{-1}, priskirta pirazino žiedo kvėpavimo virpesiui. Kita plati juosta, apie 758 cm^{-1} skirtuminiame SHINERS spektre, siejama su pulcherimino izobutilo grandinės valentiniais virpesiais, taip pat pastebimais ties 800 cm^{-1} išskirto pigmento Ramano spektre. Kelios intensyvios juostos 1010–1070 cm^{-1} srityje užregistruotos ATR-FTIR pulcherimino miltelių spektre, tačiau tik viena juosta ties 1169 cm^{-1} skirtuminiame SHINERS spektre koreliuoja su aiškia juosta 1173 cm^{-1} pigmento miltelių Ramano spektre. Taigi ši juosta priskirta izobutilo grandinės valentiniams ν(C−C) virpesiams kartu su CH_3 ir CH_2 grupių deformaciniais virpesiais. Vis dėlto verta paminėti, kad skirtuminis SHINERS spektras visiškai nesutampa su pigmento Ramano spektru. Nesutapimus lemia bent kelios priežastys: (1) skirtinga pigmento būsena mielių ląstelėse ir milteliuose; (2) pulcherimino struktūros ir Ramano spektro priklausomybė nuo geležies koncentracijos ir (3) mielių ląstelių sienelės komponentų struktūros pokyčiai priklausomai nuo pigmento kiekio ląstelėse.

Apibendrinus gautus rezultatus, galima teigti, kad SHINERS metodas leidžia gauti atsikartojančius ir patikimus duomenis, spektruose gausu virpesinės informacijos apie ląstelės sienelę ir jos pagrindinius funkcinius elementus (baltymus, manano-baltymus, lipidus, amiorūgštis ir polisacharidus).

4. IŠVADOS

1. Lyginant SiO_2, MnO_2 ir TiO_2 nanodalelių apvalkalus SHINERS spektroskopijai, optimaliausias – SiO_2, nes šio sluoksnio virpesinės juostos mažiausio intensyvumo. Taip pat dėl didelio stabilumo rūgštinėje ir neutralioje terpėje SiO_2 apvalkalas labiau tinkamas biomolekulių tyrimuose nei kitos prigimties apvalkalai. Patobulinta apvalkalais dengtų nanodalelių sintezės metodika pakeitus kaitinimo būdą iš konvekcinio į mikrobangų. Mikrobangų poveikyje išorinis nanodalelių apvalkalas susiformuoja mažiau defektingas nei formuojamas kaitinant konvekciniu būdu, taip pat pasiekiamas didesnis nanodalelių dydis (90 ± 10 nm) redukuojant ir stabilizuojant sidabro nitratą tik natrio citratu.

2. Imidazolo žiedo IMHA monosluoksnyje pK_a vertė (3,14 ± 0,34) skiriasi nuo laisvo histidino tirpale (5,9[59]) vertės per 2,76. Taip pat nustatyta, kad mežėjant monosluoksnio tankiui, Im žiedo pK_a vertė – didėja. Toliau, aptiktas naujas imidazolo žiedo vandenilinio ryšio stiprio Ramano žymuo – juosta ties 1492 cm^{-1}. Elektocheminėje fazių riboje potencialas kontroliuoja Im žiedo vandenilio ryšio sąveikos stiprį. Silpniausia sąveika ties –0,4 V ir stiprėja elektrodo potencialui neigiamėjant iki –0,8 V ir teigiamėjant iki 0,2 V (atž. Ag/AgCl).

3. Charakteringų grafeno virpesių dažnio sumažėjimas SHINERS spektre parodė, kad riboflavino molekulė sąveikauja su grafeno monosluoksniu per π elektroninę sistemą. Skirtingai nei GERS metodas, SHINERS metodas įgalino detaliau charakterizuoti adsorbuotą Rf molekulę, kadangi stebimi ne tik žiedo, bet ir ribitilo grupės virpesiai. Riboflavino adsorbcija iššaukė lokalų grafeno plokštumos išsilenkimą ir pakrypimą, todėl registruotas defektų D juostos sustiprėjimas SHINERS spektre.

4. Dėl žymiai sumažėjusios tiesioginės sąveikos tarp biomolekulių ir metalo SHINERS metodas leido gauti patikimus ir atsikartojančius spektrus nuo mielių ląstelių paviršiaus. Nustatytos mielių ląstelių sieneles sudarančios funkcinės molekulės: manano-baltymai, lipidai, amino rūgštys, polisacharidai.

5. LITERATŪROS SĄRAŠAS

1. Jia, M., Li, S., Zang, L., Lu, X. & Zhang, H. Analysis of biomolecules based on the surface enhanced raman spectroscopy. *Nanomaterials* vol. 8 (2018).
2. McArthur, S. L., Fowler, G. J. S. & Mishra, G. Surface Analysis of Biomolecules: Unravelling biointerfacial interactions. *J. Surf. Anal.* **14**, 370–375 (2008).
3. Niaura, G. Raman Spectroscopy in Analysis of Biomolecules. *Encyclopedia of Analytical Chemistry* 1–34 (John Wiley & Sons, Ltd, 2014). doi:10.1002/9780470027318.a0212.pub3.
4. Li, J. F. *et al.* Shell-isolated nanoparticle-enhanced Raman spectroscopy. *Nature* **464**, 392–395 (2010).
5. Li, J. F. *et al.* Surface analysis using shell-isolated nanoparticle-enhanced Raman spectroscopy. *Nat. Protoc.* **8**, 52–65 (2013).
6. Liu, F., Liu, J. & Cao, X. Microwave-assisted Synthesis Silver Nanoparticles and Their Surface Enhancement Raman Scattering. *Rare Met. Mater. Eng.* **46**, 2395–2398 (2017).
7. Liao, S. M., Du, Q. S., Meng, J. Z., Pang, Z. W. & Huang, R. B. The multiple roles of histidine in protein interactions. *Chem. Cent. J.* **7**, 9–11 (2013).
8. Riauba, L., Niaura, G., Eicher-Lorka, O. & Butkus, E. A study of cysteamine ionization in solution by Raman spectroscopy and theoretical modeling. *J. Phys. Chem. A* **110**, 13394–13404 (2006).
9. Raman, C. V. A new radiation. *Indian J. Phys.* **2**, 387–398 (1928).
10. Šablinskas, V. Čeponkus, J. Modernioji molekulių virpesinė spektrometrija. 240 (2014).
11. Fleischmann, M., Hendra, P. J. & McQuillan, A. J. Raman spectra of pyridine adsorbed at a silver electrode. *Chem. Phys. Lett.* **26**, 163–166 (1974).
12. Albrecht, M. G. & Creighton, J. A. Anomalously intense Raman spectra of pyridine at a silver electrode. *J. Am. Chem. Soc.* **99**, 5215–5217 (1977).
13. Jeanmaire, D. L. & Van Duyne, R. P. Surface raman spectroelectrochemistry. Part I. Heterocyclic, aromatic, and aliphatic amines adsorbed on the anodized silver electrode. *J. Electroanal. Chem.* **84**, 1–20 (1977).
14. Ferraro, J. R., Nakamoto, K. & Brown, C. W. *Introductory Raman Spectroscopy*. *Elsevier* (2003). doi:10.1038/sj.embor.embor770.
15. Guillot, N. & de la Chapelle, M. L. The electromagnetic effect in surface enhanced Raman scattering: Enhancement optimization using precisely controlled nanostructures. *J. Quant. Spectrosc. Radiat. Transf.* **113**, 2321–

2333 (2012).

16. Petryayeva, E. & Krull, U. J. Localized surface plasmon resonance: Nanostructures, bioassays and biosensing-A review. *Anal. Chim. Acta* **706**, 8–24 (2011).

17. Bhushan, B. *Encyclopedia of nanotechnology*. (Springer, 2013).

18. Li, M., Cushing, S. K. & Wu, N. Plasmon-enhanced optical sensors: A review. *Analyst* **140**, 386–406 (2015).

19. Benz, F. *et al.* SERS of Individual Nanoparticles on a Mirror: Size Does Matter, but so Does Shape. *J. Phys. Chem. Lett.* **7**, 2264–2269 (2016).

20. Strobbia, P., Languirand, E. & Cullum, B. M. Recent advances in plasmonic nanostructures for sensing: a review. *Opt. Eng.* **54**, 100902 (2015).

21. Nallathamby, P. D., Huang, T. & Xu, X. H. N. Design and characterization of optical nanorulers of single nanoparticles using optical microscopy and spectroscopy. *Nanoscale* **2**, 1715–1722 (2010).

22. Baida, H. *et al.* Quantitative determination of the size dependence of surface plasmon resonance damping in single Ag@SiO2 nanoparticles. *Nano Lett.* **9**, 3463–3469 (2009).

23. Huang, T. & Xu, X. H. N. Synthesis and characterization of tunable rainbow colored colloidal silver nanoparticles using single-nanoparticle plasmonic microscopy and spectroscopy. *J. Mater. Chem.* **20**, 9867–9876 (2010).

24. Li, M. *et al.* Shape-dependent surface-enhanced Raman scattering in gold-Raman-probe- silica sandwiched nanoparticles for biocompatible applications. *Nanotechnology* **23**, (2012).

25. Cao, J., Sun, T. & Grattan, K. T. V. Gold nanorod-based localized surface plasmon resonance biosensors: A review. *Sensors Actuators, B Chem.* **195**, 332–351 (2014).

26. Tiedemann, D. *et al.* Reprotoxicity of gold, silver, and gold-silver alloy nanoparticles on mammalian gametes. *Analyst* **139**, 931–942 (2014).

27. Ding, S. Y., You, E. M., Tian, Z. Q. & Moskovits, M. Electromagnetic theories of surface-enhanced Raman spectroscopy. *Chem. Soc. Rev.* **46**, 4042–4076 (2017).

28. Wei, S., Zheng, M., Xiang, Q., Hu, H. & Duan, H. Optimization of the particle density to maximize the SERS enhancement factor of periodic plasmonic nanostructure array. *Opt. Express* **24**, 20613 (2016).

29. Mosier-Boss, P. A. Review of SERS substrates for chemical sensing. *Nanomaterials* **7**, 1–30 (2017).

30. Lin, X. M., Cui, Y., Xu, Y. H., Ren, B. & Tian, Z. Q. Surface-enhanced raman

spectroscopy: Substrate-related issues. *Anal. Bioanal. Chem.* **394**, 1729–1745 (2009).

31. Anema, J. R., Li, J. F., Yang, Z. L., Ren, B. & Tian, Z. Q. Shell-isolated nanoparticle-enhanced raman spectroscopy: Expanding the versatility of surface-enhanced raman scattering. *Annu. Rev. Anal. Chem.* **4**, 129–150 (2011).

32. Zong, C. *et al.* Surface-Enhanced Raman Spectroscopy for Bioanalysis: Reliability and Challenges. *Chem. Rev.* **118**, 4946–4980 (2018).

33. Mullins, D. R. & Campion, A. Unenhanced Raman scattering from pyridine chemisorbed on a stepped silver surface: Implications for proposed sers mechanisms. *Chem. Phys. Lett.* **110**, 565–570 (1984).

34. Rodriguez, J. A. & Goodman, D. W. The nature of the metal-metal bond in bimetallic surfaces. *Science (80-.).* **257**, 897–903 (1992).

35. Zhang, J., Sasaki, K., Sutter, E. & Adzic, R. R. Stabilization of platinum oxygen-reduction electrocatalysts using gold clusters. *Science (80-.).* **315**, 220–222 (2007).

36. Huang, Y. F. *et al.* Vibrational signature of double-end-linked molecules at Au nanojunctions probed by surface-enhanced raman spectroscopy. *Chem. - A Eur. J.* **16**, 1449–1453 (2010).

37. Schmid, T., Opilik, L., Blum, C. & Zenobi, R. Nanoscale chemical imaging using tip-enhanced raman spectroscopy: A critical review. *Angew. Chemie - Int. Ed.* **52**, 5940–5954 (2013).

38. Li, J. F., Zhang, Y. J., Ding, S. Y., Panneerselvam, R. & Tian, Z. Q. Core-shell nanoparticle-enhanced raman spectroscopy. *Chem. Rev.* **117**, 5002–5069 (2017).

39. Zdaniauskienė, A. *et al.* Electrochemical Shell-Isolated Nanoparticle-Enhanced Raman Spectroscopy: Bonding, Structure, and Ion-Pairing of the Positive Charge Bearing Pyridinium Ring Terminated Monolayer at Smooth Gold Electrode. *J. Phys. Chem. C* **122**, 1234–1242 (2018).

40. Kneipp, K., Kneipp, H., Itzkan, I., Dasari, R. R. & Feld, M. S. Surface-enhanced Raman scattering and biophysics. *J. Phys. Condens. Matter* **14**, (2002).

41. Njoki, P. N. *et al.* Size correlation of optical and spectroscopic properties for gold nanoparticles. *J. Phys. Chem. C* **111**, 14664–14669 (2007).

42. Hong, S. & Li, X. Optimal size of gold nanoparticles for surface-enhanced Raman spectroscopy under different conditions. *J. Nanomater.* **2013**, (2013).

43. Kumari, G., Kandula, J. & Narayana, C. How Far Can We Probe by SERS? *J. Phys. Chem. C* **119**, 20057–20064 (2015).

44. Tanwar, S., Haldar, K. K. & Sen, T. DNA Origami Directed Au Nanostar Dimers for Single-Molecule Surface-Enhanced Raman Scattering. *J. Am. Chem. Soc.* **139**, 17639–17648 (2017).

45. Roy, S., Muhammed Ajmal, C., Baik, S. & Kim, J. Silver nanoflowers for single-particle SERS with 10 pM sensitivity. *Nanotechnology* **28**, 465705 (2017).

46. Lin, X.-D. *et al.* Synthesis of ultrathin and compact Au@MnO_2 nanoparticles for shell-isolated nanoparticle-enhanced Raman spectroscopy (SHINERS). *J. Raman Spectrosc.* **43**, 40–45 (2012).

47. Tom, R. T. *et al.* Freely dispersible Au@TiO2, Au@ZrO2, Ag@TiO2, and Ag@ZrO2 core-shell nanoparticles: One-step synthesis, characterization, spectroscopy, and optical limiting properties. *Langmuir* **19**, 3439–3445 (2003).

48. Tu, W. & Liu, H. Rapid synthesis of nanoscale colloidal metal clusters by microwave irradiation. *J. Mater. Chem.* **10**, 2207–2211 (2000).

49. Zhu, Y. J. & Chen, F. Microwave-assisted preparation of inorganic nanostructures in liquid phase. *Chem. Rev.* **114**, 6462–6555 (2014).

50. Kumar, A., Kuang, Y., Liang, Z. & Sun, X. Microwave chemistry, recent advancements, and eco-friendly microwave-assisted synthesis of nanoarchitectures and their applications: a review. *Mater. Today Nano* **11**, 100076 (2020).

51. Murugasenapathi, N. K., Jebakumari, K. A. E., Mohamed, S. J., Giribabu, K. & Palanisamy, T. Pinhole-Free Shell-Isolated Nanoparticle Enhanced Raman Spectroscopy for Interference-Free Probing of Electrochemical Reactions. *J. Phys. Chem. Lett.* **12**, 7046–7052 (2021).

52. Sundberg, R. J. Interactions of histidine and other imidazole derivatives with transition metal ions in chemical and biological systems. *Chem. Rev.* **74**, 471–517 (1974).

53. Zaitouna, A. J. & Lai, R. Y. Design and characterization of a metal ion-imidazole self-assembled monolayer for reversible immobilization of histidine-tagged peptides. *Chem. Commun.* **47**, 12391–12393 (2011).

54. Hwang, S. *et al.* Faradaic impedance titration and control of electron transfer of 1-(12-mercaptododecyl)imidazole monolayer on a gold electrode. *Electrochim. Acta* **53**, 2630–2636 (2008).

55. Tappura, K., Vikholm-Lundin, I. & Albers, W. M. Lipoate-based imprinted self-assembled molecular thin films for biosensor applications. *Biosens. Bioelectron.* **22**, 912–919 (2007).

56. Saada, M. C. *et al.* Carbonic anhydrase activators: Gold nanoparticles coated

with derivatized histamine, histidine, and carnosine show enhanced activatory effects on several mammalian isoforms. *J. Med. Chem.* **54**, 1170–1177 (2011).

57. Pourrostam-Ravadanaq, P., Safa, K. D. & Abbasi, H. Study of imidazole performance as pseudo-affinity ligand in the purification of IgG from bovine milk. *Anal. Biochem.* **597**, 113693 (2020).

58. Durainatarajan, P., Prabakaran, M., Ramesh, S. & Periasamy, V. Self-assembly on copper surface by using imidazole derivative for corrosion protection. *J. Adhes. Sci. Technol.* **32**, 1733–1749 (2018).

59. Ashikawa, I. & Itoh, K. Raman spectra of polypeptides containing L-histidine residues and tautomerism of imidazole side chain. *Biopolymers* **18**, 1859–1876 (1979).

60. Matulaitiene, I., Kuodis, Z., Eicher-Lorka, O. & Niaura, G. SERS characterization of imidazole ring terminated self-assembled monolayer formed from lipoic acid histamide on silver electrode. *J. Electroanal. Chem.* **700**, 77–85 (2013).

61. Garfinkel, D. & Edsall, J. T. Raman Spectra of Amino Acids and Related Compounds. VIII. Raman and Infrared Spectra of Imidazole, 4-Methylimidazole and Histidine. *J. Am. Chem. Soc.* **80**, 3807–3812 (1958).

62. Ashikawa, I. & Itoh, K. Raman scattering study on tautomerism of L-histidine. *Chem. Lett.* **7**, 681–684 (1978).

63. Mesu, J. G., Visser, T., Soulimani, F. & Weckhuysen, B. M. Infrared and Raman spectroscopic study of pH-induced structural changes of l-histidine in aqueous environment. *Vib. Spectrosc.* **39**, 114–125 (2005).

64. Martusevičius, S., Niaura, G., Talaikyte, Z. & Razumas, V. Adsorption of L-histidine on copper surface as evidenced by surface-enhanced Raman scattering spectroscopy. *Vib. Spectrosc.* **10**, 271–280 (1996).

65. Carter, D. A. & Pemberton, J. E. Raman spectroscopy and vibrational assignments of 1- and 2-methylimidazole. *J. Raman Spectrosc.* **28**, 939–946 (1997).

66. Takeuchi, H. Raman structural markers of tryptophan and histidine side chains in proteins. *Biopolym. - Biospectroscopy Sect.* **72**, 305–317 (2003).

67. Miura, T., Satoh, T., Hori-i, A. & Takeuchi, H. Raman Marker Bands of Metal Coordination Sites of Histidine Side Chains in Peptides and Proteins. *J. Raman Spectrosc.* **29**, 41–47 (1998).

68. Matulaitiene, I., Pociute, E., Kuodis, Z., Eicher-Lorka, O. & Niaura, G. Interaction of 4-imidazolemethanol with a copper electrode revealed by isotope-edited SERS and theoretical modeling. *Phys. Chem. Chem. Phys.* **17**, 16483–16493 (2015).

69. Toyama, A., Ono, K., Hashimoto, S. & Takeuchi, H. Raman spectra and normal coordinate analysis of the N1-H and N3-H tautomers of 4-methylimidazole: Vibrational modes of histidine tautomer markers. *J. Phys. Chem. A* **106**, 3403–3412 (2002).

70. Tasumi, M., Harada, I., Takamatsu, T. & Takahashi, S. Raman studies of L-histidine and related compounds in aqueous solutions. *J. Raman Spectrosc.* **12**, 149–151 (1982).

71. Takeuchi, H., Kimura, Y., Koitabashi, I. & Harada, I. Raman bands of N-deuterated histidinium as markers of conformation and hydrogen bonding. *J. Raman Spectrosc.* **22**, 233–236 (1991).

72. Wu, Q., Li, F., Wang, W., Hecht, M. H. & Spiro, T. G. UV Raman monitoring of histidine protonation and H-2H exchange in plastocyanin. *J. Inorg. Biochem.* **88**, 381–387 (2002).

73. Zhao, X., Wang, D. & Spiro, T. G. A UV resonance Raman monitor of histidine protonation in proteins: Bohr protons in hemoglobin. *Journal of the American Chemical Society*. **20**, 8517–8518 (1998).

74. Wen, B. Y. *et al.* Shell-isolated nanoparticle-enhanced Raman spectroscopy study of the adsorption behaviour of DNA bases on Au(111) electrode surfaces. *Analyst* **141**, 3731–3736 (2016).

75. Li, C. Y. *et al.* In-situ electrochemical shell-isolated Ag nanoparticles-enhanced Raman spectroscopy study of adenine adsorption on smooth Ag electrodes. *Electrochimica Acta* **199**, 388–393 (2016).

76. Barbillon, G. Applications of Shell-Isolated Nanoparticle-Enhanced Raman Spectroscopy. *Photonics* **8**, 1–16 (2021).

77. Yu, Z. *et al.* Probing Interfacial Electronic Effects on Single-Molecule Adsorption Geometry and Electron Transport at Atomically Flat Surfaces. *Angew. Chemie Int. Ed.* **60**, 15452–15458 (2021).

78. Li, J. F. *et al.* Extraordinary enhancement of raman scattering from pyridine on single crystal Au and Pt electrodes by shell-isolated Au nanoparticles. *J. Am. Chem. Soc.* **133**, 15922–15925 (2011).

79. Kuodis, Z. *et al.* Reflection Absorption Infrared Spectroscopy Characterization of SAM Formation from 8-Mercapto- N -(phenethyl)octanamide Thiols with Phe Ring and Amide Groups. *Molecules* **25**, 1–14 (2020).

80. Takeuchi, H. Raman structural markers of tryptophan and histidine side chains in proteins. *Biopolymers* **72**, 305–317 (2003).

81. Balakrishnan, G. *et al.* Mode recognition in UV resonance Raman spectra of imidazole: Histidine monitoring in proteins. *J. Phys. Chem. B* **116**, 9387–9395

(2012).

82. Vericat, C. *et al.* Self-assembled monolayers of thiolates on metals: A review article on sulfur-metal chemistry and surface structures. *RSC Advances* **4** 27730–27754 (2014).

83. Bryant, M. A. & Pemberton, J. E. Surface Raman Scattering of Self-Assembled Monolayers Formed from 1-Alkanethiols: Behavior of Films at Au and Comparison to Films at Ag. *J. Am. Chem. Soc.* **113**, 8284–8293 (1991).

84. Fears, K. P., Creager, S. E. & Latour, R. A. Determination of the Surface pK of Carboxylic- and Amine-Terminated Alkanethiols Using Surface Plasmon Resonance Spectroscopy. *Langmuir* **24**, 837–843 (2008).

85. Chechik, B. V., Crooks, R. M. & Stirling, C. J. M. Reactions and Reactivity in Self-Assembled Monolayers. *Adv. Mater.* **12**, 1161–1171 (2000).

86. Reijenga, J., van Hoof, A., van Loon, A. & Teunissen, B. Development of methods for the determination of pKa values. *Anal. Chem. Insights* **8**, 53–71 (2013).

87. Andersson, M. P., Olsson, M. H. M. & Stipp, S. L. S. Predicting the pKa and Stability of Organic Acids and Bases at an Oil−Water Interface. *Int. J. Mod. Phys. Conf. Ser.* **26**, 1460087 (2014).

88. Yang, G., Li, L., Lee, W. B. & Ng, M. C. Structure of graphene and its disorders: a review. *Sci. Technol. Adv. Mater.* **19**, 613–648 (2018).

89. Banhart, F., Kotakoski, J. & Krasheninnikov, A. V. Structural defects in graphene. *ACS Nano* vol. 5 26–41 (2011).

90. Lv, R. & Terrones, M. Towards new graphene materials: Doped graphene sheets and nanoribbons. *Mater. Lett.* **78**, 209–218 (2012).

91. Lee, H., Paeng, K. & Kim, I. S. A review of doping modulation in graphene. *Synthetic Metals* **244**, 36–47 (2018).

92. Guo, Z. *et al.* Designing nitrogen and phosphorus co-doped graphene quantum dots/g-C3N4 heterojunction composites to enhance visible and ultraviolet photocatalytic activity. *Appl. Surf. Sci.* **548**, 149211 (2021).

93. Sun, L. *et al.* Role of Pyridinic-N for Nitrogen-doped graphene quantum dots in oxygen reaction reduction. *J. Colloid Interface Sci.* **508**, 154–158 (2017).

94. Kong, L., Enders, A., Rahman, T. S. & Dowben, P. A. Molecular adsorption on graphene. *Journal of Physics Condensed Matter* vol. 26 443001 (2014).

95. Phillipson, R. *et al.* Tunable doping of graphene by using physisorbed self-assembled networks. *Nanoscale* **8**, 20017–20026 (2016).

96. Dong, X. *et al.* Doping Single-Layer Graphene with Aromatic Molecules.

Small **5**, 1422–1426 (2009).

97. Yoo, E. J. *et al.* Large reversible Li storage of graphene nanosheet families for use in rechargeable lithium ion batteries. *Nano Lett.* **8**, 2277–2282 (2008).

98. Malard, L. M., Pimenta, M. A., Dresselhaus, G. & Dresselhaus, M. S. Raman spectroscopy in graphene. *Physics Reports* **473**, 51–87 (2009).

99. Lai, H., Xu, F., Zhang, Y. & Wang, L. Recent progress on graphene-based substrates for surface-enhanced Raman scattering applications. *Journal of Materials Chemistry B* **6**, 4008–4028 (2018).

100. Zólyomi, V., Koltai, J. & Kürti, J. Resonance Raman spectroscopy of graphite and graphene. *Phys. status solidi* **248**, 2435–2444 (2011).

101. Brill, A. R., Biswas, S., Caspary Toroker, M., De Ruiter, G. & Koren, E. Dipole-Induced Raman Enhancement Using Noncovalent Azobenzene-Functionalized Self-Assembled Monolayers on Graphene Terraces. *ACS Appl. Mater. Interfaces* **13**, 10271–10278 (2021).

102. Huang, S. *et al.* Molecular selectivity of graphene-enhanced raman scattering. *Nano Lett.* **15**, 2892–2901 (2015).

103. Ling, X. *et al.* Lighting Up the Raman Signal of Molecules in the Vicinity of Graphene Related Materials. *Acc. Chem. Res.* **48**, 1862–1870 (2015).

104. de la O-Cuevas, E. *et al.* Graphenic substrates as modifiers of the emission and vibrational responses of interacting molecules: The case of BODIPY dyes. *Spectrochim. Acta - Part A Mol. Biomol. Spectrosc.* **246**, 119020 (2021).

105. Silver, A. *et al.* Chemical and Bio Sensing Using Graphene-Enhanced Raman Spectroscopy. *Nanomaterials* **9**, 516 (2019).

106. Shi, H. *et al.* Measuring Local Electric Fields and Local Charge Densities at Electrode Surfaces Using Graphene-Enhanced Raman Spectroscopy (GERS)-Based Stark-Shifts. *ACS Appl. Mater. Interfaces* **11**, 36252–36258 (2019).

107. Zhang, N., Tong, L. & Zhang, J. Graphene-based enhanced raman scattering toward analytical applications. *Chem. Mater.* **28**, 6426–6435 (2016).

108. Krajczewski, J. & Kudelski, A. Shell-Isolated Nanoparticle-Enhanced Raman Spectroscopy. *Front. Chem.* **7**, 410 (2019).

109. Keeler, A. J., Salazar-Banda, G. R. & Russell, A. E. Mechanistic insights into electrocatalytic reactions provided by SERS. *Current Opinion in Electrochemistry* vol. 17 90–96 (2019).

110. El-Said, W. A., Alshitari, W. & Choi, J. woo. Controlled fabrication of gold nanobipyramids/polypyrrole for shell-isolated nanoparticle-enhanced Raman spectroscopy to detect γ-aminobutyric acid. *Spectrochim. Acta - Part A Mol. Biomol. Spectrosc.* **229**, 117890 (2020).

111. Puglieri, T. S., Madden, O. & Andrade, G. F. S. SHINERS in cultural heritage: Can SHINERS spectra always be compared with normal Raman spectra? A study of alizarin and its adsorption in the silicon dioxide shell. *J. Raman Spectrosc.* **52**, 1406–1417 (2021).

112. Boccorh, D. K. *et al.* A universal polymer shell-isolated nanoparticle (SHIN) design for single particle spectro-electrochemical SERS sensing using different core shapes. *Nanoscale Adv.* **3**, 6415–6426 (2021).

113. Zhang, Y. *et al.* Plasmonic Core–Shell Nanomaterials and their Applications in Spectroscopies. *Adv. Mater.* **33**, 2005900 (2021).

114. Negut Cioates, C. Review—Electrochemical Sensors Used in the Determination of Riboflavin. *J. Electrochem. Soc.* **167**, 037558 (2020).

115. Thakur, K., Tomar, S. K., Singh, A. K., Mandal, S. & Arora, S. Riboflavin and health: A review of recent human research. *Crit. Rev. Food Sci. Nutr.* **57**, 3650–3660 (2017).

116. Radzevič, A. *et al.* Electropolymerisation of the natural monomer riboflavin and its characterisation. *Electrochim. Acta* **222**, 1818–1830 (2016).

117. Trusovas, R. *et al.* Recent Advances in Laser Utilization in the Chemical Modification of Graphene Oxide and Its Applications. *Adv. Opt. Mater.* **4**, 37–65 (2016).

118. Trusovas, R., Ratautas, K., Račiukaitis, G. & Niaura, G. Graphene layer formation in pinewood by nanosecond and picosecond laser irradiation. *Appl. Surf. Sci.* **471**, 154–161 (2019).

119. Ferrari, A. C. & Basko, D. M. Raman spectroscopy as a versatile tool for studying the properties of graphene. *Nature Nanotechnology* vol. 8 235–246 (2013).

120. Satyanarayana, T. & Kunze, G. *Yeast biotechnology: Diversity and applications.* (Springer Netherlands, 2009). doi:10.1007/978-1-4020-8292-4.

121. Adeniran, A., Sherer, M. & Tyo, K. E. J. Yeast-based biosensors: design and applications. *FEMS Yeast Research* **15** (2015).

122. Nandy, S. K. & Srivastava, R. K. A review on sustainable yeast biotechnological processes and applications. *Microbiological Research* **207**, 83–90 (2018).

123. Arevalo-Villena, M., Briones-Perez, A., Corbo, M. R., Sinigaglia, M. & Bevilacqua, A. Biotechnological application of yeasts in food science: Starter cultures, probiotics and enzyme production. *J. Appl. Microbiol.* **123**, 1360–1372 (2017).

124. Shurson, G. C. Yeast and yeast derivatives in feed additives and ingredients: Sources, characteristics, animal responses, and quantification methods.

Animal Feed Science and Technology **235**, 60–76 (2018).

125. Lodolo, E. J., Kock, J. L. F., Axcell, B. C. & Brooks, M. The yeast Saccharomyces cerevisiae– the main character in beer brewing. *FEMS Yeast Res.* **8**, 1018–1036 (2008).

126. Lachance, M.-A. *Metschnikowia* : half tetrads, a regicide and the fountain of youth. *Yeast* **33**, 563–574 (2016).

127. Kluyver, A. J., van der Walt, J. P. & van Triet, A. J. Pulcherrimin, The Pigment of Candida Pulcherrima . *Proc. Natl. Acad. Sci.* **39**, 583–593 (1953).

128. Cook, A. H. & Slater, C. A. The structure of pulcherrimin. *J. Chem. Soc.* 4133 (1956).

129. MacDonald, J. C. The structure of pulcherriminic acid. *Can. J. Chem.* **41**, 165–172 (1963).

130. Sipiczki, M. Metschnikowia strains isolated from botrytized grapes antagonize fungal and bacterial growth by iron depletion. *Appl. Environ. Microbiol.* **72**, 6716–6724 (2006).

131. Saravanakumar, D., Ciavorella, A., Spadaro, D., Garibaldi, A. & Gullino, M. L. Metschnikowia pulcherrima strain MACH1 outcompetes Botrytis cinerea, Alternaria alternata and Penicillium expansum in apples through iron depletion. *Postharvest Biol. Technol.* **49**, 121–128 (2008).

132. Jolly, N. P., Varela, C. & Pretorius, I. S. Not your ordinary yeast: Non-Saccharomyces yeasts in wine production uncovered. *FEMS Yeast Research* **14**, 215–237 (2014).

133. Ru, E. Le & Etchegoin, P. . G. *Principles of Surface-Enhanced Raman Spectroscopy– and Related Plasmonic Effects*. (Elsevier, 2009).

134. Tian, Z. Q., Ren, B. & Wu, D. Y. Surface-enhanced Raman scattering: From noble to transition metals and from rough surfaces to ordered nanostructures. *Journal of Physical Chemistry B* **106**, 9463–9483 (2002).

135. Ding, S. Y. *et al.* Nanostructure-based plasmon-enhanced Raman spectroscopy for surface analysis of materials. *Nature Reviews Materials* **1**, 1–16 (2016).

136. Schlücker, S. Surface-Enhanced Raman Spectroscopy: Concepts and Chemical Applications. *Angew. Chemie Int. Ed.* **53**, 4756–4795 (2014).

137. Langer, J. *et al.* Present and future of surface-enhanced Raman scattering. *ACS Nano* **14**, 28–117 (2020).

138. Han, X. X., Zhao, B. & Ozaki, Y. Surface-enhanced Raman scattering for protein detection. *Analytical and Bioanalytical Chemistry* **394**, 1719–1727 (2009).

139. Culha, M., Kahraman, M., Çam, D., Sayın, I. & Keseroğlu, K. Rapid identification of bacteria and yeast using surface-enhanced Raman scattering. *Surf. Interface Anal.* **42**, 462–465 (2010).

140. Uusitalo, S. *et al.* Surface-enhanced Raman spectroscopy for identification and discrimination of beverage spoilage yeasts using patterned substrates and gold nanoparticles. *J. Food Eng.* **212**, 47–54 (2017).

141. Manikantan Syamala, K. *et al.* Inhibition assay of yeast cell walls by plasmon resonance rayleigh scattering and surface-enhanced raman scattering imaging. *Langmuir* **28**, 8952–8958 (2012).

142. Mikoliunaite, L. *et al.* The substrate matters in the Raman spectroscopy analysis of cells. *Sci. Rep.* **5**, 1–10 (2015).

143. Dedelaite, L. *et al.* Surfaces functionalized by graphene oxide nanosheets for single cell investigations. *Sensors Actuators, B Chem.* **255**, 1735–1743 (2018).

144. Chrimes, A. F. *et al.* In situ SERS probing of nano-silver coated individual yeast cells. *Biosens. Bioelectron.* **49**, 536–541 (2013).

145. Sujith, A. *et al.* Imaging the cell wall of living single yeast cells using surface-enhanced raman spectroscopy. *Anal. Bioanal. Chem.* **394**, 1803–1809 (2009).

146. Sujith, A. *et al.* Surface enhanced Raman scattering analyses of individual silver nanoaggregates on living single yeast cell wall. *Appl. Phys. Lett.* **92**, 103901 (2008).

147. Sayin, I., Kahraman, M., Sahin, F., Yurdakul, D. & Culha, M. Characterization of yeast species using surface-enhanced Raman scattering. *Appl. Spectrosc.* **63**, 1276–1282 (2009).

148. Lemma, T., Wang, J., Arstila, K., Hytönen, V. P. & Toppari, J. J. Identifying yeasts using surface enhanced Raman spectroscopy. *Spectrochim. Acta - Part A Mol. Biomol. Spectrosc.* **218**, 299–307 (2019).

149. Fang, P. P., Lu, X., Liu, H. & Tong, Y. Applications of shell-isolated nanoparticles in surface-enhanced Raman spectroscopy and fluorescence. *TrAC - Trends in Analytical Chemistry* **66**, 103–117 (2015).

SUMMARY

Introduction

Biomolecules, including macromolecules (proteins, nucleic acids, carbohydrates, lipids) and small molecules (primary metabolites, natural products), are substances present in living organisms that play an essential role in chemical, biochemical and biological processes[1]. The ability to control the interactions between biomolecules, to observe the processes occurring at interfaces is highly relevant to bioengineering, pharmaceuticals, environmental research and other scientific fields[2]. Understanding the processes at interfaces requires knowledge at the molecular level. However, studying biomolecular events at the interface at the molecular level is difficult due to the low surface concentration of the substances under investigation. Such research requires unique methods that have several essential characteristics: (i) surface specificity (contributions from the bulk or solution must be avoided), (ii) be sensitive but non-destructive enough to detect extremely small amounts of substances, and (iii) be able to provide molecular-level information on the self-assembly of biomolecules, composition, structure, function and orientation. One such research method is Surface-Enhanced Raman Spectroscopy (SERS). The popularity of SERS in biomolecular studies also comes from the weak Raman scattering of water, which allows the study of biomolecules in their natural environment[3]. However, SERS has several fundamental drawbacks that limit the application of the method in the study of biomolecules at interfaces. The main disadvantage of SERS is the requirement to use roughened or nanostructured Au, Ag, or Cu surfaces to amplify the Raman signal. Metals can directly interact with biomolecules, modifying the entire system. Also, during research in the electrochemical interface, charge transfer can possibly occur between the metal nanoparticles and other metallic substrates because their Fermi levels are different. In light of these limitations, new SERS resonators of Au and Ag nanoparticles covered by a thin SiO_2 layer (Au@SiO_2, Ag@SiO_2) were proposed more than a decade ago[4]. In this case, the nanoparticle's core amplifies the Raman scattering signal. At the same time, the inert silica shell protects the nanoparticles from agglomeration, oxidation, and also prevents direct contact between SERS-active metal cores and probe molecules/surface. Such a novel method, called Shell-Isolated Nanoparticle-Enhanced Raman Spectroscopy (SHINERS), has opened up new possibilities in studying adsorption, catalysis, charge transfer and other processes on smooth, single-crystal surfaces, also on two-dimensional materials. In other words, SHINERS

has become an up-and-coming method for studying any surface. This dissertation presents the molecular-level characterization of interfacial biomolecules by using SHINERS method. The work discusses the possibilities and challenges of this method in studying heterogeneous molecular systems and reveals the structural peculiarities and the function of different biomolecules.

The main goal of the dissertation was to apply the SHINERS method in the studies of biomolecules at the interface (from self-assembled monolayers to living microorganisms). To achieve this goal, 4 **tasks** were set:

1. to synthesize and characterize plasmonic nanoparticles coated with different dielectric shells, find the optimal conditions for the synthesis of nanoparticles with a plasmonic core larger than 50 nm and a shell thickness of 2-3 nm.

2. to characterize the self-assembled monolayer formed from alkanethiol with imidazole ring and intrachain amide group using the electrochemical SHINERS (EC-SHINERS) method.

3. to demonstrate the application possibilities of the SHINERS method in order to obtain molecular-level information about adsorbates on the graphene and structural defects of graphene.

4. to study a complex molecular system - living yeast cells using the SHINERS method.

The novelty of the work

Different research and analysis methods were applied to achieve the set tasks. All research and analysis methods can be divided into 3 groups according to application areas: synthesis and characterization of nanoparticles, formation of monolayers and other model molecular systems, and study and analysis of biomolecular systems.

Firstly, gold and silver core-shell nanoparticles with shells of different materials were synthesized in several ways by modifying J.F. Li et al. and F. Liu et al. synthesis methods[5,6]. After that, the stability of different inert shells was tested in 17 organic solvents. For the first time, optimal synthesis conditions were found for Ag nanoparticles with a core size of 90 ± 10 nm with a 2.5 – 3 nm thick SiO_2 shell using silver nitrate and only one reducing and stabilizing agent, sodium citrate. For inert shell formation over Ag core nanoparticles (3-aminopropyl)triethoxysilane (APTES) and sodium silicate

solution were used. Based on the stability of $Au@SiO_2$ nanoparticles in organic solvents, it was shown that the more commonly used silane in the shell formation step - (3-aminopropyl)trimethoxysilane (APTMS) – is not very suitable for achieving longer stability of core-shell nanoparticles. APTES by-product ethanol has a less disruptive effect on the shell's integrity compared to the APTMS by-product methanol. The size, shape, shell thickness and defects of the synthesized nanoparticles were characterized by high-resolution transmission electron microscopy, UV-Vis spectroscopy, cyclic voltammetry and Raman spectroscopy methods.

SHINERS experiments started with studies of self-organized monolayers on smooth, single-crystal Au surfaces. A new compound – N-(2-(1H-imidazol-4-yl)ethyl)-6-mercaptohexanamide (IMHA) was synthesized for the PhD work, which has four functional parts: (i) thiol group (SH); (ii) hydrocarbon chain ($-(CH_2)_5-$); (iii) amide group ($-CO-NH-$); (iv) imidazole ring. The imidazole ring (Im) is a side chain group of the amino acid histidine that participates in a wide range of molecular interactions. One of the most important types of interactions involving the Im ring is the coordination of metal ions in active centres of enzymes, so imidazole plays a crucial role in their structure and activity[7]. In addition, the introduction of amide group into the alkyl chain significantly increases the stability of the monolayer forming network hydrogen bonds between the adjacent molecular chains[8]. After adsorbing IMHA on Au surfaces for different periods of time, the reflection-absorption infrared spectroscopy (RAIRS) method found that after almost three hours (162 min), the formation of an orderly monolayer is halved, and after 6 hours, the monolayer becomes neat and suitable for further studies. The adsorption of IMHA on the surface caused a tautomeric change of the IMHA molecule from tautomer I (N1–H, N3) to tautomer II (N1, N3–H). EC-SHINERS data demonstrated that the tautomer II predominates over the entire potential window, and only a tiny fraction of the molecules become tautomer I form when the electrode potential becomes −0.8 V (vs. Ag/AgCl). Raman temperature and density functional theory (DFT) simulation data helped determine the freedom of movement of the imidazole ring and a hydrogen-bond strength-sensitive vibrational band at 1492 cm^{-1}. Analysis of this band revealed a potential-dependent behaviour of the Im ring: at an electrode polarization of −0.8 V , the Im ring is much more confined and H-bonded than at −0.4 V (vs. Ag/AgCl). Also, the pK_a value of the imidazole ring in the IMHA monolayer was found for the first time, which is 3.14 ± 0.34.

The characteristics of graphene-enhanced Raman spectroscopy (GERS) and SHINERS methods were compared for the first time in the study of adsorbed riboflavin on graphene. In the case of GERS, the vibrations of only those atoms in the riboflavin ring that participate in π-electron interaction are amplified. Meanwhile, SHINERS spectroscopy provides detailed information not only on the vibrations of the Rf ring but also on some vibrations of the ribityl chain. It was also found that the normalized to laser power relative intensity of the 1349 cm^{-1} band of Rf increased by a factor of 26 in SHINERS spectrum compared with GERS. In addition, it was revealed that the vibrational bands of the carbon network and graphene defects of copper oxide, on which the graphene monolayer is formed, are clearly visible in the SHINERS spectrum. However, one of the most exciting results in the SHINERS spectrum is the intense, broad band around 1321 cm^{-1}. The origin and nature of the band was helped to be clarified by quantum chemistry modelling data, when it was established that the appearance of the 1321 cm^{-1} band can be associated with the bending and tilting of the graphene layer caused by riboflavin adsorption. This observation highlights the capabilities of the SHINERS method in detecting local system perturbations.

Finally, Au@SiO_2 nanoparticles were applied in studies of *Metschnikowia pulcherrima* yeast when SHINERS spectra of *Metschnikowia pulcherrima* were recorded for the first time. The obtained results helped to identify the yeast cell wall and its functional elements – proteins, lipids and amino acids. It has been shown that the spectra of yeast cells are reproducible when using coated nanoparticles, the frequencies of the vibrational bands do not change, the inert shell does not allow the interaction of metal nanoparticles with the cells, so no additional vibrational bands appear in the spectra, in contrast to the use of bare nanoparticles. Amino acids, C-N, amide vibrations indicate the bioactivity of a living cell, ongoing protein secretion, and changes in the secondary structure. All these results show that SHINERS method is suitable for *in situ* monitoring biochemical processes in living cells.

The defense statements of the work

1. SiO_2 nanoparticle shells are optimal for SHINERS spectroscopy because the vibrational bands of this layer have the lowest intensity. The improved methodology by changing the heating method from convective to microwave for the synthesis of core-shell nanoparticles allows to form a less defective shell. Ag core silica shell nanoparticles are larger in size when the reduction and stabilization of silver nitrate with sodium citrate are done under microwave irradiation.

2. In IMHA monolayer, the pK_a value of the imidazole ring is lower than in the solution of free histidine. At the electrochemical interface, when the potential changes from –0.4 V to –0.8 V (vs. Ag/AgCl), the hydrogen bond interaction of the imidazole ring becomes stronger.

3. The riboflavin molecule interacts with the graphene monolayer through the π electronic system. The SHINERS method allows for a more detailed study of adsorbed riboflavin on graphene compared to the GERS method. Riboflavin adsorption induces bending of the graphene plane.

4. The SHINERS method makes it possible to obtain reliable and repeatable spectra from the yeast cell surface, from which the functional elements forming the yeast cell walls can be determined.

This thesis presents 6 scientific articles that solve some challenges and provide new perspectives in studying and analyzing biomolecules or biological systems. The first 3 publications cover the first dissertation task, publication 4 the second, 5 the third and 6 the fourth.

Main results

Nanoparticles: opportunities and challenges

Due to the relatively simple preparation, biocompatibility, optical and electronic properties, gold or silver nanoparticles (AuNPs, AgNPs) are widely used for labelling, delivery, imaging and sensing[9]. The plasmonic properties of AuNPs and AgNPs allow SERS detection of different analytes. However, a direct interaction of research object with bare nanoparticles is an important disadvantage. Inert shells (SiO_2, MnO_2, TiO_2, etc.) perfectly solve this problem because they prevent chemical and electrical contact among plasmonic cores and probe substrates, analytes and environment. Measurement technique – SHINERS with such particles spread over a surface of analyzed material was firstly published in 2010. Since then, SHINERS has been used in surface and biological sciences, semiconductor materials, electrochemistry, food and environment safety etc.[10]. In this work, the synthesized gold nanoparticles (50 – 60 nm) were coated with thin (1.5 – 8 nm) layers of silicon, manganese and titanium dioxides. For comparison, each type of nanoparticle's SHINERS spectra were recorded. It is noticeable that Au@MnO_2 and Au@TiO_2 NPs have specific spectra that overlap with the spectrum of the probe molecule, thiophenol, in 400 – 700 cm^{-1} and 1200 – 1600 cm^{-1} regions, respectively. Au@SiO_2 NPs also have a specific spectrum, but the intensity of vibrational bands is extremely low compared to the SHINERS spectra of thiophenol; this can affect data minimally.

T. Charkova, A. Zdaniauskienė. Synthesis and comparison of gold nanoparticles coated with silicon, manganese, and titanium dioxides. Chemija ***31*** *(2020) 197–202.*

The chemical structure of the shell determines the external surface charge of a nanoparticle. A partially negative shell charge does not always allow studying molecular systems with negatively charged functional groups. Due to the electrostatic interaction, the nanoparticles cannot get close enough to the probe surface and enhance the Raman scattering. In order to change the charge of the nanoparticle, the covering shell is modified. Modification can be done by attaching molecules with partially positively charged groups, e.g., NH_2. The shell is also modified for other reasons: binding and detection of metal ions in solution, attracting large molecular structures, catalyzing reactions, etc.[10]. Modification of the outer shell is often carried out in organic solvents, so the stability of the SiO_2 shell in 17 different solvents was investigated during the studies. The obtained practical results help to choose

the suitable conditions for the modification of the SiO_2 shell and thus optimize the further stages of nanoparticle synthesis.

T. Charkova, A. Zdaniauskienė, I. Ignatjev. Silica shell-isolated gold nanospheres: synthesis, investigation of stability in organic solvents, and application in shell-isolated nanoparticle-enhanced Raman spectroscopy. Chemical Data Collections 29 (2020) 100497.

In the SERS community, new and simple ways of producing large diameter (above 50 nm) noble metal nanoparticles are highly welcomed because they shift the localized surface plasmon resonance to higher wavelengths where spectroscopic measurements are typically taken. This work presents a facile microwave-assisted synthesis of above-average diameter silver-core silica-shell nanoparticles ($Ag@SiO_2$) using a chemical reduction method. UV/vis spectroscopy and HR-TEM imaging showed that core-shell nanoparticles are spherical with an average diameter of 90 nm ± 10 nm and are covered with a 2.5–3 nm thick silica shell. Silver salt was reduced and stabilized with sodium citrate to produce core nanoparticles, which were subsequently coated with silicon shells using APTES and sodium silicate. Based on our previous results on $Au@SiO_2$ nanoparticles, we selected APTES for silanization instead of the more commonly used APTMS because the APTES by-product ethanol has a less disruptive effect on the shell's integrity compared to the APTMS by-product methanol.

*E. Daublytė, A. Zdaniauskienė, M. Talaikis, A. Drabavičius, T. Charkova. A facile microwave-assisted synthesis of $Ag@SiO_2$ nanoparticles for Raman spectroscopy. New Journal of Chemistry **45** (2021) 10952.*

EC-SHINERS of imidazole ring functionalized monolayer on smooth gold electrode

Self-assembled monolayers (SAMs) of functional thiol molecules at a metal surface are widely used to study various functional groups' interactions with solution components or adjacent thiols in the monolayer[11]. Imidazole ring terminated molecules can thus interact with other aromatic residues as well as form hydrogen bonds with polar and charged residues because they can exist in neutral or positively charged forms within a pH range of 5.0 to 7.0. The introduction of amide functionality in the hydrocarbon chain of adsorbing molecules greatly increases the stability of SAM due to hydrogen bonds forming between the adjacent molecular chains in the monolayer[12]. Interfaces between biologically active molecules and metals are an important issue in biocatalysis, biocompatibility, and biosensors. SAMs at metal surfaces

provide a possibility to create stable molecular structures suitable for probing potential-driven molecular structure changes[13]. SERS is a powerful spectroscopic technique to study molecular structure and interaction mechanisms between a terminal functional group of a monolayer and solution species at metal/electrolyte interfaces. Nonetheless, SERS is limited by SERS-active substrates (mostly Ag, Au, and Cu), and the requirement to use roughened or nanostructured surfaces restrict the applicability of this analysis method. Therefore, Tian et al. suggested a novel SERS technique – SHINERS[4]. To study the H-bonding interactions of imidazole ring at electrified interfaces, first molecule with interchain amide group and terminal imidazole functional group (IMHA) was synthesized and then studied IMHA SAMs adsorbed on atomically-smooth Au surfaces using SHINERS and RAIRS techniques. From RAIRS data, molecules adsorb on a surface chaotically, but with time (transition midpoint was 162 min), their intrachain amide groups become nearly perpendicular to the surface, which points to the more neatly organized SAM. Adsorption on a surface induced a tautomeric transition in IMHA molecules from Tautomer-I (N1–H, N3) to Tautomer-II (N1, N3–H). Temperature-Raman and DFT modeling identified the 1492 cm^{-1} mode as sensitive to imidazole ring confinement and H-bonding strength. Additionally, it was revealed that the imidazolium ring pK_a value in IMHA monolayer is 3.14 ± 0.34. The presented data on the construction, structure, and potential dependence of imidazole ring group functionalized SAMs will be valuable for developing biosensors or molecular electronics.

A. Zdaniauskienė, M. Talaikis, T. Charkova, R. Sadzevičienė, L. Labanauskas, G. Niaura. Electrochemical shell-isolated nanoparticle-enhanced Raman spectroscopy of imidazole ring functionalized monolayer on smooth gold electrode. Molecules ***27*** *(2022) 6531.*

SHINERS for probing riboflavin on graphene

Electronic properties and function of graphene depend on the surface structure, origin of defects and adsorption of molecules at the surface. Riboflavin can be employed in electrochemistry for different purposes as well as it can be detected electrochemically due to its aromatic nature. Riboflavin has been used as an electrode modifier in sensor construction for other important compounds such as iodate, hydrogen peroxide, and persulphate[14]. Graphene science and developing graphene-based technologies require controlling adsorption processes and obtaining molecular-level surface knowledge. To understand surface and interfacial chemistry, sensitive spectroscopic technique is needed. SERS is one of the most sensitive surface

analysis techniques and fulfils such requirements. Unfortunately, SERS is limited by certain substrates (mostly Ag, Au, and Cu) and the requirement to use roughened/nanostructured surface restrict the applicability of this method. Consequently, Tian et al. approached a novel SERS technique – SHINERS. In this study, SHINERS was used to probe the structure of adsorbed riboflavin at graphene layers at the molecular level. This paper provided a detailed vibrational spectroscopy study of the graphene-riboflavin surface. Several experimental vibrational spectroscopy methods, including ordinary Raman (riboflavin solution and powder spectra), resonance Raman (graphene spectra), graphene-enhanced Raman, and shell-isolated nanoparticle-enhanced Raman spectroscopies, were employed to probe the structure and bonding of both single-layer graphene grown on copper and riboflavin adsorbate. We found that riboflavin adsorption induces the blue-shift of the 2D and G bands by 11 and 3 cm^{-1}, respectively, indicating doping of the graphene. In addition, well-defined signatures of under-layered Cu_2O oxide were obtained. We demonstrated that contrary to GERS approach, SHINERS method provides more detailed information about the interfaces; not only the riboflavin ring but also vibrational modes of ribityl chain and intense D-band of graphene were detected. DFT modelling suggested that this D-band may be activated because of riboflavin adsorption induced local perturbations (tilt and distortions) in the graphene structure. Our work highlighted the ability of SHINERS spectroscopy to probe the local structural perturbations in graphene.

*A. Zdaniauskienė, I. Ignatjev, T. Charkova, M. Talaikis, A. Lukša, A. Šetkus, G. Niaura. Shell-isolated nanoparticle-enhanced Raman spectroscopy for probing riboflavin on graphene. Materials **15** (2022) 1636.*

SHINERS for characterization of living yeast cells

SERS is one of the most sensitive vibrational spectroscopic methods for *in situ* studies of surface and biological systems in aqueous solutions. Large enhancement can be provided by roughened surfaces and nanoparticles of Ag, Au or Cu metals. Recently, Ag and Au nanoparticles have been used for the identification of living yeast cells by SERS approach[15]. However, the high luminescent background and direct interaction of living yeast cells with metal colloids were the main disadvantages. Consequently, Tian et al. suggested a novel SERS technique – SHINERS[4]. Yeasts *Metschnikowia* spp. are capable to produce a red pigment when iron (III) ions present in the growth media. They are potential biocontrol agents against various pathogenic microorganisms. SHINERS method employing synthesized spherical gold

nanoparticles with 46 ± 6 nm core size and SiO_2 shell of 3 nm thickness allowed to obtain significantly enhanced SHINERS spectra of *Metschnikowia* spp. compared to the Raman spectra. Based on the results, the yeast cell wall and its functional elements (proteins, lipids, amino acids) were identified. It has been determined that spectra, when used $Au@SiO_2$ NPs in combination with yeast cells, demonstrate the repeatability, vibrational bands do not change and there are no additional bands due to chemical interactions with nanoparticles. Amino acids, C – N , amide vibrations indicate the bioactivity of the living cell. Consequently, SHINERS technique allow to collect molecular level information from yeast for a better understanding of their cell wall biochemical structures.

A. Zdaniauskienė, T. Charkova, I. Ignatjev, V. Melvydas, R. Garjonytė, I. Matulaitienė, M. Talaikis, G. Niaura. Shell-isolated nanoparticle-enhanced Raman spectroscopy for characterization of living yeast cells. Spectrochimica Acta Part A: Molecular and Biomolecular Spectroscopy ***240*** *(2020) 118560.*

Conclusions

1. When comparing SiO_2, MnO_2 and TiO_2 nanoparticle shells for SHINERS spectroscopy, SiO_2 is optimal, as the vibrational bands of this layer have the lowest intensity. Also, due to its high stability in an acidic medium, the SiO_2 shell is more suitable for biomolecule research than other types of shells. Improved methodology for the synthesis of coated nanoparticles by changing the heating method from convective to microwave. Under the influence of microwaves, the outer shell of nanoparticles is formed less defective than formed by convection heating, and a larger size of nanoparticles (90 ± 10 nm) is also achieved by reducing and stabilizing silver nitrate with sodium citrate only.

2. The pK_a value of the imidazole ring in IMHA monolayer (3.14 ± 0.34) differs from that of histidine in solution (5.9 according to ref. [16]) by 2.76. It was also found that as the packing density of the monolayer decreases, the pK_a value of the Im ring increases. A new strong Raman marker of the hydrogen bond of the imidazole ring was determined – the band at 1492 cm^{-1}. At the electrochemical interface electrode potential controls the hydrogen bonding interaction strength at Im ring site; the weakest interaction was observed at –0.4 V (vs. Ag/AgCl) potential and increased at more negative (–0.8 V) and more positive (0.2 V) electrode polarizations.

3. The decrease in the frequency of the characteristic vibrations of graphene in the SHINERS spectrum showed that the riboflavin molecule interacts with the graphene monolayer through the π electronic system. Unlike the GERS method, the SHINERS method enabled a more detailed characterization of the adsorbed molecule, as not only the ring but also ribityl group vibrations are observed. The adsorption of riboflavin caused an enhancement of the D band of graphene defects in the SHINERS spectrum. The appearance of this band indicates that the graphene plane locally bends and becomes less ordered.

4. Due to the significantly reduced direct interaction between biomolecules and the metal, the SHINERS method allowed obtaining reliable and reproducible spectra from the surface of yeast cells. Functional molecules forming yeast cell walls have been identified: mannan-proteins, lipids, amino acids, polysaccharides.

References

1. Jia, M., Li, S., Zang, L., Lu, X. & Zhang, H. Analysis of biomolecules based on the surface enhanced raman spectroscopy, *Nanomaterials* **8** (2018).

2. McArthur, S. L., Fowler, G. J. S. & Mishra, G. Surface Analysis of Biomolecules: Unravelling biointerfacial interactions. *J. Surf. Anal.* **14**, 370–375 (2008).

3. Niaura, G. Raman Spectroscopy in Analysis of Biomolecules, *Encyclopedia of Analytical Chemistry* 1–34 (John Wiley & Sons, Ltd, 2014).

4. Li, J. F. et al. Shell-isolated nanoparticle-enhanced Raman spectroscopy. *Nature* **464**, 392–395 (2010).

5. Li, J. F. et al. Surface analysis using shell-isolated nanoparticle-enhanced Raman spectroscopy. *Nat. Protoc.* **8**, 52–65 (2013).

6. Liu, F., Liu, J. & Cao, X. Microwave-assisted synthesis silver nanoparticles and their surface enhancement Raman scattering. *Rare Met. Mater. Eng.* **46**, 2395–2398 (2017).

7. Liao, S. M., Du, Q. S., Meng, J. Z., Pang, Z. W. & Huang, R. B. The multiple roles of histidine in protein interactions. *Chem. Cent. J.* **7**, 9–11 (2013).

8. Riauba, L., Niaura, G., Eicher-Lorka, O. & Butkus, E. A study of cysteamine ionization in solution by Raman spectroscopy and theoretical modeling. *J. Phys. Chem. A* **110**, 13394–13404 (2006).

9. Fang, P. P., Lu, X., Liu, H. & Tong, Y. Applications of shell-isolated nanoparticles in surface-enhanced Raman spectroscopy and fluorescence. *TrAC - Trends in Analytical Chemistry* **66**, 103–117 (2015).

10. Li, J. F., Zhang, Y. J., Ding, S. Y., Panneerselvam, R. & Tian, Z. Q. Core-shell nanoparticle-enhanced Raman spectroscopy. *Chem. Rev.* **117**, 5002–5069 (2017).

11. Love, J. C. et al. Self-assembled monolayers of thiolates on metals as a form of nanotechnology, *Chem. Rev.* **105**, 1103-69 (2005).

12. Kuodis, Z. et al. Reflection absorption infrared spectroscopy characterization of SAM formation from 8-mercapto-N-(phenethyl)octanamide thiols with Phe ring and amide groups, *Molecules* **25**, 5633 (2020).

13 Vericat, C et al. Self-assembled monolayers of thiolates on metals: A review article on sulfur-metal chemistry and surface structures, *RSC Adv.* **4**, 27730–27754 (2014).

14. Radzevič, A., Niaura, G., Ignatjev, I., Rakickas, T., Celieš iūtė, R., Pauliukaitė, R. Electropolymerisation of the natural monomer riboflavin and its characterisation. *Electrochimica Acta* **222**, 1818–1830 (2016).

15. Culha, M., Kahraman, M., Çam, D., Sayın, I. Kemal Keseroğlu. Rapid identification of bacteria and yeast using surface-enhanced Raman scattering, *Surf. Interface Anal.* **42**, 462-465 (2010).

16. Ashikawa, I. & Itoh, K. Raman spectra of polypeptides containing L-histidine residues and tautomerism of imidazole side chain. *Biopolymers* **18**, 1859–1876 (1979).

PADĖKA

Dėkoju doktorantūros studijų moksliniam vadovui prof. habil. dr. Gediminui Niaurai už mokslines idėjas, įžvalgas, patarimus, padrąsinimus ir pagalbą atliekant eksperimentus, rengiant publikacijas ir disertaciją. Ačiū už mokslu degančias akis, kurios net ir sunkiausiomis dienomis, skatino nenuleisti rankų. Ypač dėkoju dr. Martynui Talaikiui už didelį norą padėti, už praktinius patarimus ir pagalbą eksperimentų bei diskusijų metu; ačiū, kad galėjau bet kada ir bet ko klausti.

Taip pat dėkoju visiems kolegoms ir draugams iš Organinės chemijos skyriaus. Esu dėkinga už puikų kolektyvą, kuris visada palaikė ir motyvavo, iš visų Jūsų daug ko išmokau. Tatjana ir Edvinai, be Jūsų šie doktorantūros metai nebūtų taip greitai prabėgę, ačiū už pokalbius prie arbatos, kurie šildė ne tik kūną, bet ir sielą.

Dėkoju visiems, kurie vienaip ar kitaip prisidėjo prie šios disertacijos. Dėkoju šeimai, draugams ir artimiesiams, be visų Jūsų palaikymo ir supratimo nebūčiau pasiryžusi šiam dideliam gyvenimo nuotykiui. Ačiū Dievui, kuris mane ir artimuosius saugojo bei globojo visus šiuos metus.

PUBLIKACIJŲ KOPIJOS

CHEMIJA. 2020. Vol. 31. No. 4. P. 197–202

Synthesis and comparison of gold nanoparticles coated with silicon, manganese and titanium dioxides

Tatjana Charkova*,

Agnė Zdaniauskienė

Department of Organic Chemistry,
Center for Physical Sciences and Technology,
3 Saulėtekio Avenue,
10257 Vilnius, Lithuania

The synthesized gold nanoparticles (50–60 nm) were coated with thin (1.5–8 nm) layers of silicon, manganese and titanium dioxides. The obtained three species of nanospheres were applied for the analysis of self-assembled monolayer of thiophenol by shell-isolated nanoparticle-enhanced Raman spectroscopy method. Detailed synthesis and comparison of the particle properties are provided in this report.

Keywords: gold core–shell nanoparticles, shell-isolated nanoparticle-enhanced Raman spectroscopy, thiophenol

INTRODUCTION

Metal and oxide-based nanoparticles are widely used in electronics, medicine, food, and environment protection [1–3]. Gold and silver nanoparticles covered by a thin layer of dielectric are the most popular for plasmonic sensing by shell-isolated nanoparticle-enhanced Raman spectroscopy (SHINERS) analysis method [4, 5].

Gold nanoparticles (Au NPs) are relatively easy to prepare. The reduction by citrates is the most used chemical method [6, 7]. The modification by inert silica shell has been proposed to expand the application of nanoparticles [8] because such coating prevents the gold core from interactions with the analysed object and environment. Consequently, stable gold core–silica shell nanoparticles became the most popular for SHINERS experiments [9]. Various metal and nonmetal coatings (graphene, polymers, SiO_2, MnO_2, TiO_2, Al_2O_3, ZnO, SnO_2, ZrO_2, etc.) have been tested for successful analysis of different bioconjugates (proteins, DNA, bacteria, etc.) [4]. Due to their catalytic activity, chemical stability, nontoxicity, and low-cost gold combinations with semiconductor oxides they are also used for catalytic applications [10], solar energy utilization [11], radiotherapy in the treatment of tumors [12], etc.

In this research, gold nanoparticles were covered by silicon, manganese and titanium dioxides. All synthesized core-shell nanoparticles were successfully employed for SHINERS measurements with thiophenol as a model compound. In this way, it was shown that three types of nanoparticles – gold core–silicon dioxide shell (Au@SiO_2), gold core–manganese dioxide shell (Au@MnO_2) and gold core–titanium dioxide shell (Au@TiO_2) – could complement each other in SHINERS experiments.

EXPERIMENTAL

Materials

Gold (III) chloride trihydrate ($HAuCl_4 \cdot 3H_2O$, 99%), trisodium citrate dihydrate (HOC(COONa)$(CH_2COONa)_2 \cdot 2H_2O$, 99%), (3-aminopropyl)trimethoxysilane ($H_2N(CH_2)_3Si(OCH_3)_3$, APTMS, 97%),

* Corresponding author. Email: tatjana.charkova@ftmc.lt

sodium silicate solution in water (NaOH, 10%; SiO_2, 27%), potassium permanganate ($KMnO_4$, 99%), potassium hydroxide (KOH, 85%), potassium oxalate ($K_2C_2O_4 \cdot H_2O$, 99%), titanium (IV) (triethanolaminato)isopropoxide solution in isopropanol (TTEAIP, 80%), ammonia solution in water (NH_4OH, 25%), isopropanol (99%), ethanol (99%) and thiophenol (98%) were purchased from Merck and used without additional treatment. Purified in the Millipore system Mili-Q water (18.2 MΩ·cm) was used in all experiments. The Tienta SpectRIM steel substrate from Merck was employed for Raman experiments.

General equipment

A Lambda 25 spectrophotometer was used for recording UV/Vis spectra (300–1100 nm) of the synthesized nanoparticles.

High-resolution transmission electron microscopy (HR-TEM) analyses of the nanoparticles were carried out using a FEI Tecnai G2 F20 X-TWIN microscope; specimens for the measurements were prepared by a FEI Helios Nanolab 650 dual beam microscope.

SHINERS spectra were taken using a Perkin-Elmer RamanFlex 400 Echelle type spectrometer with a 785 nm beam diode laser and a thermoelectrically cooled (–50°C) CCD detector. The spectra were recorded by the accumulation of 10 scans with an integration time of 10 s; the laser power was 50 mW.

Synthesis of Au NPs

To boiling 100 mL of 0.01% $HAuCl_4$ solution, 0.7 mL of 0.9% sodium citrate was added. The reaction mixture was refluxed for 30 min and self-cooled to room temperature within 1 h.

Synthesis of Au@SiO_2 nanoparticles

To 30 mL of Au NPs solution, 0.4 mL of 1 mM APTMS was added and stirred at 20°C for 15 min. Then 3.2 mL of 0.54% sodium silicate solution was added and stirred for another 3 min. After stirring at 90°C for 45 min, it was cooled in an ice bath for 30 min. The Au@SiO_2 nanoparticles were centrifuged at 3000 rpm for 20 min and washed twice with water.

Synthesis of Au@MnO_2 nanoparticles

All reagents were cooled to 10°C before use. 30 mL of Au NPs solution was alkalized to pH = 9.8 by the addition of 0.2 mL 0.1 M KOH with stirring. Then, to the cooled mixture 0.3 mL of 10 mM $KMnO_4$ and 1.5 mL of 10 mM $K_2C_2O_4$ were added. Next, it was kept at 20°C for 5 min and at 60°C for 1 h without stirring. The reaction mixture was cooled at room temperature for 15 min and in an ice bath for 15 min. The Au@MnO_2 nanoparticles were centrifuged at 3000 rpm for 20 min and washed twice with water.

Synthesis of Au@TiO_2 nanoparticles

18 mL of Au NPs were centrifuged at 3000 rpm for 20 min. Concentrated Au NPs were diluted in 1 mL of water and 3 mL of isopropanol was added. Next, 100 µl of 1.1 mM APTMS was added and stirred at 20°C for 10 min; 100 µl of 2.5 mM TTEAIP was added and stirred at 20°C for 30 min; 20 µl of 25% NH_4OH was added (mixture pH = 11.2) and stirred at 20°C for 1 h. The Au@TiO_2 nanoparticles were centrifuged at 3000 rpm for 20 min and washed one time with isopropanol and one time with water.

Raman and SHINERS measurements

Synthesized Au@SiO_2, Au@MnO_2 and Au@TiO_2 nanoparticles were dropped onto the Tienta steel substrate and dried at room temperature. Then the Raman spectra of the nanoparticles were recorded. Next, an evaporated gold layer on a cleaned glass substrate was incubated in 10^{-3} M thiophenol solution in ethanol for 1 h, washed with ethanol and dried. Then, 3 µL of synthesized nanoparticles were spread on the plate with the formed self-assembled monolayer, dried at room temperature, and the SHINERS spectra of thiophenol were obtained.

RESULTS AND DISCUSSION

Gold core–silica shell [13, 14], gold core–manganese shell [15, 16] and gold core–titanium shell [17, 18] nanoparticles were synthesized earlier. However, the search for new more effective, low-cost and environment-friendly methods continues. Anyway, the synthesis of nanoparticles must ensure the main properties of core–shell structures, which determine their further application. In our case, the core should be 50–100 nm in diameter, which is suitable for SHINERS measurements. Also, a chemically and electrically inert shell should be compact and thin enough (about 2–10 nm) avoiding decreasing signal intensity [13]. The pin holes were experimentally obtained in shells with the thickness under

2 nm of SiO_2 [13], 1.2 nm of MnO_2 [15] and 3 nm of TiO_2 [18]. Besides, each coating has its specific properties. The silica shell can dissolve in strong alkaline media, but manganese dioxide is stable under such conditions [15]; titanium dioxide is thermally stable and has a high laser damage threshold [19]. Based on these observations, it was set to create three different types of 50–60 nm gold nanoparticles with 3–5 nm SiO_2, MnO_2 and TiO_2 coatings suitable for SHINERS. The HR-TEM method was used to identify the thickness of the shell, the form and size of the nanoparticles. Other properties of the synthesized nanoparticles were observed visually during synthesis, and employing spectroscopic UV/Vis and Raman techniques (Table).

First, gold nanoparticles were synthesized by Tian's protocol, and the silica shell was coated over the core by the modified procedure [13, 20]. The standard reagents – gold (III) chloride and sodium citrate, were used for the synthesis of Au NPs. In the boiling $HAuCl_4$ solution the citrate ions reduce $AuCl_4^-$ to Au^+. Then an electrostatically stable complex of citrate and Au^+ ions forms microdomains and the self-catalyzed disproportionation of Au^+ to Au^0 occurs. Citrate oxidizes to byproducts, which stabilize initial nuclei in agglomerates; finally, they grow into gold nanospheres (Fig. 1). Next, the silica shell is formed over the Au NPs, using APTMS coupling agent and sodium silicate [21]. The 50 ± 5 nm Au@SiO_2 nanospheres with 2–3.5 nm of SiO_2 were synthesized in this way (Fig. 2a).

The exchange in colour (from yellow to wine red) during the synthesis and the data from the UV/Vis spectrum suggest the formation of Au NPs. The UV/Vis absorption peak of Au NPs is 538 nm, and 539 nm that of silica covered gold nanoparticles. After one month keeping at 8–10°C, we notice the exchange in colour (from wine red to grey) and a red-shifted broadened peak (about 750 nm) in the UV/Vis spectrum of aggregated gold core–shell nanoparticles (Fig. 3).

Lin's reported synthesis was modified for the Au@MnO_2 nanoparticles [15]. In neutral, weak acid and weak alkaline media permanganate ions are reduced by oxalates to form manganese dioxide. The high concentration of hydrogen ions leads to the loss of the shell [15]. Seeing that, pH plays an important role in the formation of MnO_2 defects, some conditions of media (pH = 9–14) were tested. The pH = 9.8 was observed as perfectly suitable for the synthesis of 55 ± 5 nm Au@MnO_2 with 2–4.5 nm MnO_2 shell (Fig. 2b, Fig. 3). Consequently, the conditions were successfully optimized and the reaction time decreased twice. The Au@MnO_2 nanospheres were stable up to 3 weeks keeping cold (8–10°C). Then the purple colour exchanges to grey and a broadened peak above 750 nm occurs in the UV/Vis spectrum.

The Au@TiO_2 nanoparticles were prepared using TTEAIP and APTMS. Optimization of the ratio of the reagents allowed a significant shortening of the Hartman's protocol (from 12 to 1 h) [18]. Also,

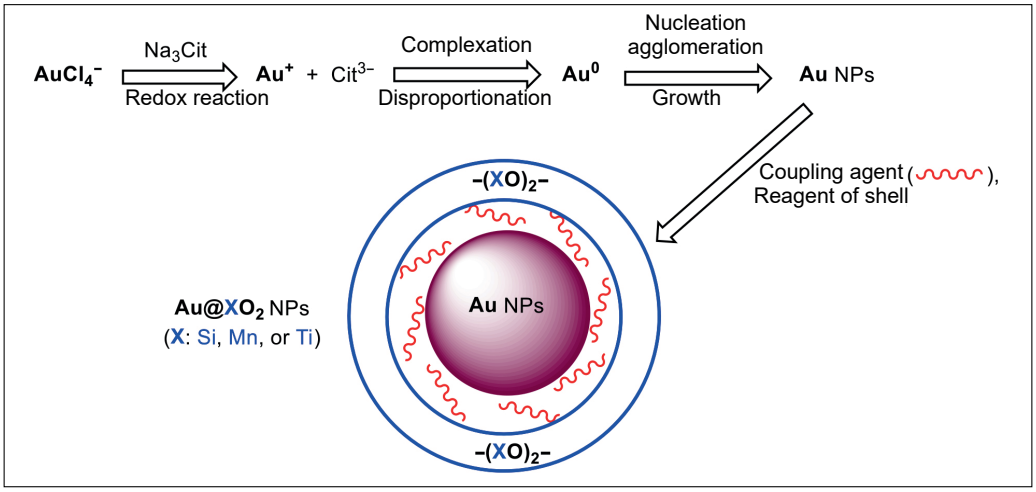

Fig. 1. The formation process of gold core–shell nanoparticles (coloured online)

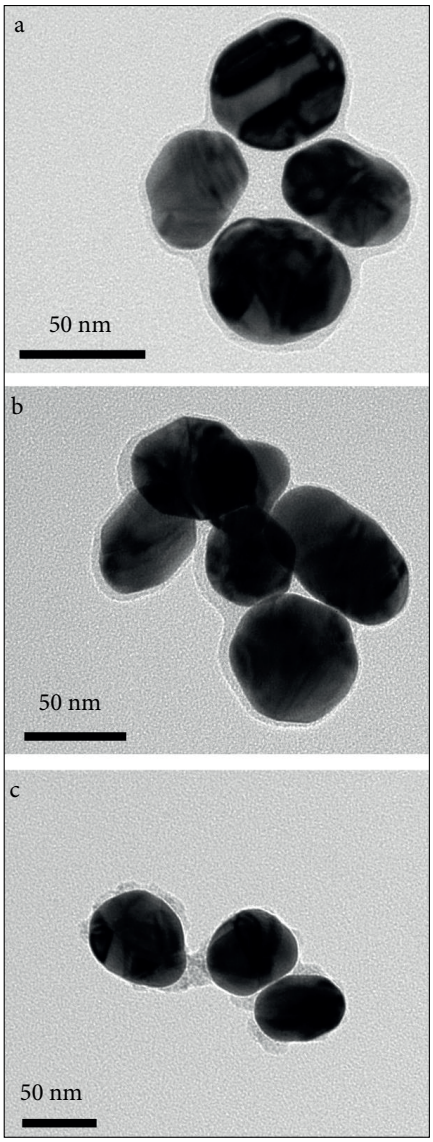

Fig. 2. HR-TEM images of 50 ± 5 nm $Au@SiO_2$ nanospheres with 2–3.5 nm of SiO_2 (a), 55 ± 5 nm $Au@MnO_2$ nanospheres with 2–4.5 nm MnO_2 (b) and 55 ± 5 nm $Au@TiO_2$ nanospheres with 1.5–8 nm TiO_2 (c)

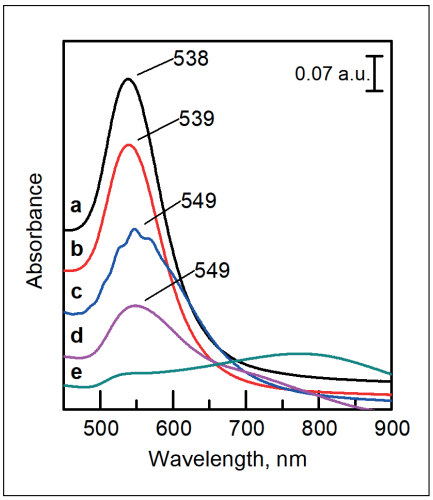

Fig. 3. UV/Vis spectra of Au NPs (a), $Au@SiO_2$ (b), $Au@MnO_2$ (c), $Au@TiO_2$ (d), and aggregated gold core–shell nanoparticles (e) (coloured online)

the centrifugation was clarified. Our modified procedure allows obtaining 55 ± 5 nm $Au@TiO_2$ with 1.5–8 nm TiO_2 shell (Fig. 2c, Fig. 3). Unfortunately, the conditions for the formation of an even TiO_2 shell were not optimized. Probably of this, the $Au@TiO_2$ nanospheres were stable only for 1–2 weeks. It was not possible to observe the colour change visually because the particles were dark grey from the beginning. However, the aggregation of the nanoparticles was confirmed by a red-shifted broadened peak (>750 nm) in the UV/Vis spectrum.

For SHINERS experiments a self-assembled monolayer of thiophenol onto smooth gold was formed. Three species of the synthesized nanoparticles amplify Raman signals of thiophenol. All assignments of spectra were based on reported earlier data [21]. The vibrational mode at 419 cm^{-1} is related to C–S out-of-plane bending vibrations. Other vibrational modes can be attributed with benzene ring: 693 cm^{-1}, 999 cm^{-1} suitable with ring out-of-plane deformation, and C–H out-of-plane bending. The band at 1073 cm^{-1} is assigned to the ring in-plane deformation and C–C symmetric stretching. The most intensive and strong feature near 1574 cm^{-1} is associated with C–C symmetric stretching vibrations. No matter which nanoparticles ($Au@SiO_2$, $Au@MnO_2$ or $Au@TiO_2$) were used to amplify Raman signals, the most important modes and their relative intensities of thiophenol coincide (Fig. 4). However, the most intensive and clear features of thiophenol were obtained with $Au@SiO_2$ nanoparticles.

For comparison, the spectra of each type of the nanoparticles were recorded onto the Tienta steel substrate. This allowed obtaining vibrational regions of the nanoparticles in the SHINERS

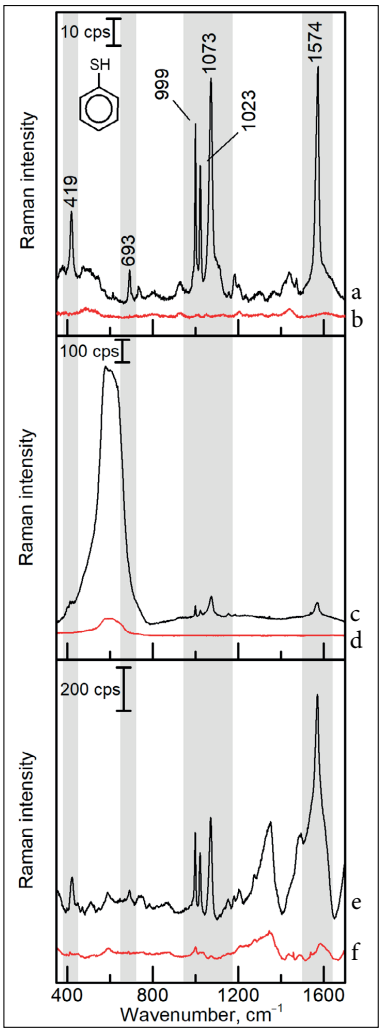

Fig. 4. SHINERS spectra of thiophenol with $Au@SiO_2$ (a), $Au@MnO_2$ (c) and $Au@TiO_2$ (e) – black lines. Raman spectra of $Au@SiO_2$ (b), $Au@MnO_2$ (d) and $Au@TiO_2$ (f) – red (online) lines. The SHINERS spectra are background corrected

spectra (Table). It is noticeable that $Au@MnO_2$ and $Au@TiO_2$ NPs have specific spectra that overlap with the thiophenol spectrum in 400–700 cm^{-1} and 1200–1600 cm^{-1} regions, respectively. $Au@SiO_2$ NPs also have a specific spectrum, but the intensity of vibrational bands is extremely low compared to the SHINERS spectra of thiophenol; this can affect data minimally (Fig. 4).

The different properties of nanoparticles allow choosing each type of them for specific experimental conditions. However, there is no doubt that three synthesized types of nanoparticles ($Au@SiO_2$, $Au@MnO_2$ or $Au@TiO_2$) could perform a comprehensive research of complex structures, complementing each other in SHINERS experiments.

CONCLUSIONS

Three species of gold core–shell nanoparticles ($Au@SiO_2$, $Au@MnO_2$, $Au@TiO_2$) were successfully synthesized and used for the analysis of self-assembled monolayer of thiophenol by the SHINERS method. The produced gold core–silica shell nanoparticles were the smallest compared to the others. However, the SiO_2 coating was the most even and the thinnest. For this reason, the most stable $Au@SiO_2$ nanospheres mainly amplify thiophenol signals in the SHINERS spectrum.

ACKNOWLEDGEMENTS

Authors gratefully acknowledge Algirdas Selskis for Au films preparation and Martynas Skapas for TEM recordings from the Department of Characterisation of Materials Structure of Center for Physical Sciences and Technology.

Received 31 August 2020
Accepted 15 September 2020

Table. **Experimental data on the obtained properties of the synthesized nanoparticles**

Obtained property	$Au@SiO_2$	$Au@MnO_2$	$Au@TiO_2$
Form	Nanospheres	Nanospheres	Nanospheres
Diameter	50 ± 5 nm	55 ± 5 nm	55 ± 5 nm
Formation of shell	45 min	1 h	1 h
Thickness of shell	2–3.5	2–4.5	1.5–8
UV/Vis absorption peak	539	549	549
Vibrational region of nanoparticles in SHINERS spectra	Low intensity	400–700 cm^{-1}	1200–1600 cm^{-1}
Stability keeping at 8–10°C	1 month	3 weeks	2 weeks

References

1. K. K. Harish, V. Nagasamy, B. Himangshu, K. Anuttam, *Biomed. J. Sci. Tech. Res*., **4(2)**, 3765 (2018).
2. A. M. Ealias, M. P. Saravanakumar, *IOP Conf. Ser. Mater. Sci. Eng*., **263**, 032019 (2017).
3. I. Khan, K. Saeed, I. Khan, *Arab. J. Chem*., **12(7)**, 908 (2019).
4. J.-F. Li, Y.-J. Zhang, S.-Y. Ding, R. Panneerselvam, Z.-Q. Tian, *Chem. Rev.*, **117(7)**, 5002 (2017).
5. J. Krajczewski, A. Kudelski, *Front. Chem*., **7(410)**, 1 (2019).
6. J. Turkevich, P. C. Stevenson, J. Hillier, *Discuss. Faraday Soc*., **60**, 55 (1951).
7. G. Frens, *Colloid Polym. Sci*., **250**, 736 (1972).
8. L. M. Liz-Marzán, M. Giersig, P. Mulvaney, *Langmuir*, **12(18)**, 4329 (1996).
9. J. F. Li, Y. F. Huang, Y. Ding, et al., *Nature*, **464**, 392 (2010).
10. M. Lukosi, H. Zhu, S. Dai, *Front Chem. Sci. Eng*., **10(1)**, 39 (2016).
11. W. Li, A. Elzatahry, D. Aldhayan, D. Zhao, *Chem. Soc. Rev*., **47**, 8203 (2018).
12. X. Yi, L. Chen, X. Zhong, et al., *Nano Res*., **9(11)**, 3267 (2016).
13. J. F. Li, X. D. Tian, S. B. Li, et al., *Nat. Protoc*., **8(1)**, 52 (2013).
14. T. A. Galloway, L. Cabo-Fernandez, I. M. Aldous, F. Braga, L. J. Hardwick, *Faraday Discuss*., **205**, 469 (2017).
15. X.-D. Lin, V. Uzayisenga, J.-F. Li, et al., *J. Raman Spectrosc*., **43(1)**, 40 (2012).
16. T. Simao, D. M. Chevrier, J. Jakobi, et al., *J. Phys. Chem*. C, **120**, 22635 (2016).
17. X.-F. Wu, H.-Y. Song, J.-M. Yoon, Y.-T. Yu, Y.-F. Chen, *Langmuir*, **25(11)**, 6438 (2009).
18. T. Hartman, B. M. Weckhuysen, *Chem. Eur. J*., **24(15)**, 3733 (2018).
19. R. T. Tom, A. S. Nair, N. Singh, et al., *Langmuir*, **19(8)**, 3439 (2003).
20. A. Zdaniauskienė, T. Charkova, I. Matulaitienė, et al., *J. Phys. Chem*. C, **122(2)**, 1234 (2018).
21. T. Charkova, A. Zdaniauskienė, I. Ignatjev, *Chem. Data Collect*., **29**, 100497 (2020).

Tatjana Charkova, Agnė Zdaniauskienė

DENGTŲ SILICIO, MANGANO IR TITANO DIOKSIDAIS AUKSO NANODALELIŲ SINTEZĖ IR PALYGINIMAS

Santrauka

Susintetintos aukso nanodalelės (50–60 nm) sėkmingai padengtos plonais (1,5–8 nm) silicio dioksido, mangano dioksido ir titano dioksido sluoksniais. Gautos trijų rūšių (Au@SiO_2, Au@MnO_2, Au@TiO_2) nanosferos pritaikytos tiofenolio monosluoksnio analizei panaudojant nanodalelių, padengtų apsauginiu sluoksniu, sustiprintos Ramano spektroskopijos metodą (angl. shell-isolated nanoparticle-enhanced Raman spectroscopy). Straipsnyje išsamiai aprašytos sintezių metodikos ir pateiktas dalelių palyginimas.

Chemical Data Collections 29 (2020) 100497

Contents lists available at ScienceDirect

Chemical Data Collections

journal homepage: www.elsevier.com/locate/cdc

Silica shell-isolated gold nanospheres: Synthesis, investigation of stability in organic solvents, and application in shell-isolated nanoparticle-enhanced Raman spectroscopy

Tatjana Charkova*, Agnė Zdaniauskienė, Ilja Ignatjev

Department of Organic Chemistry, Center for Physical Sciences and Technology, Saulėtekio Ave. 3, LT-10257 Vilnius, Lithuania

ARTICLE INFO

Article history:
Received 14 April 2020
Revised 16 June 2020
Accepted 27 July 2020
Available online 29 July 2020

Keywords:
Gold nanoparticles
Shell-isolated nanoparticle-enhanced
Raman spectroscopy
Thiophenol

ABSTRACT

Shell-isolated nanoparticles spread over the surface of sample material are widely used in various fields of analysis. Their stability has not yet been well established. In this report, the silica shell-isolated gold nanospheres were synthesized in aqueous medium. Their stability in water and 17 organic solvents was observed visually and employing spectroscopic UV and Raman techniques. The nanoparticles onto self-assembled monolayer of thiophenol were used to amplify Raman signal.

Specifications table

Subject area	Spectroscopy, Physical Chemistry, Colloidal chemistry.
Compounds	Silica shell-isolated gold nanospheres.
Data category	Spectral, synthesized.
Data acquisition format	UV, TEM, SHINERS
Data type	Analyzed
Procedure	Synthesis of silica shell-isolated gold nanospheres; stability experiment of the nanoparticles in water and 17 organic solvents; recording Raman spectra of thiophenol on gold surface.
Data accessibility	Data is available with this article.

1. Rationale

Recent developments in nanoparticles research indicate their application in complex studies such as structure, functions, molecular behavior, and so on [1–3]. The nature of the particles and the aims of the study determine the methods and experimental conditions.

The surface enhanced Raman spectroscopy (SERS) technique is helpful for surface analysis of the matter. However, the method has a limitation to use mostly Ag, Au, and Cu roughened surfaces [4,5]. The plasmonic property of Au, Ag, Au/Ag mixed nanoparticles allows to use them for SERS – a layer of such nanoparticles distributed on the research surface generates an enhanced Raman signal. Unfortunately, a destructive interaction of the bare nanoparticles with an analyzed object

* Corresponding author.
E-mail address: tatjana.charkova@ftmc.lt (T. Charkova).

https://doi.org/10.1016/j.cdc.2020.100497
2405-8300/

and an environment often occurs. Ultrathin inert coating (SiO_2, MnO_2, TiO_2 etc.) increases the stability of the nanoparticles and prevents their metal cores from contacts with substrates, analytes, and environment [6–8].

In 1996, Mulvaney [9] reported the preparation of silica shell-isolated nanoparticles; in 2010 Tian and coworkers [10,11] modified the procedure and adapted the nanoparticles for SERS. Since, the highly sensitive technique with the nanoparticles – shell-isolated nanoparticle-enhanced Raman spectroscopy (SHINERS) emerged. SHINERS is suitable for investigation of various materials with different morphologies. Therefore, this perspective method is widely used in surface, semiconductor, biotechnological sciences, and food, environment safety [7].

Due to the biocompatibility, optical and electronic properties gold nanoparticles (AuNPs) are one of the most used for labeling, delivery, and sensing of different bioconjugates [12–14]. Certainly, bare AuNPs are appropriate for SERS and relatively easy prepared. Usually, they are synthesized by reduction of auric chloride with sodium citrate in aqueous medium [15]. Au nanospheres less than 55 nm in diameter can be obtained in the way mentioned below. Various reducing (citrates, ascorbic acid, $NaBH_4$ etc.) and stabilizing (ammonium salts, polymers etc.) agents are used to get larger particles of a certain shape [7]. Such nanoparticles are more attractive for SERS, because they can generate a higher Raman signal enhancement [16–18]. The size and shape depend on the temperature and concentration of reactants. All of them are necessary for nanoparticles preparation and prevent them from aggregation. However, a trace of unreacted reagents can affect the object of research. Usually, many of used reactants are insoluble in water and partially removed by centrifugation. Organic solvents can resolve the washing problem, because they dissolve organic reactants perfectly. However, the nanoparticles must remain stable in such an environment. There are many research works with a detailed description of AuNPs stability under different stabilizing agents, pH and other conditions [19–23]. Still, there is a lack of information about shell-isolated nanoparticle stability in various solvents. As a result, the purification of the nanoparticles remains a relevant problem. Therefore, in this report, classic silicon dioxide covered spherical gold nanoparticles ($Au@SiO_2$) were synthesized and their stability was determined in water and different 17 organic solvents. Moreover, our experiment was done in order to use the resulting data for any future modification of gold core silicon shell nanoparticles and SHINERS research in a non-aqueous medium.

2. Procedure

2.1. Materials and methods

The following reagents were purchased from Merck and used as received: gold (III) chloride trihydrate ($HAuCl_4.3H_2O$, 99%), trisodium citrate dihydrate ($HOC(COONa)(CH_2COONa)_2{\bullet}2H_2O$, 99%), (3-aminopropyl)trimethoxysilane ($H_2N(CH_2)_3Si(OCH_3)_3$, APTMS, 97%), sodium silicate solution (10% NaOH, 27% SiO_2), thiophenol (98%). All organic solvents from Merck (99%) were used without farther purification: acetone (Ac), acetonitrile (AcN), benzene, toluene, chloroform, dichloromethane (DCM), N,N-dimethylformamide (DMF), n-octane, n-hexane, methyl alcohol (MetOH), ethyl alcohol (EtOH), propyl alcohol (PrOH), isopropyl alcohol (iPrOH), butyl alcohol (BuOH), isobutyl alcohol (iBuOH), pentyl alcohol (PentOH), isopentyl alcohol (iPentOH). In all procedures was used deionized Milli-Q water of 18.2 MΩ·cm resistivity. A highly polished stainless steel substrate with an ultrathin hydrophobic coating (Tienta SpectRIM, Merck) was used for Raman measurements.

UV/Vis absorption spectra were obtained by using Lambda 25 Spectrophotometer in the range 300-1100 nm; 10 µL of silica shell-isolated gold nanospheres in 3 mL of each solvent were used as UV samples.

High-resolution transmission electron microscopy (HR-TEM) images were recorded by using FEI Tecnai G2 F20 X-TWIN microscope with scanning TEM module, equipped with a high-angle annular dark-field detector for Z-contrast imaging and an X-ray energy-dispersive spectroscopy detector for elemental mapping. FEI Helios Nanolab 650 dual beam microscope with an Omniprobe manipulator was used to prepare specimens for the measurements.

Raman and SHINERS spectra were recorded using Echelle type spectrometer RamanFlex 400 (PerkinElmer, Inc.) equipped with a thermoelectrically cooled (–50°C) CCD camera, a fiber-optic cable and the diode laser of the 785 nm beam. The 180° scattering geometry was employed. The laser power at the sample was restricted to 30 mW and the beam was focused to a 200 μm diameter spot on the sample. The integration time was 10 s. Each spectrum was recorded by accumulation of 10 scans, yielding total 100 s time accumulation.

2.2. Synthesis procedure of $Au@SiO_2$ nanoparticles

200 mL of an aqueous $HAuCl_4$ solution (0.01 wt %: 0.02 g in 200 mL H_2O) was prepared and kept in the dark at room temperature (20°C) for 4 days before was used. Then it was boiled in a hot oil bath (125°C) with vigorous stirring. After solution reached boiling temperature (in 5 min) the 1.4 mL of sodium citrate (0.91 wt %: 0.0501 g in 5,5 mL H_2O) was added. The mixture was refluxed for 30 min and left without stirring for 2 h at room temperature. As a result, the wine red colloid solution of AuNPs was obtained.

Next silicon dioxide shell over the gold nanoparticles was formed. 2.67 mL of APTMS (1mM: 7.2 µL in 40 mL H_2O) was added to 200 mL of AuNPs solution. The mixture was stirred vigorously at room temperature for 15 min. Then 21.33 mL of sodium silicate solution (0.54 wt %/wt: 208.6 µL in 50 mL H_2O) was added and the mixture was stirred for additional 3 min. Next, the flask was placed in a water bath and stirred at 90°C temperature for 50 min. To stop the reaction process, it was placed in an ice bath (3-5°C) for 1 h. Finally, cold mixture was centrifuged at 5500 rpm for 15 min. The supernatant was removed and $Au@SiO_2$ nanoparticles as a concentrated brown suspension were obtained.

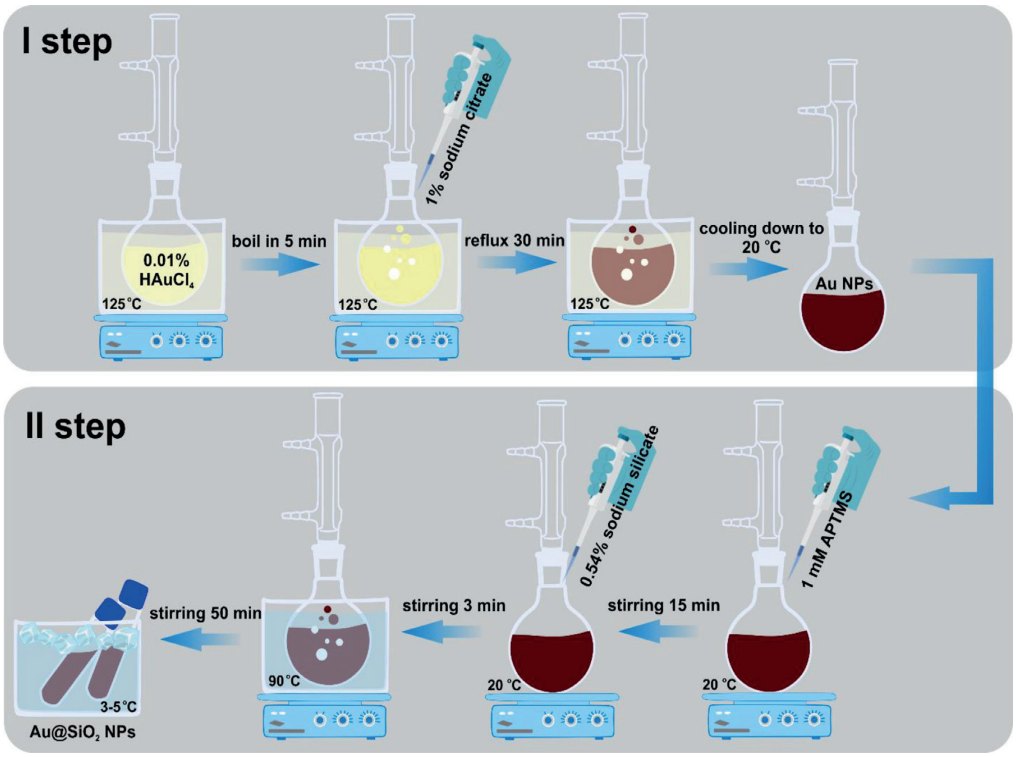

Fig. 1. Synthesis of $Au@SiO_2$ nanoparticles.

2.3. Self-assembled monolayer formation

Au film was deposited on cleaned glass substrate by magnetron sputtering using a Quorum 150T sputter and 99.99% Au target. Then the gold substrate was rinsed with ethyl alcohol, dried and transferred into thiophenol (10^{-2} M) alcohol solution for 1 hour to form self-assembled monolayer onto gold surface. After incubation, the plate with the already formed monolayer was removed from the solution. Then it was rinsed with the alcohol abundantly to remove any possible overlayers of thiophenol, and finally dried.

2.4. Raman measurements

Raman spectrum of $Au@SiO_2$ was obtained after the nanoparticles were dropped onto steel substrate and dried at room temperature. For self-assembled monolayers investigations Raman spectra were recorded in situ in an aqueous medium from a smooth gold surface on which the thiophenol monolayer was formed before. In order to amplify the Raman scattering signal, $Au@SiO_2$ nanoparticles were injected into the system (ratio with water 1:500). The maximum intensity of the spectrum was obtained after 2 hours.

3. Data, value and validation

3.1. Synthesis and characterization of Au@SiO_2 nanoparticles

The most used synthesis protocol was modified and applied to larger quantities [24]. The spherical gold nanoparticles with silica shell were successfully synthesized by the procedure of two steps (Fig. 1).

Firstly, bare AuNPs were prepared from auric chloride using sodium citrate as reductant and stabilizer (Fig. 2) [24,25]. Noticeably, that process of nanoparticles formation accompanied by a change of colors: yellow, colorless, gray, lilac, and wine red.

During the synthesis, citrate oxidize to acetone dicarboxylate ions, acetone, formaldehyde and other byproducts, which facilitate nanoparticle growth (Fig. 3) [26,27].

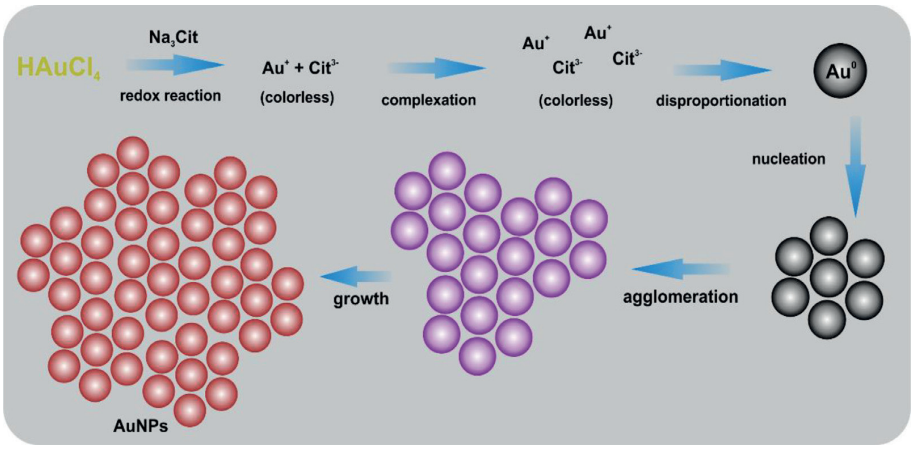

Fig. 2. The mechanism of AuNPs growth.

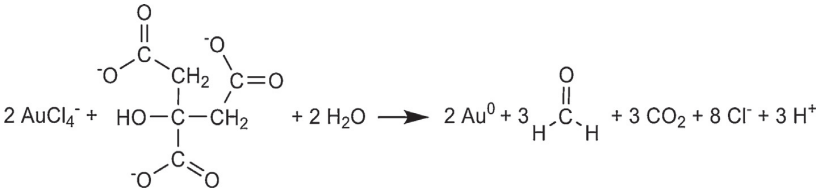

Fig. 3. Summarized redox reaction of AuNPs synthesis.

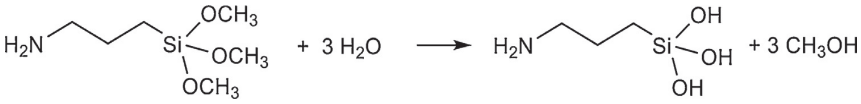

Fig. 4. Hydrolysis of APTMS.

The second step was silica shell formation over the nanoparticles using (3-aminopropyl)trimethoxysilane (APTMS) and sodium silicate [10]. The hydrolysis of the coupling agent occurs easily in aqueous medium (Fig. 4).Then the amine groups bind to the gold and the hydroxy groups form covalent bonds with sodium silicate [28]. At elevated temperatures, the products are further hydrolyzed and a net containing SiOSi and SiOH groups are formed (Fig. 5).

Presence of unreacted OH groups leads to defects in silica layer [29,30]. The silica shell thickness is determined by the heating temperature and time. Longer heating at 90°C gives thicker silica layer over the particles [31]. Nanoparticles with thick silica layer are stable, but when the shell thickness increases, the SHINERS signal of probe molecules decreases rapidly. It was reported, that the most appropriate dielectric layer thickness for SHINERS measurements is 2-4 nm [11]. Based on these observations, spherical 55 nm gold nanoparticles with thin 3 nm silica shell (Fig. 6A and 6B) were prepared and tested in 18 different solvents observing their stability.

3.2. Stability experiments

It was observed, that colloidal Au@SiO_2 particles could be stable in water up to 1 month kept in a dark at 8-10°C. The wine red color of stable nanoparticles exchanged to purple after two weeks and a gray precipitate occurred after 1 month. The exchange in color and UV/Vis spectra suggest that aggregation occurs in solution: purple color indicates the beginning, and grey one – practically the end of process (Fig. 7). UV absorption peak of stable Au@SiO_2 is about 540 nm. We attribute the broad peak around 745 nm as the absorbance of the aggregated particles. Wagers et al. [22] assign the same exchange of color and red-shifted broadened peak (721 nm) for aggregated AuNPs too. In our case, there is a silica shell, which preserve gold core, however HR-TEM images show its unevenness (2-3 nm). Shell defects in thin areas can initiate fragmentation of silica layer and commence the aggregation of nanoparticles (Fig. 6C).

For stability investigation acetone, acetonitrile, benzene, toluene, chloroform, dichloromethane, N,N-dimethylformamide, n-octane, n-hexane, and available alcohols were chosen (Table 1). 10 µL of Au@SiO_2 were dispersed in 3 mL of each organic

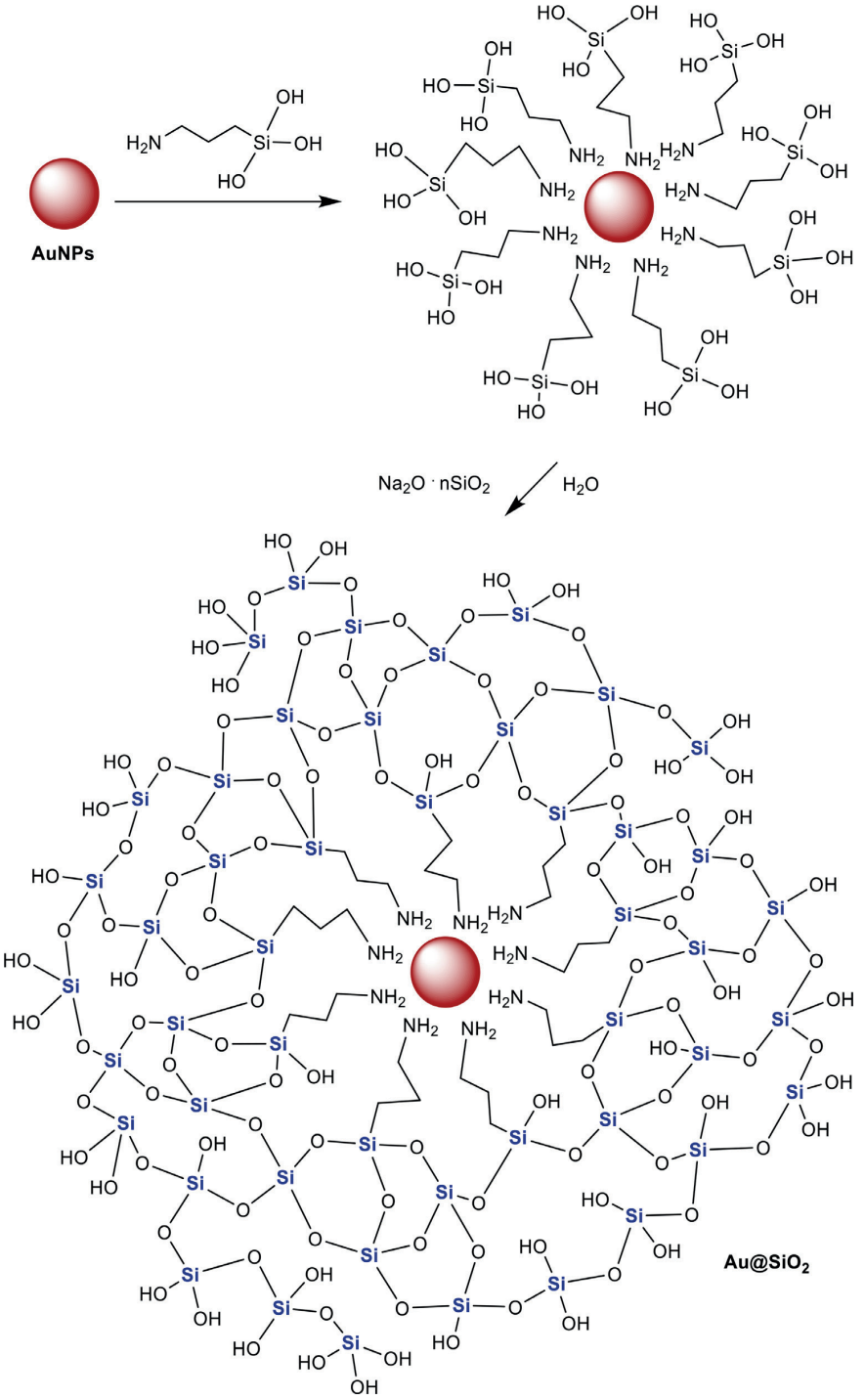

Fig. 5. The silica shell formation over AuNPs.

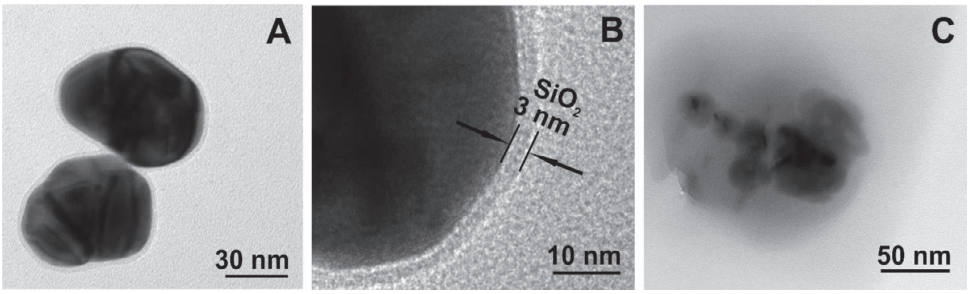

Fig. 6. HR-TEM images of 55 nm Au@SiO_2 with 3 nm silica shell (A and B) and aggregated Au@SiO_2 (C).

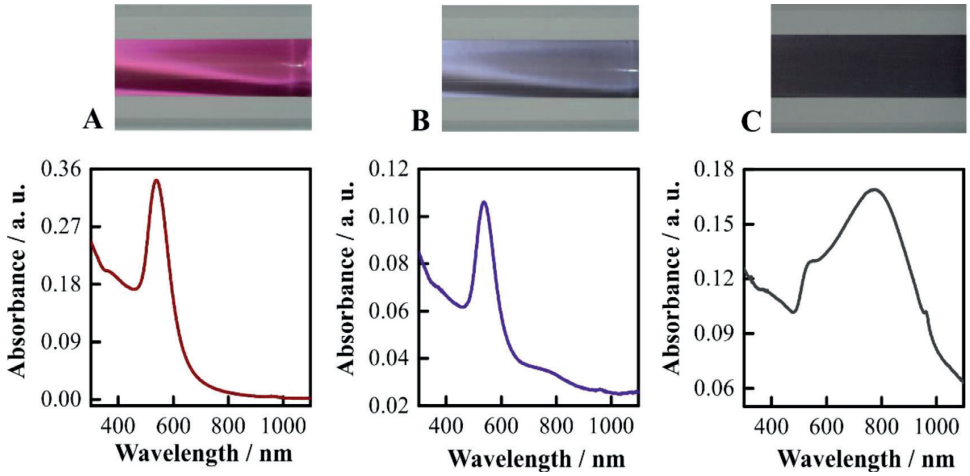

Fig. 7. Optical images (upper panel) and UV/Vis spectra (lower panel) of Au@SiO_2 in water after 1 day (A), after 2 weeks (B), and after 1 month (C).

Table 1
Au@SiO_2 stability in water and organic solvents.

Solvent	0 min	10 min	20 min	30 min	1 h	24 h	48 h	96 h
H_2O	+	+	+	+	+	+	+	+
Ac	+	+	+	+	+	+	+	+
AcN	-	-	-	-	-	-	-	-
Benzene	Em.+	Em.+	Em.+	Em.+	Em.-	Em.-	Em.-	Em.-
Toluene	Em.+	Em.+	Em.+	Em.+	Em.-	Em.-	Em.-	Em.-
Chloroform	Em.+	Em.+	Em.-	Em.-	Em.-	Em.-	Em.-	Em.-
DCM	Em.+	Em.-	Em.-	Em.-	Em.-	Em.-	Em.-	Em.-
DMF	+	+	+	+	+	+	+	+
n-Octane	Em.+	Em.+	Em.+	Em.+	Em.-	Em.-	Em.-	Em.-
n-Hexane	Em.+	Em.+	Em.+	Em.+	Em.-	Em.-	Em.-	Em.-
MetOH	+	+	-	-	-	-	-	-
EtOH	+	+	+	+	+	+	+	+
PrOH	-	-	-	-	-	-	-	-
iPrOH	+	+	+	+	+	+	+	+
ButOH	-	-	-	-	-	-	-	-
iButOH	-	-	-	-	-	-	-	-
PentOH	-	-	-	-	-	-	-	-
iPentOH	-	-	-	-	-	-	-	-

+ stable nanoparticles;
- aggregated particles;
Em.+ emulsion of stable nanoparticles;
Em.- emulsion of aggregated particles.

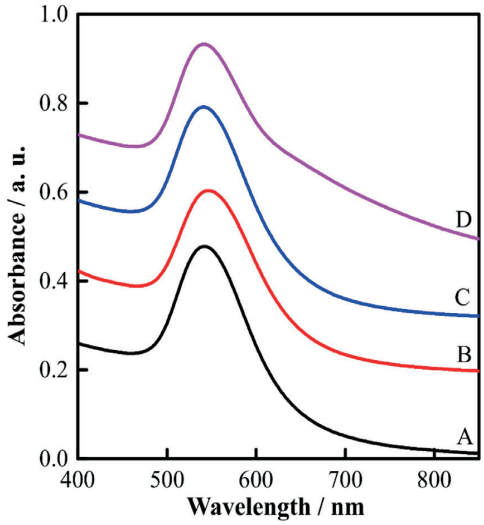

Fig. 8. UV/Vis spectra of Au@SiO_2 in acetone (A – black), N,N-dimethylformamide (B – red), ethyl alcohol (C – blue), and isopropyl alcohol (D – purple) after 96 h.

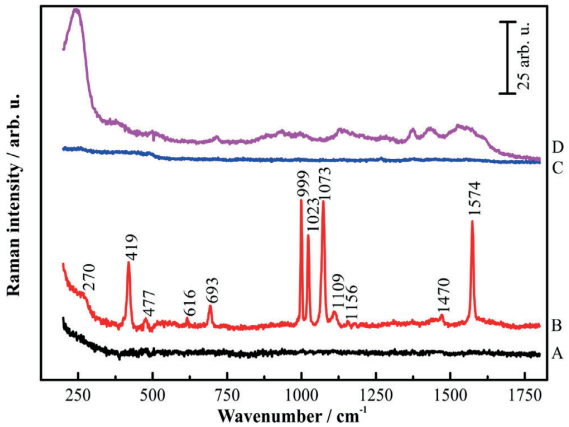

Fig. 9. Raman spectrum of thiophenol adsorbed on smooth Au surface without nanoparticles (A – black), and SHINERS spectrum of thiophenol with Au@SiO_2 nanoparticles (B – red). Raman spectrum of aggregated Au@SiO_2 nanoparticles (C – blue), and Raman spectrum of stable Au@SiO_2 nanoparticles (D – purple) onto Tienta substrate.

solvent. Then the dispersions were left in glass tubes and their stability was observed at room temperature during 96 h. A purple color appearance was considered as a beginning of nanoparticle aggregation process.

Nanoparticles dispersed in acetone, N,N-dimethylformamide, ethyl and isopropyl alcohols were stable during all the time of experiment. The broad peak (745 nm) of aggregated nanoparticles was also not observed in their UV/Vis spectra (Fig. 8). However, aggregation occurred immediately in acetonitrile, propyl, butyl, isobutyl, pentyl and isopentyl alcohols; proceeded after 10 min in dichloromethane, after 20 min – in chloroform, and methyl alcohol, after 1 h – in benzene, toluene, n-octane, and n-hexane.

3.3. Raman spectra analysis

A self-assembled monolayer of thiophenol onto gold surface was formed; and Au@SiO_2 nanoparticles were used to amplify Raman signal. A clear enhanced SHINERS spectrum of thiophenol on smooth gold surface was obtained only with the nanoparticles (Fig. 9, curves A and B). To compare stable and aggregated particles we dropped them onto steel substrate, dried and recorded Raman spectra. Logically, that there is no Raman spectrum with aggregated particles (Fig. 9, curve C), and contrarily – stable Au@SiO_2 significantly enhance every impurity of environment (Fig. 9, curve D). In this way, we

Table 2
SHINERS data of thiophenol adsorbed on Au surface.

Assignments	$\Delta\nu$, cm^{-1}
Au–S stretching	270
C–S stretching	419
C–S out-of-plane bending	477
Ring in-plane deformation	616
Ring out-of-plane deformation	693
Ring out-of-plane deformation and C–H out-of-plane bending	999
Ring in-plane deformation and C–C symmetric stretching	1023
C–C asymmetric stretching	1073
C–H and/or S–C stretching	1109
C–H in-plane bending	1156
C–H in-plane bending	1470
C–C symmetric stretching	1574

assured, that themselves nanoparticles have a specific spectrum, but the intensity of vibrational bands was extremely low compared to SHINERS spectrum of thiophenol.

The SHINERS spectrum (Fig. 9, curve B) represents all specific vibrational modes of thiophenol onto smooth gold surface; all assignments (Table 2) are based on reported data [32].

4. Conclusions

Silica shell gold nanoparticles are typically prepared in water. However, their farther application or modification often requires using other solvents. The instability problem of particles often is not reported. Only a few authors offer to use other polar or nonpolar solvents instead of water [33,34]. However, usually many investigators cover bare nanoparticles with different capping agents, which increase stability of dispersion [35–37]. Our stability experiment with 17 organic solvents is unique, because we investigate gold-silica core-shell nanoparticles without any additional stabilizer. The most popular Au@SiO_2 nanospheres were prepared by modified procedure of Tian's group [11]. Stability was observed visually according changes in color and by spectroscopic UV/Vis and Raman techniques. The nanoparticles dispersed in water, acetone, N,N-dimethylformamide, ethyl and isopropyl alcohols were much more stable than dispersed in benzene, toluene, n-hexane, n-octane, chloroform, dichloromethane, acetonitrile, methyl alcohol, and other tested alcohols. The obtained results will make it easier to choose the suitable solvents for further research and modification of Au@SiO_2 nanoparticles.

Declaration of Competing Interest

The manuscript entitled, Silica Shell-Isolated Gold Nanospheres: Synthesis, Investigation of Stability in Organic Solvents, and Application in Shell-Isolated Nanoparticle-Enhanced Raman Spectroscopy by Tatjana Charkova, Agnė Zdaniauskienė, Ilja Ignatjev has not been published and is not under consideration for publication elsewhere. We have no conflicts of interest to declare. The manuscript does not describe any experiments with animals, human subjects, or human tissue samples.

Acknowledgments

The authors gratefully acknowledge Gediminas Niaura from Laboratory of Spectroelectrochemistry, Department of Organic Chemistry of Center for Physical Sciences and Technology for comments and support. We also thank Martynas Skapas from Department of Characterisation of Materials Structure for HR-TEM recordings.

References

[1] A.M. Ealias, M P Saravanakumar, A review on the classification, characterisation, synthesis of nanoparticles and their application, IOP Conf. Ser. 263 (2017) 032019, doi:10.1088/1757-899X/263/3/032019.
[2] M. Holzinger, A. Le Goff, S. Cosnier, Nanomaterials for biosensing applications: a review, Front. Chem. 2 (2014) 00063, doi:10.3389/fchem.2014.00063.
[3] H. Kumar K, N. Venkatesh, H. Bhowmik, A. Kuila, Metallic nanoparticle: a review, Biomed. J. Sci. Tech. Res. 4 (2) (2018) 3765–3775 https://biomedres.us/fulltexts/BJSTR.MS.ID.001011.php.
[4] E. Le Ru, P.G. Etchegoin, in: Principles of Surface Enhanced Raman Spectroscopy and Related Plasmonic Effects, Elsevier, Amsterdam, 2009, pp. 1–27. https://www.elsevier.com/books/principles-of-surface-enhanced-raman-spectroscopy/le-ru/978-0-444-52779-0. Chpt. 1.
[5] Z.-Q. Tian, B. Ren, D.-Y. Wu, Surface-enhanced Raman scattering: from noble to transition metals and from rough surfaces to ordered nanostructures, J. Phys. Chem. B 106 (37) (2002) 9463–9483, doi:10.1021/jp0257449.
[6] S. Liu, M.-Y. Han, Silica-coated metal nanoparticles, Chem. Asian J. 5 (2010) 36–45, doi:10.1002/asia.200900228.
[7] J.-F. Li, Y.-J. Zhang, S.-Y. Ding, R. Panneerselvam, Z.-Q. Tian, Core–shell nanoparticle-enhanced Raman spectroscopy, Chem. Rev. 117 (7) (2017) 5002–5069, doi:10.1021/acs.chemrev.6b00596.
[8] H.B. Abdulrahman, J. Krajczewski, A. Kudelski, Modification of surfaces of silver nanoparticles for controlled deposition of silicon, manganese, and titanium dioxides, Appl. Surf. Sci. 427 (B) (2018) 334–339, doi:10.1016/j.apsusc.2017.08.163.
[9] L.M. Liz-Marzán, M. Giersig, P. Mulvaney, Synthesis of nanosized gold–silica core–shell particles, Langmuir 12 18 (1996) 4329–4335, doi:10.1021/la9601871.

[10] J.F. Li, Y.F. Huang, Y. Ding, Z.L. Yang, S.B. Li, X.S. Zhou, F.R. Fan, W. Zhang, Z.Y. Zhou, D.Y. Wu, B. Ren, Z.L. Wang, Z.Q. Tian, Shell-isolated nanoparticle-enhanced Raman spectroscopy, Nature 464 (2010) 392–395, doi:10.1038/nature08907.
[11] J.F. Li, X.D. Tian, S.B. Li, J.R Anema, Z.L. Yang, Y. Ding, Y.F. Wu, Y.M. Zeng, Q.Z. Chen, B. Ren, Z.L. Wang, Z.Q. Tian, Surface analysis using shell-isolated nanoparticle-enhanced Raman spectroscopy, Nat. Protoc. 8 (1) (2013) 52–65, doi:10.1038/nprot.2012.141.
[12] M. Homberger, U. Simon, On the application potential of gold nanoparticles in nanoelectronics and biomedicine, Phil. Trans. R. Soc. A 368 (2010) 1405–1453, doi:10.1098/rsta.2009.0275.
[13] Y.-C. Yeh, B. Creran, V.M. Rotello, Gold nanoparticles: preparation, properties, and applications in bionanotechnology, Nanoscale 4 (2012) 1871–1880 https://dx.doi.org/10.1039%2Fc1nr11188d.
[14] Y. Li, Q. Wei, F. Ma, X. Li, F. Liu, M. Zhou, Surface-enhanced Raman nanoparticles for tumor theranostics applications, Acta Pharm. Sin. B 8 (3) (2018) 349–359, doi:10.1016/j.apsb.2018.03.007.
[15] J. Turkevich, P.C. Stevenson, J. Hillier, A study of the nucleation and growth processes in the synthesis of colloidal gold, Discuss. Faraday Soc. 11 (1951) 55–75 https://pubs.rsc.org/en/content/articlelanding/1951/df/df9511100055.
[16] J. Reguera, J. Langer, D. Jiménez de Aberasturi, L.M. Liz-Marzán, Anisotropic metal nanoparticles for surface enhanced Raman scattering, Chem. Soc. Rev. 46 (2017) 3866–3885, doi:10.1039/c7cs00158d.
[17] P.A. Mosier-Boss, Review of SERS substrates for chemical sensing, Nanomaterials 7 (6) (2017) 142, doi:10.3390/nano7060142.
[18] M.J. Ashley, M.R. Bourgeois, R.R. Murthy, C.R. Laramy, M.B. Ross, R.R. Naik, G.C. Schatz, C.A. Mirkin, Shape and size control of substrate-grown gold nanoparticles for surface-enhanced Raman spectroscopy detection of chemical analytes, J. Phys. Chem. C 122 (4) (2018) 2307–2314, doi:10.1021/acs.jpcc.7b11440.
[19] A.M. Alkilany, A.I.B. Yaseen, M.H. Kailani, Synthesis of monodispersed gold nanoparticles with exceptional colloidal stability with grafted polyethylene glycol-g-polyvinyl alcohol, J. Nanomater. (2015) 712359, doi:10.1155/2015/712359.
[20] J. Tournebize, A. Boudier, A. Sapin-Minet, P. Maincent, P. Leroy, R. Schneider, Role of gold nanoparticles capping density on stability and surface reactivity to design drug delivery platforms, ACS Appl. Mater. Interfaces 4 (11) (2012) 5790–5799, doi:10.1021/am3012752.
[21] S. Vijayakumar, S. Ganesan, Biocompatibility and toxicity of nanobiomaterials, J. Nanomater. (2012) 734398, doi:10.1155/2012/734398.
[22] K. Wagers, T. Chui, S. Adem, Effect of pH on the stability of gold nanoparticles and their application for melamine detection in infant formula, J. Appl. Chem. 7 (8) (2014) 15–20, doi:10.9790/5736-07821520.
[23] A. Wang, H.P. Ng, Y. Xu, Y. Li, Y. Zheng, J. Yu, F. Han, F. Peng, L. Fu, Chemical functionalization, self-assembly, and applications of nanomaterials and nanocomposites, J. Nanomater. (2014) 451232, doi:10.1155/2014/451232.
[24] J. Turkevich, P.C. Stevenson, J. Hillier, A study of the nucleation and growth processes in the synthesis of colloidal gold, Discuss. Faraday Soc. 11 (1951) 55–75, doi:10.1039/df9511100055.
[25] G. Frens, Particle size and sol stability in metal colloids, Colloid Polym. Sci. 250 (7) (1972) 736–741, doi:10.1007/BF01498565.
[26] J. Polte, T.T. Ahner, F. Delissen, S. Sokolov, Mechanism of gold nanoparticle formation in the classical citrate synthesis method derived from coupled in situ XANES and SAXS evaluation, J. Am. Chem. Soc. 132 (4) (2010) 1296–1301, doi:10.1021/ja906506j.
[27] W. Leng, P. Pati, P.J. Vikesland, Room temperature seed mediated growth of gold nanoparticles: mechanistic investigations and life cycle assesment, Environ. Sci. 2 (2015) 440–453, doi:10.1039/C5EN00026B.
[28] W. Su-Feng, H. Da-Wei, W. Yong-Sheng, H. Yin, D. Jia-Hua, F. Ming, W. Wen-Shuo, Silica-covered Au nanoresonators for fluorescence modulating of a graphene quantum dot, Chin. Phys. B 23 (9) (2014) 097803, doi:10.1088/1674-1056/23/9/097803.
[29] Chpt. 1 R.K. Iler American Chemical Society, Washington, 1994, pp. 1–47. Chpt. 1, doi:10.1021/ba-1994-0234.
[30] C.J. Brinker, G.W. Scherer, in: Sol-Gel Science: The Physics and Chemistry of Sol–Gel Processing, Academic Press, Boston, 1990, pp. 96–223, doi:10.1016/B978-0-08-057103-4.50008-8. Chpt. 3.
[31] A. Zdaniauskiene, T. Charkova, I. Matulaitiene, O. Eicher-Lorka, A. Matijoska, M. Skapas, A. Selskis, G. Niaura, Electrochemical shell-isolated nanoparticle-enhanced Raman spectroscopy: bonding, structure, and ion-pairing of the positive charge bearing pyridinium ring terminated monolayer at smooth gold electrode, J. Phys. Chem. C 122 (2) (2018) 1234–1242, doi:10.1021/acs.jpcc.7b09970.
[32] S. Li, D. Wu, X. Xu, R. Gu, Theoretical and experimental studies on the adsorption behavior of thiophenol on gold nanoparticles, J. Raman Spectrosc. 38 (2007) 1436–1443, doi:10.1002/jrs.1791.
[33] Y. Lu, Y. Yin, Z.-Y. Li, Y. Xia, Synthesis and self-assembly of Au@SiO_2 core–shell colloids, Nano Lett. 2 (7) (2002) 785–788, doi:10.1021/nl025598i.
[34] N.M. Bahadur, S. Watanabe, T. Furusawa, M. Sato, F. Kurayama, I.A. Siddiquey, Y. Kobayashi, N. Suzuki, Rapid one-step synthesis, characterization and functionalization of silica coated gold nanoparticles, Colloids Surf. A 392 (2011) 137–144, doi:10.1016/j.colsurfa.2011.09.046.
[35] D. Gontero, A.V. Veglia, A.G. Bracamonte, D. Boudreau, Synthesis of ultraluminescent gold core–shell nanoparticles as nanoimaging platforms for biosensing applications based on metal-enhanced fluorescence, RSC Adv. 7 (2017) 10252–10258, doi:10.1039/C6RA27649K.
[36] A. López-Millán, P. Zavala-Rivera, R. Esquivel, R. Carrillo, E. Alvarez-Ramos, R. Moreno-Corral, R. Guzmán-Zamudio, A. Lucero-Acuña, Aqueous-organic phase transfer of gold and silver nanoparticles using thiol-modified oleic acid, Appl. Sci. 7 (2017) 273, doi:10.3390/app7030273.
[37] J. Yang, J.Y. Lee, J.Y. Ying, Phase transfer and its applications in nanotechnology, Chem. Soc. Rev. 40 (2011) 1672–1696, doi:10.1039/B916790K.

NJC

ROYAL SOCIETY OF CHEMISTRY

PAPER

Cite this: *New J. Chem.*, 2021, **45**, 10952

A facile microwave-assisted synthesis of Ag@SiO_2 nanoparticles for Raman spectroscopy†

Edita Daublytė,[a] Agnė Zdaniauskienė,[a] Martynas Talaikis,[b] Audrius Drabavičius[c] and Tatjana Charkova *[a]

Received 23rd March 2021,
Accepted 14th May 2021

DOI: 10.1039/d1nj01439k

rsc.li/njc

In the SERS community, new and simple ways of producing large diameter (above 50 nm) noble metal nanoparticles are highly welcomed because they shift the localized surface plasmon resonance to higher wavelengths where spectroscopic measurements are typically taken. In this work, we present a facile microwave-assisted synthesis of above average diameter silver-core silica-shell nanoparticles (Ag@SiO_2) using a chemical reduction method. Ag@SiO_2 were synthesized in two steps of the core synthesis and the shell capping procedure by stepped temperature ramping. UV/vis spectroscopy and HR-TEM imaging showed that core–shell nanoparticles are spherical with an average diameter of 90 nm ± 10 nm and are covered with a 2.5–3 nm thick silica shell. Particles were tested using Raman measurements of a 4-mercaptobenzoic acid monolayer. The proposed synthesis approach produces stable core–shell nanoparticles that can be stored at 8–10 °C in the dark for two months with only minimal indication of decay.

Introduction

The use of silver nanoparticles (Ag NPs) has become widespread in the fields of medicine, biotechnology, catalysis, and industrial applications.[1–3] Such popularity comes from the exceptional optical properties of silver that especially suit surface-enhanced Raman spectroscopy (SERS) allowing the probing of not only in the visible but also in the infrared portion of the spectrum.[4–6] However, the antimicrobial properties of Ag NPs limit their use when working with living organisms.[7–10] This limitation is overcome by covering nanoparticles with a protective semiconductor layer (SiO_2, MnO_2, TiO_2, *etc.*) that not only prevents undesirable interactions between analyte and metal cores but also suppresses exposure of the cores to the environment, resolving the issues with their toxicity and stability. Overall, the plasmonic–dielectric core–shell architecture is thought to be chemically inert and well suited for SERS. Since the first publication in 2010, these composite nanoparticles of various shapes and coatings have emerged as a new and valuable addition to the SERS technique and has been titled shell-isolated nanoparticle-enhanced Raman spectroscopy (SHINERS).[11,12]

The chemical reduction of silver cations is considered to be a classic way for producing Ag NPs, among many other chemical, physical, and biological methods. Generally, the reduction reaction is carried out in citrate, borohydride, hydrazine, ethylene glycol, or other reducer solutions.[2,10] The size and shape of nanoparticles can be controlled by selecting stabilizing agents (ammonium derivatives, polyols, *etc.*). Moreover, the synthesis rate and the type of final nanoparticle critically depend on the precursor, reducing and capping agents, solvent, and reaction temperature.[11,13,14] Although the synthesis approach that was used in the first SHINERS publication has been vastly adapted by other authors to produce different types of shell-isolated nanoparticles,[15] the majority of these methods, to this day, are still highly time-consuming and need plenty of stabilizers, extreme care and consistency, and purification steps in the postproduction using different solvents.

Microwave irradiation is an attractive, rapid, and energy-saving technique compared to the other particle production methods (laser ablation, electrochemical, photochemical methods, *etc.*). It does not require expensive equipment and yields nanostructures with a narrower size distribution and higher stability in a shorter reaction time.[16,17] In the present work, we demonstrated a facile, cost- and energy-efficient microwave-assisted preparation for silicon-coated silver nanoparticles, by using only simple precursors, a reducer and water. We were

[a] *Department of Organic Chemistry, Center for Physical Sciences and Technology, Saulėtekio Ave. 3, LT-10257 Vilnius, Lithuania. E-mail: tatjana.charkova@ftmc.lt*
[b] *Department of Bioelectrochemistry and Biospectroscopy, Institute of Biochemistry, Life Sciences Center, Vilnius University, Saulėtekio Ave. 7, LT-10257 Vilnius, Lithuania*
[c] *Department of Characterization of Materials Structure, Center for Physical Sciences and Technology, Saulėtekio Ave. 3, LT-10257 Vilnius, Lithuania*

† Electronic supplementary information (ESI) available. See DOI: 10.1039/d1nj01439k

able to avoid additional stabilizers and solvents that would complicate further spectral analysis. Seeking the highest SHINERS performance, we aimed at synthesizing Ag NPs with a diameter close to 100 nm, because such nanoparticles have been shown to have the highest scattering cross-section.[18,19] To the best of our knowledge, it is the first attempt to produce SERS-optimal size silver–silica core–shell nanoparticles with the aid of microwave synthesis and without an additional stabilization step which is typically used in order to increase the diameter. To meet SHINERS requirements, such particles must be larger than 50 nm in diameter and covered with a thin dielectric shell for the optimal surface-enhancement and reduced interaction of the analyte with the plasmonic-metal cores.[11,20] In this study, we show a successful microwave-assisted synthesis method for large (90 nm in diameter with a ~3 nm silica shell) and stable Ag@SiO_2 nanospheres using a simple reduction method. The functionality of the nanoparticles was subsequently tested using 4-mercaptobenzoic acid (4-MBA).

Experimental section

Materials

Silver nitrate ($AgNO_3$, 99%), trisodium citrate dihydrate (Na_3Cit, $HOC(COONa)(CH_2COONa)_2{\cdot}2H_2O$, 99%), (3-aminopropyl)triethoxysilane (APTES, $H_2N(CH_2)_3Si(OC_2H_5)_3$, 99%) and sodium silicate solution (10% NaOH, 27% SiO_2) were purchased from Merck and used without any further purification. Deionized Milli-Q water of 18.2 MΩ cm resistivity was used in all procedures. A highly polished stainless steel substrate (Tienta SpectRIM, Merck) was used to collect the Raman spectrum of the nanoparticles. 4-Mercaptobenzoic acid (4-MBA, 99%) was purchased from Merck.

General methods and equipment

The silver nanoparticles were synthesized using a microwave synthesizer Discover SP (CEM Corporation), equipped with the infrared temperature control system, built-in magnetic stirring, and cooling systems. The microwave reactor has a maximum power of 300 W. The plasmonic properties of the Ag NPs and Ag@SiO_2 were evaluated by UV/vis spectroscopy using a Lambda 25 spectrophotometer in the range of 200–1100 nm. To obtain high-resolution transmission electron microscopy (HR-TEM) images, a Tecnai F20 X-TWIN (FEI) microscope with an accelerating voltage of 200 kV equipped with an EDX (EDAX) spectrometer, and a Gatan Orius CCD camera was employed. The analysis was carried out using a bright-field regime. Raman and SHINERS spectral data were collected using an Echelle type spectrometer RamanFlex 400 (PerkinElmer, Inc.) equipped with a 785 nm edge diode laser, thermoelectrically cooled (−50 °C) CCD camera, and fiber-optic cable. A 180° scattering geometry and 30 mW laser power were used. Each spectrum was recorded by accumulating 10 scans with an integration time of 10 s (total accumulation time 100 s).

Synthesis of Ag nanoparticles

10 mL (10 mM) of an aqueous $AgNO_3$ (prepared by dissolving 0.09 g of the salt in 50 mL H_2O) was added to 10 mL (10 mM) of trisodium citrate (prepared by dissolving 0.147 g of the salt in 50 mL H_2O) solution at 20 °C. The reaction mixture was stirred for 2 min at room temperature. Then it was transferred to the microwave reactor and subjected to the ramped three-step irradiation procedure. First, the temperature was ramped to 35 °C in 1 min and kept for 2 min (at the power of 50 W); second, it was heated to 65 °C in 1 min and held for 2 min (100 W); third, it was heated to 95 °C in 1 min followed by holding for 5 min (100 W). After the synthesis, the mixture was cooled to 50 °C in 3 min and left without stirring for 30 min at room temperature. The microwave heating procedure is depicted in Fig. 1. The result was a greenish-yellow suspension of Ag NPs.

Synthesis of Ag@SiO_2 nanoparticles

15 mL of Ag NPs suspension was mixed with 0.2 mL (1 mM) of APTES (prepared by dissolving 9.2 μL of the reagent in 40 mL H_2O) and stirred for 10 min at room temperature. Then 1.6 mL (0.54%) of silicate solution (prepared by dissolving 208.6 μL of the reagent in 50 mL H_2O) was added and stirred for another 2 min. Next, the mixture was heated under microwave irradiation (at the power of 100 W) to 60 °C in 1 min with a holding time of 0.5 min; and finally, it was heated to 95 °C in 1 min, followed by holding for 5 min. The microwave reactor cooled the mixture to 50 °C in 3 min. Then, it was left without stirring for 30 min at room temperature. The microwave heating procedure is depicted in Fig. 2. The core–shell nanoparticles were cleaned

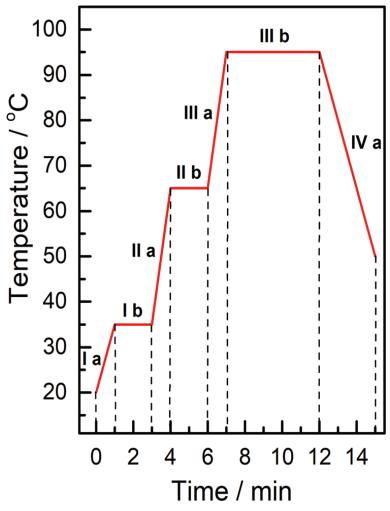

Fig. 1 Temperature evolution in Ag NPs three-stage heating microwave synthesis. Ia, IIa, and IIIa regions correspond to a stepped temperature increase up to 35 °C, 65 °C, and 95 °C, while Ib, IIb, and IIIb regions indicate maintained temperature by applying a 50–100 W microwave power. The IVa region corresponds to a temperature decrease to 50 °C.

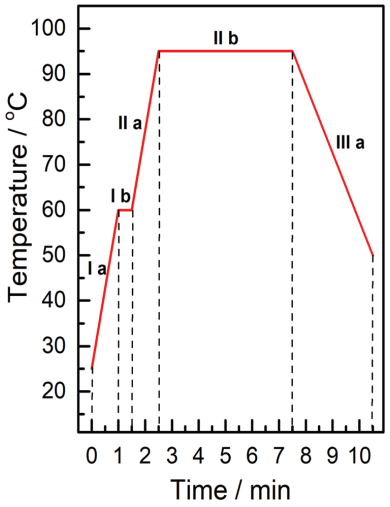

Fig. 2 Temperature evolution in the silica shell formation. The Ia and IIa regions correspond to stepped temperature increases up to 60 °C and 95 °C, while the Ib and IIb regions indicate maintained temperature by applying 100 W microwave power. The IIIa region corresponds to a temperature decrease to 50 °C.

with water by centrifugation twice (20 min at 3500 rpm), resulting in a greenish-yellow concentrated suspension of $Ag@SiO_2$, that was collected and stored at 8–10 °C in the dark.

Self-assembled monolayer formation

An Au film was deposited on a cleaned glass substrate by magnetron sputtering using a Quorum 150T sputter and a 99.99% Au target. After the sputtering, the gold slide was rinsed with ethyl alcohol and transferred to 4-MBA (5×10^{-3} M) alcohol solution, and kept for 1 hour to form a self-assembled monolayer. The slide then was removed from the solution, rinsed with the alcohol, and dried.

Raman and SHINERS measurements

To collect the Raman spectrum of pure nanoparticles, 1 μL of $Ag@SiO_2$ suspension was diluted four times with water and dried on a Tienta steel substrate at room temperature. To register the nanoparticle enhanced SHINERS spectrum, the $Ag@SiO_2$ solution was spread on the smooth gold thin-film adsorbed with the 4-MBA self-assembled monolayer. The nanoparticle solution was dried before measurement.

Results and discussion

Previous studies have shown successful silver nanoparticle synthesis under microwave irradiation using various reducing and capping agents, such as formaldehyde,[21] polyvinylpyrrolidone,[22] ethanol,[23] glycerol,[24] ethylene glycol,[25] and biological extracts, enzymes, bacteria, *etc.*[26] Typically, capping agents are used to stabilize and produce larger or shaped nanoparticles. Bahadur *et al.* reported the microwave synthesis

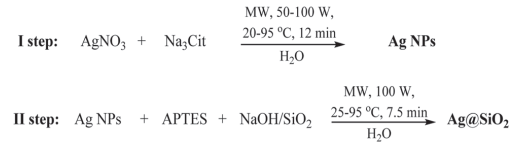

Scheme 1 Synthesis route of $Ag@SiO_2$ nanoparticles.

of small 17 nm $Au@SiO_2$ with a 2–5 nm SiO_2 shell.[27] Karimipour *et al.* presented large 50–200 nm $Ag@SiO_2$ particles with 20–30 nm silica shells produced under microwave irradiation using oleylamine as a capping agent.[28] We show a method of preparing 90 nm $Ag@SiO_2$ nanospheres using the microwave reactor without additional stabilization. The advantages of these nanoparticles for the SHINERS experiment are the optimal size and chemically inert thin ~3 nm silica coating.

The general two-step synthesis procedure under microwave irradiation depicted in Scheme 1 requires only the simplest precursor ($AgNO_3$), reducer (Na_3Cit), and solvent (H_2O). To create nanoparticles in the proposed way, the use of an additional stabilizer to increase the diameter of nanoparticles is not required as it is done in a more conventional approach. According to the Faxian *et al.* procedure, we chose the optimal 1 : 1 molar ratio of silver nitrate and trisodium citrate.[29] Citrate concentration has a strong impact on the nanoparticle size and the mechanism by which they grow. While low concentrations produce small defined-size Ag nanoparticles, at concentrations above 1.5 mM nanoparticles they tend to grow by clustering due to the highly destabilizing ionic strength of the solution.[30] Here we have also used a rather complex heating profile that was based on the empirical observations. From the tested one-, two-, and three-stage temperature increasing methods (Fig. S1, S2, ESI† and Fig. 1 respectively) the three-stage procedure resulted in the largest particles according to UV/vis data (Fig. S3, ESI†). Their absorption maximum was found at 457 nm compared to 426 nm and 428 for the one- and two-stage procedures. Such a shift is attributed to the time the reaction solution had been subjected to low and medium-high temperatures. For example, in the temperature-dependent synthesis of the spherical silver nanoparticles, the 32 °C temperature (out of the 15–55 °C range) was found to produce the largest size particles with an average diameter of 48 nm.[31] This observation was rationalized by the fusion processes of preformed particles in their early growth phase.

To emphasize the importance of the 35 °C temperature step regime, which is denoted as 'Ib' in Fig. 1, we compare three- and two-stage synthesis methods (Fig. S2, ESI†). Adding the heating step at 35 °C results in larger diameter particles, which have their plasmonic resonance rather strongly redshifted by 29 nm. Despite this shift, the optimal duration for heating at 35 °C is yet to be examined, and this might be a valuable instrumental control for particle size and distribution. On the other hand, we can conclude that the second 65 °C heating stage in a three-stage regime (IIb in Fig. 1) has a limited effect on the nanoparticle size. Comparing the absorption of nanoparticles produced in one- and two-stage regimes (Fig. S3, ESI†),

the introduction of an additional 60 °C step redshifts the absorption by 2 nm, increases the band intensity, and only slightly increases the absorption bandwidth from 212 nm to 220 nm.

Temperature ramping is another important aspect while considering a trade-off between particle size and their size distribution. For the gold nanoparticle synthesis in citrate, a positive correlation was found between slower ramping speeds (°C min^{-1}) and the larger nanoparticles with a higher size distribution.[32] Faster ramping produces a multitude of small primary nanoparticles with high uniformity. Seol found that for given conditions, the inflection ramping rate from which any additional increase in the rate does not affect particle size and the distribution is *ca.* 42 °C min^{-1}.[32] Motivated by that, we chose fairly slow ramping speeds of 15 °C min^{-1} and 30 °C min^{-1} in the three-stage synthesis in order to obtain larger particles, however, at the expense of an increased size distribution.

To coat nanoparticles with silica shells using the microwave synthesis method, Tian's protocol from ref. 33 was adapted by selecting (3-aminopropyl)triethoxysilane (APTES) and sodium silicate. The intermediate separation of Ag NPs from the suspension was not carried out. We chose the APTES reagent instead of the more typical (3-aminopropyl)trimethoxysilane (APTMS) because ethanol is a by-product of the APTES hydrolysis (Scheme 2). Ethanol has a low effect on nanoparticle stability in their synthesis. For example, Pal *et al.* have successfully used ethanol in the microwave synthesis of Ag NPs.[23] Moreover, other authors often use this solvent in nanoparticle purification procedures.[34–37] On the contrary, the hydrolysis of APTMS releases methanol, which may affect the formation of silica shells in the next step of the synthesis.[38] Therefore, APTES was used as the metal surface modifier as a safer alternative to cap silver cores with silica. The amine groups of the reagent bind to the metal core while the hydroxy groups bind to sodium silicate. Further hydrolysis of the intermediate products results in silica shells containing SiOSi and SiOH groups.[38]

The silica shell was formed using the two-stage microwave synthesis method, for which an optimal condition was found experimentally (Fig. 2). The optimal shell thickness is in a range between 2 nm and 4 nm, because such shells must be chemically inert, have a minimum amount of pinholes, and also be thin enough not to quench the electromagnetic field.[20,33] Nanoparticles with shell layers of 10 nm and beyond, although pinhole-free, lose their enhancement capabilities. The heating time has a direct correlation with shell thickness. For example, increasing the heating time in a non-microwave shell preparation method from 20 min to 80 min increased shell thickness from 1.3 nm to 10 nm.[39] The other factors that contribute to shell thickness are reagents and their concentration, and synthesis time. Here we show an approach that produces particles coated with a 2.5–3 nm layer of SiO_2.

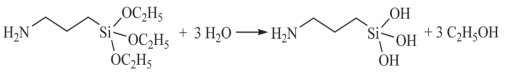

Scheme 2 Hydrolysis reaction of APTES.

After the shell capping procedure, the excess of non-reacted agents and by-products was removed by centrifugation and washing with water. All reagents eluted because they dissolve, hydrolyze or mix with water. The growth of nanoparticles was followed by using UV/vis spectroscopy. The absorption peak shifts from 457 nm to 460 nm when the silica shell for Ag NPs is formed (Fig. 3A). According to HR-TEM images, synthesis resulted in spherical Ag@SiO_2 nanoparticles that are about 90 nm in diameter and covered with 2.5–3 nm of silica shells (Fig. 3B–D). Qualitative analysis indicates the diameter of 90 nm ± 10 nm (Fig. 3E).

From the UV/vis data, the concentrated aqueous suspension of Ag@SiO_2 nanoparticles is stable after being stored for 2 months in the dark at 8–10 °C (Fig. 3A(c)). Over three months, the color of the suspension changes from greenish-yellow to grey, indicating that particles have lost their stability and underwent aggregation. This was corroborated by UV/vis spectrometry data (Fig. 3A(d)), which indicated that particles are completely aggregated. It is known that the defects in thin shell areas lead to accelerated aggregation and instability of nanoparticles.[38] However, given the considerable shelf-life with little to no changes in the UV/vis and SHINERS spectra, the amount of pinholes and defects in nanoparticle shells is considered to be small.

There is a trade-off between the particle electromagnetic enhancement factor (EF) and their isolating properties, with EF being appreciably cut down for shell-isolated particles compared to simple core nanoparticles. The minimal thickness required for a pinhole-free SiO_2 shell was previously reported to lie in the range of 2–4 nm, but again, such a layer thickness has a negative effect on EF.[20] On the other hand, the factor that might positively contribute to EF is the plasmonic coupling between the nanoparticle core and smooth plasmonic surface. Smooth plasmonic Au and Ag surfaces are typically used in the construction of organic self-assembled monolayers using thiol chemistry. However, such coupling mildly contributes to the total EF. For example, sphere-shaped Au nanoparticles directly placed on a Pt surface have higher EF by one order of magnitude compared to the ones placed on the Si surface.[40] Moreover, such a contribution to EF is highly dependent on the separation distance between the nanoparticle and surface. Therefore, a small-scale addition to the total EF allows the effect to be omitted from the further consideration of particle performance.

To test the enhancement capability of Ag@SiO_2, we collected the SHINERS spectrum from the smooth gold substrate-adsorbed 4-MBA monolayer (Fig. 4d). The enhanced Raman spectrum of pure Ag@SiO_2 nanoparticles was recorded to ensure that nanoparticles are free from unreacted reagents that would interfere with the SHINERS spectrum. Despite that, nanoparticles have an intrinsic Raman band that might be associated with vibrations from the particle shell. However, these bands are broad and of low intensity, as can be seen from

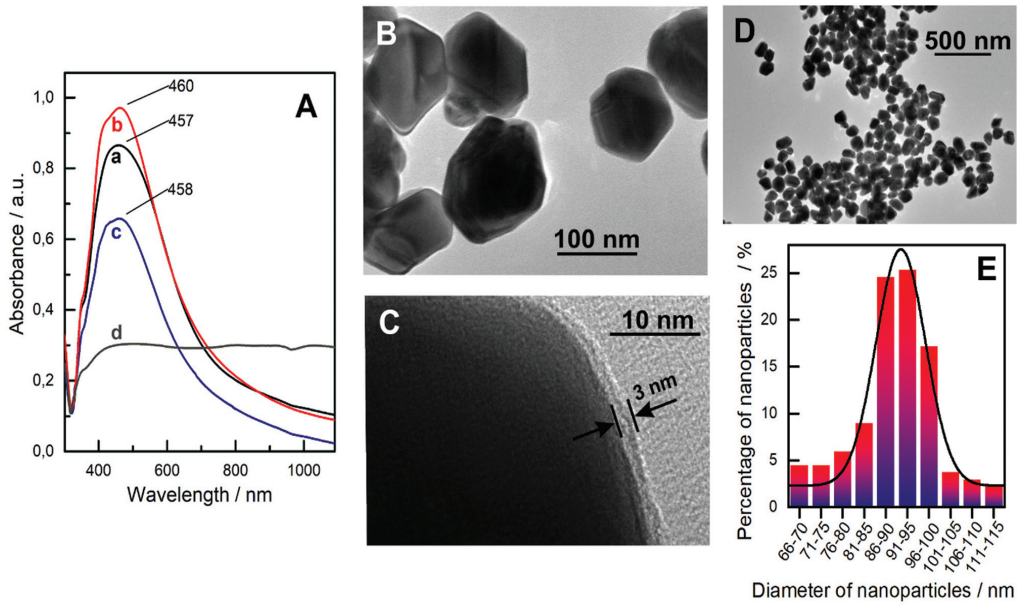

Fig. 3 (A) UV/vis spectra of Ag NPs (a), fresh Ag@SiO_2 (b), the Ag@SiO_2 after 2 months (c), and aggregated Ag@SiO_2 after 3 months (d) in the range of 300–1100 nm. (B–D) HR-TEM image of Ag@SiO_2 with the emphasis on silica shells in (C). Distribution histogram of particle size acquired from HR-TEM images (E).

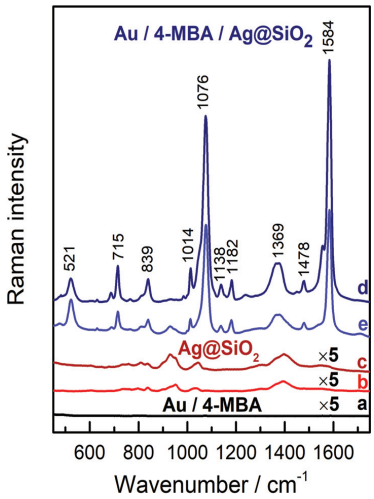

Fig. 4 Raman spectrum of 4-MBA adsorbed on a smooth Au surface without nanoparticles (a), Raman spectra of Ag@SiO_2 placed onto a Tienta steel substrate on the synthesis day (b) and after 2 months (c), and SHINERS spectra of 4-MBA with Ag@SiO_2 on the synthesis day (d) and after 2 months (e). The bottom spectra (a)–(c) were multiplied by 5 to increase visibility.

Fig. 4, where fresh and aged Ag@SiO_2 spectra are multiplied by 5 to increase the clarity. Specifically, these bands do not overlap with 4-MBA's vibrational modes. The SHINERS spectrum of the Au-adsorbed monolayer (Fig. 4d) shows the typical vibrational modes of 4-MBA. The assignments are based on previously reported data from ref. 41–43 and are presented in Table 1. Dominant vibrational modes at 1076 cm^{-1} and 1584 cm^{-1} are assigned to the aromatic ring breathing, coupled C–S stretching and C–C stretching mode of the ring respectively. The ring out-of-plane bending and breathing modes are recognized at 521 cm^{-1} and 1014 cm^{-1}. The carboxyl group (COO^- symmetric stretching) vibration is assigned to 1369 cm^{-1}. Two peaks at 1138 cm^{-1} and 1182 cm^{-1} are identified as C–H bending vibrational modes.

To test Ag@SiO_2 stability, SHINERS measurement of the 4-MBA monolayer was completed with the aged nanoparticles that were held at 8–10 °C in the dark for two months. A close

Table 1 Assignment of gold surface adsorbed 4-MBA spectral modes

Assignment	$\Delta\nu$, cm^{-1}
Ring oop bending	521
δ_{oop}(CCC)	715
δ(COO^-)	839
Ring breathing	1014
Ring breathing, ν(C–S), $\delta_{sym,ip}$(C–H)	1076
δ(C–H)	1138
δ(C–H)	1182
ν(COO^-)	1369
Ring bending	1478
Ring ν(C–C), $\delta_{as,ip}$(C–H)	1584

Abbreviations: oop, out-of-plane; ip, in-plane; sym, symmetric; as, asymmetric; δ, bending; ν, stretching.

inspection of the spectra collected using fresh and aged nanoparticles shows minor differences (Fig. 4d and e). These differences may be related to the structural and orientation irregularities of the two individually prepared 4-MBA monolayers, and the higher spectral contribution from impurities coming from the aged nanoparticles. Spectral bands assigned to the impurities appear as a broad feature in the range of 850–1000 cm^{-1} in the monolayer spectrum, however, of low-intensity. Despite that, the differences are rather minimal, and the resulting 4-MBA spectrum matches well with the one recorded with fresh nanoparticles, allowing us to conclude that the nanoparticles are durable and retain their surface-enhanced properties for several months.

Conclusion

A two-step microwave-assisted synthesis of SERS-optimal size $Ag@SiO_2$ nanoparticles is reported. Silver salt was reduced with sodium citrate to produce core nanoparticles, which were subsequently coated with silicon shells by using APTES and sodium silicate. Based on our previous results on $Au@SiO_2$ nanoparticles, we selected APTES for silanization instead of the more commonly used APTMS, because the APTES by-product ethanol has a less disruptive effect on the shell's integrity compared to the APTMS by-product methanol.[38] The resulting $Ag@SiO_2$ nanospheres are of an SERS-optimal diameter of 90 nm $\pm$ 10 nm and have a thin 2.5–3 nm insulating shell. These nanoparticles were of good stability after being stored at 8–10 °C in the dark for two months and showed only minor differences in the SHINERS spectrum of the 4-MBA monolayer compared to the one collected using fresh nanoparticles.

Author contributions

Edita Daublytė – investigation, validation, methodology, formal analysis; Agnė Zdaniauskienė – formal analysis, data curation, visualization; Martynas Talaikis – visualization, writing; Audrius Drabavičius – formal analysis; Tatjana Charkova – conceptualization, methodology, writing, supervision, project administration.

Conflicts of interest

All authors have no conflict of interest to declare.

Acknowledgements

The authors thank Algirdas Selskis from the Department of Characterisation of Materials Structure of Center for Physical Sciences and Technology for the preparation of Au films.

References

1 K. K. Harish, V. Nagasamy, B. Himangshu and K. Anuttam, *Biomed. J. Sci. Tech. Res.*, 2018, **4**, 3765–3775.
2 H. D. Beyene, A. A. Werkneh, H. K. Bezabh and T. G. Ambaye, *Sustainable Mater. Technol.*, 2017, **13**, 18–23.
3 A. Haider and I. K. Kang, *Adv. Mater. Sci. Eng.*, 2015, **2015**, 165257.
4 B. Sharma, R. R. Frontiera, A.-I. Henry, E. Ringe and R. P. Van Duyne, *Mater. Today*, 2012, **15**, 16–25.
5 R. Pilot, R. Signorini, C. Durante, L. Orian, M. Bhamidipati and L. Fabris, *Biosensors*, 2019, **9**, 1–99.
6 T. B. V. Neves, S. M. Landi, L. A. Sena, B. S. Archanjo and G. F. S. Andrade, *RSC Adv.*, 2015, **5**, 59373–59378.
7 A. C. Burdușel, O. Gherasim, A. M. Grumezescu, L. Mogoantă, A. Ficai and E. Andronescu, *Nanomaterials*, 2018, **8**, 1–25.
8 M. Murphy, K. Ting, X. Zhang, C. Soo and Z. Zheng, *J. Nanomater.*, 2015, **2015**, 696918.
9 J. Talapko, T. Matijević, M. Juzbašić, A. Antolović-Požgain and I. Škrlec, *Microorganisms*, 2020, **8**, 1–13.
10 A. Salleh, R. Naomi, N. D. Utami, A. W. Mohammad, E. Mahmoudi, N. Mustafa and M. B. Fauzi, *Nanomaterials*, 2020, **10**, 1–20.
11 J. F. Li, Y. J. Zhang, S. Y. Ding, R. Panneerselvam and Z. Q. Tian, *Chem. Rev.*, 2017, **117**, 5002–5069.
12 J. Krajczewski and A. Kudelski, *Front. Chem.*, 2019, **7**, 1–6.
13 N. L. Pacioni, C. D. Borsarelli, V. Rey and A. V. Veglia, *Silver nanoparticle applications in the fabrication and design of medical and biosensing devices*, Springer International Publishing, 2015, pp. 13–46.
14 B. Khodashenas and H. R. Ghorbani, *Arabian J. Chem.*, 2019, **12**, 1823–1838.
15 J. F. Li, Y. F. Huang, Y. Ding, Z. L. Yang, S. B. Li, X. S. Zhou, F. R. Fan, W. Zhang, Z. Y. Zhou, D. Y. Wu, B. Ren, Z. L. Wang and Z. Q. Tian, *Nature*, 2010, **464**, 392–395.
16 M. Tsuji, M. Hashimoto, Y. Nishizawa, M. Kubokawa and T. Tsuji, *Chem. – Eur. J.*, 2005, **11**, 440–452.
17 Y. J. Zhu and F. Chen, *Chem. Rev.*, 2014, **114**, 6462–6555.
18 G. Kumari, J. Kandula and C. Narayana, *J. Phys. Chem. C*, 2015, **119**, 20057–20064.
19 H. Guo, Z. Zhang, B. Xing, A. Mukherjee, C. Musante, J. C. White and L. He, *Environ. Sci. Technol.*, 2015, **49**, 4317–4324.
20 X. D. Tian, B. J. Liu, J. F. Li, Z. L. Yang, B. Ren and Z. Q. Tian, *J. Raman Spectrosc.*, 2013, **44**, 994–998.
21 H. Yin, T. Yamamoto, Y. Wada and S. Yanagida, *Mater. Chem. Phys.*, 2004, **83**, 66–70.
22 H. Jiang, K. S. Moon, Z. Zhang, S. Pothukuchi and C. P. Wong, *J. Nanopart. Res.*, 2006, **8**, 117–124.
23 A. Pal, S. Shah and S. Devi, *Mater. Chem. Phys.*, 2009, **114**, 530–532.
24 A. Nirmala Grace and K. Pandian, *Mater. Chem. Phys.*, 2007, **104**, 191–198.
25 M. Nishioka, M. Miyakawa, H. Kataoka, H. Koda, K. Sato and T. M. Suzuki, *Nanoscale*, 2011, **3**, 2621–2626.
26 D. Hebbalalu, J. Lalley, M. N. Nadagouda and R. S. Varma, *ACS Sustainable Chem. Eng.*, 2013, **1**, 703–712.
27 N. M. Bahadur, S. Watanabe, T. Furusawa, M. Sato, F. Kurayama, I. A. Siddiquey, Y. Kobayashi and N. Suzuki, *Colloids Surf., A*, 2011, **392**, 137–144.

28 M. Karimipour, E. Shabani, M. Mollaei and M. Molaei, *J. Nanopart. Res.*, 2015, **17**, 1–8.
29 L. Faxian, L. Jie and C. Xueling, *Rare Met. Mater. Eng.*, 2017, **46**, 2395–2398.
30 A. Henglein and M. Giersig, *J. Phys. Chem. B*, 1999, **103**, 9533–9539.
31 X. C. Jiang, W. M. Chen, C. Y. Chen, S. X. Xiong and A. B. Yu, *Nanoscale Res. Lett.*, 2011, **6**, 1–9.
32 S. K. Seol, D. Kim, S. Jung and Y. Hwu, *Mater. Chem. Phys.*, 2011, **131**, 331–335.
33 J. F. Li, X. D. Tian, S. B. Li, J. R. Anema, Z. L. Yang, Y. Ding, Y. F. Wu, Y. M. Zeng, Q. Z. Chen, B. Ren, Z. L. Wang and Z. Q. Tian, *Nat. Protoc.*, 2013, **8**, 52–65.
34 C. Xionghui and Z. Aixia, *Rare Met.*, 2010, **29**, 407–412.
35 H. B. Abdulrahman, J. Krajczewski and A. Kudelski, *Appl. Surf. Sci.*, 2018, **427**, 334–339.
36 S. C. Purdy and A. J. Muscat, *J. Nanopart. Res.*, 2016, **18**, 1–10.
37 Y. Wu, P. Liang, Q. Dong, Y. Bai, Z. Yu, J. Huang, Y. Zhong, Y.-C. Dai, D. Ni, H. B. Shu and C. U. Pittman, *Food Chem.*, 2017, **237**, 974–980.
38 T. Charkova, A. Zdaniauskienė and I. Ignatjev, *Chem. Data Collect.*, 2020, **29**, 1–9.
39 A. Zdaniauskiene, T. Charkova, I. Matulaitiene, O. Eicher-Lorka, A. Matijoška, M. Skapas, A. Selskis and G. Niaura, *J. Phys. Chem. C*, 2018, **122**, 1234–1242.
40 S.-Y. Ding, J. Yi, J.-F. Li, B. Ren, D.-Y. Wu, R. Panneerselvam and Z.-Q. Tian, *Nat. Rev. Mater.*, 2016, 16021.
41 C. H. Ho and S. Lee, *Colloids Surf., A*, 2015, **474**, 29–35.
42 W. Q. Ma, Y. Fang, G. L. Hao and W. G. Wang, *Chin. J. Chem. Phys.*, 2010, **23**, 659–663.
43 H. Huh, H. D. Trinh, D. Lee and S. Yoon, *ACS Appl. Mater. Interfaces*, 2019, **11**, 24715–24724.

Electronic Supplementary Material (ESI) for New Journal of Chemistry.

Supporting Information

Facile microwave-assisted synthesis of Ag@SiO_2 nanoparticles for Raman spectroscopy

Edita Daublytė[1], Agnė Zdaniauskienė[1], Martynas Talaikis[2], Audrius Drabavičius[3], Tatjana Charkova[1*]

[1]Department of Organic Chemistry, Center for Physical Sciences and Technology, Saulėtekio Ave. 3, LT-10257 Vilnius, Lithuania

[2]Department of Bioelectrochemistry and Biospectroscopy, Institute of Biochemistry, Life Sciences Center, Vilnius University, Saulėtekio Ave. 7, LT-10257 Vilnius, Lithuania

[3]Department of Characterization of Materials Structure, Center for Physical Sciences and Technology, Saulėtekio Ave. 3, LT-10257 Vilnius, Lithuania

*Corresponding author, email: tatjana.charkova@ftmc.lt, ORCID: 0000-0002-2043-9024

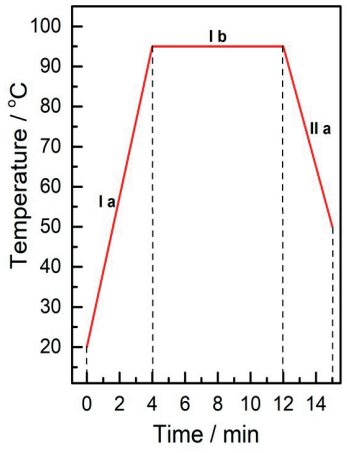

Fig. S1 Temperature evolution in Ag NPs one-stage microwave synthesis. I a region corresponds to stepped temperature increase up to 95 °C, while I b region indicates maintained temperature by applying 100 W microwave power. II a region corresponds to temperature decrease to 50 °C.

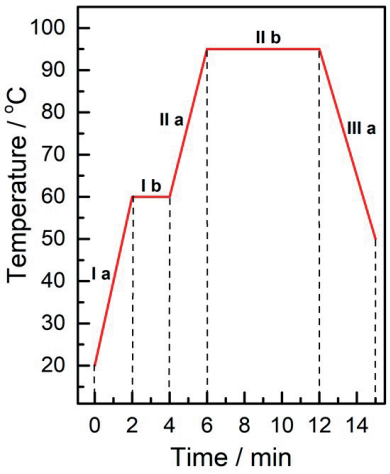

Fig. S2 Temperature evolution in Ag NPs two-stage microwave synthesis. I a, II a regions correspond to stepped temperature increase up to 60 °C and 95 °C, while I b, II b regions indicate maintained temperature by applying 100 W microwave power. III a region corresponds to temperature decrease to 50 °C.

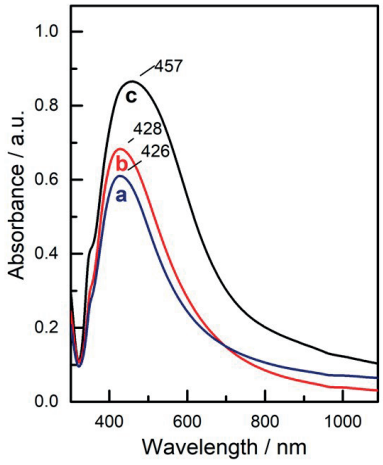

Fig. S3 UV/Vis spectra of Ag NPs synthesized by one-stage temperature regime (**a**), two-stage temperature regimes (**b**), and three-stage temperature regimes (**c**) in the range of 300–1100 nm.

molecules

MDPI

Article

Electrochemical Shell-Isolated Nanoparticle-Enhanced Raman Spectroscopy of Imidazole Ring Functionalized Monolayer on Smooth Gold Electrode

Agnė Zdaniauskienė [1], Martynas Talaikis [2,*], Tatjana Charkova [1], Rita Sadzevičienė [1], Linas Labanauskas [1] and Gediminas Niaura [1,2,*]

[1] Center for Physical Sciences and Technology (FTMC), Department of Organic Chemistry, Sauletekio Ave. 3, LT-10257 Vilnius, Lithuania
[2] Life Sciences Center, Institute of Biochemistry, Department of Bioelectrochemistry and Biospectroscopy, Vilnius University, Sauletekio Ave. 7, LT-10257 Vilnius, Lithuania
* Correspondence: martynas.talaikis@gmc.vu.lt (M.T.); gediminas.niaura@ftmc.lt (G.N.)

Abstract: The imidazole ring (Im) of histidine side chains plays a unique role in the function of proteins through covalent bonding with metal ions and hydrogen bonding interactions with adjusted biomolecules and water. At biological interfaces, these interactions are modified because of the presence of an electric field. Self-assembled monolayers (SAMs) with the functional Im group mimic the histidine side chain at electrified interfaces. In this study, we applied in-situ shell-isolated nanoparticle-enhanced Raman spectroscopy (SHINERS) to probe the structure and hydrogen bonding of Im-functionalized SAM on smooth Au at the electrochemical interface. The self-assembly of molecules on the Au induced the proton shift from N1 atom (Tautomer-I), which is the dominant form of Im in the bulk sample, to N3 atom (Tautomer-II). The impact of electrode potential on the hydrogen bonding interaction strength of the Im ring was identified by SHINERS. Temperature-Raman measurements and density functional theory (DFT) analysis revealed the spectral marker for Im ring packing (mode near 1496–1480 cm^{-1}) that allowed us to associate the confined and strongly hydrogen bonded interfacial Im groups with electrode polarization at −0.8 V. Reflection adsorption IR (RAIR) spectra of SAMs with and without Im revealed that the bulky ring prevented the formation of a strongly hydrogen bonded amide group network.

Keywords: $Ag@SiO_2$; core-shell nanoparticles; temperature-dependent Raman; hydrogen bonding interaction; histidine; SHINERS; RAIRS

Citation: Zdaniauskienė, A.; Talaikis, M.; Charkova, T.; Sadzevičienė, R.; Labanauskas, L.; Niaura, G. Electrochemical Shell-Isolated Nanoparticle-Enhanced Raman Spectroscopy of Imidazole Ring Functionalized Monolayer on Smooth Gold Electrode. *Molecules* **2022**, *27*, 6531. https://doi.org/10.3390/molecules27196531

Academic Editor: Wen-Bin Cai

Received: 22 August 2022
Accepted: 23 September 2022
Published: 3 October 2022

1. Introduction

Histidine plays a crucial role in the architecture and activity of enzymes, as it is often found to ligate transition metal ions at the active sites of metalloproteins [1,2]. Such a versatility comes from its side chain imidazole (Im) ring that can take part in many interactions, for example (i) cation-π_{Im}, (ii) π-π stacking, (iii) $hydrogen_{Im}$-π, (iv) coordination with metal cations through nitrogen lone electron pair, and (v) hydrogen bonding (H-bonding) [2]. This versatility makes Im particularly suitable for surface applications through the SAM chemistry [3–8]. The Im-derivatives functionalized SAMs have been used in biosensing applications, modulations of enzyme activity, purification of biologically relevant molecules, corrosion prevention, and others [5–8].

The pK_a for imidazole is around 5.9. Thus, two forms of histidine side-chain functional group, Tautomer-I (T-I; N1–H, N3) and Tautomer-II (T-II; N1, N3–H), are possible under the physiological conditions. In neutral pH and room temperature, T-I is the more energetically favorable [9]. However, owing to the intermolecular Im interactions and the surface charge effect, the tautomeric equilibrium of surface-adsorbed Im derivatives might differ from that of the solution phase. Indeed, a clear transition from T-I to T-II was observed

for Im functionalized lipoic acid compound as it adsorbed on the silver electrode [10]. Vibrational spectroscopy, especially Raman, is particularly useful in Im studies because of the diagnostic technique's ability to differentiate between two tautomeric forms, probe ring protonation state and interactions with transition metal cations [9–18]. For example, the analysis of the three well-established Raman band pairs at 1568/1585, 1282/1260, and 983/1004 cm^{-1} allows to discriminate between T-I and T-II [19]. The coordination with metal ion effectively decreases the Im ring C4=C5 bond length, so that the related ν(C4=C5) increases by 5–20 cm^{-1} from the initial positions at 1568–1573 and 1583–1588 cm^{-1} for T-I and T-II, respectively [16]. The deuterium exchanged imidazolium cation (ImD_2^+) exhibits an intensive spectral mode near 1405 cm^{-1}, which is particularly valuable in determining the imidazole deuteration state using regular Raman spectroscopy [20,21]. A special case to be mentioned is the investigation of Im ring deuteration state in proteins based on 1405 cm^{-1} spectral mode in UV-resonance Raman [22,23].

Surface-enhanced Raman spectroscopy (SERS) provides detailed molecular-level information on the bonding, orientation, and structure of surface-adsorbed molecules in situ [24–29]. However, SERS is restricted by the necessity to use corrugated noble metal surfaces. Recently developed shell-isolated nanoparticle-enhanced Raman spectroscopy (SHINERS) overcomes such a limitation [30,31]. The method is based on the Raman signal amplification by the plasmonic core nanoparticles (usually Au or Ag) that are covered with thin (2–3 nm) isolating shells from SiO_2, TiO_2, or other dielectric material. The inert shell protects the probed molecules from interactions with the metal core, increases nanoparticle stability, and acts as a barrier between the probe and the core, preventing from charge transfer and disturbance of the double layer. The SHINERS method has already shown great potential for the in-situ analysis of the molecule adsorption, interfacial structure, and interactions of molecules on smooth and well-defined surfaces and at electrochemical interfaces [32–43].

This research aims to attain molecular level insights into the structure and hydrogen bonding of the imidazole ring at the electrified interface. We report the synthesis and vibrational spectroscopy characterization of the imidazole ring terminated alkanethiol molecule with intrachain amide group, N-(2-(1H-imidazol-4-yl)ethyl)-6-mercaptohexanamide (IMHA). The use of in-situ electrochemical SHINERS and ex-situ reflection-absorption infrared spectroscopy (RAIRS) techniques allowed for probing IMHA SAM that was adsorbed on the highly defined, atomically smooth Au surfaces. The effect of electrode potential on monolayer structure, tautomerism, and hydrogen bonding interaction strength of imidazole ring at electrochemical interface was spectroscopically assessed.

2. Materials and Methods

2.1. Synthesis of N-(2-(1H-Imidazol-4-yl)ethyl)-6-mercaptohexanamide (IMHA) and 6-Mercapto-N-methylhexanamide (Fragment Molecule)

Materials were purchased from Apollo Scientific (histamine dihydrochloride), Alfa Aesar (6-bromohexanoic acid, oxalyl chloride, NaOMe (30 wt% in methanol)), TCI (1-(3-dimethylaminopropyl)-3-ethylcarbodiimide hydrochloride (EDCI Cl), methylamine (40% in methanol), and Sigma Aldrich (thioacetic acid, K_2CO_3, 1,4-dithio-DL-threitol (DTT), CH_2Cl_2 (DCM), methanol, triethylamine, dimethylformamide (DMF), 4-dimethylaminopyridine (DMAP)). DMSO-d6 (99.5 atom% D) and $CDCl_3$ (99.8 atom% D) for nuclear magnetic resonance spectroscopy were obtained from Apollo Scientific. IMHA was synthesized from histamine dihydrochloride and 6-bromohexanoic acid, as shown in Figure 1. The details of synthesis and related analytical data of the IMHA, imidazole-truncated IMHA (6-mercapto-*N*-methylhexanamide) (fragment molecule), and their intermediates are presented in the Supplementary data file (General methods section, Scheme S1, and Figure S1).

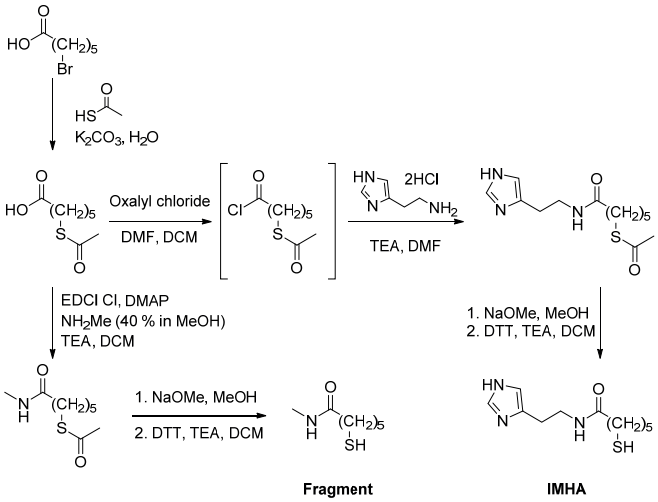

Figure 1. Synthesis scheme of IMHA and fragment molecule.

2.2. Synthesis of Silicon Dioxide Covered Spherical Silver Nanoparticles (Ag@SiO$_2$)

The reagents and solvents were used without further purifications: silver nitrate ($AgNO_3$, 99%), trisodium citrate dihydrate (99%), (3-aminopropyl)triethoxysilane (99%), and sodium silicate solution (NaOH 10%, SiO_2 27%) (Merck). All solutions were prepared with ultra-pure water (resistivity of 18.2 MΩ·cm) from Direct-Q 3UV (Merck, Darmstadt, Germany). Nanoparticles (NPs) were synthesized under microwave irradiation according to the previously published method [44]. Briefly, the bare silver-core NPs were prepared by the $AgNO_3$ reduction with sodium citrate and capped with silica shell. Then, core-shell NPs were purified by a repeated centrifugation, supernatant removal, and resuspension. Figure 2 shows the Ag@SiO_2 NPs images obtained by high-resolution transmission electron microscopy (HR-TEM). HR-TEM images were collected by an FEI Tecnai G2 F20 X-TWIN TEM (FEI, Netherlands) microscope with an accelerating voltage of 200 kV. The microscope was equipped with an EDX (EDAX) spectrometer and Gatan Orius CCD camera. The measurements were carried out in a bright-field regime.

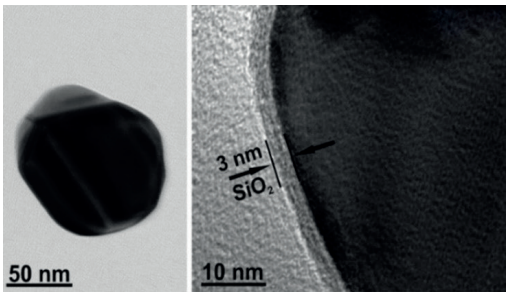

Figure 2. HR-TEM images of Ag@SiO_2 nanoparticles. Ag core and SiO_2 sizes were 85 ± 5 nm and 3 nm.

2.3. Preparation and Characterization of SAM

A 120-nm Au film was deposited on clean glass slides by using a Quorum 150T magnetron-sputtering machine and a 99.99% Au target. After that, the slides were incubated in 10^{-3} M IMHA ethanol solution for twenty-four hours unless indicated otherwise; then

rinsed with ethanol and dried under N_2. For SHINERS experiments, the slides were mounted into an electrochemical cell and filled with Milli-Q water. After that, 3 μL of $Ag@SiO_2$ were carefully injected directly on the surface of Au and left to rest for 10 min for nanoparticles to adsorb. Then, the cell was thorough rinsed with 0.01 M phosphate buffer (pH 7) containing 0.1 M Na_2SO_4.

Reflection absorption IR spectroscopy (RAIRS) spectra were obtained by using a Vertex 80v FTIR spectrometer (Bruker, Germany) equipped with the LN-MCT narrow band detector and the horizontal reflection accessory. The spectral resolution was set at 4 cm^{-1}. Spectra were acquired by 400 scans at a grazing angle of 80° by using p-polarized light. The sample chamber and the spectrometer were evacuated during the measurements to approximately 2 hPa pressure. The spectrum of deuterium substituted octadecanethiol (ODT-d38) SAM adsorbed on Au was used as a reference. FTIR transmission spectrum was recorded from KBr pellet-dispersed IMHA using an Alpha spectrometer (Bruker, Germany) equipped with an RT-DTGS detector. The resolution was set to 4 cm^{-1}; 50 interferogram scans were co-added.

SHINERS spectra were recorded using high throughput (instrument NA = 0.22) Tornado HyperFlux spectrometer (Tornado Spectral Systems, Mississauga, ON, Canada) equipped with fiber-optic cable for excitation and collection of the Raman spectra. The 785 nm beam of the diode laser was used as the excitation source. The laser power at the sample was set to 38 mW, and the beam was focused on a 100 μm diameter spot on the sample. Spectra were recorded for 300 s by co-adding thirty 10-s scans. For temperature-controlled Raman measurements, the LinKam temperature control system PE95/T95 with the accuracy of 0.05 °C was used. IMHA powder was measured with 80 mW laser power and 100 s integration time, at 22, 130, and 135 °C. Spectroelectrochemical measurements were carried out in a three-electrode cell, where slides with Au film were used as a working electrode, platinum wire as a counter electrode, and KCl saturated Ag/AgCl as a reference electrode.

Raman wavenumbers were calibrated according to the polystyrene spectrum. Band frequencies were obtained by fitting experimental contours with mixed Gaussian-Lorentzian form components by using the GRAMS/AI 8.0 (Thermo Scientific, Waltham, MA, USA) software.

Theoretical modeling study of IMHA molecule was performed using Gaussian package version G09 D.01 [45]. Geometry optimization and frequency calculation were completed with the DFT method using the hybrid B3LYP functional and 6-311++G(2d,p) basis set. The polarizable continuum model (IEFPCM) was used to emulate the water environment. The frequency calculation ended with no imaginary wavenumbers, indicating the geometry at minimum energy. Frequency and intensity scaling were applied according to the previously described procedure [46].

3. Results and Discussion

3.1. Assignments of Raman Bands

The studied IMHA molecule comprises four functional units: (i) the surface-active thiol group (SH), (ii) the hydrocarbon chain ($-(CH_2)_5-$), (iii) the amide group ($-CO-NH-$), and (iv) the terminal Im ring (Figure 3). To facilitate Raman band assignments, we have synthesized a compound similar to IMHA thiol without the terminal Im ring (fragment compound) (Figure 3). Detailed assignments of the Raman bands are provided in the Supplementary Data file (Figure S2 and related discussion) and Table 1.

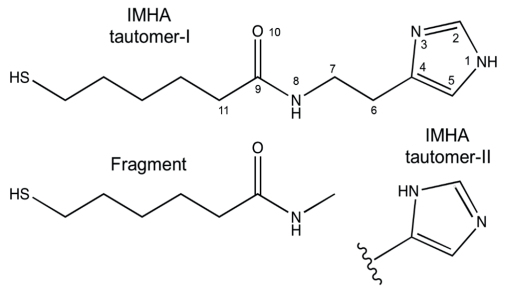

Figure 3. Molecular structure of Tautomer-I and Tautomer-II form of IMHA and the structure of fragment molecule.

Table 1. Temperature-Raman, SHINERS, and DFT frequencies and assignments of IMHA.

Raman, cm^{-1}			SHINERS, cm^{-1}	DFT	Ref.	Assignment
22 °C	130 °C	135 °C	H_2O, −0.8 V			
3142	3139	3144 sh		3158		ν(C5–H)
3120	3118	3118		3139		ν(C2–H)
2926	2925	2928	2921	2935		$\nu_{as}(CH_2)$
2852	2857	2859	2856	2913		$\nu_s(CH_2)$
2572	2574	2574	n.a.	2602		ν(S–H)
1636	1643	1650	1680 1631	1642		ν(C=O) Amide-I
		1582 T-II	1597 T-II	1587 T-II	[9,18,19]	
1566 T-I	1564 T-I	1564 T-I	1573 T-I	1570 T-I		ν(C4=C5) + ν(C4–C6) + β(C5H)
				1530		ν(C–N) + δ(NH) Amide-II
1497	1493	1480	1490 sh	1496	[10,18]	ν(C2–N3) + β(C2H) + ν(C2–N1) + ν(C5–N1)
1464	1461			1458		$\delta(CH_2)$ scissoring
1442	1439	1437	1434	1443		$\delta(CH_2)$ scissoring
1362	1360		1372	1381		$w(CH_2)$
		1345 T-II	1352 sh T-II		[19]	
1321 T-I	1318 T-I		1326 sh T-I	1335 T-I		$\delta(CH_2)$ + ν(Im) breathing + δ(C5H)
1299	1299	1305	1302	1303		$t(CH_2)$
1257 T-II	1257 T-II	1263 T-II	1262 T-II		[9,19,47]	ν(Im) breathing + β(C2H)
1230	1228	1230	1238	1240	[18]	β(C5H) + β(C2H) + ν(C5–N1)
1191	1190	1190	1192	1202		$t(C6H_2)$ + δ(N8H)
1167	1163			1130	[13]	ν(C2–N1) + δ(N1H)
1087	1087	1105		1089		$\nu(C–C)_T$ + δ(CSH) + δ(CCS)
1036	1037	1059	1051	1045		$\nu(C–C)_T$
1019	1018		1014	1018		ν(C6–C7)
983	979	971		977	[9,19]	β(CH) Im for T-I
931	931	931		943		$t(CH_2)$ + $r(CH_2)$
921			916	948	[13]	β(CH) Im
911	906			907		δ(N8C9C11)
841	842		839	835		γ(C2H)
753	750			750	[48]	γ(C5H) + $r(CH_2)$
732	730	734		730	[48]	$r(CH_2)$ + $\nu(S–C)_T$
711	709	710	701	712		$\nu(S–C)_T$
685	682			694		γ(Im)
653	655	654	634	n.a.	[49]	$\nu(S–C)_G$ + δ(Im)

Abbreviations: n.a., not applicable; sh, shoulder; G, gauche; T, trans; r, rocking; w, wagging; t, twisting; δ, deformation; β, in-plane deformation; γ, out-of-plane deformation; ν, stretching; Im, imidazole; T-I, Tautomer-I; T-II, Tautomer-II.

To evaluate Raman modes related to intra- and intermolecular interactions and those sensitive to the ordering of alkyl chain, we performed a temperature-dependent Raman study of powder IMHA compound (Figure 4). Changes in temperature provoke structural or phase transitions and a variety of conformational alterations in a molecular system. In general, an increase in temperature induces disordering in the molecular arrangement. Such disordering may be reflected in changes of spectral mode bandwidths (related to vibrational energy distribution), peak position (energy of particular vibration), and relative intensities (distribution of two or more different forms of a molecule). Therefore, temperature-Raman

provides additional means for scrutinizing a given compound. The medium intensity modes near 1566, 1321, and 983 cm^{-1} in the 22 °C spectrum are related to vibrations of the Tautomer-I (N1–H, N3) form of Im ring and are assigned to ν(C4=C5) stretching, ν(Im) breathing + δ(C5H), and β(CH) deformation, respectively [19]. At the elevated temperatures (130–135 °C), the shoulders appear at 1582 and 1345 cm^{-1} specific to the Tautomer-II (N1, N3–H) form of Im. The relative percentage of T-II determined by the integral intensity ratio $A_{1582}/(A_{1582} + A_{1564})$ is 16% for the compound at 130 °C and 32% for the one at 135 °C. It should be noted that the frequency of an intense band at 1321 cm^{-1} downshifts to 1305 cm^{-1} at 135 °C. In addition, the band notably broadens. Such spectral changes reflect a decrease in H-bonding interaction strength primarily at N3 site, because of a considerable contribution from ν(N3−C2) vibration to this mode for Tautomer-I [19].

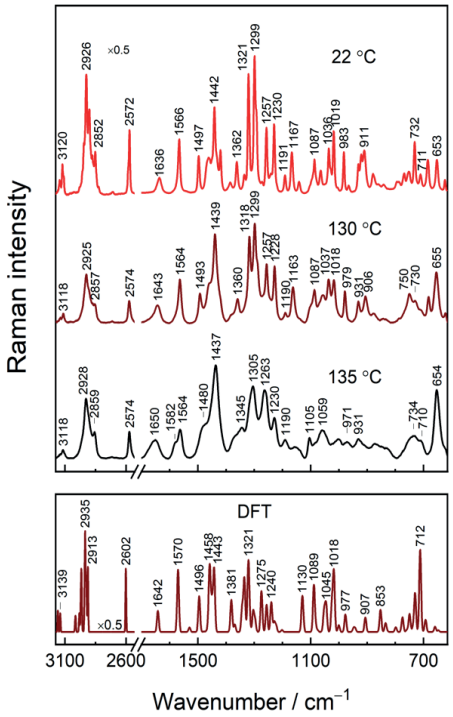

Figure 4. Temperature-dependent Raman spectra of solid IMHA at 22, 130, and 135 °C (upper panel) and DFT spectrum of IMHA (bottom panel). The intensity of the 2530–3175 cm^{-1} region is scaled by 0.5.

The 1497 cm^{-1} band assigned to ν(N1–C2) + β(C2H) motion is not sensitive to Im tautomerism [19]. The band, however, shifts to higher wavenumbers with the coordination of metal cation at the nitrogen lone electron pair. Moreover, electrode polarization also induces shifting for imidazole-copper pair (9 ± 2 $cm^{-1}V^{-1}$) [18]. We found a 17 cm^{-1} downshift of the spectral mode to 1480 cm^{-1} and a clear increase in full width at half-maximum (FWHM) with the temperature raised to 135 °C. These spectral changes are associated with the increased motional freedom of the Im ring. Therefore, the spectral changes near 1496–1480 cm^{-1} may serve as a useful spectral marker for Im ring packing.

Nested within the alkane chain, the amide group acts as an intermolecular stabilizing agent, which forms the extended H-bond network between neighboring molecular chains. It has been already shown that such an interaction radically increases the desorption temperature and chemical stability of the monolayer [50]. From the temperature-Raman

spectra of the powder compound, only the medium-low intensity Amide-I (Am-I) band at 1636 cm^{-1} can be recognized. This spectral mode is related to C=O stretching (83%) coupled with out-of-phase ν(C−N) and δ(C–C−N) and can serve as a diagnostic tool in identifying the secondary structure of peptides [47]. The 14 cm^{-1} frequency upshift during the solid-to-liquid transition with the temperature elevation, clearly shows the weakening of the H-bonding at the amide's C=O group.

3.2. RAIRS Analysis of the Monolayer Formation

Figure 5 shows RAIRS spectra of the IMHA monolayer adsorbed on a smooth gold surface. The spectral features at 1645, 1556, and 1264 cm^{-1} are assigned to amide bands, Am-I, Am-II, and Am-III, respectively, whereas the ones near 1460 and 1380 cm^{-1} to methylene scissoring and wagging deformations, $\delta(CH_2)$. The RAIRS-surface selection rule allows interrogating the orientation of molecular groups because the intensity of particular spectral mode directly depends on the projection of the mode's transition dipole moment (TDM) on the surface normal [51]. While Am-I and Am-II have TDMs oriented perpendicular to each other in the amide bond plane, they also have perpendicular and parallel TDM orientations with respect to carbohydrate chain [51]. Thus, for the neatly packed IMHA monolayer, the Am-II is expected to dominate the spectrum. Indeed, at progressively longer incubation time, the Am-II intensity at 1556 cm^{-1} increases and the intensity of Am-I at 1645 cm^{-1} decreases. The integral intensity ratio Am-II/Am-I provides a qualitative measure of the molecular reorientation (Figure 5B). The experimental data of Am-II/Am-I were fitted with a sigmoidal function:

$$A = A_0 + \frac{a}{1 + \left(\frac{t}{t_m}\right)^b} \quad (1)$$

where t_m is the transition inflection point found at 162 min. At 10 s incubation time, the Am-II/Am-I ratio was 1.4, which is slightly above 0.9 calculated for IMHA molecules chaotically dispersed in KBr pellet (Figure S3). The ratio doubled in 10 min and after 24 h it reached 11.2, so most molecules had a planar amide group oriented perpendicularly to the surface. Such an orientation is strengthened by the H-bonding interaction involving the amide group (C=O···H) and dipole–dipole interaction between the C=O groups [52]. The link between Amide-I and -II wavenumbers and the H-bonding strength at C=O and N–H groups has been clearly established [53–55]. We find marginal Am-I frequency decrease with the development of SAM (by 3 cm^{-1} during the 120 min incubation) revealing minor increase of the H-bonding strength at C=O. The frequency of the Am-II band remained constant.

In the RAIRS spectrum of 24 h-incubated fragment SAM, the Amide-II spectral band is blue-shifted by 12 cm^{-1} compared to the IMHA SAM (after 24 h incubation), showing the stronger H-bonding at the N–H group for fragment molecule. Interestingly, surface-adsorption of molecules from solution phase induced spectral shift of Am-II mode by −20 for IMHA and 13 cm^{-1} for the fragment molecule (Table 2). Such frequency shifting is related to different molecular packing efficiency in bulk and SAM. The Im ring in IMHA molecule introduces sterical hindrances for the neighboring amides to engage in the formation of an optimal H-bonding network.

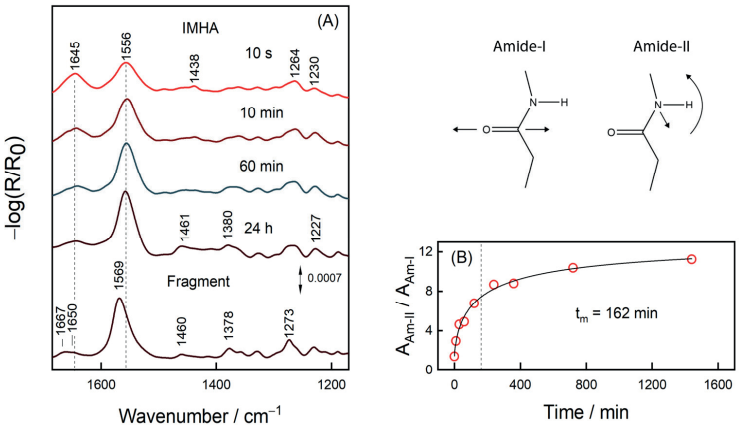

Figure 5. (**A**) The immersion time dependent RAIRS spectra of IMHA and the spectrum of the fragment molecule after 24 h-incubation. (**B**) Dependence of integral intensity ratio Am-II/Am-I on the immersion time fitted with the sigmoidal curve (R^2 = 0.9925). The transition midpoint at 162 min marked by a dashed line. Cartoon depicts the atom motions in Amide-I and Amide-II vibrations.

Table 2. Wavenumbers and FWHM (bold) of Am-I and Am-II modes of IMHA and fragment molecule obtained from samples in powder form and SAMs.

	IMHA			Fragment		
	SAM, 24 h	**Powder**	δ	**SAM, 24 h**	**Powder**	δ
Am-II, cm^{-1}	1557, **29**	1577, **37**	−20	1569, **28**	1556, **52**	13
Am-I, cm^{-1}	1642, **42**	1638, **27**	6	1650, **28;** 1667, **16**	1647, **41**	3; 20

Abbreviation: δ, wavenumber shift, $\nu_{SAM}-\nu_{powder}$.

3.3. General Features of IMHA Monolayer SHINERS Spectrum

Figure 6A presents evidence of Ag@SiO_2 functionality. The Raman spectrum of nanoparticles has virtually no vibrational modes until the nanoparticles are placed on top of smooth surface-adsorbed IMHA monolayer. The intense mode at 702 cm^{-1} corresponds to $\nu(C–S)_T$ stretching vibration of the molecules, which adopt a nearly vertical orientation with the surface at the C–S bond, whereas the corresponding gauche mode $\nu(C–S)_G$ appears as a weak feature at 622 cm^{-1}. The predominant trans configuration agrees with the vertical orientation of molecules at the amide group in mature SAM as revealed by RAIRS. Weak Am-I bands at 1685 and 1640 cm^{-1} were immediately ascribed to surface molecules that are involved in strong and weak H-bonding at amide groups, respectively. The rather complex 1500–1700 cm^{-1} region contains no Am-II mode because this mode is typically either very weak or not detectable in Raman spectra [56]. Two strong bands at 1062 and 1019 cm^{-1} were found to be not sensitive to H/D exchange and were assigned to stretching vibrations of hydrocarbon chain, $\nu(C–C)_T$ and ν(C–C), respectively (Table 1). The higher frequency component was assigned to the in-phase vibration of $–(CH_2)_5–$ chain in extended all-trans conformation based on DFT calculations (1089 cm^{-1} band) and previously reported temperature-dependent SERS studies of SAMs [57]. The 1019-cm^{-1} band was assigned to the C–C stretching vibration of hydrocarbon chain connecting amide and Im groups based on DFT suggestion (1018 cm^{-1} band).

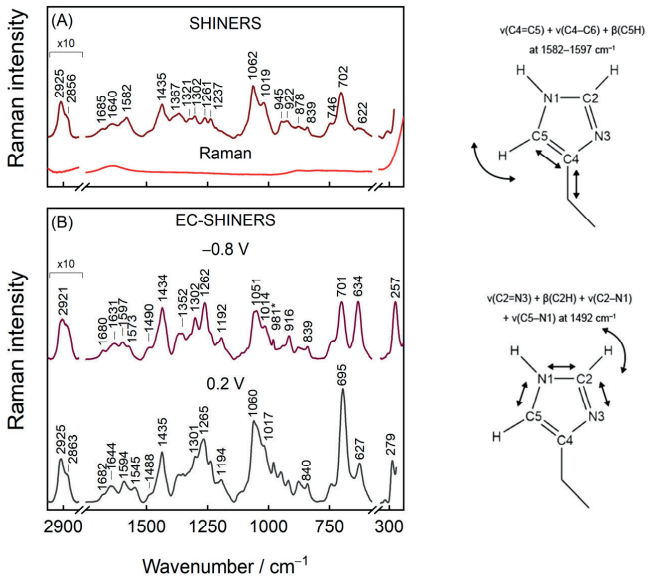

Figure 6. (**A**) SHINERS and Raman spectra of IMHA SAM on a smooth Au electrode in H_2O. (**B**) EC-SHINERS spectra recorded at −0.8 and 0.2 V potentials in phosphate buffer solution (PBS; pH 7.0, with 0.1 M Na_2SO_4). Asterisk (*) at 981 cm^{-1} marks SO_4^{2-} vibrational mode from the solution. Cartoon depicts the selected imidazole ring motions.

The tautomeric equilibrium of Au-adsorbed IMHA could certainly differ from that of the solution phase. Indeed, ν(C4=C5) + ν(C4–C6) + β(C5H) mode at 1582 cm^{-1} fall close to the 1588−1583 cm^{-1} range typical for T-II [16]. While in the case of T-I conformer, this mode is expected to be observed at considerably lower wavenumbers (1573–1568 cm^{-1}). The downshift of this mode to 1575 cm^{-1} in D_2O solution immediately confirms H/D exchange at nitrogen sites of Im ring in the monolayer. Another couple of bands, at 1261 for H_2O and 1257 cm^{-1} for D_2O solutions, confirm the T-II surface form of IMHA [16].

3.4. Potential-Controlled SHINERS Measurements of IMHA Monolayer

Negative electrode polarization at −0.8 V potential was applied for 30 s in the beginning of each potential-controlled measurement to desorb impurities of low surface affinity, which may originate from nanoparticles. Preliminary examination showed that pretreatment of the monolayer at negative potentials increases the reproducibility of results. Figure 6B shows SHINERS spectra from the smooth Au electrode adsorbed IMHA at −0.8 and 0.2 V electrode polarizations.

Plenty of SERS research on metal–sulfur bond has been carried out for the roughened metal adsorbed monolayers [57,58]. However, only with SHINERS approach the well-defined and smooth substrate adsorbed molecules become more accessible to Raman spectroscopy [37,59]. The Au–S stretching mode found at 257 cm^{-1} upshifts to 279 cm^{-1} (δ = 22 cm^{-1}) when the potential is tuned from −0.8 to 0.2 V attesting the increase in Au–S bond strength. A similar value was found in a previous study on flat Au-adsorbed N-(6-mercapto)hexylpyridinium [37], whose high tuning rate was ascribed to force constant changes in Au–S bond strength because of electrode polarization and to some extent to the Stark effect [37,60]. As for C–S bond, the populations of gauche and trans molecular conformers were matching at −0.8 V, but with positive electrode polarization trans became strongly favored (Figure S4). Both conformational bands redshift with the tuning rate of -5.3 ± 0.2 and -6.9 ± 0.2 $cm^{-1}V^{-1}$, respectively, indicating potential-induced decrease in C–S bond strength, while at the same time Au–S bond became increasingly stronger at

more positive potentials [61]. Within the tested potential window, the trans/gauche ratio (I_{701}/I_{633}) increases from 1 to 3 with transition midpoint potential of -0.34 ± 0.02 V. Notably, all spectral changes are reversible as the electrode potential is set to -0.8 V. Two strong bands at 1051 and 1014 cm^{-1} were assigned to stretching vibrations of hydrocarbon chain, $\nu(C–C)_T$ and $\nu(C–C)$, respectively (Table 1). It should be noted that the relative intensity of $\nu(C-C)_T$ band increases at more positive electrode potentials together with growing $\nu(C-S)_T$ mode. In the high frequency region of Figure 6B, symmetric and asymmetric stretching vibrations of methylene groups $\nu(CH_2)$ near 2858 and 2921 cm^{-1} were found (E = -0.8 V). These modes will be discussed in more detail later in the manuscript.

To interpret the rather complex midrange region that is occupied by the imidazole ring, amide group vibrations, and the deformations of the methylene groups, a separate H/D exchange experiment was performed for the IMHA monolayer. The H/D exchange process was accomplished at the open circuit potential (0.17 V) by exchanging phosphate buffer solution (PBS) (with 0.1 M Na_2SO_4, pH 6.9) to pure D_2O (Figure 7). Amide-I spectral mode is found to be composed of low- and high-energy components at 1643 and 1676 cm^{-1}, both of which downshift by 7–8 cm^{-1} upon the exchange. We find that vibrational modes in the 1300–1610 cm^{-1} were sensitive to the solvent exchange. For example, the Tautomer-II related C=C stretching mode of the Im ring ν(C4=C5) clearly downshifts from 1590 to 1571 cm^{-1} [16]. The well-defined feature at 1492 cm^{-1} assigned to ν(C2–N3) coupled with β(C2H) downshifts to 1483 cm^{-1} in accordance with literature data [18]. The intense band at 1333 cm^{-1} develops in D_2O solutions. This band was identified as a Tautomer-II marker band for N3D protonated histidine [62]. Interestingly, the mode at 1545 cm^{-1} becomes significantly pronounced at 0.2 V potential (Figure 7A) and almost disappears due to the H/D exchange. Its assignment remains not fully clear because the contribution from the Am-II could be almost certainly ruled out since the deuteration of amide's N atom would introduce Am-II' with additional spectral intensity near 1450 cm^{-1} [63,64]. The only possible proximal spectral modes are expected near 1535 cm^{-1} for deprotonated 4-methylimidazole and doubly protonated histidine, both of which in neutral pH are not likely [13,62]. Presented SHINERS data revealed that the imidazole ring in the SAM at relatively positive electrode potentials is in the N3H protonation state (Tautomer-II).

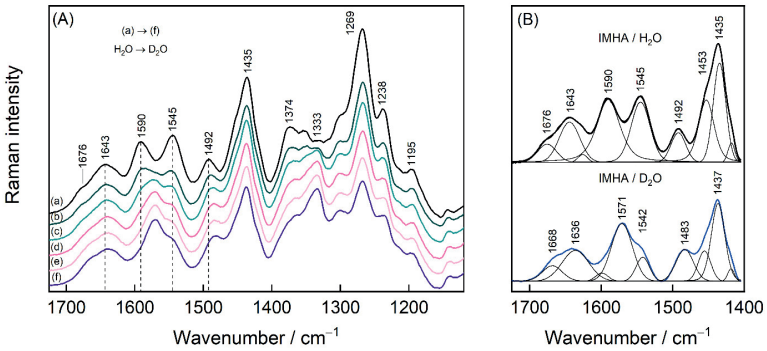

Figure 7. (**A**) SHINERS spectra in 1120–1725 cm^{-1} region of IMHA monolayer at open circuit potential in PBS solution (a), which was gradually exchanged to D_2O (b)–(f). In each step, 20 vol% of the solution was removed from the cell and then the same amount of D_2O was added. (**B**) The spectra of the first and the last step of the H/D exchange fitted with Gaussian-Lorentzian shape components.

Figure 8 shows the detailed SHINERS analysis of biased potential induced structural changes in IMHA SAM. An 11.2 cm^{-1} upshift in the frequency of dominant Amide-I component is detected with more positive electrode potentials (Figure 8C). To complement that, we analyzed the relative intensities of Am-I modes of strongly (ca. 1631 cm^{-1}) and loosely H-bonded (ca. 1680 cm^{-1}) molecules. The intensity ratio of these expressed as

I_{1631}/I_{1680} monotonically decreased from 3.4 to 2.3 with the negative to positive potential excursion. Both frequency shift and relative intensity changes show that a positive bias potential disengages molecules from the more strongly H-bounded network at the C=O moiety of amide groups.

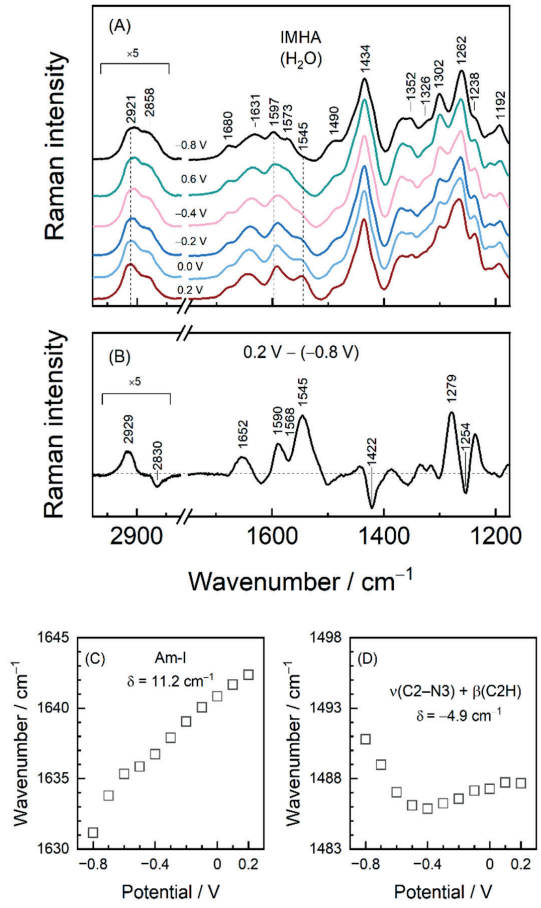

Figure 8. (**A**) EC-SHINERS spectra in 1120–1750 cm^{-1} and 2750–3050 cm^{-1} regions at indicated potentials. Spectra correspond to the ones in Figure 6. (**B**) EC-SHINERS difference spectrum constructed by subtracting 0.2 V spectrum from the one registered at −0.8 V. (**C**) Potential dependence of the Amide-I and (**D**) ν(C2–N3) + β(C2H) mode wavenumbers.

As Figures 6 and 8 show, the positions of imidazole-tautomerism marker bands near 1262, and 1597 cm^{-1} remain consistent with N3–H protonation (Tautomer-II) within the tested potential window [19]. However, at −0.8 V potential, a shoulder at 1573 cm^{-1} associated with Tautomer-I protonation form of Im becomes visible. Positive polarization diminishes mode intensity, while its T-II counterpart at 1597 cm^{-1} becomes stronger. Thus, SHINERS data show the T-II being the preferred tautomeric form at each tested potential, with a minor portion of molecules adopting T-I at the most negative polarizations. Potential induces a slight shift of the 1597 cm^{-1} to lower wavenumbers by 3.6 cm^{-1} due to lengthening of the C4=C5 bond. Interestingly, the Im ring mode at 1490 cm^{-1} assigned to C2–N3 stretching coupled with in-plane deformation β(C2H), ν(C2–N1), and ν(C5–N1) shows the nonmonotonous dependency on potential [10,18]. This mode shifts

by −4.9 cm^{-1} (tuning rate 13.3 $cm^{-1}V^{-1}$) in the range from −0.8 to −0.4 V and then upshifts by 1.8 cm^{-1} (Figure 8D). Besides, the spectral mode notably increases in FWHM by ca. 10 cm^{-1} of the −0.4 V spectrum compared to the −0.8 V one. From temperature-Raman measurements, decreasing mode frequency and increasing FWHM were linked with liberated imidazole ring motion. Thus, spectral data show that Im ring confinement in the monolayer at more positive electrode potentials is relaxed. The strong band at 1262 cm^{-1} (−0.8 V) due to Im ring breathing vibration coupled with C2–H in-plane deformation is very sensitive to potential perturbation; frequency of this band upshifts to 1266 cm^{-1} at electrode polarization 0.2 V. Consequently, the potential-difference spectrum clearly shows derivative-like feature at 1279/1254 cm^{-1} (Figure 8B). Temperature-dependent Raman study of bulk IMHA compound revealed an upshift in the position of this mode at elevated temperature (135 °C) (Figure 4). This might be related to decreased H-bonding interaction strength at the Im ring site. Such spectral observations are consistent with decreased H-bonding interaction strength at both amide (Am-I band) and Im ring sites at more positive electrode polarization.

3.5. Raman Markers for H-Bonding Interaction

In order to better understand the way H-bonding interaction affects imidazole ring structure and its vibrational frequencies, DFT modeling was carried out for 5-ethyl-1H-imidazole (Im-CH_2-CH_3) molecule isolated in vacuum and coordinated with one and two explicit water molecules (Figure 9). Calculations of T-II form molecule predict that 1608-cm^{-1} mode is mainly C4=C5 stretching motion; 1499 cm^{-1} mode is assigned to ν(C2–N1) + ν(C2–N3) + β(C2H) and associated with 1492 cm^{-1} mode in SHINERS spectra. The 1423 cm^{-1} mode emerges due to β(N3H) + ν(N3–C4) + ν(N3–C2) vibrations; 1382 cm^{-1} mode is tautomerism sensitive Im breathing mode. With increasing H-bonding coordination number, the 1499-cm^{-1} mode shifts to higher frequencies by 2–6 cm^{-1} (coordination number 1) and by 9 cm^{-1} (coordination number 2). The same holds for a compound in T-I form, for which an 8 cm^{-1} shift was found when in contact with two H_2Os. The predicted wavenumber shift confirms the principal mode's sensitivity to H-bonding interaction at the Im group and agrees with the temperature-Raman data presented in Figure 4 where the higher wavenumbers were associated with stronger hydrogen bonding interactions for the sample at room temperature. We already ascribed the decrease in position of 1492 cm^{-1} mode with liberated Im ring based on temperature-Raman. However, DFT proves that such a liberation is hydrogen bonding strength-related. Thus, the sharp wavenumber drop from −0.8 to −0.4 V potentials in Figure 8D clearly indicates reduction of H-bonding at Im, which is followed by a slight strengthening in −0.4/0.2 V range.

Interestingly, we found stronger H-bonding interactions for Im coordinated with two H_2O molecules rather than one H_2O. In this case, the length of N1···H_2O and N3–H···H_2O bonds decreased by 1.9 and 2.7 pm with an introduction of the second H_2O molecule (insets in Figure 9). A much higher, up to 30 cm^{-1}, frequency shift was found for 1423-cm^{-1} mode. However, this mode was difficult to identify in experimental SHINERS spectra of IMHA SAM because of the overlapping with methylene deformation vibrations.

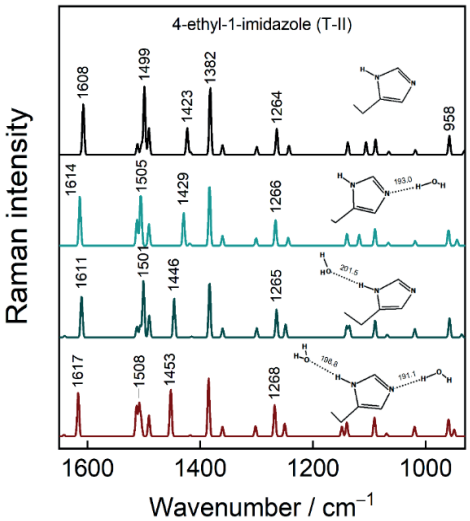

Figure 9. DFT spectra and optimized structures of Tautomer-II form of model compound 4-ethyl-1-imidazole with H-bonding coordination number from 0 to 2. The lengths of H-bonds are indicated in pm.

4. Conclusions

Hydrogen bonding is fundamental in protein architecture, interactions, and molecular recognition. Imidazole group of histidine amino acid is a major player in active centers of enzymes and protein secondary structure because of its ability to accept and donate H-bonding. To study H-bonding interactions of imidazole ring at electrified interfaces, first, we synthesized alkanethiol molecule with interchain amide group and terminal imidazole functional group (IMHA), then studied IMHA SAMs adsorbed on atomically smooth Au surfaces by means of SHINERS and RAIRS techniques.

(i) From RAIRS data molecules adsorb on a surface chaotically but with time (transition midpoint was 162 min), their intrachain amide groups become nearly perpendicular to the surface, which points to the more neatly organized SAM. However, the formation of an optimal H-bond network among amide groups was precluded by the steric hindrances introduced by bulky IMHA's imidazole group, as revealed by a study of the imidazole-truncated fragment molecule. For further endeavors, mixed IMHA/fragment molecule SAMs are suggested.

(ii) Adsorption on a surface induced a tautomeric transition in IMHA molecules from Tautomer-I (N1–H, N3) to Tautomer-II (N1, N3–H). The Tautomer-II was strongly favored at electrode polarization close to open circuit potential. However, an increased portion of Tautomer-I molecules was observed at -0.8 V.

(iii) Temperature-Raman and DFT modeling identified the 1492 cm^{-1} mode as sensitive to imidazole ring confinement and H-bonding strength. The analysis of this mode revealed the potential-dependent behavior of the interfacial Im ring, such that the Im is the most strongly confined and H-bonded at -0.8 V electrode polarization and the weakest confined and H-bonded at -0.4 V.

The presented data on construction, structure, and potential dependence of imidazole ring group-functionalized SAMs will possibly be valuable for the development of biosensors, molecular electronics, environmental, and pollution studies.

Supplementary Materials: The following supporting information can be downloaded at: https://www.mdpi.com/article/10.3390/molecules27196531/s1, Scheme S1: Synthesis scheme of IMHA compound and fragment molecule; Figure S1: 1H NMR and 13C NMR spectra of N-(2-(1H-imidazol-4-yl)ethyl)-6-mercaptohexanamide (IMHA); Figure S2: (A) Raman spectra of powder IMHA, fragment molecule, and histidine. (B) Raman spectra of powder fragment molecule and the 0.33 M solutions in H_2O and D_2O. Figure S3: FTIR transmission spectra of IMHA and fragment molecule powders dispersed in KBr pellets. Am-I and Am-II spectral modes were approximated using Gaussian shape components. The full-widths at half maxima of Am-I and Am-II bands are given next to corresponding wavenumbers; Figure S4: (A) SHINERS spectra of IMHA adsorbed on smooth Au electrode at indicated potentials in the 600–750 cm^{-1} spectral region. Spectra were recorded in 0.1 M Na_2SO_4 aqueous solution containing 0.01 M phosphate buffer (pH 7). The excitation wavelength was 785 nm. (B) Dependence of relative integrated intensity I_{701}/I_{633} ratio of IMHA bands on electrode potential fitted with the sigmoidal curve (Boltzmann model, R^2= 0.99658). The transition midpoint potential value was determined at –0.34 ± 0.02 V, shown by the dashed line. The grey bar around the midpoint line shows the error in the fitting value. (C) Dependence of $\nu(C–S)_G$ and $\nu(C–S)_T$ modes wavenumbers of IMHA on electrode potential. Data in (B) and (C) sections were presented as an average of three independent measurements.

Author Contributions: Conceptualization, M.T., and G.N.; methodology, A.Z., T.C., R.S. and L.L.; software, M.T.; validation, A.Z. and M.T.; formal analysis, A.Z., and M.T.; investigation, A.Z., M.T., T.C. and R.S.; resources, G.N and L.L.; data curation, A.Z. and M.T.; writing—original draft preparation, A.Z. and M.T.; writing—review and editing, G.N.; visualization, A.Z. and M.T.; supervision, G.N. All authors have read and agreed to the published version of the manuscript.

Funding: This research received no external funding.

Institutional Review Board Statement: Not applicable.

Informed Consent Statement: Not applicable.

Data Availability Statement: All data supporting the findings of this study are available from the corresponding author upon reasonable request.

Acknowledgments: G.N. gratefully acknowledges the Center of Spectroscopic Characterization of Materials and Electronic/Molecular Processes (SPECTROVERSUM Infrastructure) for use of Raman and FT-IR spectrometers.

Conflicts of Interest: The authors declare no conflict of interest.

Sample Availability: Samples of the compounds are available from the authors.

References

1. Sundberg, R.J.; Martin, R.B. Interactions of histidine and other imidazole derivatives with transition metal ions in chemical and biological systems. *Chem. Rev.* **1974**, *74*, 471–517. [CrossRef]
2. Liao, S.-M.M.; Du, Q.-S.S.; Meng, J.-Z.Z.; Pang, Z.-W.W.; Huang, R.-B.B. The multiple roles of histidine in protein interactions. *Chem. Cent. J.* **2013**, *7*, 44. [CrossRef] [PubMed]
3. Zaitouna, A.J.; Lai, R.Y. Design and characterization of a metal ion-imidazole self-assembled monolayer for reversible immobilization of histidine-tagged peptides. *Chem. Commun.* **2011**, *47*, 12391–12393. [CrossRef]
4. Hwang, S.; Lee, B.S.; Chi, Y.S.; Kwak, J.; Choi, I.S.; Lee, S.G. Faradaic impedance titration and control of electron transfer of 1-(12-mercaptododecyl)imidazole monolayer on a gold electrode. *Electrochim. Acta* **2008**, *53*, 2630–2636. [CrossRef]
5. Tappura, K.; Vikholm-Lundin, I.; Albers, W.M. Lipoate-based imprinted self-assembled molecular thin films for biosensor applications. *Biosens. Bioelectron.* **2007**, *22*, 912–919. [CrossRef]
6. Saada, M.C.; Montero, J.L.; Vullo, D.; Scozzafava, A.; Winum, J.Y.; Supuran, C.T. Carbonic anhydrase activators: Gold nanoparticles coated with derivatized histamine, histidine, and carnosine show enhanced activatory effects on several mammalian isoforms. *J. Med. Chem.* **2011**, *54*, 1170–1177. [CrossRef]
7. Pourrostam-Ravadanaq, P.; Safa, K.D.; Abbasi, H. Study of imidazole performance as pseudo-affinity ligand in the purification of IgG from bovine milk. *Anal. Biochem.* **2020**, *597*, 113693. [CrossRef]
8. Durainatarajan, P.; Prabakaran, M.; Ramesh, S.; Periasamy, V. Self-assembly on copper surface by using imidazole derivative for corrosion protection. *J. Adhes. Sci. Technol.* **2018**, *32*, 1733–1749. [CrossRef]
9. Ashikawa, I.; Itoh, K. Raman spectra of polypeptides containing L-histidine residues and tautomerism of imidazole side chain. *Biopolymers* **1979**, *18*, 1859–1876. [CrossRef]

10. Matulaitienė, I.; Kuodis, Z.; Eicher-Lorka, O.; Niaura, G. SERS characterization of imidazole ring terminated self-assembled monolayer formed from lipoic acid histamide on silver electrode. *J. Electroanal. Chem.* **2013**, *700*, 77–85. [CrossRef]
11. Garfinkel, D.; Edsall, J.T. Raman Spectra of Amino Acids and Related Compounds. VIII. Raman and Infrared Spectra of Imidazole, 4-Methylimidazole and Histidine. *J. Am. Chem. Soc.* **1958**, *80*, 3807–3812. [CrossRef]
12. Ashikawa, I.; Itoh, K. Raman Scattering Study on Tautomerism of L-Histidine. *Chem. Lett.* **1978**, *7*, 681–684. [CrossRef]
13. Mesu, J.G.; Visser, T.; Soulimani, F.; Weckhuysen, B.M. Infrared and Raman spectroscopic study of pH-induced structural changes of L-histidine in aqueous environment. *Vib. Spectrosc.* **2005**, *39*, 114–125. [CrossRef]
14. Martusevičius, S.; Niaura, G.; Talaikytė, Z.; Razumas, V. Adsorption of L-histidine on copper surface as evidenced by surface-enhanced Raman scattering spectroscopy. *Vib. Spectrosc.* **1996**, *10*, 271–280. [CrossRef]
15. Carter, D.A.; Pemberton, J.E. Raman spectroscopy and vibrational assignments of 1- and 2-methylimidazole. *J. Raman Spectrosc.* **1997**, *28*, 939–946. [CrossRef]
16. Takeuchi, H. Raman structural markers of tryptophan and histidine side chains in proteins. *Biopolymers* **2003**, *72*, 305–317. [CrossRef]
17. Miura, T.; Satoh, T.; Hori-i, A.; Takeuchi, H. Raman marker bands of metal coordination sites of histidine side chains in peptides and proteins. *J. Raman Spectrosc.* **1998**, *29*, 41–47. [CrossRef]
18. Matulaitienė, I.; Pociūtė, E.; Kuodis, Z.; Eicher-Lorka, O.; Niaura, G. Interaction of 4-imidazolemethanol with a copper electrode revealed by isotope-edited SERS and theoretical modeling. *Phys. Chem. Chem. Phys.* **2015**, *17*, 16483–16493. [CrossRef]
19. Toyama, A.; Ono, K.; Hashimoto, S.; Takeuchi, H. Raman spectra and normal coordinate analysis of the N1-H and N3-H tautomers of 4-methylimidazole: Vibrational modes of histidine tautomer markers. *J. Phys. Chem. A* **2002**, *106*, 3403–3412. [CrossRef]
20. Tasumi, M.; Harada, I.; Takamatsu, T.; Takahashi, S. Raman studies of L-histidine and related compounds in aqueous solutions. *J. Raman Spectrosc.* **1982**, *12*, 149–151. [CrossRef]
21. Takeuchi, H.; Kimura, Y.; Koitabashi, I.; Harada, I. Raman bands of N-deuterated histidinium as markers of conformation and hydrogen bonding. *J. Raman Spectrosc.* **1991**, *22*, 233–236. [CrossRef]
22. Wu, Q.; Li, F.; Wang, W.; Hecht, M.H.; Spiro, T.G. UV Raman monitoring of histidine protonation and H-2H exchange in plastocyanin. *J. Inorg. Biochem.* **2002**, *88*, 381–387. [CrossRef]
23. Zhao, X.; Wang, D.; Spiro, T.G. A UV Resonance Raman Monitor of Histidine Protonation in Proteins: Bohr Protons in Hemoglobin. *J. Am. Chem. Soc.* **1998**, *120*, 8517–8518. [CrossRef]
24. Mosier-Boss, P.A. Review of SERS substrates for chemical sensing. *Nanomaterials* **2017**, *7*, 142. [CrossRef]
25. Langer, J.; De Aberasturi, D.J.; Aizpurua, J.; Alvarez-Puebla, R.A.; Auguié, B.; Baumberg, J.J.; Bazan, G.C.; Bell, S.E.J.; Boisen, A.; Brolo, A.G.; et al. Present and future of surface-enhanced Raman scattering. *ACS Nano* **2020**, *14*, 28–117. [CrossRef]
26. Niaura, G.; Gaigalas, A.K.; Vilker, V.L. Surface-enhanced Raman spectroscopy of phosphate anions: Adsorption on silver, gold, and copper electrodes. *J. Phys. Chem. B* **1997**, *101*, 9250–9262. [CrossRef]
27. Silva, E.F.; Wysard, J.S.; Bandeira, M.C.E.; Mattos, O.R. Electrochemical and surface enhanced Raman spectroscopy study of Guanine as corrosion inhibitor for copper. *Corr. Sci.* **2021**, *191*, 109714. [CrossRef]
28. Silva, E.F.; Wysard, J.S.; Bandeira, M.C.E.; Mattos, O.R.; Alves, W.A. On the 4-methylimidazole behavior at a copper electrode: A view from surface-enhnaced Raman scattering. *J. Raman Spectrosc.* **2019**, *50*, 1438–1444. [CrossRef]
29. Gutowski, L.; Liszewska, M.; Bartosewicz, B.; Budner, B.; Weyher, J.L.; Jankiewicz, B.J. Investigation of organic monoradicals reactivity using surface-enhanced Raman spectroscopy. *Spectrochim. Acta A* **2022**, *278*, 121312. [CrossRef]
30. Anema, J.R.; Li, J.-F.F.; Yang, Z.-L.L.; Ren, B.; Tian, Z.-Q.Q. Shell-Isolated Nanoparticle-Enhanced Raman Spectroscopy: Expanding the Versatility of Surface-Enhanced Raman Scattering. *Annu. Rev. Anal. Chem.* **2011**, *4*, 129–150. [CrossRef]
31. Li, J.F.; Huang, Y.F.; Ding, Y.; Yang, Z.L.; Li, S.B.; Zhou, X.S.; Fan, F.R.; Zhang, W.; Zhou, Z.Y.; Wu, D.Y.; et al. Shell-isolated nanoparticle-enhanced Raman spectroscopy. *Nature* **2010**, *464*, 392–395. [CrossRef]
32. Wen, B.Y.; Jin, X.; Li, Y.; Wang, Y.H.; Li, C.Y.; Liang, M.M.; Panneerselvam, R.; Xu, Q.C.; Wu, D.Y.; Yang, Z.L.; et al. Shell-isolated nanoparticle-enhanced Raman spectroscopy study of the adsorption behaviour of DNA bases on Au(111) electrode surfaces. *Analyst* **2016**, *141*, 3731–3736. [CrossRef] [PubMed]
33. Li, C.Y.; Chen, S.Y.; Zheng, Y.L.; Chen, S.P.; Panneerselvam, R.; Chen, S.; Xu, Q.C.; Chen, Y.X.; Yang, Z.L.; Wu, D.Y.; et al. In-situ electrochemical shell-isolated Ag nanoparticles-enhanced Raman spectroscopy study of adenine adsorption on smooth Ag electrodes. *Electrochim. Acta* **2016**, *199*, 388–393. [CrossRef]
34. Barbillon, G. Applications of Shell-Isolated Nanoparticle-Enhanced Raman Spectroscopy. *Photonics* **2021**, *8*, 46. [CrossRef]
35. Li, J.F.; Zhang, Y.J.; Ding, S.Y.; Panneerselvam, R.; Tian, Z.Q. Core-shell nanoparticle-enhanced Raman spectroscopy. *Chem. Rev.* **2017**, *117*, 5002–5069. [CrossRef]
36. Yu, Z.; Xu, Y.X.; Su, J.Q.; Radjenovic, P.M.; Wang, Y.H.; Zheng, J.F.; Teng, B.; Shao, Y.; Zhou, X.S.; Li, J.F. Probing Interfacial Electronic Effects on Single-Molecule Adsorption Geometry and Electron Transport at Atomically Flat Surfaces. *Angew. Chem. Int. Ed. Engl.* **2021**, *60*, 15452–15458. [CrossRef]
37. Zdaniauskiene, A.; Charkova, T.; Matulaitiene, I.; Eicher-Lorka, O.; Matijoška, A.; Skapas, M.; Selskis, A.; Niaura, G. Electrochemical Shell-Isolated Nanoparticle-Enhanced Raman Spectroscopy: Bonding, Structure, and Ion-Pairing of the Positive Charge Bearing Pyridinium Ring Terminated Monolayer at Smooth Gold Electrode. *J. Phys. Chem. C* **2018**, *122*, 1234–1242. [CrossRef]
38. Zdaniauskienė, A.; Ignatjev, I.; Charkova, T.; Talaikis, M.; Lukša, A.; Šetkus, A.; Niaura, G. Shell-Isolated Nanoparticle-Enhanced Raman Spectroscopy for Probing Riboflavin on Graphene. *Materials* **2022**, *15*, 1636. [CrossRef]

39. Li, J.-F.F.; Ding, S.-Y.Y.; Yang, Z.-L.L.; Bai, M.-L.L.; Anema, J.R.; Wang, X.; Wang, A.; Wu, D.-Y.Y.; Ren, B.; Hou, S.-M.M.; et al. Extraordinary Enhancement of Raman Scattering from Pyridine on Single Crystal Au and Pt Electrodes by Shell-Isolated Au Nanoparticles. *J. Am. Chem. Soc.* **2011**, *133*, 15922–15925. [CrossRef]
40. Krajczewski, J.; Kudelski, A. Shell-isolated nanoparticle-enhanced Raman spectroscopy. *Front. Chem.* **2019**, *7*, 410. [CrossRef]
41. Niciński, K.; Krajczewski, J.; Kudelski, A.; Witkowska, E.; Trzcińska-Danielewicz, J.; Girstun, A.; Kamińska, A. Detection of circulating tumor cells in blood by shell-isolated nanoparticle-enhanced Raman spectroscopy (SHINERS) in microfluidic device. *Sci. Rep.* **2019**, *9*, 9267. [CrossRef] [PubMed]
42. Krajczewski, J.; Michałowska, A.; Kudelski, A. Star-shaped plasmonic nanostructures: New, simply synthesized materials for Raman analysis of surfaces. *Spectrochim. Acta A* **2020**, *225*, 117469. [CrossRef] [PubMed]
43. Haryanto, A.; Lee, C.W. Shell isolated nanoparticle enhanced Raman spectroscopy for mechanistic investigation of electrochemical reactions. *Nano Convergence* **2022**, *9*, 9. [CrossRef] [PubMed]
44. Daublytė, E.; Zdaniauskienė, A.; Talaikis, M.; Drabavičius, A.; Charkova, T. A facile microwave-assisted synthesis of Ag@SiO_2 nanoparticles for Raman spectroscopy. *New J. Chem.* **2021**, *45*, 10952–10958. [CrossRef]
45. Frisch, M.J.; Trucks, G.W.; Schlegel, H.B.; Scuseria, G.E.; Robb, M.A.; Cheeseman, J.R.; Scalmani, G.; Barone, V.; Petersson, G.A.; Nakatsuji, H.; et al. *Gaussian 09*; Revision D.01; Gaussian, Inc.: Wallingford, CT, USA, 2013.
46. Talaikis, M.; Eicher-Lorka, O.; Valinčius, G.; Niaura, G. Water-induced structural changes in the membrane-anchoring monolayers revealed by isotope-edited SERS. *J. Phys. Chem. C* **2016**, *120*, 22489–22499. [CrossRef]
47. Niaura, G. Raman Spectroscopy in Analysis of Biomolecules. In *Encyclopedia of Analytical Chemistry*; John Wiley & Sons, Ltd.: Hoboken, NJ, USA, 2014; pp. 1–34. [CrossRef]
48. Nelson, P.N. Chain Length and Thermal Sensitivity of the Infrared Spectra of a Homologous Series of Anhydrous Silver(I) n –Alkanoates. *Int. J. Spectrosc.* **2016**, *2016*, 3068430. [CrossRef]
49. Riauba, L.; Niaura, G.; Eicher-Lorka, O.; Butkus, E. A study of cysteamine ionization in solution by Raman spectroscopy and theoretical modeling. *J. Phys. Chem. A* **2006**, *110*, 13394–13404. [CrossRef]
50. Kim, M.; Hohman, J.N.; Serino, A.C.; Weiss, P.S. Structural manipulation of hydrogen-bonding networks in amide-containing alkanethiolate monolayers via electrochemical processing. *J. Phys. Chem. C* **2010**, *114*, 19744–19751. [CrossRef]
51. Kuodis, Z.; Matulaitienė, I.; Špandyreva, M.; Labanauskas, L.; Stončius, S.; Eicher-Lorka, O.; Sadzevičienė, R.; Niaura, G. Reflection Absorption Infrared Spectroscopy Characterization of SAM Formation from 8-Mercapto-N-(phenethyl)octanamide Thiols with Phe Ring and Amide Groups. *Molecules* **2020**, *25*, 5633. [CrossRef]
52. Jackson, M.; Mantsch, H.H. The Use and Misuse of FTIR Spectroscopy in the Determination of Protein Structure. *Crit. Rev. Biochem. Mol. Biol.* **1995**, *9238*, 95–120. [CrossRef]
53. Clegg, R.S.; Hutchison, J.E. Hydrogen-bonding, self-assembled monolayers: Ordered molecular films for study of through-peptide electron transfer. *Langmuir* **1996**, *12*, 5239–5243. [CrossRef]
54. Kocherbitov, V.; Latynis, J.; Misiūnas, A.; Barauskas, J.; Niaura, G. Hydration of lysozyme studied by Raman spectroscopy. *J. Phys. Chem. B* **2013**, *117*, 4981–4992. [CrossRef] [PubMed]
55. Myshakina, N.S.; Ahmed, Z.; Asher, S.A. Dependence of amide vibrations on hydrogen bonding. *J. Phys. Chem. B* **2008**, *112*, 11873–11877. [CrossRef]
56. Talaikis, M.; Strazdaitė, S.; Žiaunys, M.; Niaura, G. Far-Off Resonance: Multiwavelength Raman Spectroscopy Probing Amide Bands of Amyloid-β-(37–42). *Molecules* **2020**, *25*, 3556. [CrossRef]
57. Matulaitienė, I.; Kuodis, Z.; Matijoška, A.; Eicher-Lorka, O.; Niaura, G. SERS of the Positive Charge Bearing Pyridinium Ring Terminated Self-Assembled Monolayers: Structure and Bonding Spectral Markers. *J. Phys. Chem. C* **2015**, *119*, 26481–26492. [CrossRef]
58. Holze, R. The adsorption of thiophenol on gold—A spectroelectrochemical study. *Phys. Chem. Chem. Phys.* **2015**, *17*, 21364–21372. [CrossRef] [PubMed]
59. Nyamekye, C.K.A.; Weibel, S.C.; Smith, E.A. Directional Raman scattering spectra of metal–sulfur bonds at smooth gold and silver substrates. *J. Raman Spectrosc.* **2021**, *52*, 1246–1255. [CrossRef]
60. Vericat, C.; Vela, M.E.; Corthey, G.; Pensa, E.; Cortés, E.; Fonticelli, M.H.; Ibañez, F.; Benitez, G.E.; Carro, P.; Salvarezza, R.C. Self-assembled monolayers of thiolates on metals: A review article on sulfur-metal chemistry and surface structures. *RSC Adv.* **2014**, *4*, 27730–27754. [CrossRef]
61. Bryant, M.A.; Pemberton, J.E. Surface Raman Scattering of Self-Assembled Monolayers Formed from 1-Alkanethiols at Ag. *J. Am. Chem. Soc.* **1991**, *113*, 3629–3637. [CrossRef]
62. Balakrishnan, G.; Jarzecki, A.A.; Wu, Q.; Kozlowski, P.M.; Wang, D.; Spiro, T.G. Mode recognition in UV resonance Raman spectra of imidazole: Histidine monitoring in proteins. *J. Phys. Chem. B* **2012**, *116*, 9387–9395. [CrossRef]
63. Xu, M.; Shashilov, V.; Lednev, I.K. Probing the cross-β core structure of amyloid fibrils by hydrogen-deuterium exchange deep ultraviolet resonance Raman spectroscopy. *J. Am. Chem. Soc.* **2007**, *129*, 11002–11003. [CrossRef] [PubMed]
64. Razmute-Razmė, I.; Kuodis, Z.; Eicher-Lorka, O.; Niaura, G. SERS observation of soft C-H vibrational mode of bifunctional alkanethiol molecules adsorbed at Au and Ag electrodes. *Phys. Chem. Chem. Phys.* **2010**, *12*, 4564–4568. [CrossRef] [PubMed]

Supplementary Data

Electrochemical Shell-Isolated Nanoparticle-Enhanced Raman Spectroscopy of Imidazole Ring Functionalized Monolayer on Smooth Gold Electrode

Agnė Zdaniauskienė [1], Martynas Talaikis [2,*], Tatjana Charkova [1], Rita Sadzevičienė [1], Linas Labanauskas [1], Gediminas Niaura [1,2,*]

[1] Center for Physical Sciences and Technology (FTMC), Department of Organic Chemistry, Sauletekio Ave. 3, LT-10257 Vilnius, Lithuania

[2] Vilnius University, Life Sciences Center, Institute of Biochemistry, Department of Bioelectrochemistry and Biospectroscopy, Sauletekio Ave. 7, LT-10257 Vilnius, Lithuania

*correspondence: martynas.talaikis@gmc.vu.lt; gediminas.niaura@ftmc.lt

Materials and Methods

Synthesis and characterization of N-(2-(1H-imidazol-4-yl)ethyl)-6-mercaptohexanamide (IMHA) and 6-mercapto-N-methylhexanamide (Fragment molecule)

General methods

Compounds NMR spectra were recorded on a Bruker Ascend 400 spectrometer in DMSO-d6 or $CDCl_3$. Chemical shifts are reported in ppm relative to solvent resonance signal as an internal standard. Melting points were recorded in open capillary using Mettler Toledo FP90 Central processor equipped with Mettler Toledo FP81HT MBC Cell and are not corrected. Chromatography was performed using Apollo Scientific Zeoprep 60 35-70 μm silica gel for flash chromatography and Merck TLC Silica gel 60 F_{254} plates for TLC. Starting materials were purchased from Apollo Scientific (histamine dihydrochloride), Alfa Aesar (6-bromohexanoic acid, oxalyl chloride, NaOMe (30% w/w in methanol)), TCI (1-(3-dimethylaminopropyl)-3-ethylcarbodiimide hydrochloride (EDCI Cl), methylamine (40% in methanol, ca 9.8 mol/L) and Sigma Aldrich (thioacetic acid, potassium carbonate, 1,4-dithio-DL-threitol (DTT), dichloromethane, methanol, triethylamine, dimethylformamide (DMF), 4-dimethylaminopyridine (DMAP)). DMSO-d6 (99.5 atom% D) and $CDCl_3$ (99.8 atom% D) for NMR spectroscopy were obtained from Apollo Scientific.

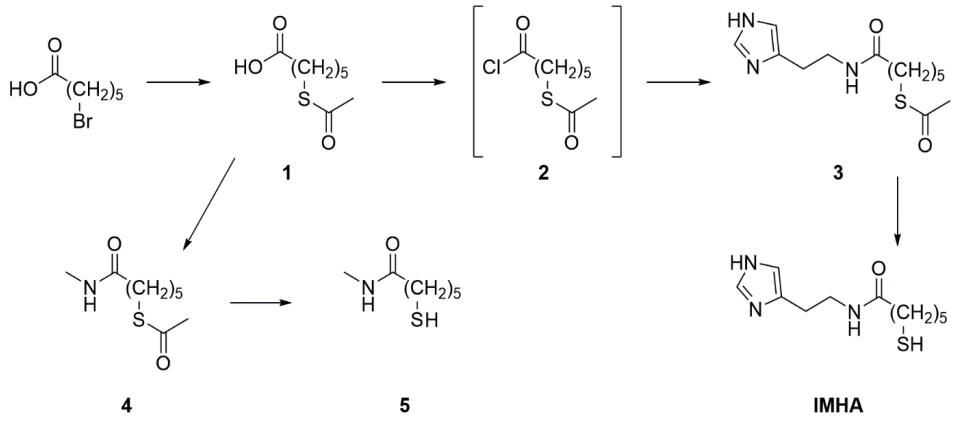

Scheme S1. Synthesis scheme of IMHA compound and fragment molecule **5.**

6-(acetylthio)hexanoic acid (1)

To a solution of K_2CO_3 (9.2 g, 66.6 mmol) in deionized water (30 mL), thioacetic acid (4.3 mL, 61.5 mmol) was added dropwise at 10 °C under argon atmosphere. After 30 min solution of 6-bromohexanoic acid (10 g, 51.3 mmol) and K_2CO_3 (7.09 g, 51.3 mmol) in deionized water (50 mL) was added at 10–12 °C, resulting mixture was stirred at room temperature overnight. Reaction mixture was washed with CH_2Cl_2 (2 × 25 mL) then acidified to pH 2 with 6 M HCl. Product was extracted with CH_2Cl_2 (2 × 50 mL and 1 × 25 mL), washed with water (1 × 50 mL) and brine (1 × 25 mL), dried with anhydrous Na_2SO_4, filtered through a short plug of silica gel. Solvent was evaporated under reduced pressure to afford compound **1** (8.46 g, 86.7%) as light yellow oil.

S-(6-chloro-6-oxohexyl) ethanethioate (2)

To a solution of compound **1** (5 g, 26.4 mmol) and DMF (0.1 mL, 1.31 mmol) in dichloromethane (150 mL), under argon atmosphere, oxalyl chloride (3.4 mL, 39.4 mmol) was added dropwise at 0–3 °C, then stirred at room temperature for 2 hours. Reaction mixture was evaporated to dryness. Obtained intermediate **2** was used immediately in the next step.

S-(6-((2-(1H-imidazol-4-yl)ethyl)amino)-6-oxohexyl) ethanethioate (3)

To a suspension of histamine dihydrochloride (9.67 g, 52.6 mmol) in DMF (52 mL), triethylamine (29.5 mL, 210 mmol) was added under argon atmosphere, than solution of intermediate **2** (all from previous step, 26.4 mmol) in DMF (26 mL) was added dropwise at 0–5 °C, mixture was stirred at the same temperature for 1 hour, then at room temperature overnight. Reaction mixture was diluted with deionized water (150 mL), product was extracted with CH_2Cl_2 (1 × 200 mL) and a mixture of CH_2Cl_2 with MeOH (2 × 100 mL CH_2Cl_2 : 25 mL MeOH). Organic layers were combined, evaporated to dryness and subjected to flash chromatography (CH_2Cl_2/MeOH 90:10) to afford compound **3** (5.42 g, 72.8 %) as white crystals, m.p 114–117 °C, R_f 0.7 (4:1 CH_2Cl_2/MeOH).

^{1}H NMR (400 MHz, DMSO-d_6) δ 11.70 (brs, 1H) 7.83 (s, 1H), 7.52 (s, 1H), 6.78 (s, 1H), 3.23–3.28 (m, 2H), 2.82 (t, J = 7.2 Hz, 2H), 2.62 (t, J = 7.4 Hz, 2H), 2.32 (s, 3H), 2.04 (t, J = 7.4 Hz, 2H), 1.45–

1.53 (m, 4H), 1.23–1.32 (m, 2H). ^{13}C NMR (101 MHz, DMSO-d_6) δ 195.31, 171.80, 134.57, 38.64, 35.21, 30.57, 28.91, 28.26, 27.74, 24.75.

N-(2-(1H-imidazol-4-yl)ethyl)-6-mercaptohexanamide (IMHA)

To a solution of compound **3** (3.5 g, 12.4 mmol) in MeOH (40 mL), under argon atmosphere, NaOMe (9.1 mL, 49.4 mmol, 30% w/w in MeOH) was added dropwise at room temperature, and was allowed to stir overnight. Reaction mixture was cooled in an ice bath, neutralized (~7 pH) with 2 M HCl and brine (10 mL) was added. Product was extracted with CH_2Cl_2 (1 × 100 mL) and a mixture of CH_2Cl_2 with MeOH (50 mL CH_2Cl_2 : 10 mL MeOH). Organic layers were combined and evaporated to dryness. Remaining mixture was dissolved in a mixture of CH_2Cl_2 with MeOH (20 mL CH_2Cl_2 : 5 mL MeOH), DTT (3.8 g, 24.7 mmol) then triethylamine (3.44 mL, 24.7 mmol) was added, and allowed to stir under argon atmosphere overnight. Solvents were evaporated to dryness and subjected to flash chromatography (CH_2Cl_2/MeOH 85:15) to give **IMHA** (1.47 g, 49%) as white crystals, m.p 130–131 °C, R_f 0.65 (4:1 CH_2Cl_2/MeOH).

^{1}H NMR (400 MHz, DMSO-d_6) δ 7.85 (t, J = 5.7 Hz, 1H), 7.52 (d, J = 1.1 Hz, 1H), 6.77 (d, J = 1.1 Hz, 1H), 3.24 (td, J = 7.5, 5.5 Hz, 2H), 2.60 (t, J = 7.4 Hz, 2H), 2.45 (q, J = 7.3 Hz, 2H), 2.21 (t, J = 7.7 Hz, 1H), 2.03 (t, J = 7.3 Hz, 2H), 1.43–1.55 (m, 4H), 1.25–1.33 (m, 2H). ^{13}C NMR (101 MHz, DMSO-d_6) δ 171.88, 134.57, 134.32, 116.89, 38.64, 35.31, 33.12, 27.36, 27.00, 24.74, 23.65.

S-(6-(methylamino)-6-oxohexyl) ethanethioate (4)

To a solution of compound **1** (4.755 g, 25 mmol) in dichloromethane (125 mL), DMAP (0.305 g, 2.5 mmol) and EDCI Cl (6.47 g, 33.75 mmol) was added at 0–5 °C under argon atmosphere. Then methylamine (40% solution in MeOH, 3.82 mL, 37.5 mmol) was added dropwise followed by addition of triethylamine (5.23 mL, 37.5 mmol) at 0–5 °C and left to stir at room temperature for 24 hours. Reaction mixture was washed with water (1 × 20 mL), 1 M HCl (2 × 25 mL), saturated $NaHCO_3$ with brine (1 × 50 mL, 1:1) and dried with anhydrous Na_2SO_4. Solvent was evaporated to dryness and subjected to flash chromatography (CH_2Cl_2/MeOH 96:4) to give product **4** (3.86 g, 76% yield, containing 5% of compound **5**) as white crystals, R_f 0.35.

^{1}H NMR (400 MHz, $CDCl_3$) δ 5.83 (s, 1H), 2.83 (t, *J* = 7.3 Hz, 2H), 2.78 (d, *J* = 3.8 Hz, 3H), 2.30 (s, 3H), 2.17 (t, *J* = 7.6 Hz, 2H), 1.67–1.53 (m, 4H), 1.41–1.35 (m, 2H). ^{13}C NMR (101 MHz, $CDCl_3$) δ 196.14, 173.74, 36.34, 30.74, 29.34, 28.94, 28.41, 26.42, 25.27.

6-mercapto-N-methylhexanamide (5) (Fragment molecule)

To a solution of compound **4** (3 g, 14.78 mmol) in MeOH (40 mL), under argon atmosphere, NaOMe (2.8 mL, 14.78 mmol, 30% w/w in MeOH) was added dropwise at room temperature, and was allowed to stir for 2 hours. Solvent was evaporated and remaining mixture was dissolved in water (20 mL) and acidified with 3 M HCl (5 mL). Product was extracted with CH_2Cl_2 (3 × 30 mL), washed with brine (1 × 10 mL), dried with anhydrous Na_2SO_4. Solvent was evaporated to dryness under reduced pressure. Remaining mixture was dissolved in CH_2Cl_2 (20 mL), DTT (1.13 g, 7.38 mmol) then triethylamine (1.03 mL, 7.38 mmol) was added, and allowed to stir under argon atmosphere overnight. Reaction mixture was washed with 0.5 M HCl (1 × 10 mL), 0.25 M HCl (2 × 20 mL), water (1 × 20 mL), dried with anhydrous Na_2SO_4. Solvent was evaporated to dryness and subjected to flash chromatography (CH_2Cl_2/MeOH 97:3) to give product **5** (1.88 g, 79%) as white crystals, m.p 30–31 °C, R_f 0.36 (96:4 CH_2Cl_2/MeOH).

^{1}H NMR (400 MHz, DMSO-d_6) δ 7.68 (s, 1H), 2.54 (d, *J* = 4.6 Hz, 3H), 2.45 (q, *J* = 7.3 Hz, 2H), 2.20 (t, *J* = 7.6 Hz, 1H), 2.03 (t, *J* = 7.4 Hz, 2H), 1.55–1.43 (m, 3H), 1.33–1.26 (m, 2H). ^{13}C NMR (101 MHz, DMSO-d_6) δ 172.41, 35.21, 33.10, 27.42, 25.38, 24.71, 23.63.

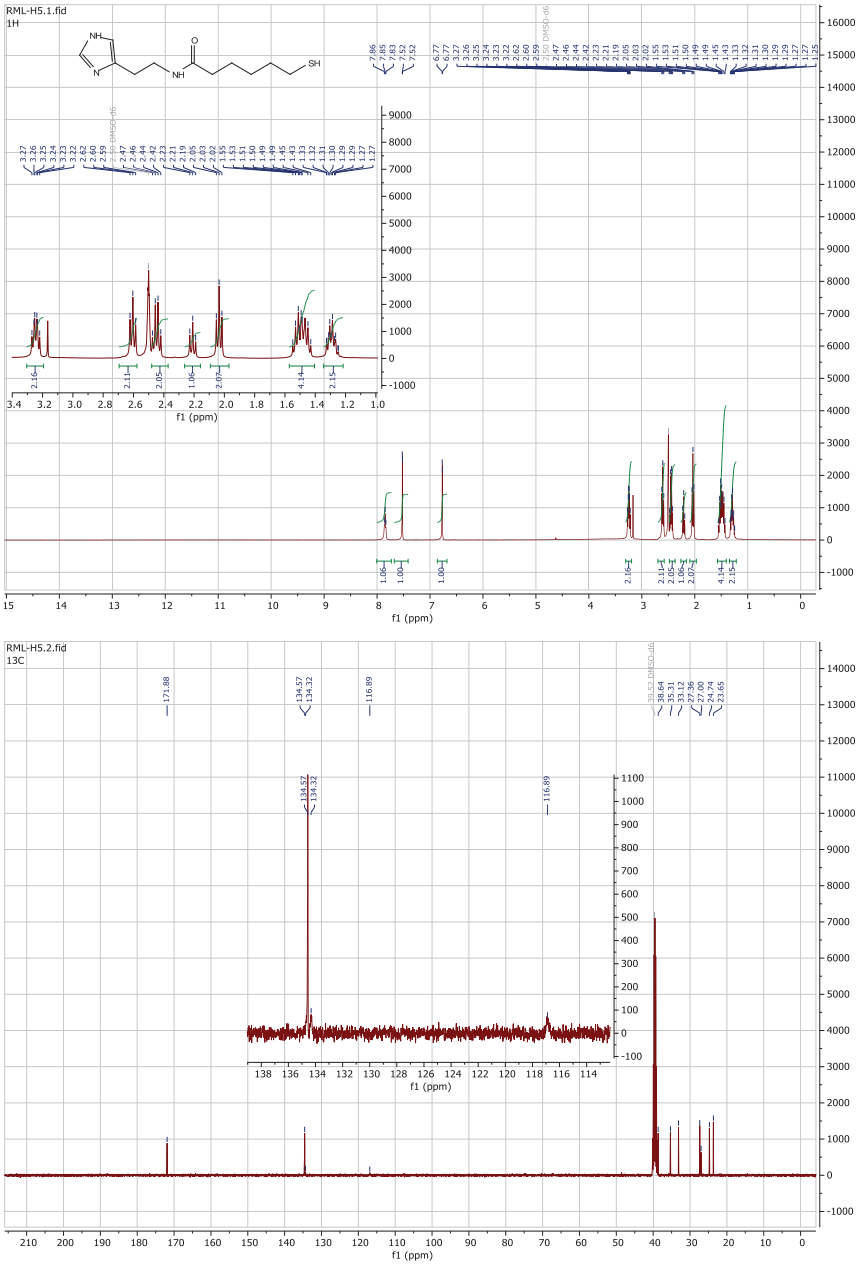

Figure S1. ^{1}H NMR and ^{13}C NMR spectra of N-(2-(1H-imidazol-4-yl)ethyl)-6-mercaptohexanamide (IMHA).

Results

Assignments of Raman Bands

Figure S2 compares Raman spectra of powder IMHA, fragment molecule, and histidine and the spectra of fragment molecule dissolved in H_2O and D_2O. Figure S2A compares spectra of Im-molecules (His and IMHA) with a spectrum of fragment molecule, which allows to identify Raman bands related with Im ring vibrations. Spectra in Figure S2B of powder fragment molecule and dissolved in H_2O and D_2O allow to ascertain the amide and thiol groups related modes. Table 1 presents the spectral band assignment of IMHA based on DFT calculations, temperature-Raman, H_2O/D_2O exchange Raman measurements, and the literature data of similar compounds [1–6].

S–H stretching vibration appears as an intense mode at 2572 cm^{-1}, while corresponding S–D band visible at 1876 cm^{-1} in D_2O solution Raman spectrum of fragment molecule (Figure S2B). Alkanethiol-universal C–S stretching duplet of $–CH_2–CH_2–S–$ moiety in gauche/trans conformations, which is typically found in 600–750 cm^{-1} region, is less straightforward to identify, because the same spectral region is occupied by rocking vibrations of five-methylene-segment and Im deformations. The rocking motion is highly sensitive to the packing of carbohydrate chains [7], thus the initially sharp and separated bands become broadened with the melting of the IMHA. The 653 cm^{-1} mode appears as medium intensity feature in IMHA and L-histidine spectra and as a very weak mode in fragment molecule spectrum in Figure S2A. We tentatively assigned it to Im ring motion with some character expected from the stretching of S–C in gauche conformation. This band becomes greatly intensified with the fragment compound dissolution in H_2O (Figure S2B) suggesting that C–S bond undergoes isomerization reaction from gauche to trans. Notably, in D_2O solvent this band is less intense and upshifted by 5 cm^{-1} due to the decoupling of vibrational modes. Such a frequency upshift induced by D_2O/H_2O exchange was observed previously for the $\nu(C–S)_G$ mode of cysteamine cation ($SH–CH_2–CH_2–NH_3^+$) [8]. Similarly, in temperature-Raman measurements the mode at 654 cm^{-1} intensify when IMHA is heated to a melting point. Thus, we conclude the 653 cm^{-1} band's assignment to the Im motion + $\nu(C–S)_G$. Based on H_2O/D_2O exchange and temperature-Raman measurements, modes at 732 and 753 cm^{-1} are assigned to methylene rocking, while 711 cm^{-1} mode to $\nu(C–S)_T$. DFT modeling predicts $\nu(C–S)_T$ at 712 cm^{-1} (potential energy distribution, PED = 50%).

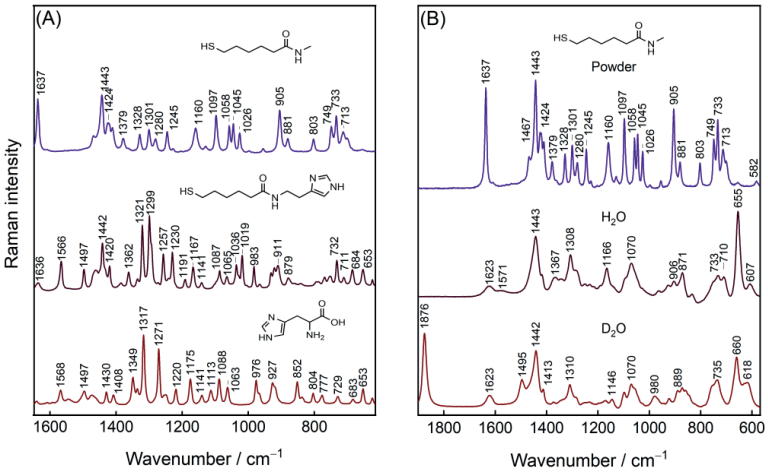

Figure S2. (A) Raman spectra of powder IMHA, fragment molecule, and histidine. (B) Raman spectra of powder fragment molecule and the 0.33 M solutions in H_2O and D_2O.

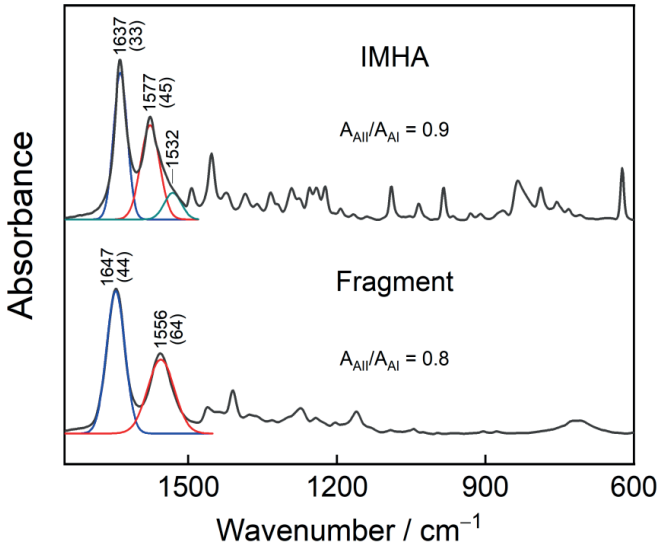

Figure S3. FTIR transmission spectra of IMHA and fragment molecule powders dispersed in KBr pellets. Am-I and Am-II spectral modes were approximated using Gaussian shape components. The full-widths at half maxima of Am-I and Am-II bands are given next to corresponding wavenumbers.

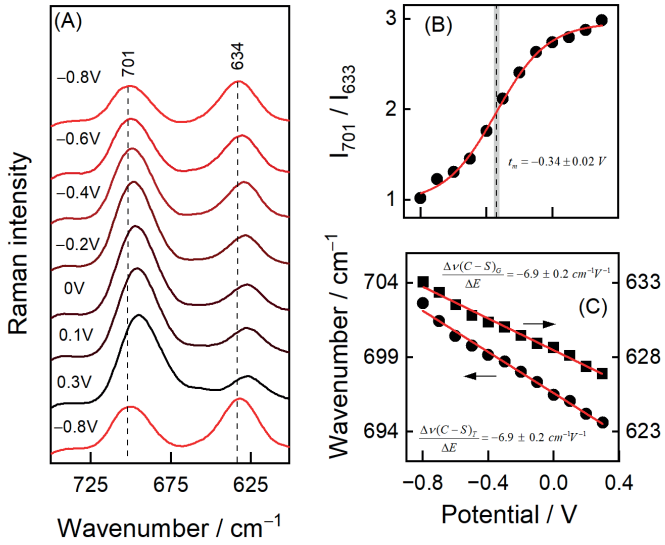

Figure S4. (A) SHINERS spectra of IMHA adsorbed on smooth Au electrode at indicated potentials in the 600–750 cm^{-1} spectral region. Spectra were recorded in 0.1 M Na_2SO_4 aqueous solution containing 0.01 M phosphate buffer (pH 7). The excitation wavelength was 785 nm. (B) Dependence of relative integrated intensity I_{701}/I_{633} ratio of IMHA bands on electrode potential fitted with the sigmoidal curve (Boltzmann model, R^2= 0.99658). The transition midpoint potential value was determined at –0.34 ± 0.02 V, shown by the dashed line. The grey bar around the midpoint line shows the error in the fitting value. (C) Dependence of $\nu(C–S)_G$ and $\nu(C–S)_T$ modes wavenumbers of IMHA on electrode potential. Data in **(B)** and **(C)** sections were presented as an average of three independent measurements.

References

1. Ashikawa, I.; Itoh, K. Raman spectra of polypeptides containing L-histidine residues and tautomerism of imidazole side chain. *Biopolymers* **1979**, *18*, 1859–1876. https://doi.org/10.1002/bip.1979.360180804.
2. Matulaitienė, I.; Kuodis, Z.; Eicher-Lorka, O.; Niaura, G. SERS characterization of imidazole ring terminated self-assembled monolayer formed from lipoic acid histamide on silver electrode. *J. Electroanal. Chem*. **2013**, *700*, 77–85. https://doi.org/10.1016/j.jelechem.2013.04.017.
3. Mesu, J.G.; Visser, T.; Soulimani, F.; Weckhuysen, B.M. Infrared and Raman spectroscopic study of pH-induced structural changes of L-histidine in aqueous environment. *Vib. Spectrosc*. **2005**, *39*, 114–125. https://doi.org/10.1016/j.vibspec.2005.01.003.
4. Matulaitienė, I.; Pociūtė, E.; Kuodis, Z.; Eicher-Lorka, O.; Niaura, G. Interaction of 4-imidazolemethanol with a copper electrode revealed by isotope-edited SERS and theoretical modeling. *Phys. Chem. Chem. Phys*. **2015**, *17*, 16483–16493. https://doi.org/10.1039/c5cp01290b.
5. Toyama, A.; Ono, K.; Hashimoto, S.; Takeuchi, H. Raman spectra and normal coordinate analysis of the N1-H and N3-H tautomers of 4-methylimidazole: Vibrational modes of histidine tautomer markers. *J. Phys. Chem. A*. **2002**, *106*, 3403–3412. https://doi.org/10.1021/jp0124185
6. Niaura, G. **2014**. "Raman Spectroscopy in Analysis of Biomolecules." In Encyclopedia of Analytical Chemistry, 1–34. John Wiley & Sons, Ltd. https://doi.org/10.1002/9780470027318.a0212.
7. Nelson, P.N. Chain Length and Thermal Sensitivity of the Infrared Spectra of a Homologous Series of Anhydrous Silver(I) n –Alkanoates. *Int. J. Spectrosc*. **2016**, *2016*, 1–9. https://doi.org/10.1155/2016/3068430.
8. Riauba, L.; Niaura, G.; Eicher-Lorka, O.; Butkus, E. A study of cysteamine ionization in solution by Raman spectroscopy and theoretical modeling. *J. Phys. Chem. A*. **2006**, *110*, 13394–13404. https://doi.org/10.1021/jp063816g.

*these references are also cited in the Manuscript.

materials

MDPI

Article

Shell-Isolated Nanoparticle-Enhanced Raman Spectroscopy for Probing Riboflavin on Graphene

Agnė Zdaniauskienė [1], Ilja Ignatjev [1], Tatjana Charkova [1], Martynas Talaikis [1], Algimantas Lukša [2], Arūnas Šetkus [2] and Gediminas Niaura [1,*]

[1] Department of Organic Chemistry, Center for Physical Sciences and Technology (FTMC), LT-10257 Vilnius, Lithuania; agne.zdaniauskiene@ftmc.lt (A.Z.); ilja.ignatjev@ftmc.lt (I.I.); tatjana.charkova@ftmc.lt (T.C.); martynas.talaikis@gmc.vu.lt (M.T.)

[2] Department of Physical Technologies, Center for Physical Sciences and Technology (FTMC), LT-10257 Vilnius, Lithuania; algimantas.luksa@ftmc.lt (A.L.); arunas.setkus@ftmc.lt (A.Š.)

* Correspondence: gediminas.niaura@ftmc.lt

Abstract: Graphene research and technology development requires to reveal adsorption processes and understand how the defects change the physicochemical properties of the graphene-based systems. In this study, shell-isolated nanoparticle-enhanced Raman spectroscopy (SHINERS) and graphene-enhanced Raman spectroscopy (GERS) coupled with density functional theory (DFT) modeling were applied for probing the structure of riboflavin adsorbed on single-layer graphene substrate grown on copper. Intense and detailed vibrational signatures of the adsorbed riboflavin were revealed by SHINERS method. Based on DFT modeling and detected downshift of prominent riboflavin band at 1349 cm^{-1} comparing with the solution Raman spectrum, π-stacking interaction between the adsorbate and graphene was confirmed. Different spectral patterns from graphene-riboflavin surface were revealed by SHINERS and GERS techniques. Contrary to GERS method, SHINERS spectra revealed not only ring stretching bands but also vibrational features associated with ribityl group of riboflavin and D-band of graphene. Based on DFT modeling it was suggested that activation of D-band took place due to riboflavin induced tilt and distortion of graphene plane. The ability to explore local perturbations by the SHINERS method was highlighted. We demonstrated that SHINERS spectroscopy has a great potential to probe adsorbed molecules at graphene.

Keywords: SHINERS; GERS; DFT; riboflavin; ribityl; graphene; Raman

Citation: Zdaniauskienė, A.; Ignatjev, I.; Charkova, T.; Talaikis, M.; Lukša, A.; Šetkus, A.; Niaura, G. Shell-Isolated Nanoparticle-Enhanced Raman Spectroscopy for Probing Riboflavin on Graphene. *Materials* **2022**, *15*, 1636. https://doi.org/10.3390/ma15051636

Academic Editor: Polina P. Kuzhir

Received: 26 January 2022
Accepted: 19 February 2022
Published: 22 February 2022

1. Introduction

Electronic properties and function of graphene depend on the surface structure, origin of the defects [1,2], doping type and nature of dopants [3–6], and adsorption of molecules and ions at the surface [7,8]. Adsorbed molecules may modify the carrier mobility of underlying graphene layer [8]. In the case of uncontrolled adsorption it is difficult to construct electronic systems with predictable and reliable properties. Graphene science and development of graphene-based technologies require to control adsorption processes and understanding how the defects and impurities modify physico-chemical properties of these systems at molecular level [9]. It was revealed that adsorbed aromatic molecules on single layer graphene modulate Fermi energy [10]. Furthermore, in order to increase the lithium storage capacity of graphene nanosheets in rechargeable lithium-ion batteries, it is necessary to modify the structure of the graphene [11]. Therefore, understanding the surface and interface chemistry of graphene-based systems is an important topic in physical chemistry and material science.

Raman spectroscopy is a non-destructive, sensitive, and powerful technique able to provide detailed structural information about various carbon nanostructures [12,13]. In addition, resonance Raman investigations can afford important information about the electronic structure of the material [14]. Because of extended π-electron system of graphene

and graphene oxide, excitation in the visible spectral region affords resonantly enhanced Raman spectra [12,14]. Nevertheless, resonance Raman spectroscopy provides information on the structure of graphene skeleton [12]; usually, no direct information on the structure of molecular groups covalently attached to the carbon matrix or adsorbed compounds can be acquired. In some cases, adsorbed organic molecules can be probed by graphene-enhanced Raman spectroscopy (GERS) [15–21]. In GERS the dominant Raman signal enhancement mechanism is chemical enhancement due to charge transfer excitation [17,21]. Thus, the enhancement strongly depends on (i) appropriate energy levels of adsorbate and (ii) the structure of the molecule [17]. Flat molecules possessing D_{nh} symmetry are favorable because of better compatibility with graphene structure [17]. Being dependent on chemical enhancement mechanism, GERS demonstrate distinctive molecular selectivity [16].

To observe functional groups of graphene oxide, adsorbed impurities or purposely-adsorbed compounds on graphene, the alternative spectroscopic technique is required. Recently, Tian et al. approached a novel surface-enhanced Raman spectroscopy (SERS) technique and called it "shell-isolated nanoparticle-enhanced Raman spectroscopy" (SHINERS) [22]. The method is based on the enhancement of Raman signal by strong electromagnetic field provided by metallic core nanoparticles surrounded by a few nanometer thick dielectric shell [22–28]. Dielectric shell-covered nanoparticles have significant advantages over bare nanoparticles. The inert shell prevents the interaction between the metal core and the system. Moreover, the shell protects the core from aggregation, oxidation, and also from contaminating the system under study. SHINERS has been used to obtain molecular-level knowledge of a diverse set of surfaces, from adsorbates on flat meta-single-crystals to semiconductors and from food samples to spectroscopic analysis of living cells and detection of circulating tumor cells in blood [23–35].

Riboflavin (Rf) or vitamin B_2 is a water-soluble vitamin that plays an essential role in cellular biochemistry [36]. Renewed interest in its monitoring and investigation of molecular interactions stems from the important role of Rf in the prevention of health diseases like migraine, cancer, hypertension, and chronic diseases associated with oxidative stress [37]. Rf can be employed in electrochemistry for different purposes as well as it can be detected electrochemically due to its aromatic nature (Figure 1). Previously, we investigated electropolymerisation of riboflavin in diverse media [38]. Riboflavin films were characterized spectroscopically, microscopically, and electrochemically. Promising sensors may be constructed from hybrid Rf-graphene conjugates. For a molecular-level understanding of the bonding and structure of adsorbed Rf, vibration spectroscopy seems to be very promising. However, it was hard to research adsorbed Rf onto highly oriented pyrolytic graphite by Raman spectroscopy [38]. Thus, surface-enhanced Raman spectroscopy methods should be applied.

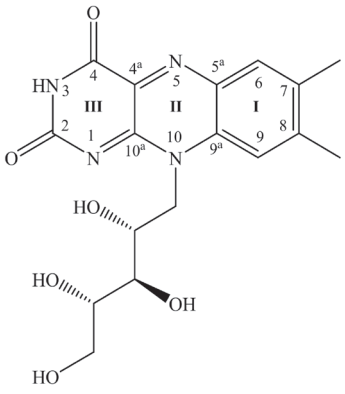

Figure 1. Riboflavin molecular structure and numbering of isoalloxazine ring atoms.

The main aim of our work was to demonstrate the applicability of the SHINERS technique to acquire molecular-level information for adsorbed Rf on the graphene surfaces. The detailed insights into the interaction of Rf and graphene are provided from the analysis of coupled SHINERS, GERS, and DFT modeling approaches.

2. Materials and Methods

2.1. Materials

All used reagents and solvents (Merck, Darmstadt, Germany) were used without further purifications: gold (III) chloride trihydrate ($HAuCl_4 \cdot 3H_2O$, 99%), trisodium citrate dihydrate ($HOC(COONa)(CH_2COONa)_2 \cdot 2H_2O$, 99%), (3-aminopropyl)trimethoxysilane ($H_2N(CH_2)_3Si(OCH_3)_3$, APTMS, 97%), sodium silicate solution (10% NaOH, 27% SiO_2). Graphene substrate was received from Graphenea (Donostia-San Sebastian, Spain), and riboflavin was obtained from Alfa Aesar (Ward Hill, MA, USA). All solutions were prepared with ultrapure water (resistivity of 18.2 MΩ cm) from Direct-Q 3UV (Merck, Darmstadt, Germany) water purification system.

2.2. Synthesis of Silicon Dioxide Covered Spherical Gold Nanoparticles

Initially, 50 mL of an aqueous $HAuCl_4$ solution (0.01 wt%) was brought into a round-bottom flask and boiled in an oil bath (150 °C) with vigorous stirring. The solution reached boiling temperature in 3 min. Then 0.35 mL of sodium citrate (1 wt%) were quickly added into the boiling solution and the mixture was refluxed for 30 min. Next, the solution was left to attain room temperature (about 2 h); so the red colloid of gold nanoparticles (Au NPs) was obtained. For the growth of an ultrathin layer of silicon dioxide over nanoparticles, 0.6 mL APTMS (1 mM) was added to 45 mL of Au NPs. The mixture was vigorously stirred for 15 min; then 4.8 mL of sodium silicate solution (0.54% wt/wt) was added and the mixture was stirred again for 3 min at room temperature. The flask was placed in an 85–90 °C water bath and stirred for 45 min. Then, to stop the reaction process, the flask was placed in the ice bath (3 °C) for 30 min. The cold mixture was transferred into several 1.5 mL test tubes and centrifugated at 5500 rpm for 15 min. After that, the supernatant was removed, the 1.5 mL of water was added, and nanoparticles were dispersed again. Next, tubes were centrifuged for another 15 min and supernatant was removed again to obtain $Au@SiO_2$ nanoparticles as a concentrated colloidal suspension. Therefore, cleaned $Au@SiO_2$ nanoparticles were kept in the dark at low temperature (5 °C) until were used in SHINERS experiments.

2.3. High-Resolution Transmission Electron Microscopy (HR-TEM)

High-resolution transmission electron microscopy (HR-TEM) image was recorded by Tecnai G2 F20 X-TWIN microscope (FEI, Eindhoven, The Netherlands) equipped with scanning TEM module and high-angle annular dark-field detector for Z-contrast imaging. FEI Helios Nanolab 650 dual beam microscope with an Omniprobe manipulator (FEI, Eindhoven, The Netherlands) was employed to prepare specimens for the measurement.

2.4. Riboflavin Adsorption

Commercially available graphene substrate grown onto Cu foil was washed with water. Chemisorbed riboflavin layer onto graphene substrate was formed in 1 mM riboflavin water solution for 14 h. Later it was washed with ultrapure water and dried at room temperature in a fume hood for about 30 min. For SHINERS experiments, 5 µL of concentrated $Au@SiO_2$ solution were dropped onto pure graphene and adsorbed riboflavin onto graphene substrate surfaces and dried in a fume hood for about 30 min.

2.5. Raman Measurements

The GERS and SHINERS spectra were recorded by inVia Raman (Renishaw, Wotton-under Edge, UK) spectrometer equipped with thermoelectrically cooled to −70 °C CCD camera and a confocal Leica microscope. Two different wavelengths, 785 and 532 nm laser beams were used as the excitation source. The 180 °C scattering geometry was employed in Raman spectroscopy studies. The 50×/0.75 NA objective lens and 1200 lines/mm (for 785 nm) and 1800 lines/mm (for 532 nm) gratings were exploited to record the Raman spectra. Laser power at the sample surface was restricted to 0.9 and 0.6 mW for 785 and 532 nm excitations, respectively. Raman scattering wavenumber axis was calibrated by using the silicon peak at 520.7 cm^{-1} or by recording the polystyrene standard (ASTM E 1840) Raman spectrum. Raman spectra were corrected by polynomial function background subtraction. The GERS spectra were recorded by using 532 nm excitation wavelength, while 785 nm wavelength was applied for acquisition the SHINERS spectra. Integration time was 10 s and each spectrum was recorded by accumulation of 10 scans yielding total 100 s collection time. Both SHINERS and GERS spectra were normalized to 1 s intensity. No smoothing procedures were applied to the experimental data.

Raman spectra of riboflavin powder and riboflavin solution were recorded by using HyperFlux PRO Plus (Tornado Spectral Systems, Mississauga, ON, Canada) spectrometer at 785 nm excitation. Laser powers were 15 mW for Rf powder and 495 mW for Rf-water solution of approximately 0.3 mM. The overall accumulation time was 37.5 and 1375 s for Rf powder and Rf-water solution spectra, respectively. For excitation and collection of the Raman spectra, the fiber-optic cable was employed. The laser beam was focused to a 100 μm diameter spot. The calibration of the wavenumber axis was confirmed with the polystyrene standard (ASTM E 1840) spectrum.

Parameters of the vibrational bands were determined by fitting the experimental spectra with Gaussian-Lorentzian shape components using GRAMS/A1 8.0 software (Thermo Scientific, Waltham, MA, USA).

2.6. Theoretical Modeling

Molecular interactions of hydrogen-terminated graphene nanosheet $C_{54}H_{18}$ and riboflavin in the gas phase were modeled using Orca 5.0.1 software [39]. We used B3LYP functional with split-valence Pople and all-electron Karlsruhe basis sets. It is known that DFT theory inaccurately describes weak interactions, therefore the Becke-Johnson damping method (D3BJ) was included in computations to correct for missing dispersion forces. Molecular optimization was done and energies were calculated using Pople's 6-311G(d,p) basis set; to complement the results separate molecular optimization was carried out at def2-SVP basis set level followed by the estimation of electronic properties using the def2-TZVP. The adsorption energy E_{ad} was calculated according to the relation:

$$E_{ad} = E_{G-Rf} - \left(E_G + E_{Rf}\right) - \partial_{BSSE} \quad (1)$$

where $E_{G\text{-}Rf}$, E_G, and E_{Rf} are energies for graphene-riboflavin complex, graphene, and riboflavin. The basis set superposition error (BSSE) was corrected by a counterpoise method that introduces ∂_{BSSE} to Equation (1) [40]. Vibrational spectra were obtained at B3LYP/6-31G(d) after the geometry optimization at the same level. Theoretical spectra include (1) Rf in gas phase, (2) Rf in water simulated by conductor-like polarizable continuum model (CPCM), and (3) Rf in complex with graphene (G). The (3) was achieved by full optimization of G-Rf complex followed by freezing the G and numerical calculation of Rf frequencies. All the vibrational spectra were completed with no imaginary frequencies. The intensities and frequencies were scaled [41]. Total density of states (TDOS) and partial density of states (PDOS) [42] were calculated using Multiwfn 3.8 software (2021, Beijing Kein Research Center for Natural Sciences, Beijing, China) by means of the SCPA method [43]. Visualizations were made using ChemCraft 1.8 software (2021, Grigoriy A. Andrienko, Ivanovo, Russia) [44].

3. Results and Discussion

3.1. GERS Spectra of Riboflavin on Graphene

Figure 2 compares 532-nm excited resonance Raman spectra of graphene on a copper substrate before treatment with riboflavin solution and after the riboflavin adsorption. In the spectral region from 1200 to 3000 cm^{-1} (Figure 2a) the dominant feature at 2664 cm^{-1} visible in the spectrum of the substrate before treatment with riboflavin solution is associated with prominent 2D-band of graphene structure [12,45,46]; while the G-band appears at 1587 cm^{-1}. Both 2D and G-bands are always allowed in the resonance Raman spectra. No D-band associated with presence of defects is visible in the vicinity of 1350 cm^{-1}. The intensity ratio I(2D)/I(G) can be used for the evaluation of the number of graphene layers [45]. In the case of the monolayer, the I(2D)/I(G) > 1 and the 2D band must be fitted by using one Lorentzian form component [14]. For our studied sample, we found I(2D)/I(G) = 1.8 and Lorentzian form shape of 2D band. Thus, resonance Raman spectroscopic analysis of substrate sample before riboflavin adsorption revealed presence of high quality (without manifestation of defects) single-layer graphene. Low-frequency Raman spectrum (Figure 2B) exhibits several well-defined bands at 151, 220, and 640 cm^{-1} which are characteristic to Cu_2O compound [47].

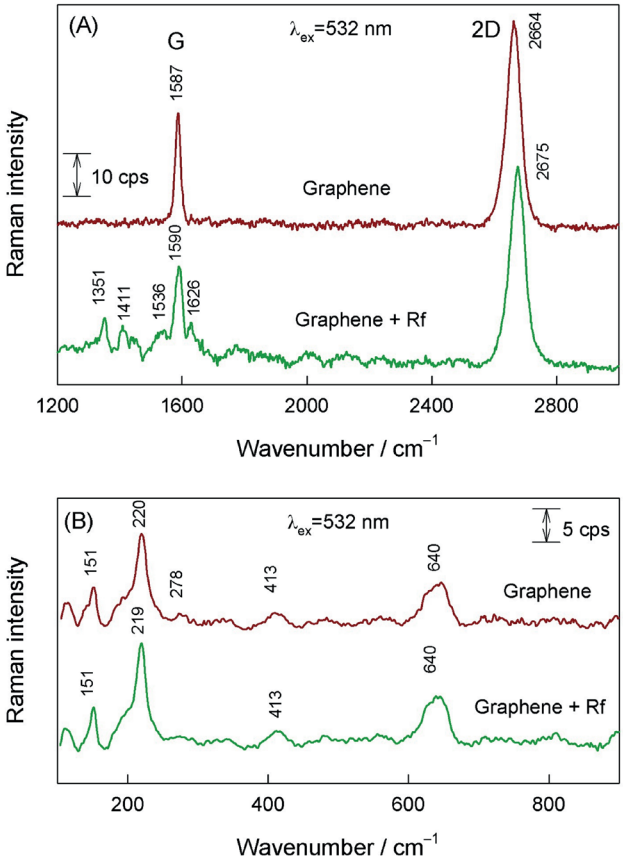

Figure 2. (**a**) Resonance Raman spectra of graphene and graphene with adsorbed riboflavin excited at 532 nm wavelength in the spectral region of 1200–2800 cm^{-1}, and (**b**) in the low frequency spectral region of 100–900 cm^{-1}.

Adsorption of riboflavin induced several clear changes in the high-frequency spectrum (Figure 2a); both characteristic graphene bands were found to be blue shifted and new low-intensity bands became visible in the spectral region 1300–1650 cm^{-1}. Shift of G and 2D bands indicates riboflavin-induced doping of graphene layer. It should be noted that the relative intensity of graphene bands remained similar as before adsorption (I(2D)/I(G) = 1.92). The new bands located at 1351, 1411, and 1536 cm^{-1} are characteristic for riboflavin ring [38] and indicate the Raman scattering enhancement by graphene substrate (GERS). Low frequency spectral region reveals no riboflavin-induced changes in Cu_2O Raman spectrum (Figure 2b). Thus, excitation at 532 nm provides the possibility to detect adsorbed riboflavin through the GERS mechanism, but the intensity of the adsorbate bands was found to be very low. More detailed analysis of riboflavin interaction with graphene substrate will be given later on in this manuscript.

3.2. SHINERS Spectra of Riboflavin on Graphene

To enhance vibrational spectrum of adsorbates on graphene, we have employed SHINERS approach. For this technique, we have prepared highly effective and stable plasmonic nanoparticles with gold core and silica shell, Au@SiO_2. The high-resolution transmission electron microscopy image of Au@SiO_2 nanoparticles is shown in Figure 3a. Image exhibits a dark gold core surrounded by a brighter SiO_2 shell. In SHINERS spectroscopy the parameters of gold core determine the efficiency of plasmonic surface enhancement, while the dielectric shell must prevent from direct interaction of metal with adsorbates and protect from degradation [22–24]. Thus, the shell must be sufficiently thick to eliminate pinholes and sufficiently thin to maintain the high surface enhancement provided by the plasmonic core. Figure 3a shows that the thickness of SiO_2 shell was about 3 nm. The size of nanoparticles was found to be 50 $\pm$ 5 nm. These nanoparticles previously were used for the analysis of self-assembled monolayers on a smooth gold substrate at the electrochemical interface [30] and for spectroscopic characterization of living yeast cells [29].

Because gold nanoparticles support the plasmonic enhancement of electric field in the red and NIR spectral region, we employed 785 nm laser line radiation for excitation of SHINERS spectra. One can see that the bare Au@SiO_2 nanoparticles exhibit low intensity spectral features (Figure 3b). Observed bands may be associated with the adsorbed compounds from the preparation of nanoparticles.

Figure 4A compares SHINERS spectra from the graphene with adsorbed riboflavin (G-Rf) and the graphene substrate before the adsorption (G) with the corresponding Raman spectra observed without the use of the Au@SiO_2 nanoparticles. Only broad band centered near 609–619 cm^{-1} was visible in the Raman spectra of the graphene and the graphene-riboflavin samples. This band evinces the presence of Cu_2O oxide under the graphene layer. Spreading of the Au@SiO_2 nanoparticles over the graphene substrate results in SHINERS spectrum with several clearly-defined bands (Figure 4(a2)). The 1592-cm^{-1} feature was assigned to G-band of graphene monolayer, while the bands in the vicinity of 1303–1336 cm^{-1} might be related with graphene D-band activated by the presence of defects in the vicinity of Au@SiO_2 nanoparticles. Other low intensity bands most likely originate from adsorbed impurities on graphene surface and/or covalently bonded functional groups at graphene plane and impurities from Au@SiO_2 nanoparticles itself. The 1446-cm^{-1} feature falls in the characteristic spectral region of scissoring deformation vibration of CH_2 groups. Different SHINERS spectrum was observed after spreading the Au@SiO_2 nanoparticles on the graphene surface with adsorbed riboflavin (Figure 4(a1)). The most intense band in the spectrum centered at 1349 cm^{-1} can be immediately assigned to riboflavin-related mode by comparing with the Raman spectrum of riboflavin powder (Figure 4B). This band is associated mainly with symmetric stretching ν_s(C2-N3-C4) + stretching of rings I, II, III vibrational mode [38,48–50]. Other riboflavin ring bands are clearly visible at 710, 740, 1158, 1407, 1457, and 1525 cm^{-1}. The band at 1525 cm^{-1} corresponds to stretching vibration of rings I, II, and III, and the 1457 cm^{-1} band to CH_3 deformation vibration coupled stretching vibrations of rings I and II and ribityl bending mode. The 740 cm^{-1} and

710 cm^{-1} modes are ring I in-plane bending and rings I, II, and III in-plane deformation vibrations, respectively. The low-intensity band 1592 cm^{-1} is associated with graphene G-band vibrational mode. The origin of intense bands at 930, 981, and 1048 cm^{-1} is not completely clear; these bands might be related with stretching vibration of ribityl chain. More detailed analysis of spectroscopy of adsorbed riboflavin and effects of interaction with graphene substrate is provided below.

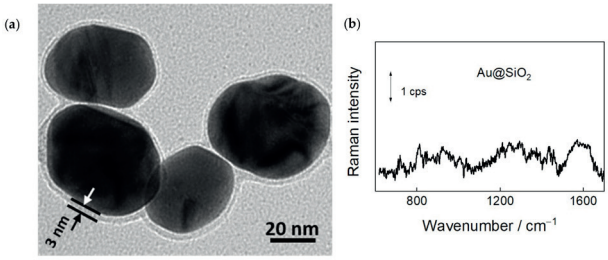

Figure 3. (**a**) High-resolution transmission electron microscopy (HR-TEM) image of $Au@SiO_2$ (50 ± 5 nm) nanoparticles employed in SHINERS experiments; (**b**) SHINERS spectrum of bare $Au@SiO_2$ nanoparticles dispersed on a steel substrate.

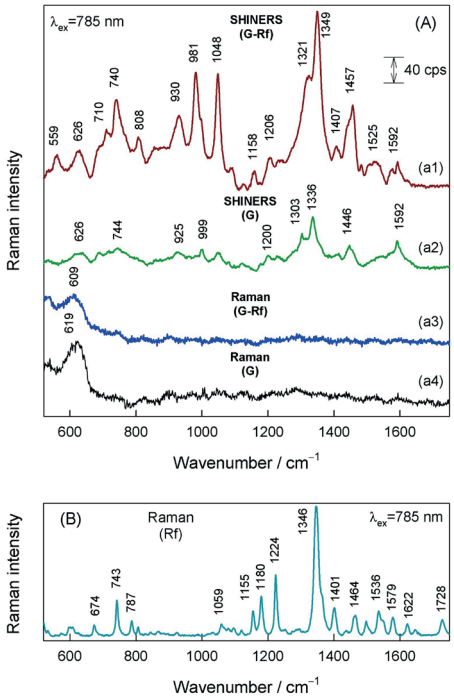

Figure 4. (**A**) SHINERS spectra of (**a1**) riboflavin adsorbed onto graphene with $Au@SiO_2$ nanoparticles, and (**a2**) pure graphene substrate with $Au@SiO_2$ nanoparticles, and Raman spectra of (**a3**) riboflavin adsorbed onto graphene without nanoparticles, and (**a4**) pure graphene substrate without nanoparticles. The luminescence background in spectra (**a3**) and (**a4**) was subtracted by using polynomial function fit. Spectra are shifted vertically for clarity. (**B**) Raman spectrum of riboflavin powder. Excitation wavelength is 785 nm.

3.3. DFT Modelling Predicts Graphene-Riboflavin Interactions

The energy minimization moves riboflavin into the orientation parallel to the graphene nanosheet, with an average 3.3 Å distance between the polycyclic Flavin moiety and the graphene (Table 1). The distance is similar to the ones predicted for similar compounds adsorbed to the graphene [51,52]. The parallel stacked configuration enables the π electron contact of graphene and riboflavin molecules and in such a way facilitates charge transfer (CT), which is considered the main mechanism for GERS [16,21]. The ribityl part of the Rf molecule during the energy minimization also comes into closer contact with the graphene plane, while the graphene slightly tilts and distorts from its initial flat shape (Figure 5).

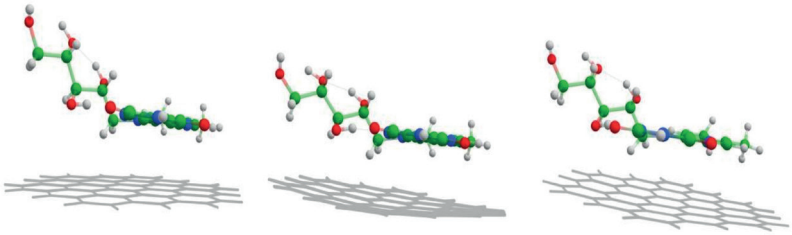

Figure 5. 1st, 15th, and 73rd (converged) geometry optimization steps at B3LYP/6-311G(d,p) theory level. Differences in molecular design are merely for convenience to the eye.

Here, we studied interactions in the gas phase. Calculations predict sufficiently negative adsorption energy E_{ad} of −22.39 for B3LYP/6-311G(d,p) and −33.35 kcal/mol for B3LYP/def2-TZVP basis sets. Generally, adsorption energy can be broken down into physically meaningful stabilizing components: electrostatic, dispersion, polarization, and charge transfer energies, and the stabilization components: Pauli repulsion and preparation energies [51]. The dispersion energy may be attributed to the overlap between the π orbitals of G and Rf. Furthermore, electron charge transfer (CT) is another important factor that facilitates adsorption. Hirshfeld population analysis provides a more robust and basis set-independent CT measure compared with Mulliken population analysis [51,53]. Hirshfeld analysis indicated the formation of donor-acceptor pair through the π-π overlay with a transfer of 0.12e from G to Rf that also adds to the net attractive interaction between the two molecules. These findings are in line with the chemical mechanism of GERS, where electronic coupling between the graphene and adsorbent through the mixing of molecular orbitals and charge transfer is required for enhancement to occur [16,54,55]. For a molecule to undergo GERS-enhancement molecular structure and energy levels have to comply with selection rules [16]. First, graphene's Fermi level must lie within adsorbate's HOMO-LOMO gap, and second, the symmetries of two molecules have to agree.

Table 1. Summary of calculations at B3LYP theory level for the G-Rf complex.

Parameters	6-311G(d,p)	def2-TZVP
d, Å	3.36	3.35
E_{ad}, kcal/mol	−22.39	−33.35
Hirshfeld charge, e	0.12 (G) [1]	0.11 (G) [1]
	−0.12 (Rf) [1]	−0.11 (Rf) [1]
E_{fund}, eV	2.39 (G-Rf) [1]	2.31 (G-Rf) [1]
	2.77 (Rf) [2]	3.43 (Rf) [2]

[1] Optimized in G-Rf complex. [2] Optimized in a gas phase. Abbreviations: E_{ad}, adsorption energy; *d*, the average distance between planes of graphene and the Flavin ring moiety; E_{fund}, fundamental energy gap ($E_{LUMO} - E_{HOMO}$).

To investigate the electronic complex structure, density of states (DOS) plots were constructed. DOS shows the distribution of energy levels that electrons can occupy at a given molecule. DOS could be plotted as total DOS (TDOS) for the full complex and as a partial DOS (PDOS) for individual components of the complex. Figure 6 shows TDOS for the G-Rf complex and PDOS for the G and Rf fragments. From PDOS, the degenerate π-orbital of HOMO and HOMO-1 states are localized at graphene near −5.13 eV, while the LUMO occupy riboflavin Flavin group at −2.73 eV. LUMO+1 and LUMO+2 are graphene's degenerate orbitals near −2.34 eV. The energy of the frontier orbitals provides a measure for ionization potentials (related to E_{HOMO}) and electron affinity (related to E_{LUMO}). The energy difference between HOMO and LUMO is regarded as the fundamental energy gap E_{fund}, which quantitatively determines chemical potential (μ), molecular hardness/softness, and electrophilicity [56]. The smaller E_{fund} signifies the higher molecular reactivity and lower kinetic stability. The predicted E_{fund} for the molecular complexes is 2.39 eV at 6-311G(d,p) and 2.31 eV at def2-TZVP basis sets calculations. These values are smaller compared to those of Rf optimized in the gas phase.

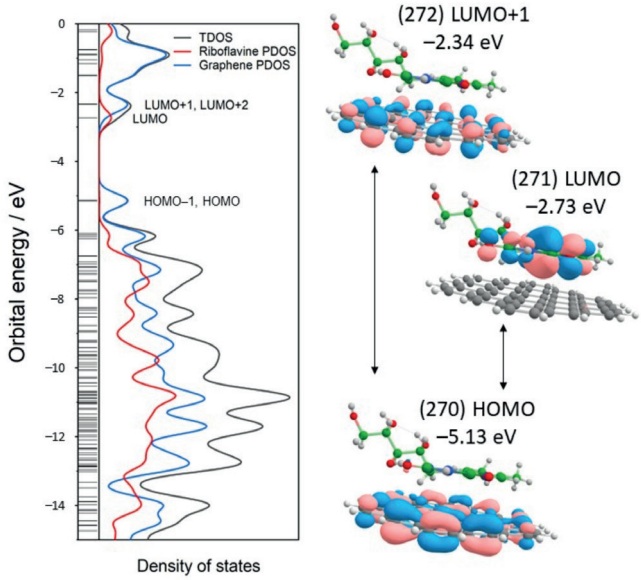

Figure 6. Total and partial density states (TDOS and PDOS) of the graphene-riboflavin complex (**left** panel). Thin horizontal lines indicate molecular orbitals (MOs), while thicker lines—degenerate MOs. HOMO, LUMO, and LUMO+1 are molecular orbitals with their energies indicated (**right** panel). Calculated at B3LYP/6-311G(d,p) theory level.

TD-DFT at B3LYP/6-311G(d,p) was used to calculate the optical gap energies E_{opt} of the G-Rf complex (Table 2). Usually, the E_{opt} is considerably smaller compared to the E_{fund} [57]. TD-DFT predicts several vertical excitations in a visible region for Rf in a gas phase. A very weak transition at 608 nm (f = 0.0003) and stronger at 457 nm (f = 0.1900) ascribed to HOMO→LUMO and HOMO-1→LUMO excitations. For the G-Rf complex, the first transition occurs at 651 nm (f = 0.0015), followed by transition at 639, 433, and 428 nm. These transitions start at different orbitals in the 267−270 range that are mainly located at graphene nanosheet and are targeted to the 271st molecular orbital located at Flavin group. Compared to the sole Rf, the introduction of graphene perturbs its electronic structure that shits absorption to the red and increases the transition probability.

Table 2. Electronic transition wavelengths (λ), energies (E), oscillator strengths (f), and corresponding orbitals of G-Rf complex and Rf in gas phase-optimized form calculated at TD-DFT B3LYP/6-311G(d,p).

G-Rf Complex			Rf (Optimized in a Gas Phase)		
λ, nm (Orbitals)	***E*, eV**	***f***	**λ, nm (Orbitals)**	***E*, eV**	***f***
651 (270 [b]↔271 [a]) [1]	1.904	0.0015	608 (99↔100) [1]	2.037	0.0003
639 (269 [b]↔271 [a])	1.940	0.0022	457 (98↔100)	2.707	0.1900
433 (268 [a,b]↔271 [a])	2.860	0.0007	402 (97↔100)	3.078	0.0495
428 (267 [b]↔271 [a])	2.893	0.0143	394 ((93,94)↔100)	3.145	0.0043

[1] Corresponds to HOMO-LUMO orbitals. [a] Located at Rf. [b] Located at G. ↔ denotes the electronic transition.

Figure 7 compares experimental and calculated Raman spectra of Rf in different environments. The dominant vibration at 1345–1353 cm^{-1} is assigned to the ν_s(C2-N3-C4) + stretching motion of rings I, II, and III (atom numeration in Figure 1) [38,48–50,58]. In fact, DFT predicts several vibrational modes that are related to the ring stretching in a 1365–1380 cm^{-1} spectral region. However, there is a difference between the intensity patterns of experimental and theoretical spectra, which might be assigned to a relatively inexpensive basis set (6-31G(d)) used for modeling. A clear 4 cm^{-1} redshift, which is also supported by DFT, is observed for the Rf transfer from aqueous solution to graphene surface. Such a frequency downshift of the vibrational modes of atoms involved in delocalized π orbitals has been previously linked to π-stacking [58,59], therefore, it is clear experimental evidence for direct Rf and G interaction. The π-stacking is supposed for crystal structure bearing Rf as well. The band in the Rf-crystal spectrum is downshifted by 8 cm^{-1} compared to the one in the solution spectrum. Comparing experimental spectra obtained from Rf in different environments, the bands in the experimental G-Rf spectrum at 1158, 808, and 740 cm^{-1} are assigned to Rf. However, DFT modeling does not predict strong bands in the 900–1000 cm^{-1} spectral region.

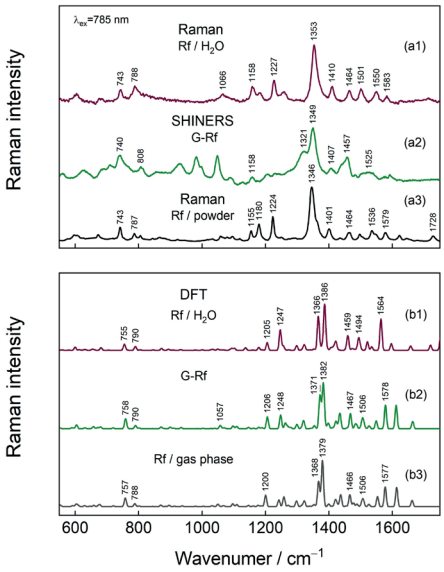

Figure 7. (**a1**) Raman spectra of Rf solution, (**a2**) G-Rf GERS-SHINERS spectrum and (**a3**) Rf powder measured with 785 nm excitation. (**b1**) DFT calculated spectra at 6-31G(d) level of Rf optimized in implicit water modeled using CPCM, (**b2**) G-Rf complex in a gas phase, and (**b3**) Rf in a gas phase.

3.4. Comparison of SHINERS and GERS

SHINERS and GERS spectroscopies exhibit very different spectral patterns from graphen-riboflavin surface. The main observed vibrational features and their assignments are listed in Table 3. GERS spectra were excited with 532 nm wavelength and the enhancement mechanism is associated with the CT excitations. Therefore, only Rf ring vibrational modes of atoms involved in π-electron interaction are enhanced. In contrast, SHINERS spectroscopy based on plasmon-enhancement mechanism provides detailed information not only on the Rf ring vibrational modes but also some vibrations of ribityl chain became visible. In addition, the normalized to laser power relative intensity of the prominent 1349 cm^{-1} band of Rf was found to increase by a factor of 26 in SHINERS spectrum comparing with GERS. In the fingerprint spectral region SHINERS spectrum exhibited three well-defined bands (1048, 981, and 930 cm^{-1}), which were tentatively assigned to vibrational modes having a high contribution from vibration of atoms in ribityl chain (Table 3). Infrared spectrum of riboflavin shows intense bands in the frequency region from 1100 to 1000 cm^{-1} due to vibration of ribityl group [58]. In solution, Raman spectrum intensity of these bands was found to be very low; only the high frequency band was visible near 1066 cm^{-1}. High downshift in frequency suggests the involvement of ribityl chain of riboflavin in interaction with graphene surface. An intriguing observation in SHINERS spectrum is the intense and broad feature near 1321 cm^{-1}. Such band was not observed nor in solution or powder spectra of Rf (Figure 7). We tentatively assign this band to D-mode of graphene substrate. Such band was not visible in the 532 nm-excited resonance Raman spectrum of graphene; however, activation of this band in SHINERS spectrum may be related with riboflavin adsorption induced tilt and distortion of graphene plane in the vicinity of Rf adsorption as predicted by DFT modeling (Figure 5). This observation highlights the ability to probe local perturbations by the SHINERS method.

Table 3. Assignments of vibrational bands observed in SHINERS and GERS study of graphene-riboflavin surface.

Peak Position (cm^{-1})	Raman Spectroscopy Method	Assignment [1]
2675 vs	RRS	2D band; graphene
1590 m/1592 vw	RRS/SHINERS	G band; graphene
1626 w	GERS	Ring I and II stretch; Rf
1536 br, w/1525 br,w	GERS/SHINERS	Ring I, II, and III stretch; Rf
1457 s	SHINERS	CH_3 deformation + Ring I, II stretch + Ribityl bend; Rf
1411 w/1407 w	GERS/SHINERS	CH_3 bend; Rf
1351 w/1349 vs	GERS/SHINERS	C2-N3-C4 symmetric stretch + Ring I, II, III stretch; Rf
1321 s	SHINERS	D band; graphene
1206 w	SHINERS	Ring I breathing + Ring II, III stretch; Rf
1158 w	SHINERS	Ring I, II, III stretch + C2-N3-C4 symmetric stretch; Rf
1048 s	SHINERS	Ring I, II, III stretch; Rf
981 s	SHINERS	C-C + C-O stretch + COH deformation; Rf ribityl [2]
930 m	SHINERS	C-C + C-N stretch + CH2 rock; Rf ribityl [2]
808 w	SHINERS	N-C=O anti-symmetric bend + Ring I, II, III in-plane deformation; Rf
740 s	SHINERS	Ring I in-plane bending; Rf
710 w	SHINERS	Ring I, II, III in-plane deformation; Rf
640 w/626 w	GERS-RRS/SHINERS	Cu_2O
559 w	SHINERS	N-C=O symmetric stretch + Ring I, II, III in-plane deformation; Rf
413 vw	GERS-RRS	Cu_2O
219 m	GERS-RRS	Cu_2O
151 w	GERS-RRS	Cu_2O

[1] Based on reference [58]. [2] Based on DFT calculations of G-Rf complex. Abbreviations: GERS, graphene-enhanced Raman scattering; SHINERS, shell-isolated nanoparticle-enhanced Raman scattering; RRS, resonance Raman scattering; Rf, riboflavin; vs, very strong; s, strong; m, middle; w, weak; vw, very weak; br, broad.

4. Conclusions

In this paper, we provided detailed vibrational spectroscopy study of graphene-riboflavin surface. Several experimental vibrational spectroscopy methods, including ordinary Raman (riboflavin solution and powder spectra), resonance Raman (graphene spectra), graphene-enhanced Raman, and shell-isolated nanoparticle-enhanced Raman spectroscopies were employed to probe the structure and bonding of both single-layer graphene grown on copper and riboflavin adsorbate. We found that riboflavin adsorption induces the blue-shift of the 2D and G bands by 11 and 3 cm^{-1} respectively, indicating doping of the graphene. In addition, well-defined signatures of under-layered Cu_2O oxide were obtained. We demonstrated that contrary to GERS approach, SHINERS method provides more detailed information about the interfaces; not only the riboflavin ring but also vibrational modes of ribityl chain and intense D-band of graphene were detected. DFT modeling suggested that this D-band may be activated because of riboflavin adsorption induced local perturbations (tilt and distortions) in the graphene structure. Our work highlighted the ability of SHINERS spectroscopy to probe the local structural perturbations in graphene.

Author Contributions: A.Z.: investigation, methodology, visualization; writing—original draft preparation; I.I.: Investigation, methodology; T.C.: investigation, visualization; M.T.: investigation, methodology, visualization, formal analysis, software; writing—review and editing; A.L.: investigation, methodology, resources; A.Š.: methodology, resources; G.N.: conceptualization, writing—original draft preparation, writing—review and editing, supervision. All authors have read and agreed to the published version of the manuscript.

Funding: This research received no external funding.

Institutional Review Board Statement: Not applicable.

Informed Consent Statement: Not applicable.

Data Availability Statement: The data presented in this article are available within this article.

Conflicts of Interest: The authors declare no conflict of interest.

References

1. Yang, G.; Li, L.; Lee, W.B.; Ng, M.C. Structure of graphene and its disorders: A review. *Sci. technol. Adv. Mater.* **2018**, *19*, 613–648. [CrossRef] [PubMed]
2. Branhart, F.; Kotakoski, J.; Krasheninnikov, A.V. Structural defects in graphene. *ACS Nano* **2011**, *5*, 26–41. [CrossRef] [PubMed]
3. Lv, R.; Terrones, M. Towards new graphene materials: Doped graphene sheets and nanoribbons. *Mater. Lett.* **2012**, *78*, 209–218. [CrossRef]
4. Lee, H.; Paeng, K.; Kim, I.S. A review of doping modulation in graphene. *Synth. Met.* **2018**, *244*, 36–47. [CrossRef]
5. Guo, Z.; Ni, S.; Wu, H.; Wen, J.; Li, X.; Tang, T.; Li, M.; Liu, M. Designing nitrogen and phosphorus co-doped graphene quantum dots/g-C_3N_4 heterojunction composites to enhance visible and ultraviolet photocatalytic activity. *Appl. Surf. Sci.* **2021**, *548*, 149211. [CrossRef]
6. Sun, L.; Luo, Y.; Li, M.; Hu, G.; Xu, Y.; Tang, T.; Wen, J.; Li, X.; Wang, L. Role of pyridinic-N for nitrogen doped graphene quantum dots in oxygen reaction reduction. *J. Colloid Interf. Sci.* **2017**, *508*, 154–158. [CrossRef]
7. Kong, L.; Enders, A.; Rahman, T.S.; Dowben, P.A. Molecular adsorption on graphene. *J. Phys. Condens. Matter.* **2014**, *26*, 443001. [CrossRef]
8. Phillipson, R.; De la Rosa, C.J.L.; Teyssandier, J.; Walke, P.; Waghray, D.; Fujita, Y.; Adisoejoso, J.; Mali, K.S.; Asselberghs, I.; Huyghebaert, C.; et al. Tunable doping of graphene by using physisorbed self-assembled networks. *Nanoscale* **2016**, *8*, 20017–20026. [CrossRef]
9. Zhao, G.; Li, X.; Huang, M.; Zhen, Z.; Zhong, Y.; Chen, Q.; Zhao, X.; He, Y.; Hu, R.; Yang, T.; et al. The physics and chemistry of graphene-on-surfaces. *Chem. Soc. Rev.* **2017**, *46*, 4417–4449. [CrossRef]
10. Dong, X.; Fu, D.; Fang, W.; Shi, Y.; Chen, P.; Li, L.J. Doping single layer graphene with aromatic molecules. *Small* **2009**, *5*, 1422–1426. [CrossRef]
11. Yoo, E.L.; Kim, J.; Hosono, E.; Zhou, H.S.; Kudo, T.; Honma, I. Large reversible Li storage of graphene nanosheet families for use in rechargeable lithium ion batteries. *Nano Lett.* **2008**, *8*, 2277–2282. [CrossRef] [PubMed]
12. Malard, L.M.; Pimenta, M.A.; Dresselhaus, G.; Dresselhaus, M.S. Raman spectroscopy in graphene. *Phys. Rep.* **2009**, *473*, 51–87. [CrossRef]

13. Lai, H.S.; Xu, F.G.; Zhang, Y.; Wang, L. Recent progress on graphene-based substrates for surface-enhanced Raman scattering applications. *J. Mater. Chem. B* **2018**, *6*, 4008–4028. [CrossRef] [PubMed]
14. Zólyomi, V.; Koltai, J.; Kürti, J. Resonance Raman spectroscopy of graphite and graphene. *Phys. Status Solidi B* **2011**, *248*, 2435–2444. [CrossRef]
15. Brill, A.R.; Biswas, S.; Toroker, M.C.; De Ruiter, G.; Koren, E. Dipole-induced Raman enhancement using noncovalent azobenzene-functionalized self-assembled monolayers on graphene terraces. *ACS Appl. Mater. Interfaces* **2021**, *13*, 10271–10278. [CrossRef]
16. Huang, S.; Ling, X.X.; Liang, L.; Song, Y.; Fang, W.; Zhang, J.; Kong, J.; Meunier, V.; Dresselhaus, M.S. Molecular selectivity of graphene-enhanced Raman scattering. *Nano Lett.* **2015**, *15*, 2892–2901. [CrossRef]
17. Ling, X.; Huang, S.; Deng, S.; Mao, N.; Kong, J.; Dresselhaus, M.S.; Zhang, J. Lighting up the Raman signal of molecules in the vicinity of graphene related materials. *Acc. Chem. Res.* **2015**, *48*, 1862–1870. [CrossRef]
18. De la O-Cuevas, E.; Alvarez-Venicio, V.; Badillo-Raminez, I.; Islas, S.R.; De Pilar Carreón-Castro, M.; Saniger, J.M. Graphene substrates as modifiers of the emission and vibrational responses of interacting molecules: The case of BODIPY dyes. *Spectrochim. Acta A* **2021**, *246*, 119020. [CrossRef]
19. Silver, A.; Kitadai, H.; Liu, H.; Granzier-Nakajima, T.; Terrones, M.; Ling, X.; Huang, S. Chemical and bio sensing using graphene-enhanced Raman spectroscopy. *Nanomaterials* **2019**, *9*, 516. [CrossRef]
20. Shi, H.T.; Zhao, B.F.; Ma, J.; Bronson, M.J.; Cai, Z.; Chen, J.H.; Wang, Y.; Cronin, M.; Jensen, L.; Cronin, S.B. Measuring local electric fields and local charge densities at electrode surfaces using graphene-enhanced Raman spectroscopy (GERS)–based Stark-shifts. *ACS Appl. Mater. Interf.* **2019**, *11*, 36252–36258. [CrossRef]
21. Zhang, N.; Tong, L.; Zhang, J. Graphene-based enhanced Raman scattering toward analytical applications. *Chem. Mater.* **2016**, *28*, 6426–6435. [CrossRef]
22. Li, J.F.; Huang, Y.F.; Ding, Y.; Yang, Z.L.; Li, S.B.; Zhou, X.S.; Fan, F.R.; Zhang, W.; Zhou, Z.Y.; Wu, D.Y.; et al. Shell-isolated nanoparticle-enhanced Raman spectroscopy. *Nature* **2010**, *464*, 392–395. [CrossRef]
23. Anema, J.R.; Li, J.F.; Yang, Z.L.; Ren, B.; Tian, Z.Q. Shell-isolated nanoparticle-enhanced Raman spectroscopy: Extending the versatility of surface-enhanced Raman scattering. *Annu. Rev. Anal. Chem.* **2011**, *4*, 129–150. [CrossRef] [PubMed]
24. Li, J.F.; Tian, X.D.; Li, S.B.; Anema, J.R.; Yang, Z.L.; Ding, Y.; Wu, Y.F.; Zeng, Y.M.; Chen, Q.Z.; Ren, B.; et al. Surface analysis using shell-isolated nanoparticle-enhanced Raman spectroscopy. *Nat. Protoc.* **2013**, *8*, 52–65. [CrossRef] [PubMed]
25. Barbillon, G. Applications of shell-isolated nanoparticle-enhanced Raman spectroscopy. *Photonics* **2021**, *8*, 46. [CrossRef]
26. Krajczewski, J.; Kudelski, A. Shell-isolated Nanoparticle-enhanced Raman spectroscopy. *Front. Chem.* **2019**, *7*, 410. [CrossRef]
27. Li, J.F.; Zhang, Y.J.; Ding, S.Y.; Panneerselvam, R.; Tian, Z.Q. Core-shell nanoparticle-enhanced Raman spectroscopy. *Chem. Rev.* **2017**, *117*, 5002–5069. [CrossRef]
28. Keeler, A.J.; Salazar-Banda, G.R.; Russell, A.E. Mechanistic insights into electrocatalytic reactions provided by SERS. *Curr. Opinion Electrochem.* **2019**, *17*, 90–96. [CrossRef]
29. Zdaniauskienė, A.; Charkova, T.; Ignatjev, I.; Melvydas, V.; Garjonytė, R.; Matulaitienė, I.; Talaikis, M.; Niaura, G. Shell-isolated nanoparticle-enhanced Raman spectroscopy for characterization of living yeast cells. *Spectrochim. Acta A* **2020**, *240*, 118560. [CrossRef]
30. Zdaniauskienė, A.; Charkova, T.; Matulaitienė, I.; Eicher-Lorka, O.; Matijoška, A.; Skapas, M.; Selskis, A.; Niaura, G. Electrochemical shell-isolated nanoparticle-enhanced Raman spectroscopy: Bonding, structure, and ion-pairing of the positive charge bearing [pyridinium ring terminated monolayer at smooth gold electrode. *J. Phys. Chem. C* **2018**, *122*, 1234–1242. [CrossRef]
31. El-Said, W.A.; Alshitari, W.; Choi, J.-W. Controlled fabrication of gold nanopyramids/polypyrrole for shell-isolated nanoparticle-enhanced Raman spectroscopy to detect γ-aminobutyric acid. *Spectrochim. Acta A* **2020**, *229*, 117890. [CrossRef] [PubMed]
32. Puglieri, T.S.; Madden, O.; Andrade, G.F.S. SHINERS in cultural heritage: Can SHINERS spectra always be comparable with normal Raman spectra? Study of alizarin and its adsorption in the silicon dioxide shell. *J. Raman Spectrosc.* **2021**, *52*, 1406–1417. [CrossRef]
33. Boccorh, D.K.; Macdonald, P.A.; Boyle, C.W.; Wain, A.J.; Berlouis, L.E.A.; Wark, A.W. A universal polymer shell-isolated nanoparticle (SHIN) design for single particle spectroelectrochemical SERS sensing using different core shapes. *Nanoscale Adv.* **2021**, *3*, 6415–6426. [CrossRef]
34. Niciński, K.; Krajczewski, J.; Kudelski, A.; Witkowska, E.; Trzcińska-Danielewicz, J.; Girstun, A.; Kamińska, A. Detection of circulating tumor cells in blood by shell-isolated nanoparticle-enhanced Raman spectroscopy (SHINERS) in microfluidic device. *Sci. Rep.* **2019**, *9*, 9267. [CrossRef]
35. Zhang, H.; Yao, J.L.; Li, J.F. Plasmonic core-shell nanomaterials and their applications in spectroscopies. *Adv. Mater.* **2021**, *33*, 2005900. [CrossRef]
36. Cioates, C.N. Review–Electrochemical sensors used in the determination of riboflavin. *J. Electrochem. Soc.* **2020**, *167*, 037558. [CrossRef]
37. Thakur, K.; Tomar, S.K.; Singh, A.K.; Mandal, S.; Arora, S. Riboflavin and health: A review of recent human research. *Crit. Rev. Food Sci. Nutrition* **2017**, *57*, 3650–3660. [CrossRef]
38. Radzevič, A.; Niaura, G.; Ignatjev, I.; Rakickas, T.; Celiešiūtė, R.; Pauliukaite, R. Electropolymerisation of the natural monomer riboflavin and its characterization. *Electrochim. Acta* **2016**, *222*, 1818–1830. [CrossRef]
39. Neese, F. The ORCA program system. *Wiley Interdiscip. Rev. Comput. Mol. Sci.* **2012**, *2*, 73–78. [CrossRef]

40. Boys, S.F.; Bernardi, F. The calculation of small molecular interactions by the differences of separate total energies. Some procedures with reduced errors. *Mol. Phys.* **1970**, *19*, 553–566. [CrossRef]
41. Talaikis, M.; Eicher-Lorka, O.; Valincius, G.; Niaura, G. Water-induced structural changes in the membrane-anchoring monolayers revealed by isotope-edited SERS. *J. Phys. Chem. C* **2016**, *120*, 22489–22499. [CrossRef]
42. Liu, Z.; Lu, T.; Chen, Q. An sp-hybridized all-carboatomic ring, cyclo[18]carbon: Electronic structure, electronic spectrum, and optical nonlinearity. *Carbon* **2020**, *165*, 461–467. [CrossRef]
43. Lu, T.; Chen, F. Multiwfn: A multifunctional wavefunction analyzer. *J. Comput. Chem.* **2012**, *33*, 580–592. [CrossRef] [PubMed]
44. Chemcraft–Graphical Software for Visualization of Quantum Chemistry Calculations. Available online: https//www.chemcraftprog.com (accessed on 25 January 2022).
45. Trusovas, R.; Račiukaitis, G.; Niaura, G.; Barkauskas, J.; Valušis, G.; Pauliukaite, R. Recent advances in laser utilization in the chemical modification of graphene oxide and its applications. *Adv. Optical Mater.* **2016**, *4*, 37–65. [CrossRef]
46. Trusovas, R.; Ratautas, K.; Račiukaitis, G.; Niaura, G. Graphene layer formation in pinewood by nanosecond and picosecond laser irradiation. *Appl. Surf. Sci.* **2019**, *471*, 154–161. [CrossRef]
47. Niaura, G. Surface-enhanced Raman spectroscopic observation of two kinds of adsorbed OH^- ions at copper electrode. *Electrochim. Acta* **2000**, *45*, 3507–3519. [CrossRef]
48. Liu, F.; Gu, H.; Lin, Y.; Qi, Y.; Dong, X.; Gao, J.; Cai, T. Surface-enhanced Raman scattering study of riboflavin on borohydride-reduced silver colloids: Dependence on concentration, halide anions and pH values. *Spectrochim. Acta A* **2012**, *85*, 111–119. [CrossRef]
49. Bowman, W.D.; Spiro, T.G. Normal mode analysis of lumiflavin and interpretation of resonance Raman spectra of flavoproteins. *Biochemistry* **1981**, *20*, 3313–3318. [CrossRef]
50. Lively, C.R.; McFarland, J.T. Assignment and the effect of hydrogen bonding on the vibrational normal modes of flavins and flavoproteins. *J. Phys. Chem.* **1990**, *94*, 3980–3994. [CrossRef]
51. Ghahghaey, Z.; Hekmati, M.; Darvish Ganji, M. Theoretical investigation of phenol adsorption on functionalized graphene using DFT calculations for effective removal of organic contaminants from wastewater. *J. Mol. Liq.* **2021**, *324*, 114777. [CrossRef]
52. Cortés-Arriagada, D. Intermolecular driving forces on the adsorption of DNA/RNA nucleobases to graphene and phosphorene: An atomistic perspective from DFT calculations. *J. Mol. Liq.* **2021**, *325*, 115229. [CrossRef]
53. Hirshfeld, F.L. Bonded-atom fragments for describing molecular charge densities. *Theor. Chim. Acta.* **1977**, *44*, 129–138. [CrossRef]
54. Fesenko, O.; Dovbeshko, G.; Dementjev, A.; Karpicz, R.; Kaplas, T.; Svirko, Y. Graphene-enhanced Raman spectroscopy of thymine adsorbed on single-layer graphene. *Nanoscale Res. Let.* **2015**, *10*, 1–7. [CrossRef] [PubMed]
55. Dolgov, L.; Pidhirnyi, D.; Dovbeshko, G.; Lebedieva, T.; Kiisk, V.; Heinsalu, S.; Lange, S.; Jaaniso, R.; Sildos, I. Graphene-enhanced Raman scattering from the adenine molecules. *Nanoscale Res. Lett.* **2016**, *11*, 1–5. [CrossRef]
56. Rad, A.S.; Shabestari, S.S.; Mohseni, S.; Aghouzi, S.A. Study on the adsorption properties of O_3, SO_2, and SO_3 on B-doped graphene using DFT calculations. *J. Solid State Chem.* **2016**, *237*, 204–210. [CrossRef]
57. Bredas, J.L. Mind the Gap! *Mater. Horizons* **2014**, *1*, 17–19. [CrossRef]
58. Yun, M.J.; Cheong, B.S.; Cho, H.G. Surface-enhanced Raman spectroscopy and density functional theory studies of riboflavin, lumiflavin, and lumichrome adsorbed on silver colloids. *Bull. Korean Chem. Soc.* **2019**, *40*, 1183–1190. [CrossRef]
59. Profit, A.A.; Felsen, V.; Chinwong, J.; Mojica, E.R.E.; Desamero, R.Z.B. Evidence of π-stacking interactions in the self-assembly of HIAPP22-29. *Proteins Struct. Funct. Bioinform.* **2013**, *81*, 690–703. [CrossRef]

Spectrochimica Acta Part A: Molecular and Biomolecular Spectroscopy 240 (2020) 118560

Contents lists available at ScienceDirect

Spectrochimica Acta Part A: Molecular and Biomolecular Spectroscopy

journal homepage: www.elsevier.com/locate/saa

Shell-isolated nanoparticle-enhanced Raman spectroscopy for characterization of living yeast cells

Agnė Zdaniauskienė [a], Tatjana Charkova [a], Ilja Ignatjev [a], Vytautas Melvydas [b], Rasa Garjonytė [a], Ieva Matulaitienė [a], Martynas Talaikis [c], Gediminas Niaura [a,*]

[a] Department of Organic Chemistry, Center for Physical Sciences and Technology (FTMC), Saulėtekio Ave. 3, LT-10257 Vilnius, Lithuania
[b] Nature Research Centre, Akademijos 2, LT-08412 Vilnius, Lithuania
[c] Department of Bioelectrochemistry and Biospectroscopy, Institute of Biochemistry, Life Sciences Center, Vilnius University, Saulėtekio av. 7, LT-10257 Vilnius, Lithuania

ARTICLE INFO

Article history:
Received 9 April 2020
Received in revised form 25 May 2020
Accepted 25 May 2020
Available online 29 May 2020

Keywords:
Metschnikowia pulcherrima yeast
$Au@SiO_2$
SHINERS
SERS
Pulcherrimin

ABSTRACT

Studying the biochemistry of yeast cells has enabled scientists to understand many essential cellular processes in human cells. Further development of biotechnological and medical progress requires revealing surface chemistry in living cells by using a non-destructive and molecular structure sensitive technique. In this study shell-isolated nanoparticle-enhanced Raman spectroscopy (SHINERS) was applied for probing the molecular structure of *Metschnikowia pulcherrima* yeast cells. Important function of studied cells is the ability to eliminate iron from growth media by precipitating the insoluble pigment pulcherrimin. Comparative SERS and SHINERS analysis of the yeast cells in combination with bare Au and shell-isolated $Au@SiO_2$ nanoparticles were performed. It was observed that additional bands, such as adenine ring-related vibrational modes appear due to interaction with bare Au nanoparticles; the registered spectra do not coincide with the spectra where $Au@SiO_2$ nanoparticles were used. SHINERS spectra of *M. pulcherrima* were significantly enhanced comparing to the Raman spectra. Based on first-principles calculations and 830-nm excited Raman analysis of pulcherrimin, the SHINERS signatures of iron pigment in yeast cells were revealed. Being protected from direct interaction of metal with adsorbate, $Au@SiO_2$ nanoparticles yield reproducible and reliable vibrational signatures of yeast cell wall constituents.

1. Introduction

The yeast cells are one of the most extensive model eukaryotic systems for basic and applied biotechnology and medicine. Living cells and microorganisms immobilized on different substrates are often applied in the design of bioelectronic devices, which are suitable for application in various fields such as bioanalysis, biosensing, environment safety, human food (wine, beer, bread etc.), and animal feed industrial processes [1–5]. In particular, yeast *Saccharomyces cerevisiae* have been used to process food and alcoholic beverages for centuries [6]. Other yeast species such as *Metschnikowia pulcherrima* (*Candida pulcherrima*) have recently become increasingly important [7]. When grown on media containing iron (III) salts, this yeast is able to form an insoluble red pigment pulcherrimin. Pulcherrimin is a ferric chelate or a salt of pulcherriminic acid (2,5-diisobutyl-3,6-dihydroxypyrazine-1,4-dioxide) or a tautomeric form of this compound [8–10]. Molecular structure of pigment is depicted in Fig. S1. Pulcherriminic acid, a precursor of pulcherrimin, is secreted by yeast cells into the environment. Due to reaction of pulcherriminic acid with iron (III) ions coupled to diffusion, red halos containing precipitated pulcherrimin are formed around yeast colonies. The size of halos decrease, their color become more intensive and the color of yeast cells turns from white to red with increasing concentration of iron (III) ions. Formation of insoluble pulcherrimin depletes iron in the medium, thus making the environment not suitable for other microorganisms that need iron for growth. Therefore *M. pulcherrima* has been considered as an effective antimicrobial agent against various bacteria, fungi and yeasts [11,12]. This yeast is often found on ripe grapes and in grape must, therefore, it may play an important role in wine quality [13].

To understand surface and interfacial chemistry in a single living yeast cell, a non-destructive and sensitive spectroscopic technique is required. Surface enhanced Raman spectroscopy (SERS) provides possibility to probe molecular structure of compounds adsorbed or nearby the metal (usually Au, Ag or Cu) nanostructures with high sensitivity, molecular specificity, and excellent spectral resolution [14–18]. Large enhancement can be provided by using roughened metal surfaces, nanoparticles of particular shape and dimensions, or regular nanostructures created on flat substrates [16–18]. A plasmonic property of the metal nanoparticles allows using them for detection and structural

* Corresponding author.
E-mail address: gediminas.niaura@ftmc.lt (G. Niaura).

https://doi.org/10.1016/j.saa.2020.118560
1386-1425/

analysis at molecular level of biomolecules and constituents of living cells [18–20]. The current status and progress expected in the SERS field was recently highlighted in excellent review article [18].

Recently, Ag and Au nanoparticles have been used for identification of yeasts by SERS approach [21–31]. These studies were focused on characterization of yeasts with colloidal suspension of Ag or Au nanoparticles incubated with the cells. It was revealed that there are many factors such as an adsorption of nanoparticles on the cells constituents or aggregation of nanoparticles that can make it difficult to obtain reproducible SERS spectra from yeast cells [21,22]. Despite the fact that Ag has a higher SERS enhancement factor than other metals, Ag nanoparticles emit toxic silver ions and it can make these nanoparticles bioincompatible. Au nanoparticles are stable, non-toxic, but still can directly interact with the cells.

An alternative approach to solve these problems is the use of shell-isolated nanoparticles [18,32–35]. Inert shells (SiO_2, MnO_2, Al_2O_3, polymer, etc.) surround plasmonic Au or Ag cores, protecting them from degradation, aggregation and thus increase stability of the nanoparticles. The shells also prevent chemical and electrical contacts among plasmonic cores and probe substrates, analytes or environment. Measurement technique with such particles spread over a surface of analyzed material is named Shell-Isolated Nanoparticle-Enhanced Raman Spectroscopy (SHINERS) [32]. The method was invented and main advantages were demonstrated by Tian group in 2010 [33]. Application of SHINERS method to living *Saccharomyces cerevisiae* cells demonstrated power of the technique to probe the structure of cell wall. Among other bands attributed to vibrations of amino acids and amide group, the spectral signatures on the presence of mannoprotein were provided [33]. In this work, SHINERS technique was applied to probe molecular structure of living *M. pulcherrima* yeasts cell wall constituents.

2. Experimental

2.1. Materials

All reagents and solvents (Merck) were used without further purifications: hydrogen tetrachloro aurate ($HAuCl_4 3H_2O$, 99%), trisodium citrate dihydrate ($HOC(COONa)(CH_2COONa)_2 \cdot 2H_2O$, 99%), (3-aminopropyl)trimethoxysilane ($H_2N(CH_2)_3Si(OCH_3)_3$, APTMS, 97%), sodium silicate solution (10% NaOH, 27% SiO_2). Milli-Q water with a resistivity of 18.2 MΩ· cm was used in all procedures. Gold nanoparticles were purified using 3.5 kDa molecular weight cutoff dialysis membrane (Fisher Scientific). A highly polished stainless steel substrate with an ultrathin hydrophobic coating *Tienta* (Tienta SpectRIM, Merck) was used for Raman measurements.

2.2. Synthesis of silicon dioxide covered spherical gold nanoparticles

In the first step, 50 mL of an aqueous $HAuCl_4$ solution (0.01 wt%) was brought into a round-bottom flask and boiled in a hot oil bath (150 °C) with vigorous stirring. The solution reached boiling temperature in 3 min. Then 0.35 mL of sodium citrate (1 wt%) was quickly added into the boiling solution and the mixture was refluxed for 30 min. Next, it was left to attain the room temperature (about 2 h). Results of this step allowed getting the red colloid solution of gold nanoparticles (Au NPs). For the growth of ultrathin layer of silicon dioxide over the nanoparticles 0.6 mL APTMS (1 mM) was added to 45 mL of Au NPs. The mixture was vigorously stirred for 15 min. Then 4.8 mL of sodium silicate solution (0.54% wt/wt) was added and the mixture was stirred for another 3 min at room temperature. The flask was placed in an 85–90 °C water bath and stirred for 45 min. Next, the flask was placed in an ice bath (3–5 °C) for 30 min to stop the reaction process. The cold mixture was transferred into several 1.5 mL test tubes and centrifuged at 5500 rpm for 15 min. The supernatant was removed, a 1.5 mL of water was added, and nanoparticles were dispersed again. Next, tubes were centrifuged for another 15 min and supernatant was removed again to obtain Au@SiO_2 nanoparticles as a concentrated colloid. The concentrate was suspended in 3 mL of water. Then it was placed in a 3.5 kDa dialysis membrane and dialyzed in water for 1 h to remove the traces of unreacted reagents. The suspension was transferred into the test tubes and centrifuged at 5500 rpm for 15 min. The water was removed and Au@SiO_2 nanoparticles were kept in the dark at low temperature (3–5 °C).

2.3. Cultivation of yeasts

M. pulcherrima was from the collection of Nature Research Centre (Vilnius, Lithuania). When cultivated on solid YEPD growth medium containing 1% yeast extract (Liofilchem), 2% peptone (Liofilchem), 2% glucose (Fluka) and 2.5% agar (Liofilchem), yeasts contained low amount of pulcherrimin (white cells). To obtain yeasts with relatively high amount of pulcherrimin (red cells), YEPD medium was additionally supplemented with $FeCl_3 \cdot 6H_2O$ (30 mg per liter). Yeasts were grown at 25 °C for three days and thereafter stored in the fridge.

2.4. Isolation of pulcherrimin from growth medium

To obtain pulcherrimin from the growth medium, *M. pulcherrima* was inoculated as separate streaks on solid YEPD medium additionally supplemented with $FeCl_3 \cdot 6H_2O$ (5 mg per liter) and allowed to grow at 25 °C for 20 days. During this time, red halos were formed around the yeast streaks. Thereafter, the yeast biomass was carefully washed out from the agar surface to remove the impurities of biological origin. Red pulcherrimin halos formed around yeast streaks were cut out from the agar medium and soaked in water acidified to pH 1 (37% HCl:water, 1:10) to liquefy the agar. The mixture was boiled for 5 min. Thereafter, the solution was cooled and the reddish precipitates were decanted. Boiling and decanting was repeated five times. After final washing with water and decanting, dark red pulcherrimin deposits were dried at 60 °C.

2.5. Transition electron microscopy measurements of gold nanoparticles

The high resolution transmission electron microscopy (HR-TEM) measurements of Au@SiO_2 nanoparticles were conducted by transmission electron microscope FEI Tecnai G2 F20 X-TWIN (TEM) with STEM module. It is equipped with a high-angle annular dark-field (HAADF) detector for *Z*-contrast imaging and an X-ray energy-dispersive spectroscopy (EDS) detector for elemental mapping. The specimens for TEM measurements were prepared by FEI Helios Nanolab 650 dual beam microscope with an Omniprobe manipulator.

2.6. Raman measurements

The Raman and SHINERS spectra of yeast were recorded by inVia Raman (Renishaw) spectrometer equipped with a thermoelectrically cooled (−70 °C) CCD camera and a confocal Leica microscope. The 785 nm beam of the diode laser was used as the excitation source. The 180° scattering geometry was employed. The long working distance 50×/0.50 NA objective lens and 1200 lines/mm grating were used to record the Raman spectra. Laser power at the sample surface was about 0.9 mW. The accumulation time was 100 s. Raman scattering wavenumber axis was calibrated by the silicon peak at 520.7 cm^{-1}. Parameters of the vibrational modes were determined by fitting the experimental spectra with Gaussian-Lorentzian shape components using GRAMS/A1 8.0 (Thermo Scientific) software. Raman spectra were corrected by polynomial function background subtraction. No smoothing procedures were applied to experimental data. Exact band frequencies were obtained by dividing the experimental spectra into several spectral regions and fitting the contours with the mixed Gaussian-Lorentzian form components.

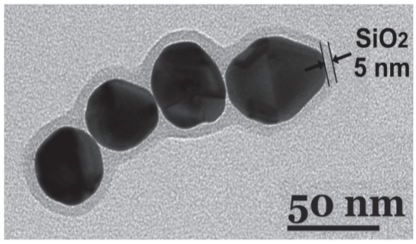

Fig. 1. High resolution transmission electron microscopy (HR-TEM) image of Au@SiO_2 (40 ± 5 nm) nanoparticles.

Raman spectrum of pulcherrimin powder was collected using 830 nm laser excitation and 830 lines/mm grating. The laser light was focused using 50×/0.50 NA objective lens and the power at the sample was set to 8.0 mW. In order to reduce fluorescent background sample was photobleached (using 830 nm laser with 8.0 mW of power for 30 min) prior the measurement. Four spectra of recorded pulcherrimin powder were co-added, which resulted in 25 min of the total time of acquisition.

2.7. Theoretical modeling

First principles calculations were conducted by Gaussian 09 software for Windows [36]. Geometry optimization and frequency calculations were completed with the DFT method using B3LYP functional. Calculations were done using 6-311++G(2d,p) basis set for C, H, N, and O atoms and LANDL2DZ with ECP for Fe atoms. Calculated frequencies and intensities were scaled according to procedure described elsewhere [38,39].

3. Results and discussion

3.1. Morphology characterization

We synthesized silica coated gold nanoparticles (Au@SiO_2) using a modified version of the earlier reported procedure [34]. The preparation of spherical Au@SiO_2 nanoparticles with 40 ± 5 nm core size and SiO_2 shell of 5 nm thickness (Fig. 1) was undertaken in three steps. First, gold colloid was prepared by reduction of auric chloride by sodium citrate; then a silica shell was grown on the colloids; and last, Au@SiO_2 were purified using dialysis membrane. In this case, the last procedure is especially important, because a trace of unreacted reagents can have a negative effect on the yeasts and distort a result of the measurements.

The advantage of Au@SiO_2 nanoparticles against aggregation comparing with naked Au nanoparticles was immediately recognized by analysis of optical images of nanostructures spread over *Tienta* substrate. Microscope images clearly show that bare Au NPs aggregate and form black spots (Fig. 2). In contrast, Au@SiO_2 nanoparticles spread over the surface form homogeneous, light color bulk. Such visual evidence confirms that inert shell does not allow nanoparticles to aggregate, even when water is removed from medium.

We chose two kinds of *M. pulcherrima* that differ in the amounts of produced red pigment (Fig. 3). The samples for Raman measurements were prepared in two steps. Firstly, living yeast cells (0.004 g) were dispersed in a Milli-Q water (2 mL). An aliquot of the solution (7 μL) was

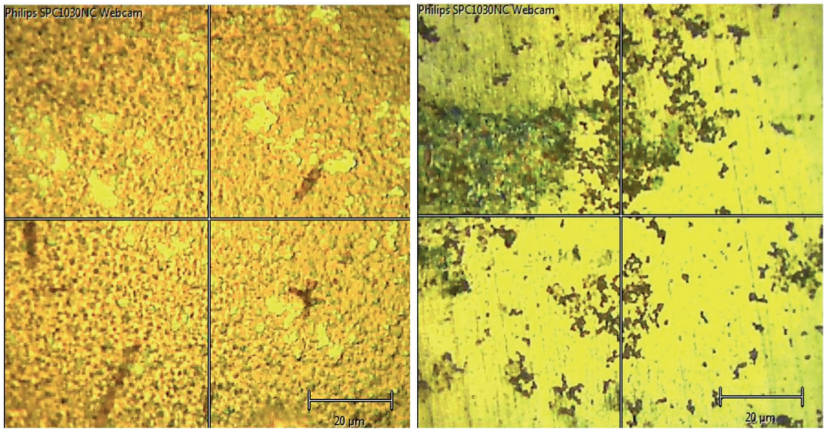

Fig. 2. Confocal Raman microscope images of Au@SiO_2 (left) and Au (right) nanoparticles onto *Tienta* slide surface.

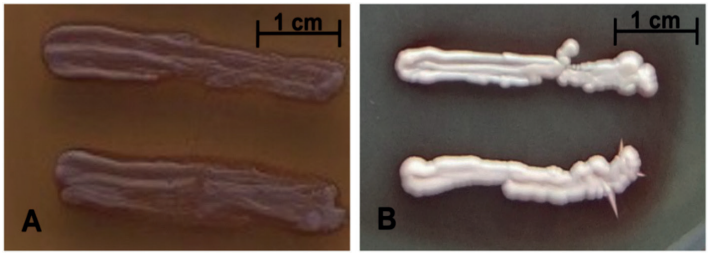

Fig. 3. Optical images of *Metschnikowia pulcherrima* strains producing larger (A) and lower (B) amount of red pigment pulcherrimin.

dropped on a *Tienta* slide surface and allowed to dry at room temperature. The sequence of it was formed 4–5 mm in diameter spots of yeast cells and Raman spectra were recorded. Secondly, the concentrated suspension (3 μL) of Au@SiO_2 nanoparticles were spread on the yeasts and dried. After that the SHINERS spectra were recorded.

3.2. Comparison of Raman, SERS and SHINERS spectra

Raman and SHINERS spectra of *Metschnikowia* spp. yeast cells with lower and larger amount of red pigment were recorded by optical focusing of laser radiation into the center of the cell. The ordinary Raman spectra of yeast cells are shown in Fig. 4a, where only fluorescence background is visible. Presence of Au@SiO_2 nanoparticles reduces fluorescence background intensity by a factor of 150 and 60 for yeast cells with large and low amount of red pigment, respectively. Fig. S2 shows raw SHINERS spectra with considerably suppressed fluorescence. No fluorescence background was detected in the SERS spectra of yeast cells (Fig. S3). It was demonstrated that fluorescence quenching in SHINERS method critically depends on the shell thickness [40]. In the case of Au@SiO_2 nanoparticles, the fluorescence would be quenched for shell thickness less than 5 nm; while for shells large than 10 nm, enhancement in fluorescence signal is expected to be observed (phenomenon known as surface enhanced fluorescence, SEF) [40]. The approximately 5 nm shell thickness of Au@SiO_2 nanoparticles used in this work was sufficiently small for effective reduction of the fluorescence signal. Thus, after background correction clear vibrational spectrum from of yeast cells was observed by SHINERS approach (Fig. 4b). Furthermore, before Au@SiO_2 nanoparticles were used to enhance Raman signal from yeast cells, SHINERS spectra of bare nanoparticles were recorded (Fig. 4c). One can observe that nanoparticles have specific vibrational spectrum, but the intensity of vibrational bands is extremely low compared to SHINERS spectra of yeasts. Fig. S4 shows SHINERS spectrum of Au@SiO_2 nanoparticles spread at *Tienta* substrate at higher sensitivity scale. Broad band near 1600 cm^{-1} and better resolved feature at 810 cm^{-1} (Fig. S4a) might be associated with adsorbed species during the production of nanoparticles and vibrations of Si—O—Si groups of the shell [41]. It should be noted that small molecular mass compounds are able to penetrate through the thin SiO_2 shell [42]. Some spectral features are also visible in the spectrum of naked Au nanoparticles (Fig. S4b). These bands might be related with adsorbed citrate anions used for reduction of gold ions and stabilization of nanoparticles.

The important issue in spectroscopic analysis of yeast cells by surface-enhanced vibrational spectroscopy is repeatability of the results. Fig. 5A shows SHINERS spectra of living yeast cells with large amount of red pigment recorded at four different sample positions. One can reveal that the main spectral features are well reproducible; peak positions do not change and there are no additional bands. In order to ensure the effect of silica shell on the Raman spectra, Au nanoparticles without the SiO_2 shell were used to enhance Raman spectra as

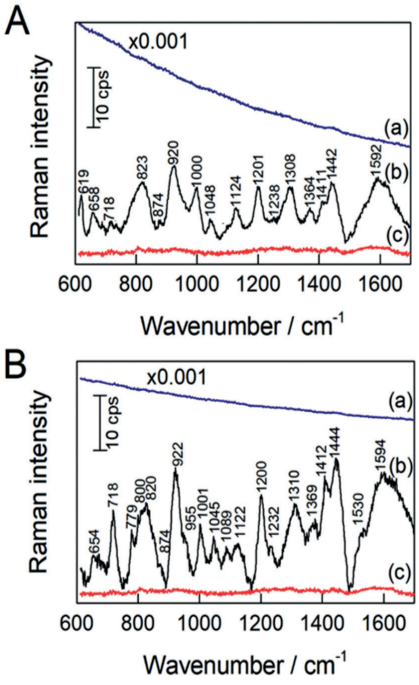

Fig. 4. (a) Raman and (b) SHINERS spectra of *Metschnikowia pulcherrima* yeast cells. (c) SHINERS spectra of bare Au@SiO_2 nanoparticles. (A) Yeast cells with larger amount of red pigment, (B) yeast cells with low amount of red pigment. SHINERS spectra are background corrected by using polynomial function fit. Excitation wavelength is 785 nm.

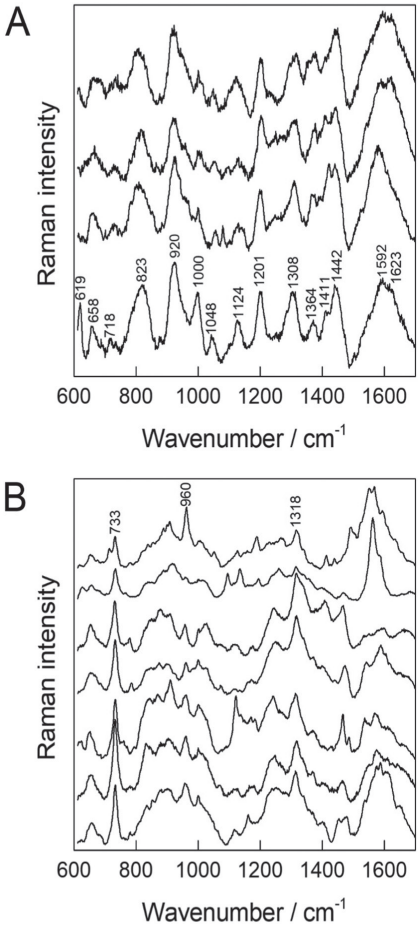

Fig. 5. Repeatability of SHINERS and SERS spectra of living yeast cells *Metschnikowia pulcherrima* with large amount of pigment. Spectra are collected at different positions. (A) SHINERS and (B) SERS spectra. Spectra are background corrected and shifted vertically for clarity.

well (Fig. 5B). In contrast to SHINERS, SERS spectra exhibited certain irreproducibility; in some cases new bands were visible. For example, the band near 1150 cm^{-1} clearly visible only in one spectrum, while the shape of strong feature near 1600 cm^{-1} differs going from one spectrum to another. The bands at 733 and 1318 cm^{-1} are visible in all the spectra although with different relative intensity. Similar behavior was detected by analysis of living yeast cells with lower amount of red pigment (Fig. S5). Observed difference in SHINERS and SERS spectra might be associated with the direct interaction of constituents of yeast cells with Au when naked nanoparticles were employed to enhance the Raman spectra. Such interaction of biomolecules with the surface of gold or silver nanoparticles depends on polarity, flexibility, nature of molecular group, and other factors and often leads to the irreproducibility of the SERS spectra from yeast cells [22]. It should be noted, that we have not detected any fluctuations in the SHINERS signals indicating absence of single molecule detection mechanism [43]. The averaged intensity of the well-defined bands in SHINERS spectra was found to be lower by approximately 6 times comparing with the similar bands in the SERS spectra.

3.3. SHINERS characterization of yeast cells with larger and lower amount of red pigment

To gain insight into the differences between the samples, we compared the mean spectra (averaged five spectra at the same place) of yeast samples with larger and lower amount of pigment (Fig. 6). In general, it can be noted that the spectrum of yeast with larger amount of pigment (Fig. 6a) is less intensive and more bands are visible in the low frequency region. Table 1 summarizes the tentative assignments of vibrational bands based on previous studies [24–35,43–68]. It should be noted that the SHINERS bands from various functional groups are overlapped. The well-defined feature near 1200–1201 cm^{-1} belongs predominantly to vibrations of Tyr and Phe functional groups of proteins [60,61]. Similar band was previously assigned to mannoprotein at cell wall [33]. The characteristic vibrational mode of Phe ring (F12) is visible near 1000–1001 cm^{-1} [68]. The intense band at 1442–1444 cm^{-1} can be assigned to scissoring bending vibration of CH_2 groups of proteins and phospholipids [59–61], while the shoulder near 1411–1412 cm^{-1} might be associated with symmetric stretching

Table 1
Peak positions of SHINERS spectra and corresponding tentative band assignments for different molecular groups of the *Metschnikowia pulcherrima* yeast cells.

Assignments[a,b]	Peak position (cm^{-1})	
	Yeast cells with larger amount of pigment	Yeast cells with lower amount of pigment
ν(ring), aromatic amino acids, proteins; $\delta(NH_2)$, proteins	1623	–
ν(ring), aromatic amino acids, proteins; mannoprotein	1592	1594
(Pigment)	1550	–
$\nu_{as}(COO^-)$, proteins	–	1530
$\delta(CH_2)$ scissoring, lipids, proteins	1442	1444
$\nu_s(COO^-)$, proteins; mannoprotein	1411	1412
$\delta_s(CH_3)$, Ala, lipids; W7, Trp, proteins; ν(ring)	1364	1369
$\tau(CH_2)$, $w(CH_2)$, lipids, proteins; ν(ring), Trp, Tyr, Phe, proteins; mannoprotein	1308	1310
Amide III, proteins	1238	1232
ν(C—N), Y7a, Tyr, proteins; amide III, proteins; mannoprotein	1201	1200
ν(C—N), proteins, lipids	1124	1122
ν(P═O), ν(C—C), lipids, pigment	1102	–
ν(C—N), proteins	–	1089
ν(C—N), ν(C—C), proteins, lipids	–	1055
ν(C—N), ν(C—C), proteins, lipids	1048	1045
F12, Phe, proteins	1000	1001
ν(C—C), ν(C—O), skeletal, proteins	955	955
ν(C—C), ν(C—O), proteins	920	922
ν(C—O—C), ν(C—C), polysaccharides; ν_s(C—C—N), Lipids;	874	874
ν_{as}(O—P—O), lipids; Y1, Tyr, Proteins; $r(CH_2)$, lipids, proteins	823	820
ν_s(O—P—O), lipids	804	800
δ(CO), ν(C—N), $r(CH_3)$, lipids, head group, phosphate group	718	718
ν(C—S), proteins; pigment	667	–
ν(C—S)$_G$, proteins	658	654
(Pigment)	619	–

[a] Based on refs. [24–35, 43–68].
[b] Abbreviations: ν, stretching; δ, deformation; τ, twisting; w, wagging; r, rocking; s, symmetric; as, asymmetric.

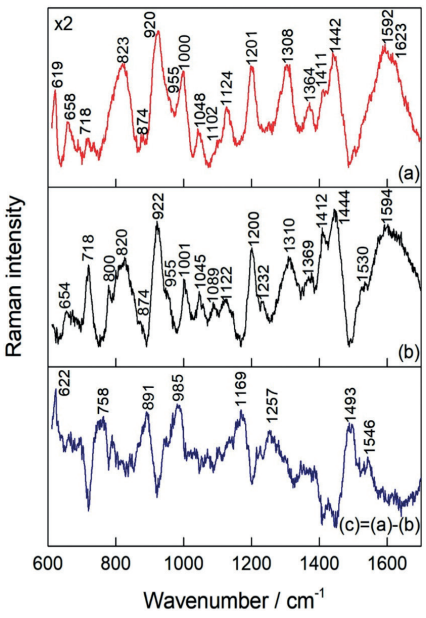

Fig. 6. SHINERS spectra of different yeast cells. (a) *Metschnikowia pulcherrima* with large amount of red pigment, (b) *Metschnikowia pulcherrima* with low amount of pigment, and (c) difference spectrum. Intensities are normalized according to the intensity of the band near 1200 cm^{-1}. Spectra are background corrected. Excitation wavelength is 785 nm.

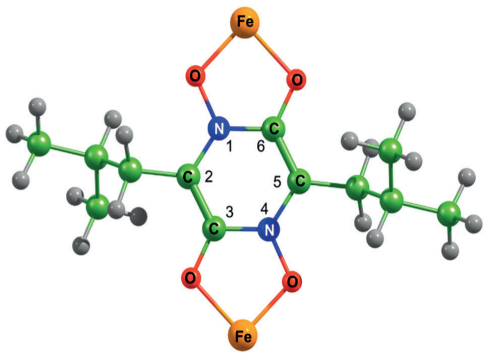

Fig. 7. Molecular structure of red pigment pulcherrimin optimized at B3LYP functional with 6-311++G(2d,p) basis set for C, H, N, and O atoms and LANDL2DZ with ECP for Fe atoms. Numbering of pyrazine ring (pz) atoms is also shown.

vibration of carboxylate group ν_s(COO). SERS band near 1421 cm^{-1} was observed in SERS spectra of mannoprotein and assigned to deformation vibrational mode δ(CH) [29] or symmetric stretching vibration of carboxylate group [28]. The band near 1308 cm^{-1} is associated mainly with deformation vibrations (wagging and twisting) of CH_2 groups with some contribution from Amide III mode of proteins in predominant α-helix and P_{II}-helix secondary structure [59,63,64]. The intense feature in the vicinity of 920–922 cm^{-1} contains high contribution from coupled C—C and C—O stretching vibrations of amino acid residues. The broad feature at 820–823 cm^{-1} is associated with rocking vibration of methylene groups, asymmetric stretching vibration of O—P—O group of lipids, ring breathing vibrational mode of Tyr residues (Y1), and stretching vibration ν(C—O—C)/ν(C—C) in polysaccharides [65,66]. The signals between 823 and 480 cm^{-1} originate from the phospholipids hydrophilic head group domain. In other words, the spectra contain vibrational information about the main component of the cell wall. In the spectral region close to vibrational bands of phospholipids, there is a non-intense band at 800 cm^{-1} which was attributed as a glucose ring in the carbohydrate structure [65].

While the reproducibility of SERS spectra is poor comparing with SHINERS, some insights into the difference between the two methods might be obtained from more detailed analysis of spectral features (Fig. 5B). Thus, pair of bands located at 733 and 1318 cm^{-1} is associated with vibrations of adenine ring [69]. The origin of adenine source is not completely clear; it might be related with presence of denaturated DNA and other adenine-containing biomolecules such as FAD, NAD, AMP, and purine-like structure containing hypoxanthine [69]. It should be noted that adenine ring characteristic bands at 733 and 1318 cm^{-1} were not detected in the SHINERS spectra (Fig. 5A). Observed spectral differences are related with interactions between yeast molecules and naked metal nanoparticles [31]; such interactions are limited in the case of SHINERS method.

3.4. Identification of pigment pulcherrimin vibrational bands

Difference SHINERS spectra of yeast cells with larger and lower amount of red pigment (Fig. 6c) were formed in order to identify pigment pulcherrimin vibrational bands. To clarify assignments of SHINERS bands we have conducted the first-principles quantum chemical calculations of structure and vibrational spectrum of pigment. Optimized molecular structure of pulcherrimin is displayed in Fig. 7. We have recorded the Raman spectrum of pulcherrimin powder using the 830 nm excitation wavelength (Fig. 8a). At this excitation conditions no resonance Raman enhancement is predicted to be observed; thus not only vibrations from the pyrazine ring (pz) and coupled O—Fe—O group but also vibrational bands from the side chains (CH_3, and CH_2) are expected to be observed. Calculated Raman spectrum provides assignments of the vibrational modes (Fig. 8b) which are listed in Table 2. Intense experimentally observed band at 1621 cm^{-1} corresponds well to calculated stretching vibration ν(C2═C3) + ν(C6═C5) of pyrazine ring (pz) at 1595 cm^{-1}. The asymmetric stretching vibration ν_{as}(CNC) of pz corresponds to intense band at 1411 cm^{-1}; another close positioned band near 1437 cm^{-1} belongs to scissoring vibration of CH_2 groups coupled with deformation motion of CH_3. Isobutyl chain and CH_2/CH_3 groups possess strong band at 1173 cm^{-1}. The characteristic pz breathing mode is visible in Raman spectrum at 625 cm^{-1}. Finally, two low frequency bands at 573 and 516 cm^{-1} are associated with in-plane deformation of pz coupled with vibration of FeO_2 group.

Comparing SHINERS difference spectrum of yeast cells (Fig. 6c) with Raman spectrum of pulcherrimin powder (Fig. 8a), several vibrational bands can be identified in the differential spectrum which can be associated with vibrations of red pigment. One can recognize the characteristic pz breathing band near 622 cm^{-1}. The broad positive-going feature near 758 cm^{-1} in the difference spectrum might be related with pulcherrimin isobutyl chain ν(C—C) stretching vibration visible at 800 cm^{-1} in the spectrum of pigment powder. The broad feature near 985 cm^{-1} in the SHINERS difference spectrum can be related with relatively broad Raman band near 1030 cm^{-1} associated with stretching vibration ν(N—O) coupled with pz stretching motion. In addition, several strong bands were detected in the ATR-FTIR spectrum of pulcherrimin powder in the vicinity of 1010–1070 cm^{-1} (Fig. S6). The positive-going feature near 1169 cm^{-1} is close to the well-defined band of bulk pigment recorded in the Raman spectrum at 1173 cm^{-1}. This band was assigned to the isobutyl chain stretching vibration ν(C—C) coupled with deformation motions of CH_3 and CH_2 groups (Table 2). However, other bands are obscure, probably because of intense features of yeast cells in the vicinity of 1440 and 1600 cm^{-1}. Thus, two positive-going bands visible in the vicinity of 1493 and 1546 cm^{-1} in the SHINERS spectrum might be tentatively associated with Raman bands recorded at 1503 and 1621 cm^{-1}, respectively (Fig. 8). The calculated spectrum shows low intensity Raman band near 1523 cm^{-1}, while strong band due to predominant stretching vibrations of C2═C3 and C5═C6 bonds coupled with deformation motion of CH_2 and CH_3 groups was predicted in infrared spectrum (Fig. S6). The higher frequency band (1621 cm^{-1}) is associated with ν(C2═C3) + ν(C5═C6) mode; however, calculations predict lower peak position wavenumber for this band (1595 cm^{-1}). The blue-shift of this band in powder spectrum might be related with conformational changes of studied compound. In addition, changes in the Raman spectrum of pulcherrimin were demonstrated depend strongly on the Fe

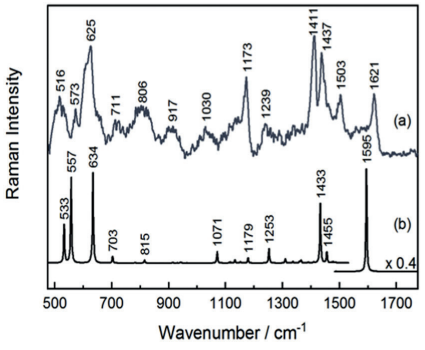

Fig. 8. Comparison of Raman spectrum of pulcherrimin powder recorded with 830 nm excitation wavelength (a) and calculated Raman spectrum (b). Calculations were accomplished using DFT method and B3LYP functional with 6–311++G(2d,p) basis set for C, H, N, and O atoms and LANL2DZ with ECP for Fe atoms.

Table 2
Experimental Raman and calculated peak wavenumbers and vibrational assignments for red pigment pulcherrimin.

Raman (cm^{-1})	Calculated (cm^{-1})	Assignments[a]
1621 s	1595	ν(C2═C3), ν(C5═C6)
1503 m	1523	ν(C2═C3), ν(C5═C6), τ(CH_2), δ(CH_3)
1437 vs	1455	δ(CH_2) scissoring, δ(CH_3)
1411 vs	1433	ν_{as}(CNC) stretching of pz in-plane, δ(CH_2) scissoring
1239 m	1253	τ(CH_2)
1173 vs	1179	ν(C—C) isobutyl chain, r(CH_3), t(CH_2)
1030 br, m	1071	ν(N—O) in-phase, ν(pz)
917 br, m	923	ν(Fe—O), r(CH_3), ν(C—CH_3), ν(C—C) isobutyl chain
806 br, m	815	ν(C—C) isobutyl chain
711 w	703	γ(pz) out-of-plane deformation
625 vs	634	ν(pz) breathing, ν_s(FeO_2), δ(CCC) isobutyl chain
573 m	557	δ(pz) in-plane, ν_{as}(FeO_2), r(CH_2)
516 m	533	δ(pz) in-plane, δ(FeO_2), r(CH_2)

[a] Abbreviations: ν, stretching; δ, deformation; τ, twisting; w, wagging; r, rocking; as, asymmetric; s, symmetric; pz, pyrazine ring; m, middle; w, weak; s, strong; vs, very strong; br, broad.

concentration [70]. It should be noted, that the difference spectrum presented in Fig. 6c and spectrum of bulk pigment pulcherrimin at Fig. 8 does not coincide completely. This might be related with three major reasons: (i) different state of pigment in yeast cells comparing with bulk sample, (ii) dependence of pulcherrimin structure and Raman spectrum on concentration of iron [70], and (iii) changes in the structure of yeast cell wall constituents for cells containing high and low amount of pigment.

4. Conclusions

For the first time shell-isolated nanoparticle-enhanced Raman spectroscopy (SHINERS) was employed to investigate the *Metschnikowia pulcherrima* yeast cells. Use of Au@SiO_2 nanoparticles with 40 ± 5 nm core diameter and 5 nm shell thickness allowed us to obtain significantly enhanced spectra of the living cells. The fluorescence background was quenched by 60–150 times in SHINERS experiments comparing with Raman spectrum. The yeast cell wall and its functional elements (proteins, mannoprotein, lipids, amino acids, and polysaccharides) were identified. Contrary to SERS analysis which was performed by using naked Au nanoparticles, no bands associated with adenine ring-related vibrations near 730 and 1318 cm^{-1} [69] were observed in SHINERS spectra. Based on density functional theory calculations and 830-nm excited Raman spectra of pigment several bands in SHINERS difference were associated with pulcherrimin vibrations.

This work provides insights into the difference of SERS and SHINERS methods to probe living cells. The SHINERS spectra of yeast cells demonstrated repeatability; vibrational bands did not change and no additional bands due to chemical interactions with the nanoparticles were observed. Absence of direct interaction with plasmonic metal and reproducibility of the spectra are the main advantages of shell-isolated nanoparticles Au@SiO_2 comparing with popular and often use bare Au nanostructures. Consequently, it was shown that SHINERS is a perspective non-destructive technique allowing the collection of molecular level information from living yeast cells for a better understanding of their cell wall biochemical structures.

CRediT authorship contribution statement

Agnė Zdaniauskienė: Conceptualization, Methodology, Investigation, Writing - original draft, Visualization. **Tatjana Charkova:** Investigation, Validation. **Ilja Ignatjev:** Investigation, Validation. **Vytautas Melvydas:** Investigation, Resources. **Rasa Garjonytė:** Methodology, Resources. **Ieva Matulaitienė:** Validation, Formal analysis. **Martynas Talaikis:** Data curation, Formal analysis, Investigation. **Gediminas Niaura:** Conceptualization, Writing - review & editing, Supervision.

Declaration of competing interest

The authors declare no competing financial interests.

Acknowledgments

G.N. gratefully acknowledges the Center of Spectroscopic Characterization of Materials and Electronic/Molecular Processes (SPECTROVERSUM Infrastructure) for use of Raman spectrometer.

Appendix A. Supplementary data

Supplementary data to this article can be found online at https://doi.org/10.1016/j.saa.2020.118560.

References

[1] T. Satyanarayana, G. Kunze (Eds.), Yeast Biotechnology: Diversity and Applications, Springer, Netherlands 2009, pp. 489–635.
[2] A. Adeniran, M. Sherer, K.E.J. Tyo, Yeast-based biosensors: design and applications, FEMS Yeast Res. 15 (2015) 1–15.
[3] S.K. Nandy, R.K. Srivastava, A review on sustainable yeast biotechnological processes and applications, Microbiol. Res. 207 (2018) 83–90.
[4] M. Arevalo-Villena, A. Briones-Perez, M.R. Corbo, M. Sinigaglia, A. Bevilacqua, Biotechnological application of yeasts in food science: starter cultures, probiotics and enzyme production, J. Appl. Microbiol. 123 (2017) 1360–1372.
[5] G.C. Shurson, Yeast and yeast derivatives in feed additives and ingredients: sources, characteristics, animal responses, and qualification methods, Animal Feed Sci. Technol. 235 (2018) 60–76.
[6] E.J. Lodolo, J.L.F. Kock, B.C. Axcell, M. Brooks, The yeast *Saccharomyces cerevisiae* – the main character in beer brewing, FEMS Yeast Res. 8 (2008) 1018–1036.
[7] M.A. Lachance, *Metschnikowia*: half tetrads, a regicide and the fountain of youth, Yeast 33 (2016) 563–574.
[8] A.J. Kluyver, J.P. Van der Walt, A.J. Van, Pulcherrimin, the pigment of *Candida pulcherrima*, Proc. Natl. Acad. Sci. U.S.A. 39 (1953) 583–593.
[9] A.H. Cook, C.A. Slater, The structure of pulcherrimin, J. Chem. Soc. (1959) 4133–4135.
[10] J.C. MacDonald, The structure of pulcherriminic acid, Can. J. Chem. 41 (1965) 165–172.
[11] M. Sipiczki, *Metschnikowia* strains isolated from botrytized grapes antagonize fungal and bacterial growth by iron depletion, Appl. Environ. Microbiol. 72 (2006) 6716–6724.
[12] D. Saravanakumar, A. Ciavorella, D. Spadaro, A. Garibaldi, M.L. Gullino, *Metschnikowia pulcherrima* starin MACH1 outcompetes *Botrytis cinerea*, *Alternaria alternate* and *Penicillium expansum* in apples through iron depletion, Postharvest Biol. Biotechnol. 49 (2008) 121–128.
[13] N.P. Jolly, C. Varela, I.S. Pretorius, Not your ordinary yeast: non-*Saccharomyces* yeast in wine production uncovered, FEMS Yeast Res. 14 (2014) 215–237.
[14] E. Le Ru, P.G. Etchegoin, Principles of Surface Enhanced Raman Spectroscopy and Related Plasmonic Effects, Elsevier, Amsterdam, 2009.
[15] Z.Q. Tian, B. Ren, D.Y. Wu, Surface-enhanced Raman scattering: from noble transition metals and from rough surfaces to ordered nanostructures, J. Phys. Chem. B 106 (2002) 9463–9483.
[16] S.Y. Ding, J. Yi, J.F. Li, B. Ren, D.Y. Wu, R. Panneerselvam, Z.Q. Tian, Nanostructure-based plasmon-enhanced Raman spectroscopy for surface analysis of materials, Nat. Rev. Mat. 1 (2016) 1–16.
[17] S. Schlücker, Surface-enhanced Raman spectroscopy: Concepts and chemical applications, Angew. Chem., Int. Ed. 53 (2014) 4756–4795.
[18] J. Langer, D.J. De Aberasturi, J. Aizpurua, R.A. Alvarez-Puebla, B. Auguié, J.J. Baumberg, G.C. Bazan, S.E.J. Bell, A. Boisen, A.G. Brolo, J. Choo, D. Cialla-May, V. Deckert, L. Fabris, K. Faulds, F.J.G. De Abajo, R. Goodacre, D. Graham, A.J. Haes, C.L. Haynes, C. Huck, T. Itoh, M. Käll, J. Kneipp, N.A. Kotov, H. Kuang, E.C. Le Ru, H.K. Lee, J.-F. Li, X.Y. Linh, S.A. Maier, T. Mayerhöfer, M. Moskovits, K. Murakoshi, J.-M. Nam, S. Nie, Y. Ozaki, I. Pastoriza-Santos, J. Perez-Juste, J. Popp, A. Pucci, S. Reich, B. Ren, G.C. Schatz, T. Shegai, S. Schlücker, L.-L. Tay, K.G. Thomas, Z.-Q. Tian, R.P. Van Duyne, T. Vo-Dinh, Y. Wang, K.A. Willets, C. Xu, H. Xu, Y. Xu, Y.S. Yamamoto, B. Zhao, L.M. Liz-Marzán, Present and future of surface-enhanced Raman scattering, ACS Nano 14 (2020) 28–117.
[19] X.X. Han, B. Zhao, Y. Ozaki, Surface-enhanced Raman scattering for protein detection, Anal. Bioanal. Chem. 394 (2009) 1719–1727.
[20] K. Kneipp, H. Kneipp, I. Itzkan, R.R. Dasari, M.S. Feld, Surface-enhanced Raman scattering and biophysics, J. Phys.: Condens. Matter 14 (2002) R597–R624.
[21] M. Culha, M. Kahraman, D. Çam, I. Sayin, K. Keseroğlu, Rapid identification of bacteria and yeast using surface-enhanced Raman scattering, Surf. Interface Anal. 42 (2010) 462–465.
[22] S. Uusitalo, A. Popov, Y.V. Ryabchikov, O. Bibikova, H.L. Alakomi, R. Juvonen, V. Kontturi, S. Siitonen, A. Kabashin, I. Meglinski, J. Hiltunen, A. Laitila, Surface-enhanced Raman spectroscopy for identification and discrimination of beverage spoilage yeasts using patterned substrates and gold nanoparticles, J. Food Eng. 212 (2017) 47–54.
[23] K.M. Syamala, H. Abe, Y. Fujita, K. Tomimoto, V. Biju, M. Ishikawa, Y. Ozaki, T. Itoh, Inhibition assay of yeast cell walls by plasmon resonance Rayleigh scattering and surface-enhanced Raman scattering imaging, Langmuir 28 (2012) 8952–8958.
[24] L. Mikoliunaite, R.D. Rodriguez, E. Sheremet, V. Kolchuzhin, J. Mehner, A. Ramanavicius, D.R.T. Zahn, The substrate matters in the Raman spectroscopy analysis of cells, Sci. Rep. 5 (2015) 13150.
[25] L. Dedelaite, R.D. Rodriguez, E. Andriukonis, M. Hietschold, D.R.T. Zahn, A. Ramanavicius, Surfaces functionalized by graphene oxide nanosheets for single cell investigations, Sensors Actuators B: Chem. 255 (2018) 1735–1743.
[26] A.F. Chrimes, K. Khoshmanesh, S.Y. Tang, B.R. Wood, P.R. Stoddart, S.S.E. Collins, A. Mitchell, K. Kalantar-zadeh, In situ SERS probing of nano-silver coated individual yeast cells, Biosens. Bioelectron. 49 (2013) 536–541.
[27] M. Culha, M. Kahraman, D. Çam, I. Sayin, K. Keseroğlu, Rapid identification of bacteria and yeast using surface-enhanced Raman scattering, J. Raman Spectrosc. 42 (2010) 462–465.
[28] A. Sujith, T. Itoh, H. Abe, K. Yoshida, M.S. Kiran, V. Biju, M. Ishikawa, Imaging the cell wall of living yeast cells using surface-enhanced Raman spectroscopy, Anal. Bioanal. Chem. 394 (2009) 1803–1809.
[29] A. Sujith, T. Itoh, H. Abe, A.A. Anas, K. Yoshida, V. Biju, M. Ishikawa, Surface enhanced Raman scattering analyses of individual silver nanoaggregates on living single yeast cell wall, Appl. Phys. Lett. 92 (2008) 103901.

[30] I. Sayin, M. Kahraman, F. Sahin, D. Yurdakul, M. Culha, Characterization of yeast species using surface-enhanced Raman scattering, Appl. Spectrosc. 63 (2009) 1276–1282.
[31] T. Lemma, J. Wang, K. Arstila, V.P. Hytönen, J.J. Toppari, Identifying yeasts using surface enhanced Raman spectroscopy, Spectrochim. Acta A 218 (2019) 299–307.
[32] J.F. Li, Y.J. Zhang, S.Y. Ding, R. Panneerselvam, Z.Q. Tian, Core-shell nanoparticle-enhanced Raman spectroscopy, Chem. Rev. 117 (2017) 5002–5069.
[33] J.F. Li, Y.F. Huang, Y. Ding, Z.L. Yang, S.B. Li, X.S. Zhou, F. Ru Fan, W. Zhang, Z.Y. Zhou, D.Y. Wu, B. Ren, Z.L. Wan, Z.Q. Tian, Shell-isolated nanoparticle-enhanced Raman spectroscopy, Nature 464 (2010) 392–395.
[34] A. Zdaniauskienė, T. Charkova, I. Matulaitienė, O. Eicher-Lorka, A. Matijoška, M. Skapas, A. Selskis, G. Niaura, Electrochemical shell-isolated nanoparticle-enhanced Raman spectroscopy: bonding, structure, and ion-pairing of the positive charge bearing pyridinium ring terminated monolayer at smooth gold electrode, J. Phys. Chem. C 122 (2018) 1234–1242.
[35] K. Kołątaj, J. Krajczewski, A. Kudelski, Silver nanoparticles with many sharp apexes and edges as efficient nanoresonators for shell-isolated nanoparticle-enhanced Raman spectroscopy, J. Phys. Chem. C 121 (2017) 12383–12391.
[36] M.J. Frisch, G.W. Trucks, H.B. Schlegel, G.E. Scuseria, M.A. Robb, J.R. Cheeseman, G. Scalmani, V. Barone, B. Mennucci, G.A. Petersson, H. Nakatsuji, M. Caricato, X. Li, H.P. Hratchian, A.F. Izmaylov, J. Bloino, G. Zheng, J.L. Sonnenberg, M. Hada, M. Ehara, K. Toyota, R. Fukuda, J. Hasegawa, M. Ishida, T. Nakajima, Y. Honda, O. Kitao, H. Nakai, T. Vreven, J.A. Montgomery Jr., J.E. Peralta, F. Ogliaro, M. Bearpark, J.J. Heyd, E. Brothers, K.N. Kudin, V.N. Staroverov, R. Kobayashi, J. Normand, K. Raghavachari, A. Rendell, J.C. Burant, S.S. Iyengar, J. Tomasi, M. Cossi, N. Rega, J.M. Millam, M. Klene, J.E. Knox, J.B. Cross, V. Bakken, C. Adamo, J. Jaramillo, R. Gomperts, R.E. Stratmann, O. Yazyev, A.J. Austin, R. Cammi, C. Pomelli, J.W. Ochterski, R.L. Martin, K. Morokuma, V.G. Zakrzewski, G.A. Voth, P. Salvador, J.J. Dannenberg, S. Dapprich, A.D. Daniels, O. Farkas, J.B. Foresman, J.V. Ortiz, J. Cioslowski, D.J. Fox, Gaussian 09, Gaussian Inc., Wallingford, CT, 2009.
[38] I. Matulaitiene, E. Pociute, Z. Kuodis, O. Eicher-Lorka, G. Niaura, Interaction of 4-imidazolemethanol with a copper electrode revealed by isotope-edited SERS and theoretical modeling, Phys. Chem. Chem. Phys. 17 (2015) 16483–16493.
[39] M. Talaikis, O. Eicher-Lorka, G. Valincius, G. Niaura, Water-induced structural changes in the membrane-anchoring monolayers revealed by isotope-edited SERS, J. Phys. Chem. C 120 (2016) 22489–22499.
[40] P.-P. Fang, X. Lu, H. Lu, Y. Tong, Applications of shell-isolated nanoparticles in surface-enhanced Raman spectroscopy and fluorescence, Trends Anal. Chem. 66 (2015) 103–117.
[41] T. Hartman, C.S. Wondergem, B.M. Weckhhuysen, Practical guidelines for shell-isolated nanoparticle-enhanced Raman spectroscopy of heterogeneous catalysts, ChemPhysChem 19 (2018) 2461–2467.
[42] J. Krajczewski, H.B. Abdulrahman, K. Kołątaj, A. Kudelski, Zirconium (IV) oxide: new coating material for nanoresonators for shell-isolated nanoparticle-enhanced Raman spectroscopy, Spectrochim. Acta A 193 (2018) 480–485.
[43] D. Radziuk, H. Moehwald, Prospects for plasmonic hot spots in single molecule SERS towards the chemical imaging of live cells, Phys. Chem. Chem. Phys. 17 (2015) 21072–21093.
[44] L.P. Hackett, L.L. Goddard, G.L. Liu, Plasmonic nanocone arrays for rapid and detailed cell lysate surface enhanced Raman spectroscopy analysis, Analyst 142 (2017) 4422–4430.
[45] N. Erjavec, G. Pinato, K. Ramser, Raman spectroscopy as a tool for detecting mitochondrial fitness, J. Raman Spectrosc. 47 (2016) 933–939.
[46] J. Li, G. Ma, H. Liu, H. Liu, Yeast cells carrying metal nanoparticles, Mater. Chem. Phys. 207 (2018) 373–379.
[47] I. Espagnon, D. Ostrovskii, R. Mathey, M. Dupoy, P.L. Joly, A. Novelli-Rousseau, F. Pinston, O. Gal, F. Mallard, D.F. Leroux, Direct identification of clinically relevant bacterial and yeast microcolonies and macrocolonies on solid culture media by Raman spectroscopy, J. Biomed. Opt. 19 (2014), 027004. .
[48] Y.F. Chiu, C.K. Huang, S. Shigeto, *In vivo* probing of the temperature responses of intracellular biomolecules in yeast cells by label-free Raman microspectroscopy, ChemBioChem 14 (2013) 1001–1005.
[49] L. Chiu, F. Hullin-Matsuda, T. Kobayashi, H. Torii, H. Hamaguchi, The origin of the 1602 cm^{-1} Raman band of yeasts; contribution of ergosterol, J. Biophotonics 5 (2012) 724–728.
[50] L. Bednárová, J. Palacký, V. Bauerová, O. Hrušková-Heidingsfeldová, I. Pichová, P. Mojzeš, Raman microspectroscopy of the yeast vacuoles, Spectrosc. Internat. J. 27 (2012) 503–507.
[51] L. Chiu, M. Ando, H. Hamaguchi, Study of the 'Raman spectroscopic signature of life' in mitochondria from budding yeast, J. Raman Spectrosc. 41 (2010) 2–3.
[52] T.K. Bhowmick, G. Pyrgiotakis, K. Finton, A.K. Suresh, S.G. Kane, B. Moudgil, J.R. Bellare, A study of the effect of JB particles on *Saccharomyces cerevisiae* (yeast) cells by Raman spectroscopy, J. Raman Spectrosc. 39 (2008) 1859–1868.
[53] O. Samek, K. Mlynarikova, S. Bernatova, J. Ježek, V. Krzyžánek, M. Šiler, P. Zemánek, F. Růžička, V. Holá, M. Mahelová, *Candida parapsilosis* biofilm identification by Raman spectroscopy, Int. J. Mol. Sci. 15 (2014) 23924–23935.
[54] G.B. Junk, I.S. Kang, Y.J. Lee, D. Kim, H.K. Park, G.J. Lee, C. Kim, Label-free noninvasive characterization of osteoclast differentiation using Raman spectroscopy coupled with multivariant analysis, Curr. Optics Photon. 1 (2017) 412–420.
[55] B. Li, M.Q. Lu, Q.Z. Wang, G.Y. Shi, W. Liao, S.S. Huang, Raman spectra analysis for single mitochondrias after apoptosis process of yeast cells stressed by acetic acid, Chin. J. Anal. Chem. 43 (2015) 643–650.
[56] I. Notingher, Raman spectroscopy of cell-based biosensors, Sensors 7 (2007) 1343–1358.
[57] I. Matulaitiene, Z. Kuodis, A. Matijoska, O. Eicher-Lorka, G. Niaura, SERS of the positive charge bearing pyridinium ring terminated self-assembled monolayers: structure and bonding spectral markers, J. Phys. Chem. C 119 (2015) 26481–26492.
[58] V. Kocherbitov, J. Latynis, A. Misiunas, J. Barauskas, G. Niaura, Hydration of lysozyme studied by Raman spectroscopy, J. Phys. Chem. B 117 (2013) 4981–4992.
[59] A. Misiunas, Z. Talaikyte, G. Niaura, V. Razumas, T. Nylander, *Thermomyces lanuginosus* lipase in the liquid-crystalline phases of aqueous phytantriol: X-ray diffraction and vibrational spectroscopy studies, Biophys. Chem. 134 (2008) 144–156.
[60] Z.-Q. Wen, Raman spectroscopy of protein pharmaceuticals, J. Pharm. Sci. 96 (2007) 2861–2878.
[61] B. Sjöberg, S. Foley, B. Cardey, M. Enescu, An experimental and theoretical study of the amino acid side chain Raman bands in proteins, Spectrochim. Acta A 128 (2014) 300–311.
[62] K. Czamara, K. Majzner, M.Z. Pacia, K. Kochan, A. Kaczor, M. Baranska, Raman spectroscopy of lipids: a review, J. Raman Spectrosc. 46 (2015) 4–20.
[63] S. Ye, H. Li, W. Yang, Y. Luo, Accurate determination of interfacial protein secondary structure by combining interfacial-sensitive amide I and amide III spectral signals, J. Am. Chem. Soc. 136 (2014) 1206–1209.
[64] A. Mirtič, J. Grdadolnik, The structure of poly-L-lysine in different solvents, Biophys. Chem. 175–176 (2013) 47–53.
[65] M. Szymanska-Chargot, M. Chylinska, P.M. Pieczywek, P. Rösch, M. Schmitt, J. Popp, A. Zdunek, Raman imaging of changes in the polysaccharides distribution in the cell wall during apple fruit development and senescence, Planta 243 (2016) 935–945.
[66] T.W. Barrett, Laser Raman spectra of mono-, oligo- and polysaccharides in solution, Spectrochim. Acta A 37 (1981) 233–239.
[67] J. Kneipp, H. Kneipp, M. McLaughlin, D. Brown, K. Kneipp, In vivo molecular probing of cellular compartments with gold nanoparticles and nanoaggregates, Nano Lett. 6 (2006) 2225–2231.
[68] S. Stewart, P.M. Fredericks, Surface-enhanced Raman spectroscopy of peptides and proteins adsorbed on an electrochemically prepared silver surface, Spectrochim. Acta A 55 (1999) 1615–1640.
[69] P. Kubbryk, R. Niessner, N.P. Ivleva, On the origin of the band at around 730 cm^{-1} in SERS spectra of bacteria: stable isotope approach, Analyst 141 (2016) 2874.
[70] O. Samek, A. Haroniková, J. Ježek, S. Bernatová, I. Márova, E. Breierová, M. Šerý, M. Šiler, P. Zemánek, Raman spectroscopy to monitor the effect of temperature regime and medium composition on microorganism growth, Proc. SPIE 10142 (2016) 101420B.

Supplementary data

Shell-isolated nanoparticle-enhanced Raman spectroscopy for characterization of living yeast cells

Agnė Zdaniauskienė[a], Tatjana Charkova[a], Ilja Ignatjev[a], Vytautas Melvydas[b], Rasa Garjonytė[a], Ieva Matulaitienė[a], Martynas Talaikis[c], Gediminas Niaura[a,*]

[a]*Department of Organic Chemistry, Center for Physical Sciences and Technology (FTMC), Saulėtekio Ave. 3, LT-10257 Vilnius, Lithuania*
[b]*Nature Research Centre, Akademijos 2, LT-08412 Vilnius, Lithuania*
[c]*Department of Bioelectrochemistry and Biospectroscopy, Institute of Biochemistry, Life Sciences Center, Vilnius University, Saulėtekio av. 7, LT-10257, Vilnius, Lithuania*

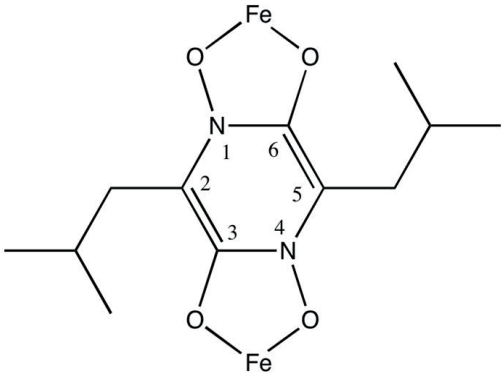

Fig. S1. Molecular structure of red pigment pulcherrimin with numbering of pyrazine ring atoms.

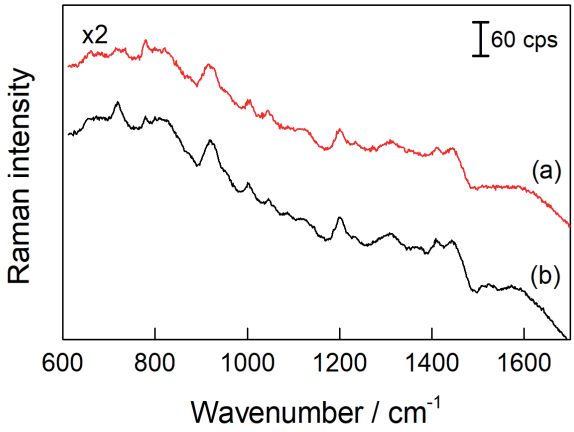

Fig. S2. Raw SHINERS spectra of *Metschnikowia pulcherrima* yeast cells. (a) Yeast cells with large amount of red pigment, and (b) yeast cells with low amount of red pigment. Excitation wavelength is 785 nm.

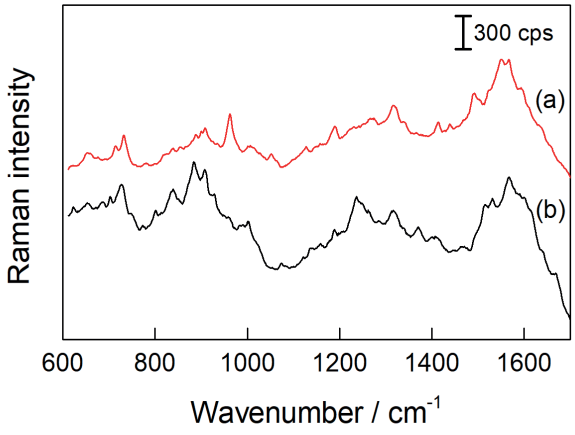

Fig. S3. Raw SERS spectra of *Metschnikowia pulcherrima* yeast cells. (a) Yeast cells with large amount of red pigment, and (b) yeast cells with low amount of red pigment. Excitation wavelength is 785 nm.

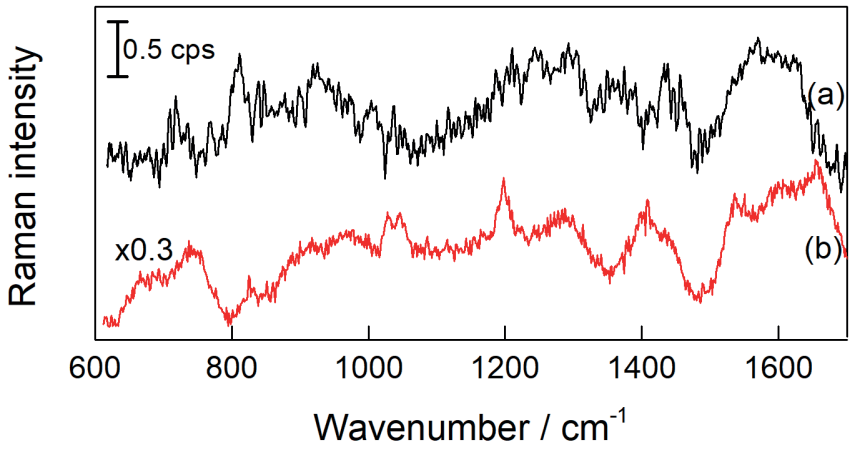

Fig. S4. Raman spectra of Au@SiO_2 (a) and bare Au (b) nanoparticles. Excitation wavelength is 785 nm.

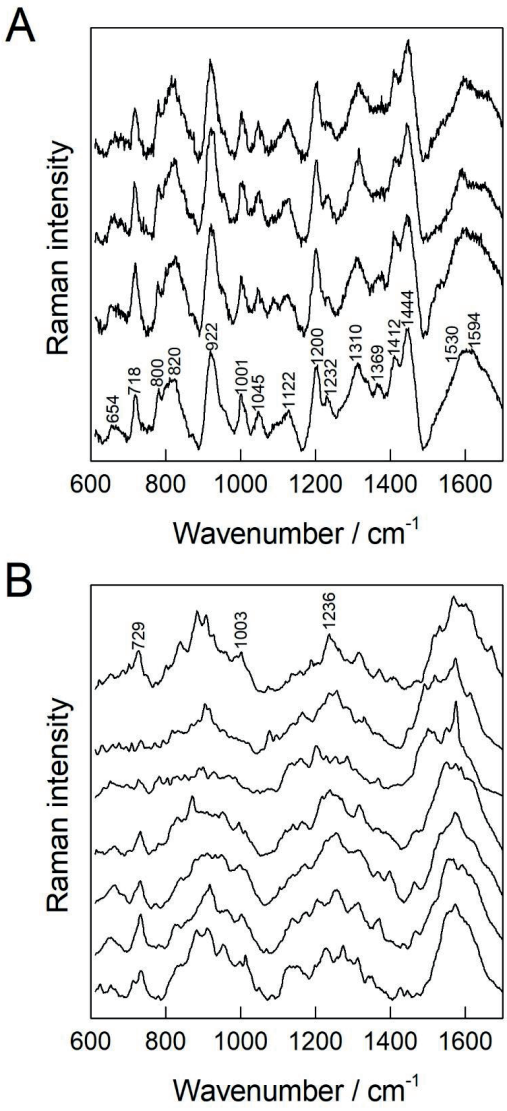

Fig. S5. Repeatability of SHINERS and SERS spectra of living yeast cells *M. pulcherrima* with low amount of pigment. Spectra are collected at different positions. (**A**) SHINERS spectra obtained with Au@SiO_2 nanoparticles, and (**B**) SERS spectra obtained with Au nanoparticles. Spectra are background corrected and shifted vertically for clarity.

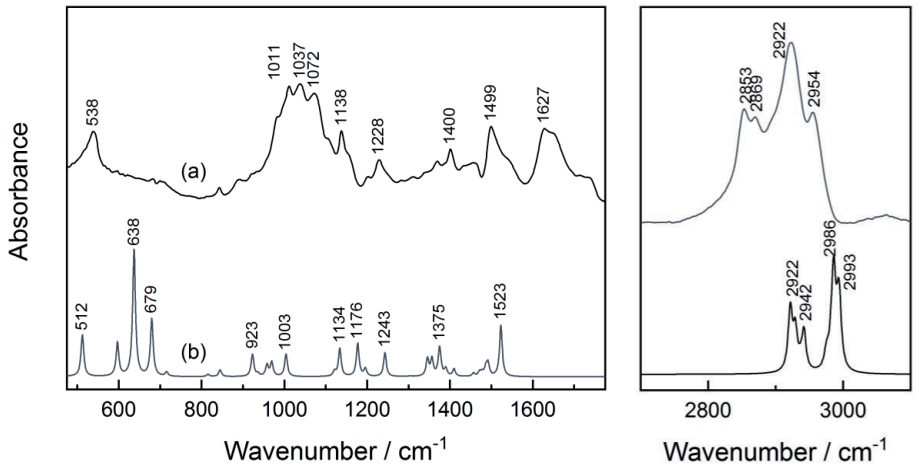

Fig. S6. ATR-FTIR spectrum of pulcherrimin powder (a) compared with the calculated infrared spectrum at B3LYP functional with 6-311++G(2d,p) basis set for C, H, N, and O atoms and LANDL2DZ with ECP for Fe atoms (b).

UŽRAŠAMS

Vilniaus universiteto leidykla
Saulėtekio al. 9, III rūmai, LT-10222 Vilnius
El. p. info@leidykla.vu.lt, www.leidykla.vu.lt
bookshop.vu.lt, journals.vu.lt
Tiražas 20 egz.